THE RATE OF THE BAINITE TRANSFORMATION

by

Philippe Opdenacker

Darwin College, Cambridge

Department of Materials Science and Metallurgy

Pembroke Street, Cambridge, CB2 3QZ

This dissertation is submitted for the degree of

Doctor of Philosophy,

at the University of Cambridge,

May 2001

Preface

This dissertation is submitted for the degree of Doctor of Philosophy at the University of Cambridge. The research described in this dissertation was conducted under the supervision of Professor H. K. D. H. Bhadeshia in the Department of Materials Science and Metallurgy, Cambridge, between January 1998 and May 2001. This work is to the best of my knowledge original, except where acknowledgement and reference is made to previous work. This dissertation is the result of my own work and includes nothing which is the outcome of work done in collaboration. Neither this, nor any substantial similar dissertation has been or is being submitted for any degree, diploma or other qualification at this, or any other, university. This dissertation contains less than 60,000 words.

Philippe Opdenacker

May 2001

Acknowledgements

I would like to thank Professor A. H. Windle for the provision of laboratory facilities in the Department of Materials Science and Metallurgy at the University of Cambridge.

I am extremely grateful to Professor Harry Bhadeshia, who as a supervisor and friend over my 3 years at the University has provided unparalleled support, enthusiasm and knowledge.

I would also like to thank the past and present members of the Phase Transformations Group, in particular Drs Carlos Capdevila Montes, Sree Harsha Lalam, Dave Cole, Franck Tancret, Shiv Brat Singh and Carlos Garcia Mateo. I must also mention Vicky Yardley, Nobuhiro Fujita, Gareth Hopkin, Miguel-Angel Yescas-Gonzales, Thomas Sourmail, Ariane Lugan, Dominique Carrouge, Daniel Gaude-Fugarolas, Chris and Dorothy Downs, Hiroshi Matsuda, Shingo Yamasaki, Jiang He and John Street for many happy days. I would like to express my gratitude to my friends Drs Francisca Garcia Caballero and Mike Lord for their humour, support and their attitude towards life that I have tried to emulate. I need also to thank Alessia, who is a very special person to me.

I am indebted to Drs Michel Piette and David Quidort as well as Matthieu Kandel and everyone at SOLLAC-CRDM and IRSID, for generously providing their skills and advice throughout this project. I wish also to acknowledge SOLLAC in conjunction with ANRT for their generous sponsorship.

To all my Darwin College and University friends for the best 3 years of my life and to those whom I am particularly indebted - Mikey, Ijoma, Rohan, Danny, Guido, Graham, Laura, Cath, Cecilia and Roxana.

To Dr Arnaud Tronche, who has been like a brother to me, for the best friendship I've ever experienced and many magnificent times.

I would like to dedicate this work to my parents, Bernadette and Mathieu for their love and support.

ABSTRACT

Bainite is an interesting solid–state transformation in steels and cast irons, one which is of increasing commercial importance. This is because it is now appreciated that with the help of phase transformation theory, the microstructure of bainite can be configured to give better mechanical properties than martensite, with fewer processing steps.

The production of commercial steels rarely involves isothermal heat treatments because they are impractical, both with respect to productivity and the need for uniform microstructures. It is necessary therefore to understand the consequences of anisothermal processing. The literature abounds with attempts at converting isothermal transformation data for bainite into continuous cooling data. All of these studies assume that the theory is appropriate; more surprisingly, there has never been a rigorous experimental validation of the procedures. The primary goal of the work presented in this thesis was, therefore, to adapt theory for the isothermal kinetics of the bainite transformation into that capable of treating anisothermal transformation, with corresponding experimental verification.

A survey of the published literature demonstrated that the most useful kinetic models for bainite deal strictly with isothermal transformation. The available kinetic theory contains various levels of empiricism, so the review helped identify the model which best represents the mechanism of the transformation. It is interesting that even with this model, a fundamental problem was discovered (and corrected); the autocatalysis function in the published model was grossly exaggerated, so much so that it was impossible to obtain certain observed shapes of isothermal transformation curves, no matter what values were assigned to the fitting constants.

Several formalisms for converting this isothermal transformation model for continuous cooling conditions were considered. The most popular method involves additivity, which essentially assumes an identical temperature dependence for each of the processes involved in the development of microstructure. Although this was demonstrated to be approximately the case, the most satisfactory method simply involves the integration of the differential equation representing reaction rate over temperature. Indeed, this is the only method which can allow properly for changes in the bainite sub–unit size as a function of temperature.

A great deal of experimental work was done to identify the exact conditions needed to produce bainite on its own, during isothermal or cooling transformations; martensite and retained austenite naturally are allowed phases at the termination of the bainite reaction. Some consideration was also given to checking reproducibility, both in terms of experimental equipment and by repeating experiments on the same apparatus. Some unique "bi–isothermal" and "two–step" experiments were designed to control the microstructure and to examine the effect of a sudden temperature change on the kinetic behaviour.

This also involved the development of a method to convert dilatometric data obtained as a function of temperature (or time) into bainite, martensite and retained austenite fractions.

An analysis of the experimental data revealed that in cases where the isothermal data are accurately represented by the theory, it is indeed possible to convert data obtained by transformation at a constant temperature, into continuous cooling transformation data. However, for reasons explained in the text, there are many cases where the maximum fraction obtained during isothermal reaction does not exactly follow theory, in which case errors arise in the conversion process.

Bearing all the difficulties in mind, it has been possible to define a theoretical framework for the conversion of isothermal experimental data for continuous cooling, and furthermore, justification has been provided for adapting the corresponding isothermal transformation theory for predicting cooling transformations.

Contents

List of Nomenclature ..... **ix**

Introduction **1**

1 The Bainite Transformation

1.1 Introduction: the Iron-Carbon Equilibrium Phase Diagram **5**

1.2 Ferrite Growth Mechanisms **7**

1.3 Reconstructive and Displacive Transformations **10**

1.3.a Reconstructive Transformations 11

1.3.b Displacive Transformations 12

1.4 Bainite Transformation Characteristics **13**

1.4.a Transformation Mechanism 13

1.4.b The Transition from Upper to Lower Bainite and Carbides 14

1.4.c Mechanism of Carbides Formation 16

1.4.d Distribution of Chemical Elements Across the Interface 18

1.4.e Shape Deformation and Crystallographic Orientations 19

1.4.f Mechanical Stabilisation 20

1.4.g The Incomplete Reaction Phenomenon 21

1.4.h Widmanstätten Ferrite, Acicular Ferrite and Overview of Transformations ... 22

1.4.i Unresolved Issues 24

1.5 Characteristic Mechanical Properties of Bainitic Microstructures **25**

1.6 Summary **27**

2 Existing Isothermal Models

2.1 Introduction **28**

2.2 General Isothermal Models **29**

2.2.a Equations for Representing Solid-State Isothermal Transformation Behaviour 29

2.2.b An Example of the Use of the JMAK Equation for Bainite 32

2.2.c The Isothermal Model due to Quidort [1999] 33
2.3 The General Theory of the Bainite Transformation 35
2.3.a The Thermodynamic Parameters 35
2.3.b The T_0 Criterion 37
2.3.c Universal Nucleation Function 40
2.3.d Growth of the Nucleus 42
2.3.e The Nucleation Rate 43
2.4 Rees and Bhadeshia Model 44
2.4.a Description 44
2.4.b Limitations of the Rees and Bhadeshia Model 46
2.5 The Singh and Bhadeshia Model 47
2.5.a Bainite Plate Volume 47
2.5.b Autocatalysis 48
2.5.c New Expression of the Nucleation Rate I_b 48
2.5.d New Empirical Constants Values 49
2.5.e Error in this Development 49
2.5.f Further Modifications to Account for Grain Size Effect 50
2.6 Factors Influencing the Bainite Transformation 51
2.6.a Austenite Enrichment in Carbon 51
2.6.b Role of Alloying Elements and Microalloying 53
2.6.c Influence of Austenite Grain Size 56
2.6.d Cooling Rate and Isothermal Transformation Temperature 58
2.7 Summary 59

3 Transition from Isothermal to Anisothermal Conditions

3.1 The Method of Increments 60
3.2 The Concept of Additivity 61
3.3 Conditions for Validity of the Additivity Rule 63
3.3.a Analytical Proof of Equation 3.6 [Christian, 1965b] 63
3.3.b Discussion 64
3.3.c Geometrical Criteria 68
3.3.d Limitations 69
3.4 Results of Previous Studies on the Additivity Rule 70
3.4.a Additivity Rule and the Pearlite Transformation 71

3.4.b Additivity Rule and the Allotriomorphic Ferrite Transformation 73
3.4.c Additivity Rule and the Bainite Transformation 74
3.4.d Additivity Rule and Precipitates 75
3.5 Summary **76**

4 Alloy Selection and Experimental Procedures

4.1 Introduction **77**
4.2 Alloy Selection **77**
4.3 Transformation Temperatures **79**
4.4 Heat Treatments and Dilatometry **81**
4.5 The Influence of the Equipment and of the Sample Size **86**
4.6 Method of Computation of the Transformed Bainite Fraction **89**
4.7 Microstructural Characterisation **92**
4.7.a Optical Microscopy 92
4.7.b Transmission Electron Microscopy (TEM) 93
4.7.c Vickers Macro-hardness 93
4.7.d Determination of the Retained Austenite Fraction 94
4.8 The Nucleation Rate **95**
4.9 Summary **98**

5 Experimental Study of Alloy A

5.1 Introduction **99**
5.2 Heat Treatments **100**
5.3 Isothermal Treatments **102**
5.4 Interrupted Quenching Experiments and Study of Expansivities **105**
5.4.a Interrupted Quenching Experiments 105
5.4.b Variation in Expansivities as Reaction Progresses 108
5.5 Transmission Electron Microscopy Characterisation (TEM) **113**
5.5.a Sample Transformed at 525°C for 5 min 114
5.5.b Sample Transformed at 475°C for 3 h 114
5.5.c Sample Transformed at 430°C for 5 min 115
5.6 Bi-isothermal Experiment **116**
5.7 Cooling Experiments **118**

5.7.a Continuous Cooling 118
5.7.b Bi-slope Experiments 118
5.8 Retained Austenite 120
5.9 Conclusions 121

6 Model Predictions for Alloy A

6.1 Introduction 122
6.2 Determination of Fitting Constants 122
6.2.a Using the Singh and Bhadeshia Model 122
6.2.b Back to Autocatalysis as Modelled by Rees and Bhadeshia 124
6.3 Isothermal Transformation 126
6.4 Bi-isothermal Transformation 130
6.5 Cooling Experiments 132
6.5.a Continuous Cooling 132
6.5.b Bi-slope Experiments 134
6.6 Conclusions 135

7 Model Predictions for Alloys B and C

7.1 Introduction 136
7.2 Heat Treatments and Analysis 139
7.3 Isothermal Transformations 139
7.3.a Alloy B 141
7.3.b Alloy C 145
7.4 Bi-isothermal Transformation 148
7.4.a Alloy B 148
7.4.b Alloy C 148
7.5 Cooling Experiments 150
7.5.a Alloy B 154
7.5.b Alloy C 157
7.6 Conclusions 159

8 Measuring the Martensite Fraction

8.1 Introduction **161**
8.2 Calculation of the Experimental Martensite Volume Fraction **161**
8.3 Conclusions **166**

9 Predictions with General Constants and Trends **167**

9.1 Predicted *CCT* Diagrams and Trends **167**
9.2 Conclusions **170**

10 Conclusions and Suggestions for Further Work **171**

Appendix 1- Heat Treatments **175**

Appendix 2- The Computer Programs **179**

1. The Physical Model **179**
1.a General Method 179
1.b The Subroutine MAP STEEL MUCG 181
2. Determination of the Experimental Bainite Fraction **186**

References **189**

List of Nomenclature

a_b	thickness of bainite sub-unit
$\bar{a}_\alpha$	ferrite lattice parameter at ambient temperature
a_α	ferrite lattice parameter at temperature T
$\bar{a}_\gamma$	lattice parameter of austenite enriched in carbon at ambient temperature
a_γ	lattice parameter of austenite enriched in carbon at temperature T
$a_{0\gamma}$	lattice parameter of non-enriched austenite in carbon at temperature T
$\bar{a}_{0\gamma}$	lattice parameter of non-enriched austenite in carbon at ambient temperature
a, b, c	constants associated with the parabolic shape of a TTT diagram in the expression of $k(T)$
a_{c_α}	activity of carbon in ferrite
a_{c_γ}	activity of carbon in austenite
a_{Fe_γ}	activity of iron in austenite
Ac_m	curve that defines the $\gamma/\gamma + Fe_3C$ phase boundary
Ac_1	temperature corresponding to Ae_1 during heating in non-equilibrium conditions
Ac_3	temperature corresponding to Ae_3 during heating in non-equilibrium conditions
Ae_1	equilibrium temperature at which the eutectoid reaction occurs
Ae_3	equilibrium $\gamma/\gamma + \alpha$ phase boundary
$Ae_3^{'}$	paraequilibrium $\gamma/\gamma + \alpha$ phase boundary
$Ae_3^{''}$	paraequilibrium $\gamma/\gamma + \alpha$ phase boundary, taking into account the stored energy
Ar_1	temperature corresponding to Ae_1 during cooling in non-equilibrium conditions
Ar_3	temperature at which ferrite α starts to transform into austenite during cooling
b_{NM}, b_N	coefficients associated with $\Delta T_{NM}, \Delta T_M$
B	magnetic induction
B_1, B_2	empirical constants associated with the expression of G_N
B_3	empirical constant representing the density of nucleation sites in the Rees and Bhadeshia model
$B_3^{'}$	empirical constant relating B_3 to d_γ

B_4, B_5	empirical constants associated with the expression of I, the nucleation rate
B_6	empirical constant related to d_γ representing the density of nucleation sites in the Singh and Bhadeshia theory
B_6'	empirical constant related to B_6 in the Singh and Bhadeshia theory
B_s	bainite-start temperature
C	variable introduced in the treatment of the bainite transformation rate
C_c	change in the austenite lattice parameter a_γ caused by the addition of unit concentration of carbon
C_1, C_2	constants
C_3, C_4	constants
d_γ	austenite grain size
dV_1^e, dV_2^e	increments in the extended volumes of phase 1 and 2
$\frac{dX}{dt}$	rate of transformation
D_i	diffusion coefficient of element i
D_{12}	interaction between the flux of two species 1 and 2
e_α	linear thermal expansion coefficient of ferrite
e_γ	linear thermal expansion coefficient of austenite
f	function describing the variable X
F	function of $h(T)$
$h(T)$	function of the time used to express the rate of transformation $\frac{dX}{dt}$ as a function of separate variables temperature T and fraction X
H_c	coercivity
g_T	the growth rate of a bainite sub-unit in the reconstructive model
$g(X)$	function of the fraction used to express the rate of transformation $\frac{dX}{dt}$ as a function of separate variables temperature T and fraction X
$G, G(T)$	growth rate
G_N	universal nucleation function
G^*	activation energy for nucleation of bainite
h	Planck constant
h, l, w	dimensions of a bainite plate in the reconstructive model
H	magnetic field
HV	Vickers hardness
$j(X)$	function of the fraction used to express the rate of transformation
$J(X)$	integral function of $g(X)$

$I, I(T)$	nucleation rate
I_b	total nucleation rate per unit volume for bainite
I_{T_h}	nucleation rate at the temperature T_h
$k, k(T)$	kinetic parameter known as the *rate constant* in the Avrami Equation
k_b	Boltzmann constant
K_1, K_2, K_3	empirical constants in Quidort's model
$\bar{L}$	mean linear intercept length of the grain size
L_0	initial length of a sample
m	kinetic parameter associated with the type of nucleation sites in the Avrami equation
M_R	remanent magnetisation
M_s	martensite-start temperature
M_{Sat}	saturation magnetisation
n	kinetic parameter known as the *time exponent* in the Avrami Equation
N_0	initial number density of nucleation sites per unit of grain boundary area
N_V^0	initial number density of nucleation sites
N_V^T	total number density of nucleation sites
P	symbol for pearlite
$Q(T)$	cooling rate, equal to $-\frac{dT}{dt}$
Q_c^γ	activation energy for the diffusion of carbon in austenite
r	radius of a cylindrical sample
R	the gas constant
S_v	number density of nucleation sites per unit volume
t_m	measured reaction time
t_p	predicted reaction time
$t_a(T)$	time taken to precipitate a certain phase fraction X_a at an arbitrary temperature T
$t_{0.5}$	time for the completion of one half of the transformation
t_s	observed start time during an isothermal transformation (time at which a dilatation increase is first detected)
T_{amb}	room temperature
T_b	bay temperature for the bainite transformation
T_c	highest temperature at which cementite can precipitate from residual austenite of a given carbon concentration
T_γ	austenitisation temperature

T_h	highest temperature at which displacive transformation to ferrite can take place
T_{iso}	isothermal transformation temperature
T_{nr}	non-recrystallisation temperature
T_{quench}	temperature at which quenching is started
T_0	temperature at which γ and α of the same composition have the same free energy
T_0'	as T_0 but accounting for the stored energy of ferrite
u	volume of a bainite sub-unit
$v, v(t)$	volume fraction of bainite
v_γ	volume fraction of austenite
$v_{\alpha'}$	volume fraction of martensite
v_i	interface velocity
v_1	volume fraction of phase 1 forming in a sample of volume V_s
$V, V(t)$	volume of bainite
V_γ	volume of austenite
V_1, V_2	volume of phase 1 or 2 forming in a sample of volume V_s
V_1^e, V_2^e	extended volume of phase 1 or 2
V_s	total volume of a sample undergoing transformation
V_{s0}	initial volume of a sample
V^e	extended bainite volume
$V(t,\tau)$	volume, at time t, of the bainite nucleated in the time interval between τ and $\tau + d\tau$
W	weight function
W_s	Widmanstätten ferrite-start temperature
$\bar{x}$	average mole fraction of carbon in an alloy
x	mole fraction of carbon
x_α	carbon concentration in ferrite
x_γ	carbon concentration in austenite
$x^{\alpha\gamma}$	mole fraction of carbon in ferrite in equilibrium or parequilibrium with austenite
$x^{\gamma\alpha}$	mole fraction of carbon in austenite in equilibrium or parequilibrium with ferrite
x_m^α	mole fraction of carbon in ferrite nucleus for maximum free energy change
x_{T_0}	carbon concentration given by the T_0 curve
$x_{T_0'}$	carbon concentration given by the T_0' curve

X	generic term for a substitutional solute element
$X, X(T)$	volume fraction of product phase formed (in the study of additivity)
X_e	thermodynamic equilibrium fraction of ferrite which can be determined from the equilibrium phase diagram with given temperature and chemical composition
Y_i	atom fraction of the ith substitutional alloying element when the presence of carbon is disregarded
z	direction perpendicular to the interface, along which diffusion happens
z_γ	distance away from a sub-unit at which the carbon concentration becomes less than $x_{T_0'}$
α	symbol for ferrite
α'	symbol for martensite
α_b	symbol for bainite
$\alpha_{b,L}$	symbol for lower bainite
$\alpha_{b,U}$	symbol for upper bainite
α_p	constant relating the bainite plate volume u to the cube of its thickness a_b
α_{th}	thermal diffusivity
β	autocatalysis factor for bainite nucleation
Δf^*	Zener ordering term
$\Delta G^{\gamma\rightarrow\alpha}$	free energy change for austenite to ferrite transformation without any composition change
$\Delta G^{\gamma\rightarrow\gamma'+\alpha}$	free energy change associated with the equilibrium decomposition of one mole of austenite into a mixture of austenite and ferrite
ΔG_1	same as $\Delta G^{\gamma\rightarrow\gamma'+\alpha}$ but expressed per mole of ferrite
ΔG_2	free energy change accompanying the formation of one mole of ferrite nuclei of composition x_α
ΔG_m	maximum molar free energy change for nucleation
ΔG_m^0	initial value ($\xi = 0$) of ΔG_m
$\Delta \bar{H}_\alpha$	excess partial molar enthalpy of solution of carbon in ferrite
$\Delta \bar{H}_\gamma$	excess partial molar enthalpy of solution of carbon in austenite
$\frac{\Delta L}{L_0}$	experimental dilatational strain recorded by dilatometry
ΔS_α	excess partial molar entropy of solution of carbon in ferrite
ΔS_γ	excess partial molar entropy of solution of carbon in austenite
ΔT_{NM}	change in the non-magnetic component of the T_0 temperature due to a chemical element

ΔT_M	change in the magnetic component of the T_0 temperature due to a chemical element
$\frac{\Delta V}{V}$	calculated value of the volume change
Φ_1, Φ_2	carbon fluxes
γ	symbol for austenite
γ_R	symbol for retained austenite
Γ_2	empirical constant
λ_1, λ_2	empirical constants relating β to $\bar{x}$
μ_0	permeability of vacuum
ν	frequency that represents the rate at which an individual site becomes a nucleus
ω_t	volume of a growing particle at time t
ω_γ	carbon-carbon interaction energy
ρ	density of a material
ρ_α	density of ferrite
ρ_γ	density of austenite
σ_γ	yield strength of austenite
σ_{Sat}	saturation magnetisation
τ	incubation time or alternatively variable for time
τ_t	incubation time for the ideal TTT curve
θ_b	maximum volume fraction of bainite possible at a given temperature
ξ	volume fraction v divided by the equilibrium or limiting volume fraction θ_b
ζ	coefficient used in the evaluation of the expected fractional change in volume

Introduction

Industrial steels with good mechanical properties are today produced by hot-rolling followed by cooling at a variety of rates. This thermomechanical processing combines heat treatment with mechanical deformation (Figure 1). By carefully controlling the steel composition and all the parameters of the thermomechanical process, one can obtain a final microstructure with enhanced mechanical properties. Hence, it is of enormous importance for the steelmakers to accurately control and optimise production parameters in order to reduce costs.

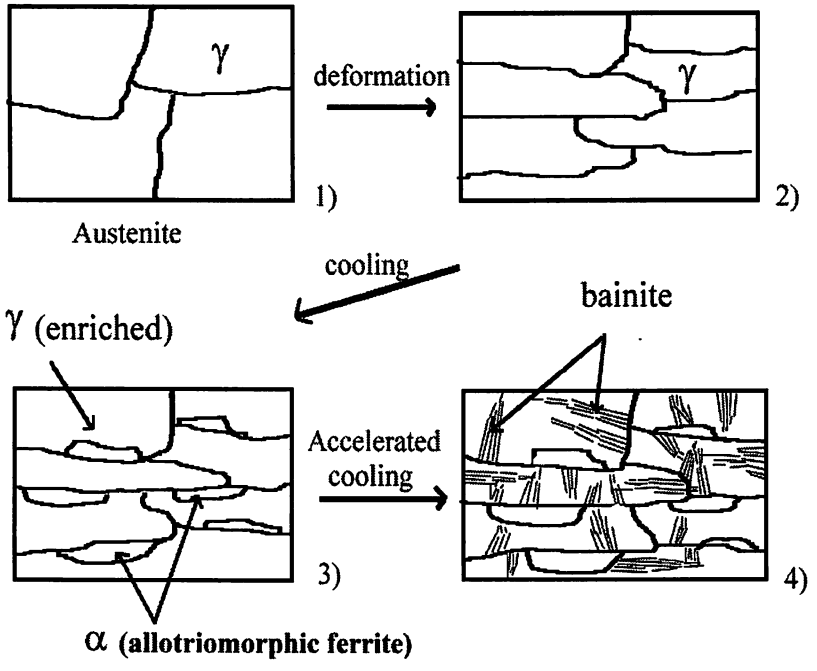

Fig. 1: Schematic illustration of the transformations which occur during cooling from the austenite phase field.

During thermomechanical processing, the development of microstructure is controlled by adjusting the deformation schedule (controlled rolling) and by resorting to accelerated cooling after rolling. The latter has been made possible by advances in rolling technology which allow

rapid cooling without undue distortion. Two main advantages result from that process:

- the final grain size can be refined. Grain refinement is the only practical method for improving both the strength and toughness of an alloy.
- with the right deformation and cooling parameters, the need for expensive post-working heat treatments disappears.

In recent years, there has been considerable interest in microstructures comprising *bainite*, which offer enhanced mechanical properties. Because of the increased feasibility of accelerated cooling, bainitic steels with leaner alloying can now be produced on a large scale. Many industrial steels now have total alloying additions that do not exceed 2 wt%. This improves weldability because of the lower 'carbon equivalent'† and reduces the cost of microalloying elements.

Bainitic steels are now used for a variety of applications:

- Tubes for the pipe-line industry are now increasingly bainitic, with low carbon contents ($0.02 < C\ (wt\%) < 0.08$) to meet the property requirements compatible with use at higher gas pressures or in deep water. Bainitic microstructures have successfully replaced ordinary ferrite-pearlite mixtures.
- Bainitic *forging steels* have advantages over martensitic alloys because they don't require complex annealing heat treatments or a high hardenability.
- Bainitic *creep resistant steels* have now been used for decades in the power generation industry [Bhadeshia *et al.*, 1998].
- *Dual-phase steels* used in the automobile industry have a microstructure comprising ferrite, and a harder phase (martensite or bainite). The mechanical properties are best when the latter is actually a mixture of bainite and retained austenite films. Thin bainite laths give high strength and toughness whereas the retained austenite films act as barriers to the propagation of cracks. The austenite also can transform to martensite under the effect of stress or plastic deformation, thereby contributing to toughness.
- Bainite can be induced to nucleate intragranularly on particles to give a chaotic microstructure in *inoculated steels*. Such a disorganised microstructure is more resistant to crack propagation than when the plates are organized in packets.

† In welding, it is essential to have a steel with a low carbon equivalent, which is a factor incorporating the effects on hardenability of the common alloying elements. A simple empirical relationship [Dearden and O'Neill, 1940], as a rough guide, is:

$$\%\,\text{carbon equivalent} = C + [\tfrac{Mn+Si}{6}] + [\tfrac{Cr+Mo+V}{5}] + [\tfrac{Ni+Cu}{15}] (\text{in wt}\%)$$

Edgar Bain and Davenport (1930) discovered bainite while studying the isothermal decomposition of austenite. Bainite is a generic term for fine aggregates of ferrite plates (or laths) and cementite particles. Bainite forms in the intermediate temperature region of a time-transformation-temperature (TTT) diagram, at temperatures typically in the range 250-550°C. It is different from pearlite and forms at higher temperatures than martensite. During continuous cooling, bainite forms at cooling rates too fast for pearlite, yet not rapid enough to induce martensitic transformation. Because of that, there has been much discussion as to whether bainite, like pearlite, is a diffusional transformation or like martensite grows by displacive transformation.

Austenite, which is face-centred cubic (fcc), may transform into a variety of body-centred cubic (bcc) ferritic products. Depending on the driving force and atomic mobility available at a given temperature, austenite can transform to allotriomorphic ferrite, pearlite, Widmanstätten ferrite, bainite or martensite by one of the two mechanisms mentioned above.

For some years there has been a need in industry for models capable of predicting the microstructures, and hence the mechanical properties, of steels with input parameters representative of industrial conditions. This enormous task was first tackled about four decades ago when researchers started to calculate phase diagrams [Hillert, 1962; Kaufman and Radcliffe, 1962]. Using experimental thermodynamic data combined with clever methods of solving systems of non-linear equations, there are now several commercially available computer programs for the calculation of phase diagrams. However, phase diagrams can only be used for equilibrium conditions, or by extrapolation of the phase boundaries, for regions where the phases are in metastable equilibrium.

Most industrial processes deviate from equilibrium. The emphasis in modelling is therefore on complex kinetic theory which enables the estimation of microstructure as a function of composition and thermomechanical treatment.

The aim of this work is to develop a kinetic model for the bainite transformation in anisothermal conditions, with the intention of validating the theory for several alloys. The model should be capable of predicting the bainite transformation-start and finish temperatures according to chemical composition for almost any kind of cooling path (continuous or discontinuous). It would be useful to estimate the amount of martensite and austenite retained in the final microstructures.

To achieve this goal, the present study will focus on the formalisms that can be used to adapt isothermal transformation theory to anisothermal conditions. The basis for the isothermal theory relies on a model developed by Bhadeshia *et al.* over the years, which is probably

the most complete and least empirical of all existing models. Surprisingly, very little work exists in the scientific literature on the transition from isothermal to anisothermal kinetics for the bainite reaction when a physical model is used; hence the present work.

The main characteristics of the bainite transformation are described in Chapter 1, including a discussion of any uncertainties. This assessment is then used to justify the approach adopted. Chapter 2 reviews the theory for isothermal transformation. However, there are limitations, so other isothermal models are discussed as well. Chapter 3 is dedicated to the formalisms behind the transition from isothermal to anisothermal kinetics. Results from published work are reviewed.

Chapter 4 introduces the experimental techniques and the range of alloys used to validate the model. The experimental results are presented in chapters 5-6.

The accuracy of a model cannot be validated on only one alloy, so Chapter 7 repeats the comparisons of Chapter 6, but for the two other alloys. Chapter 8 gives the details of the method used to measure the martensite fraction from dilatometric data. In Chapter 9, the model is used to calculate CCT diagrams in order to check that known effects of varying chemical composition are predicted well.

Chapter 10, finally, draws conclusions on the present work and suggests further areas of work, most notably the incorporation of this work in a 'Grand Model' that could take into account all phase transformations in a complex thermomechanical treatment.

Chapter 1

The Bainite Transformation

1.1 Introduction: the Iron-Carbon Equilibrium Phase Diagram

The iron-carbon equilibrium diagram (Figure 1.1) is the starting point for the discussion of phase transformations in steels. The phases found in the binary system Fe-C are also present in complex alloys, although their relative stabilities change with alloying. Figure 1.1 in fact represents part of the metastable equilibrium between iron and iron carbide (cementite). True equilibrium is associated with graphite but the latter is of little practical importance as it is difficult to obtain, except in cast irons (2-4C wt%).

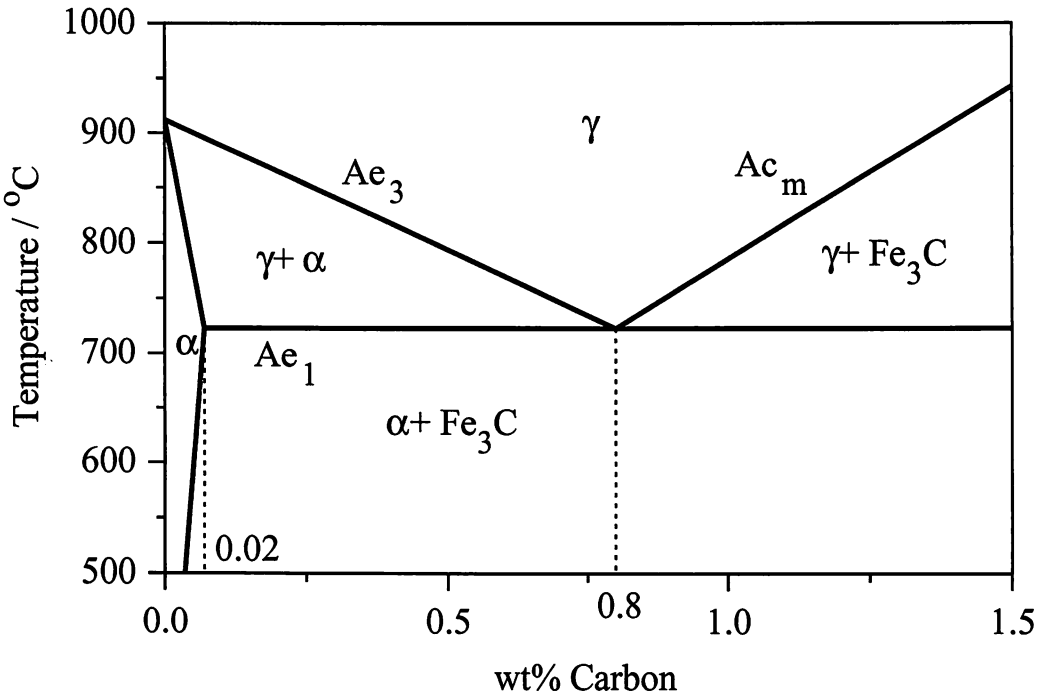

Fig. 1.1: The iron-carbon diagram (after Hansen, 1958).

The much larger field of γ-iron (austenite) compared with that of α-iron (ferrite) reflects the greater solubility of carbon in γ-iron. This high solubility is of extreme importance in

heat treatment, when solution treatment in the γ-region followed by rapid quenching to room temperature allows a supersaturated solid solution of carbon in iron to be formed. The α-iron phase field is severely restricted, with a maximum carbon solubility of 0.02 wt% at 723°C, so over the carbon range encountered in steels from 0.05 to 1.5 wt%, α-iron is normally associated with iron carbide of one form or another.

Elements such as Ni, Mn, Co and N expand the γ phase field by increasing the compositional limits within which austenite exists and are thus known as 'austenite stabilisers'. Conversely, elements such as Si, Al, Cr and Nb contract the γ phase field by reducing the stability of the austenite and are thus known as 'ferrite stabilisers'.

There are two temperatures in Figure 1.1 which are important, both from the basic and from the practical point of view. Firstly, there is the Ae_1 (equilibrium) temperature at which the eutectoid reaction occurs, which is 723°C in the binary diagram. Secondly, there is the Ae_3 temperature when α-iron transforms to γ-iron. For pure iron this occurs at 910°C, but the transformation temperature is progressively lowered by the addition of carbon. When using thermal analysis or dilatometry, the corresponding temperatures are Ac_1 and Ac_3 on heating and Ar_1 and Ar_3 during cooling. These values are sensitive to the rates of heating and cooling, as well as to the presence of alloying elements.

The transformation of $\gamma \rightarrow \alpha$-iron + Fe_3C occurs via a eutectoid reaction which plays a dominant role in heat treatment. The eutectoid temperature is 723°C while the eutectoid composition is about 0.80 wt% (Figure 1.1). On cooling alloys containing less than 0.80 wt% slowly, hypo-eutectoid ferrite is formed from austenite in the range 910-723°C resulting in the enrichment of the residual austenite with carbon, until at 723°C the remaining austenite, now containing 0.80 wt% carbon transforms to pearlite, a lamellar mixture of ferrite and cementite. In austenite containing more than 0.80 wt% carbon, on cooling slowly to 723°C, cementite first forms, progressively depleting the austenite in carbon, until at 723°C, the austenite contains 0.80 wt% carbon and transforms to pearlite. Steels with less than about 0.80 wt% carbon are thus hypo-eutectoid alloys with ferrite and pearlite as the prime constituents, the relative volume fractions being determined by the lever rule which states that as the carbon content is increased, the percentage of pearlite increases, until it is 100 % at the eutectoid composition.

Ferrite, cementite and pearlite are thus the principle constituents of the microstructure of plain carbon steels, when they have been subjected to relatively slow cooling rates to avoid the formation of metastable phases, such as bainite or martensite.

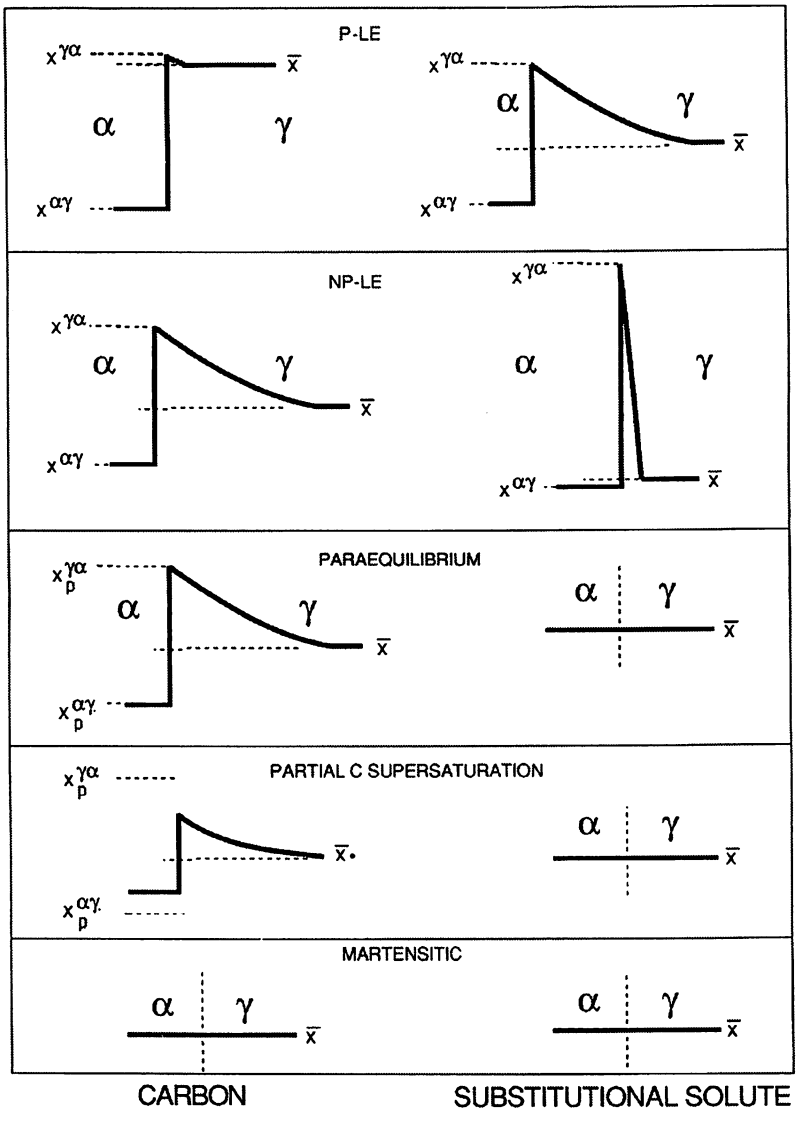

Fig. 1.2: Schematic illustration of the composition variation expected in the vicinity of the transformation interface, for a variety of growth mechanisms [Bhadeshia, 1992].

1.2 Ferrite Growth Mechanisms

In a ternary system Fe–C–X, where X represents any substitutional element (Mn, Si, Ni *etc.*), the diffusion-controlled growth of ferrite is complicated by the fact that the interstitial solute has a diffusion coefficient several orders of magnitude greater than substitutional solutes.

For the equilibrium condition to be respected at the interface (hence the name *local equilibrium*), in an alloy of average compositions $\overline{x}_1$ and $\overline{x}_2$, mass conservation requires that:

$$(x_1^{\gamma\alpha} - x_1^{\alpha\gamma})v_i = -D_1(\partial x_1/\partial z)\Big|_{z=z^*} \tag{1.1}$$

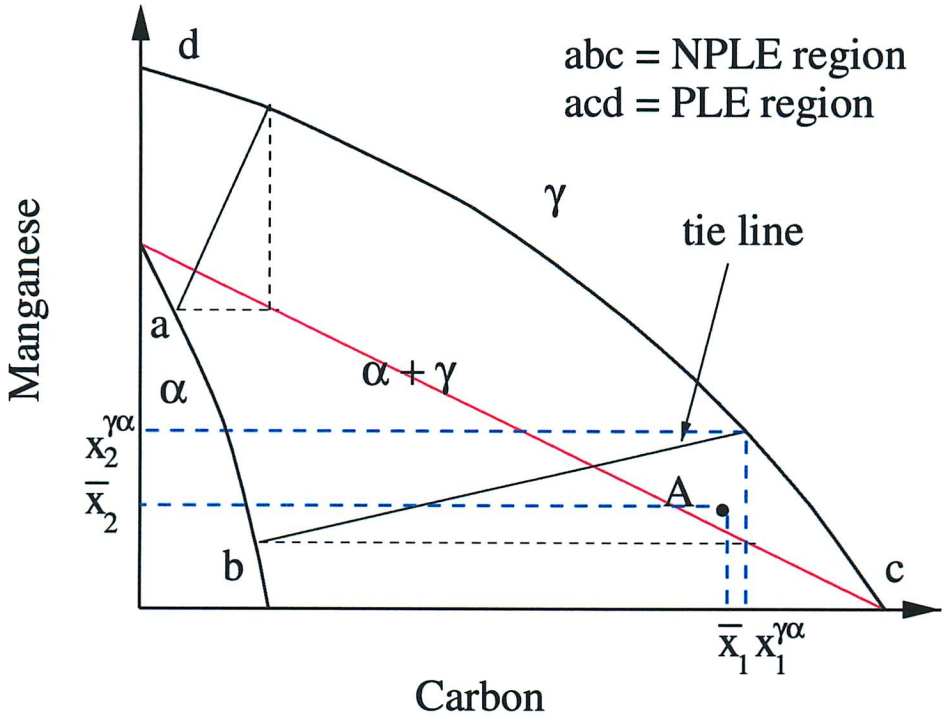

Fig. 1.3: Schematic isothermal section of the Fe-Mn-C system, illustrating conditions for ferrite growth with local equilibrium at the α/γ interface. Point A is situated in the domain where the PLE mechanism operates.

$$(x_2^{\gamma\alpha} - x_2^{\alpha\gamma})v_i = -D_2(\partial x_2/\partial z)\Big|_{z=z^*} \tag{1.2}$$

where $x_i^{\gamma\alpha}$ and $x_i^{\alpha\gamma}$ are the compositions in element i ($i = 1$ for C and $i = 2$ for X, taken as Mn for example) of γ and α at the interface and D_i is the diffusion coefficient of element i. z is the direction perpendicular to the interface, along which diffusion happens.

The interaction between the fluxes of the two species D_{12} is neglected to simplify the treatment in equations 1.1 and 1.2. It can be readily seen that for both equations to be satisfied simultaneously, there are two possibilities [Kirkaldy, 1958; Coates, 1973a], since the interface velocity v_i must be identical in the two equations:

- $(\partial x_1/\partial z)$ is close to zero.
- $(\partial x_2/\partial z)$ is close to infinity.

The first possibility corresponds to the Partitioning Local Equilibrium (PLE) mode of transformation (Figures 1.2 and 1.3) [Purdy *et al.*, 1964; Coates, 1973b]. This happens at low supersaturation, that is when the average carbon composition $\overline{x}_1$ is close to $x_1^{\gamma\alpha}$. The gradient in carbon is reduced, allowing Mn to keep up with carbon diffusion.

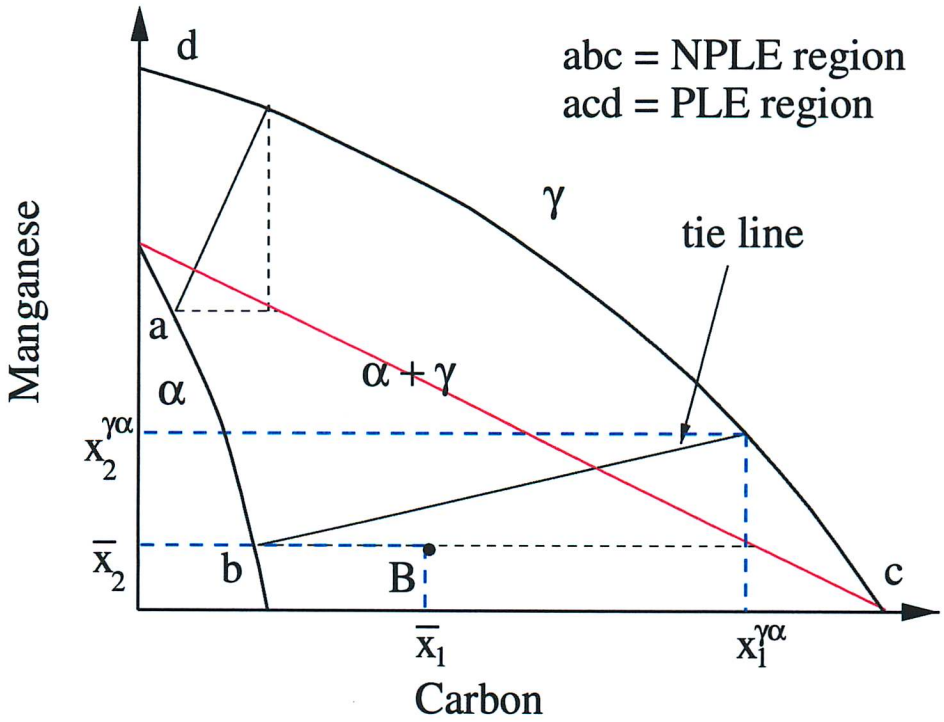

Fig. 1.4: Schematic isothermal section of the Fe-Mn-C system, illustrating conditions for ferrite growth with local equilibrium at the α/γ interface. Point B is situated in the domain where the NPLE mechanism operates.

The second corresponds to the Negligible Partitioning Local Equilibrium (NPLE) mode. This happens at high supersaturations and there is negligible partitioning of substitutional element (Mn) between the α and γ lattices (Figures 1.2 and 1.4). However, the gradient of manganese in γ near the interface is very large, which again allows Mn diffusion (confined to the immediate vicinity of the interface) to keep up with the long-range diffusion of C.

To accommodate for the PLE and NPLE modes, tie-lines in a section of the ternary equilibrium diagram Fe–C–Mn that join the equilibrium compositions of the two phases α and γ do not pass through the point representing the average composition of the alloy and the PLE and NPLE domains are delimited by the line (ac) on Figures 1.3 and 1.4. A qualitative analysis for ternary steels was first developed by Hillert [1953].

When the difference between interstitial and substitutional diffusion coefficients is high enough (for example at low enough temperatures), the situation arises where the distance over which substitutional element diffusion is allowed in the NPLE mode becomes less than the inter-atomic distance. This situation is called *paraequilibrium* [Hultgren, 1951; Rudberg, 1952; Aaronson *et al.*, 1966 a,b]. For paraequilibrium, there is absolutely no redistribution of substitutional elements across the interface (Figure 1.2). One might say that it is possible for

Fe + X atoms to move in the incoherent interface. Another interpretation of paraequilibrium is that only displacive transformation is possible. It will be seen that bainite, which was first studied in detail by Robertson [1929] and later by Davenport and Bain [1930], *nucleates* by the paraequilibrium mechanism, with the partitioning of interstitial carbon [Bhadeshia, 1981b].

A martensitic transformation is one where neither interstitial nor substitutional elements can redistribute (Figure 1.2). The growth of bainitic ferrite is martensitic.

1.3 Reconstructive and Displacive Transformations

Reconstructive and displacive transformations differ by the way the lattice atoms rearrange across the transformation interface.

In a *reconstructive* transformation, *all* the atoms are transferred across the interface in an uncoordinated manner and this is sometimes compared with the movement of civilians. The process is thermally activated and satisfies the change in lattice structure while minimising the strain energy. There is, due to the new structure, a change in volume.

The analogy with military movement is often used to describe *displacive* transformations. To accommodate the new crystal structure, at low temperatures, the only possibility is for the atoms to move in a coordinated manner across the interface, without any diffusion of substitutional atoms. Consequently, the shape of the whole crystal changes. This deformation has been shown macroscopically to be an invariant plane-strain with a relatively high shear component. To minimise the strain energy induced in the surrounding matrix by this shape deformation, the product phase must grow in the form of thin plates. The important characteristic of a displacive transformation is that there is an atomic correspondence between the phases: corresponding planes and vectors in the two phases are related in a particular way. Interstitial atoms may or may not diffuse, but if they do so because of a higher diffusivity, this does not alter the crystal structure [Christian, 1965]. The interface between the parent and product phase is coherent or semi-coherent. The interface dislocations can move conservatively, which leaves the interface glissile and capable of moving without diffusion. A discussion about the nature of the interface in the bainite transformation is presented later in this chapter.

Figure 1.5 schematically represents the differences between a reconstructive and a displacive transformation.

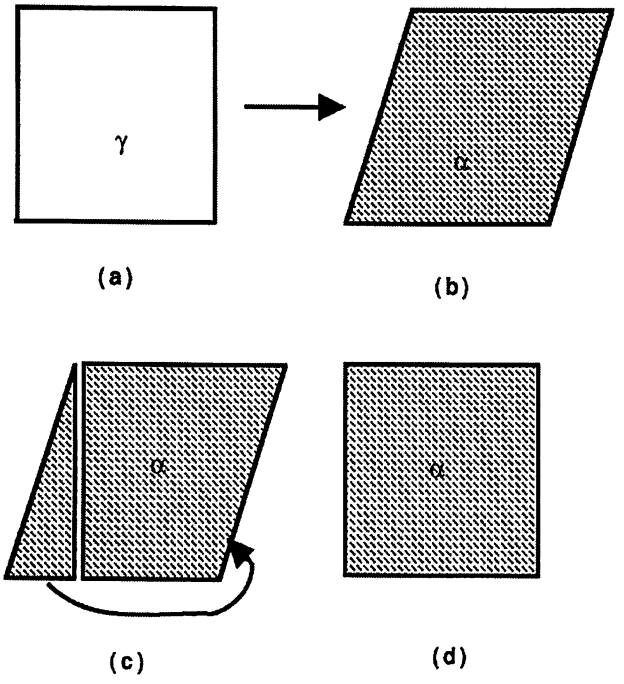

Fig. 1.5: Schematic illustration of the mass transport necessary to achieve reconstructive transformation, in both pure metals and alloys. Steps (a) to (b) represent displacive transformation, whereas (a) to (d) represent reconstructive transformation. The mass transport illustrated in (c) eliminates the shape change due to the shear [Bhadeshia, 1992].

1.3.a Reconstructive Transformations

Below the maximum temperature Ae_3 at which both austenite and α-ferrite can coexist at equilibrium, *allotriomorphic ferrite* is the first phase to form. The transformation requires all the atoms to diffuse. Nucleation is heterogeneous because it occurs only at austenite grain boundaries and allotriomorphic ferrite can grow on both sides of the boundary. *Idiomorphic ferrite* forms by the same mechanism but is nucleated inside the austenite grain, usually on non-metallic inclusions.

Pearlite is formed by the cooperative growth of ferrite and cementite (Fe_3C) which grow at similar rates and has a lamellar structure. Pearlite nodules can be initiated at grain boundaries, on inclusions or at the ferrite-austenite interface. The first pearlite constituent to nucleate is ferrite in a hypo-eutectoid steel and cementite in a hyper-eutectoid steel. It has been proposed that cementite can only form in a hypo-eutectoid steel at a given temperature, if the austenite composition lies to the right of the extrapolated curve which defines the $\gamma/\gamma+ Fe_3C$ phase boundary. This criterion is illustrated on Figure 1.11.

1.3.b Displacive Transformations

Martensite is a phase that generally forms at temperatures too low for diffusion to be significant. Indeed, martensite has been reported to form at the speed of sound in some alloys with audible clicks for the formation of each lath or plate. There is no diffusion at all during its formation, and therefore martensite can be supersaturated with carbon. This can make it very hard and brittle. Martensitic alloys are 'tempered' to give ferrite and finely dispersed carbides with a good combination of strength and toughness. The highest temperature at which martensitic transformation becomes possible is called M_s, the martensite-start temperature.

The typical time-temperature diagram (TTT) illustrated in Figure 1.6 shows that *bainite* occurs in an intermediate temperature regime between the pearlite and martensite transformations.

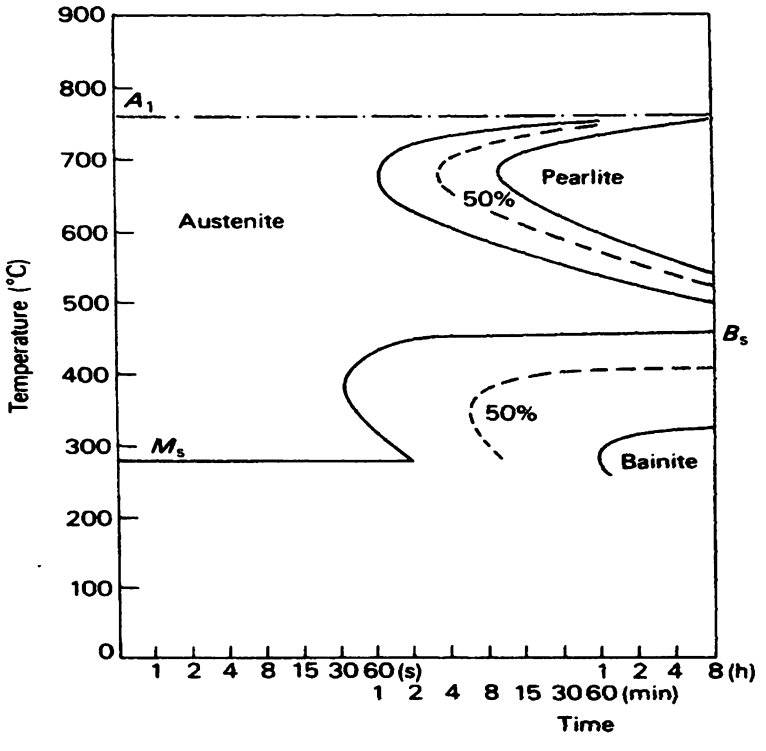

Fig. 1.6: TTT diagram for a Fe-3Cr-0.5C wt% steel [Thelning, 1975].

1.4 Bainite Transformation Characteristics

1.4.a Transformation Mechanism

By the displacive mechanism [Oblak an Hehemann, 1967], bainitic ferrite is considered to grow by the propagation of discrete martensitic sub-units, the aggregate of these sub-units constituting the classical sheaf of upper bainite. The sheaf itself has a plate-like morphology and its formation involves the autocatalytic nucleation of successive sub-units. The width of the sub-units observed by Oblak and Hehemann was about 0.5 μm, with a length of about 10 μm.

On the other hand, Aaronson and Kinsman maintain that the observed sub-units are in fact ledges (Figure 1.7) propagating along the broad faces of bainite plates [Hehemann, Kinsmann and Aaronson, 1970b]. Based on thickening rates obtained from the *in situ* thermionic emission microscopy observations following the work of Grube and Rouze [1967], they calculated an expected inter-ledge spacing of *ca.* 0.5 μm which was claimed to be consistent with the 0.3-8.0 μm ledges observed in the thickening of pro-eutectoid ferrite plates in the Fe-C system [Kinsman *et al.*, 1975]. They claimed a direct correspondence between ledges and sub-units. Additionally, they suggested that if the ledge mechanism is accepted, the apparent lengthening kinetics are consistent with a diffusion-controlled growth mechanism.

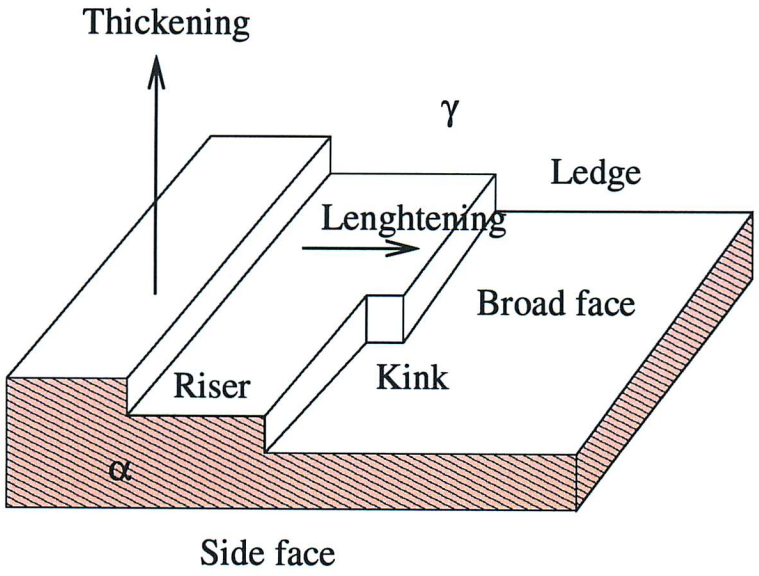

Fig. 1.7: Schematic illustration of the ledge growth mechanism proposed by Aaronson *et al.*

Bhadeshia and Edmonds [1979] undertook an examination of the structure of bainite in a silicon steel and found that the sheaf of upper bainite, which had the appearance of a

plate on the scale of optical microscopy, in fact consisted of smaller sub-units (*ca.* 0.2 μm wide). Furthermore, they showed that these could not possibly be compared with ledges since the individual sub-units were, for the most part of their interfaces, isolated by carbon-enriched retained austenite films. Their montage of transmission electron microscopy (TEM) micrographs illustrated the morphology and substructure of a whole sheaf of upper bainite [Bhadeshia and Edmonds, 1980]. A similar montage is shown on Figure 1.8.

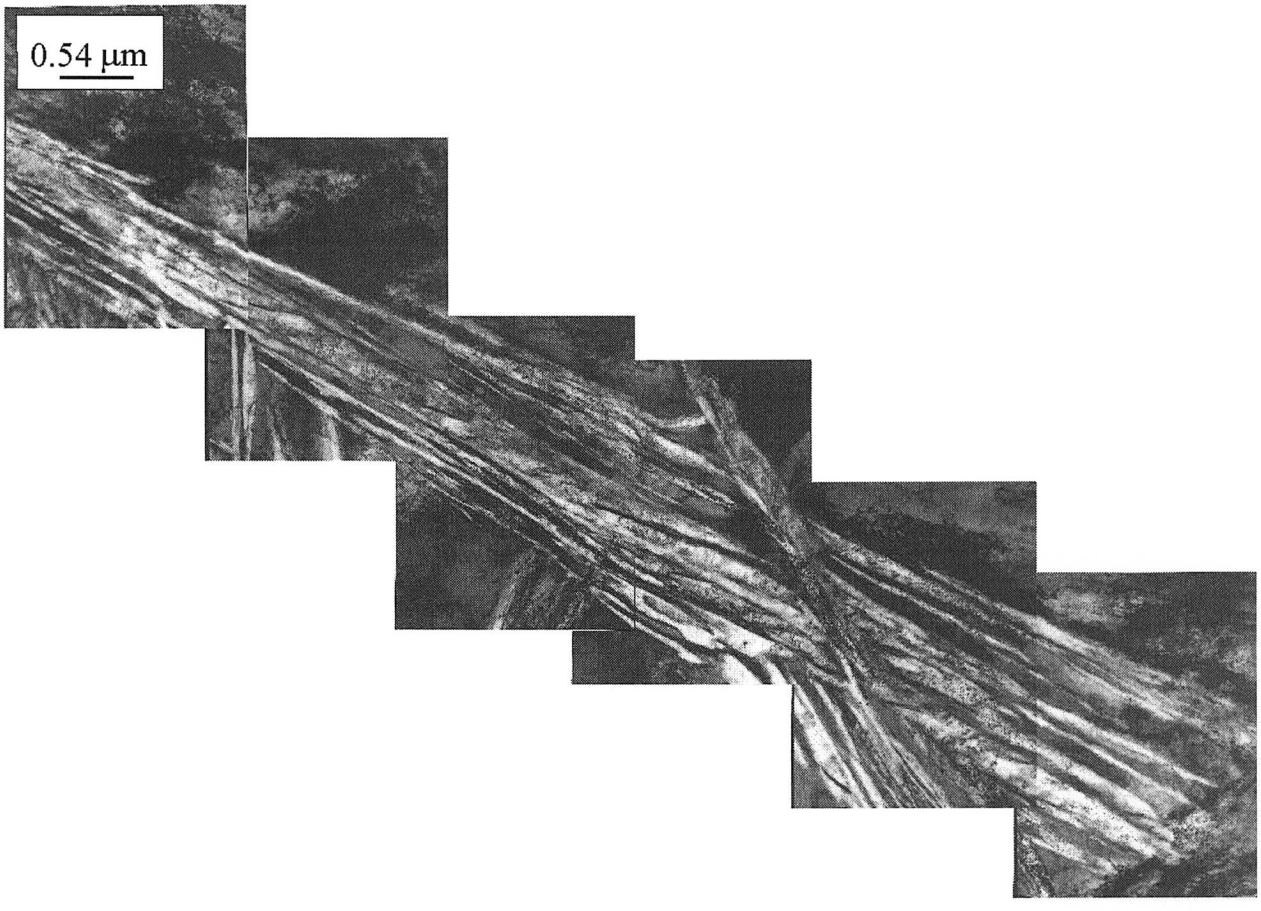

Fig. 1.8: Montage of transmission electron micrographs showing the structure of a bainite sheaf in a high-carbon high-silicon steel transformed at 200°C for 15 days [Courtesy of Garcia Mateo and Bhadeshia].

1.4.b The Transition from Upper to Lower Bainite and Carbides

A bainitic ferrite plate or lath nucleates on an austenite grain boundary or next to another lath or plate by a mechanism similar to martensitic transformation. However, during nucleation, interstitial carbon is partitioned [Bhadeshia, 1981b]. Carbon partitioning does not

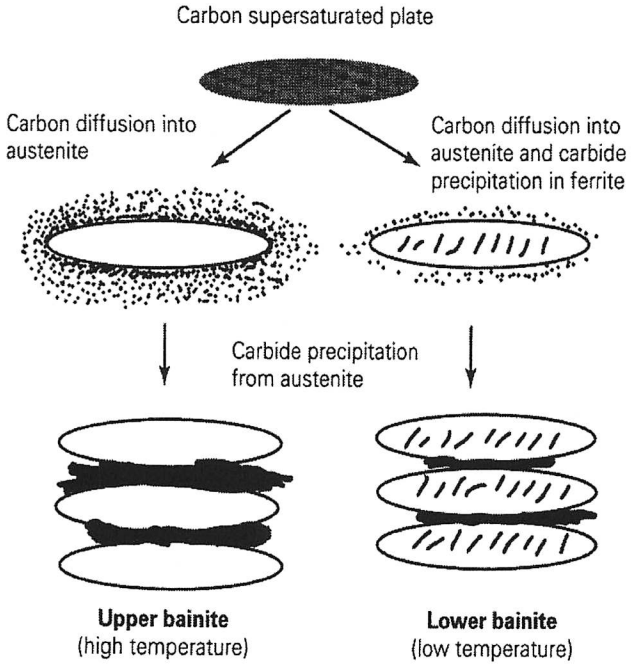

Fig. 1.9: Schematic representation of the transition from upper to lower bainite [Takahashi and Bhadeshia, 1990].

need to take place during growth. Partition during growth is not favoured as the surface to volume ratio decreases. The process for the formation of a typical microstructure is illustrated on Figure 1.9. Several bainite microstructure classifications have been proposed but they only refer to the appearance of the microstructure and not to its formation mechanism [Bramfitt and Speer, 1990; The Bainite Committee of the ISIJ, 1992; Oka and Okamoto, 1998]. All these confusing classifications have therefore been discarded in the present study.

Once the very rapid diffusionless growth of a bainite lath (or plate) is completed, the excess carbon diffuses out of the lath. This is made possible by the relatively high temperature at which transformation occurs. The *upper bainite* microstructure results, with *inter*-lath carbides. As the transformation temperature is decreased or the average carbon concentration of the alloy or of the residual austenite is increased, it becomes possible for some of the carbon to precipitate as *intra*-lath carbides. The remainder is partitioned into the residual austenite and the classical *lower bainite* structure is formed. The kinetics of diffusion of carbon out of the plate are slowed down and have to compete with the kinetics of intra-lath precipitation. Figure 1.10 shows both interlath and intralath carbides coexisting in the same microstructure.

High carbon concentrations lead to microstructures in which the ferrite laths are separated by continuous layers of cementite. When the alloy carbon concentration is low, small and discrete particles of cementite form. Intra-lath carbides exhibit the 'tempering orientation

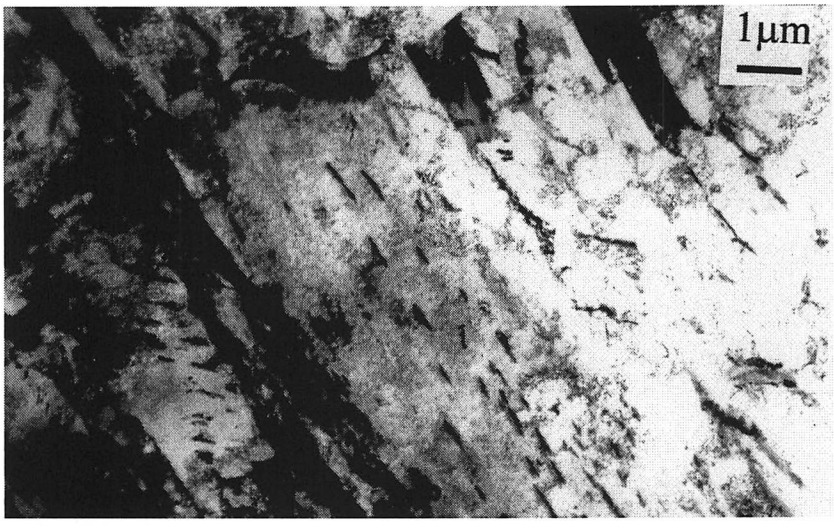

Fig. 1.10: Transmission electron micrograph of steel A transformed isothermally at 475°C for 10 minutes after austenitisation at 1200°C.

relationship' which is found when carbides precipitate during the heat treatment of martensite, often described as the Bagaryatski orientation relationship. Figure 1.11 shows the condition that the carbon concentration in residual austenite has to satisfy so that carbide precipitation can occur. The carbon concentration must exceed the value given by the extrapolated $\gamma/(\gamma+$ Fe_3C) phase boundary at a given temperature T_c.

1.4.c Mechanism of Carbides Formation

Carbides in bainitic ferrite need not always be cementite. Depending on the chemical composition and the transformation temperature, other transition carbides may precipitate first. For example, in high-carbon steels containing more than about 1 wt% silicon (which retards cementite formation), epsilon carbide is commonly observed to precipitate in the bainitic ferrite. Considerable experimental data show that the carbide precipitation associated with bainite and martensite does not lead to a partitioning of substitutional solutes [Tsivinsky *et al.*, 1955; Chance and Ridley, 1981; Bhadeshia, 1989]. The precipitation can occur under conditions where the diffusion rates of iron and substitutional atoms are incredibly small compared with the rate of precipitation. High-resolution transmission electron microscopy supports the idea that the carbide particles grow by displacive transformation [Sandvik, 1982; Nakamura and Nagakura, 1986].

In a remarkable experiment, Babu *et al.* [1993] have shown using the atom-probe tech-

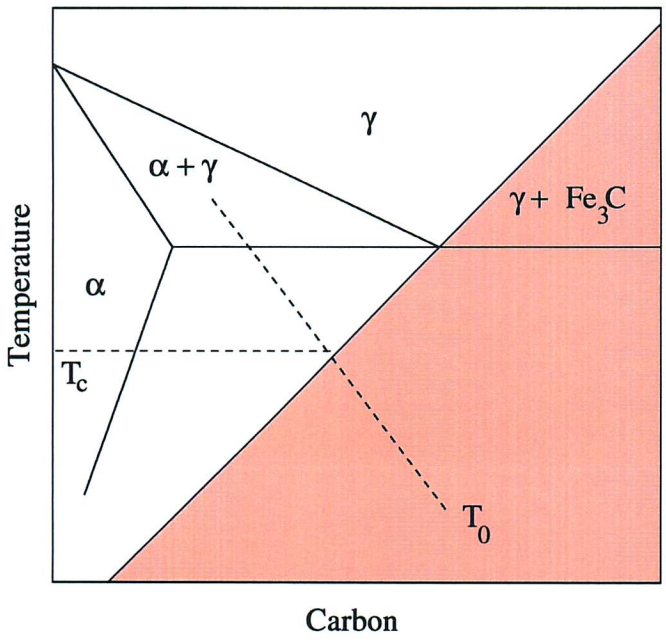

Fig. 1.11: Schematic illustration of the condition which has to be satisfied before cementite may precipitate from the residual austenite [Kriesement and Wever, 1956].

nique that the cementite obtained by tempering martensite is forced to inherit the silicon concentration of the martensite. This is in spite of the fact that the equilibrium solubility of silicon in cementite is negligible. Cementite therefore forms by a paraequilibrium transformation mechanism. In silicon containing steels, the free energy change associated with the paraequilibium precipitation of cementite must be much smaller than when the cementite is free of silicon. It is probable that this is what leads to suppression of cementite in high-silicon bainitic or martensitic steels. However, a full theory is far from established and the work is urgent given the technological significance of carbide-free bainitic steels.

In contrast to tempered martensite, the cementite particles in lower bainite frequently precipitate in just one variant of the orientation relationship, such that they form parallel arrays at about 60^o to the axis of the bainite plate. In tempered martensite, the carbides tend to precipitate in Widmanstätten arrays. This peculiar mode of precipitation in lower bainitic ferrite may arise because the carbides nucleate at the ferrite/austenite interface, and hence attempt to adopt a unique variant of the orientation relationship, one which gives an optimum match to both the austenite and ferrite with which they are in contact.

It is possible for both upper and lower bainite to coexist in a microstructure, or to be present in isolation.

1.4.d Distribution of Chemical Elements Across the Interface

Many experiments, even on the finest conceivable scale, have shown that there is indeed no redistribution of substitutional elements across the interface between autenite and bainitic ferrite, even at moderately high temperatures [Bhadeshia and Waugh, 1981, 1982; Stark *et al.*, 1988, 1990; Josefsson and Andren, 1988, 1989]. The techniques used, atom probe and quantitative chemical analysis allowed atomic scale spatial resolution. These experiments (Figure 1.12) were based on steels where other reactions, such as carbide precipitation, do not interfere with the formation of bainitic ferrite (steels with high silicon content). If the conditions of local equilibrium compatible with a certain amount of solute diffusion were satisfied, such experiments would have spotted perturbations in the substitutional solute content near the interface. This was never found, and only carbon was found to redistribute, in accordance with the paraequilibrium mechanism.

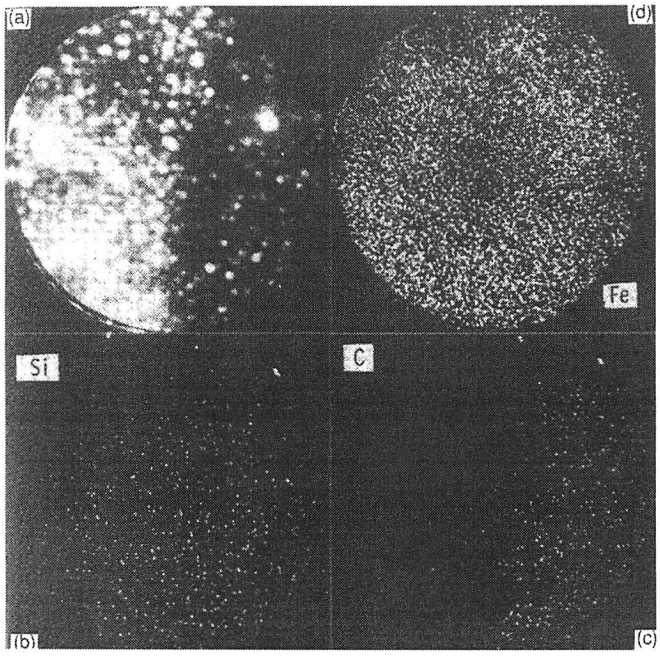

Fig. 1.12: Imaging atom-probe micrographs, taken across an austenite-bainitic ferrite interface in a Fe-C-Si-Mn alloy. The images confirm quantitative data showing the absence of any substitutional atom diffusion during transformation. (a) Field-ion image; (b) corresponding silicon map; (c) corresponding carbon map; (d) corresponding iron map [Bhadeshia and Waugh, 1982].

1.4.e Shape Deformation and Crystallographic Orientations

The bainite transformation is accompanied by a shape change of the transformation region. This corresponds to an 'invariant-plane strain' (IPS) [Ko and Cottrell, 1952; Srinivasan and Wayman, 1968] with a large shear component [Sandvik, 1982; Swallow and Bhadeshia, 1996] similar to the one for martensite. At the relatively high temperatures at which bainite forms, the austenite strength is not enough to sustain the large strains caused by the shape deformation. The austenite strength is known to decrease as a function of temperature. The strains are released by plastic deformation of the austenite, causing its yielding, which in turn increases the local density of dislocations. Intense tangles of dislocations formed by this mechanism similar to 'work-hardening' halt the movement of the glissile interface of a bainite sub-unit.

Each bainite sub-unit is therefore limited to a size that is much lower than that of an austenite grain † [Bhadeshia and Edmonds, 1979]. Bainite sub-units are typically around 10 microns long and 0.2 microns wide. This explains why successive sub-units have to nucleate and grow and there seems to be preferential sites for that at the tip or on the sides of sub-units previously formed. The typical sheaf-like structure results (Figure 1.13) [Hehemann, 1970]. Bainite laths are confined to the grain in which they grow because grain boundaries of the parent phase cannot sustain such coordinated movement of atoms. This is quite unlike reconstructive transformation products such as allotriomorphic or massive ferrite and pearlite, which are not hindered by austenite grain boundaries.

An interesting observation was made by Bhadeshia, who annealed a sample containing a mixture of bainitic ferrite plates and residual austenite for 43 days. The annealing allowed the formation of ferrite at a grossly retarded rate by a reconstructive mechanism in which there is no invariant-plane strain shape deformation with a large shear component [Bhadeshia, 1981c].

The shape change was observed on the surface of previously polished samples [Bhadeshia and Edmonds, 1980]. It implies that bainite grows by a displacive mechanism, much slower than for martensite, though, because of the reduced driving force at higher temperatures. The minimisation of the associated strain energy is responsible for the growth of bainite in thin plates. Since the crystal structure of bainite is generated by a coordinated movement of atoms,

† In practice, in TRIP-assisted steels, for which small austenite regions formed in the inter-critical domain ($\alpha + \gamma$), typically of about 1 μm in size, are then transformed to bainite, the sub-unit is about the size of the grain. This interesting case where successive sub-units have to nucleate laterally with no sheaf-like structure was studied by Jacques *et al.* [1999] and Giraud *et al.* [1999].

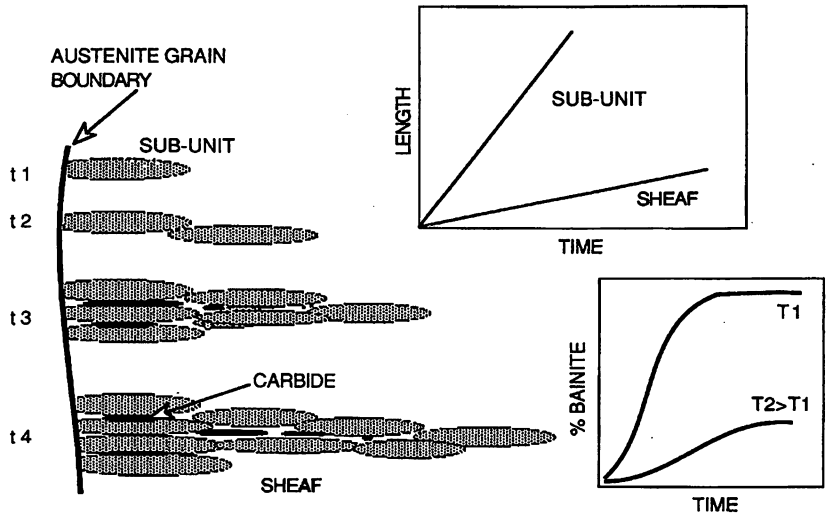

Fig. 1.13: Schematic illustration of the microstructural features relevant in the kinetic description of a bainitic microstructure [Bhadeshia, 1992].

it follows that there are orientation relationships between corresponding directions and planes in the two phases. It is not of much relevance to the work contained in this thesis to give such detailed relationships. The reader will consult [Kurdjumov and Sachs, 1930; Nishiyama, 1934; Babu and Bhadeshia, 1991] for more information.

1.4.f Mechanical Stabilisation

It is known that the deformation of austenite accelerates allotriomorphic ferrite transformation which is reconstructive. Bainite and martensite, on the other hand, form by a displacive mechanism of transformation which involves a coordinated movement of atoms during the glide of glissile interfaces. Such movements cannot be sustained against strong obstacles such as grain boundaries. Thus, martensite or bainite cannot cross grain boundaries. Defects such as dislocations also hinder the progress of any glissile interface in much the same way that ordinary slip is made more difficult by the presence of dislocation forests.

It follows that displacive transformations can be suppressed by pre-straining the parent phase which has the effect of enhancing the matrix defect density. This effect is known as *mechanical stabilisation* and is well established for martensitic transformation. At the same time, heterogeneous nucleation is increased at those defects, but the overall effect is a retardation of the displacive transformation, even though an acceleration is observed during the early stages. Tsuzaki *et al.* [1989] found that the net volume fraction of bainite that formed decreased compared with undeformed austenite. Other studies demonstrated that the bainite transformation

is mechanically stabilised [Shipway and Bhadeshia, 1995; Larn and Yang, 1999a]. Huang *et al.* [1993] showed that deformed austenite transforms to bainite at a higher temperature during continuous cooling and at a faster rate, as long as the cooling occurred sufficiently fast to suppress recovery of the austenite. Similar effects were reported by Smith and Siebert [1971].

It is important not to confuse with the situation when an appropriate applied stress favours the IPS deformation and hence the displacive transformation [Matsuzaki *et al.*, 1994]. For a diffusional transformation, defects add to the driving force and are destroyed by the growth of the new phase.

Bhadeshia proposed the very simple criterion that follows: 'there is no mechanism by which plastic deformation can retard reconstructive transformation. Likewise, only displacive transformations can be mechanically stabilised'. For reconstructive transformations, the defects are destroyed by the growth of the new phase, akin to what happens in recrystallisation. For displacive transformations, the defects are inherited by the growing phase. Widmanstätten ferrite is also susceptible to mechanical stabilisation [Shipway and Bhadeshia, 1997; Larn and Yang, 1999b].

1.4.g The Incomplete Reaction Phenomenon

Diffusionless growth requires that transformation occurs at a temperature below T_0, when the free energy of bainite becomes less than that of austenite of the same composition. The locus of the T_0 temperatures as a function of the carbon concentration is called the 'T_0 curve' [Zener, 1946], an example of which is plotted on Figure 1.14. Growth without diffusion can only occur if the carbon concentration of the austenite lies to the left of the T_0 curve. As bainite forms isothermally, residual austenite is progressively enriched in carbon (leading to a decrease of T_0) diffusing out of the bainite plates until its carbon content reaches the T_0 curve. The displacive reaction then stops and cannot resume unless the transformation temperature is lowered. The maximum permissible degree of transformation to bainitic ferrite, if we ignore the stored energy term is given by:

$$\theta_b = \frac{(x_{T_0} - \bar{x})}{(x_{T_0} - x_\alpha)} \tag{1.3}$$

where x_{T_0} is the carbon level at the locus T_0 and x_α is the amount of carbon which remains in the ferrite, *i.e.* about 0.02 wt%.

On Figure 1.14, Ae_3 is the curve that separates the γ and $\gamma + \alpha$ phase field, when the two phases are in equilibrium. In conditions of paraequilibrium, i.e when substitutional alloying elements do not redistribute during transformation, the Ae_3' curve replaces the Ae_3 curve. Both

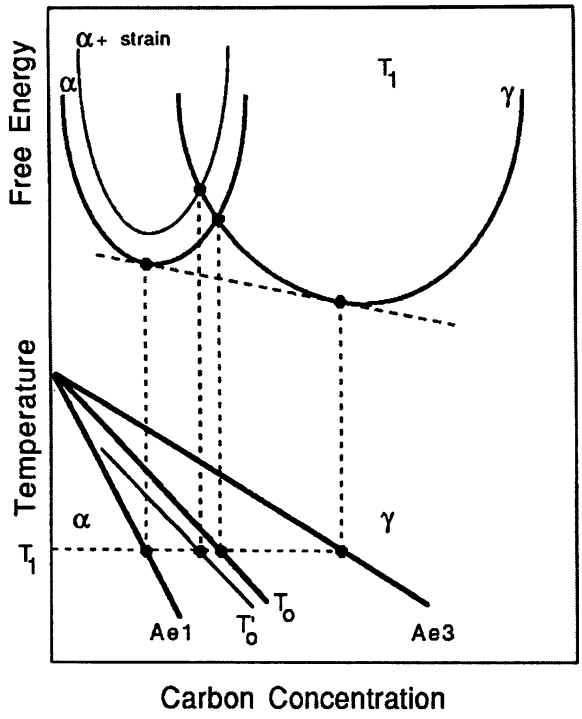

Fig. 1.14: Schematic illustration of the origin of the T_0 curve on the phase diagram. The $T_0^{'}$ curve incorporates a strain energy term for the ferrite, illustrated on the diagram by raising the free energy curve for ferrite by an appropriate quantity [Bhadeshia, 1992].

the T_0 and $Ae_3^{'}$ refer to stress-free transformation, and differ from their counterparts, the $T_0^{'}$ and $Ae_3^{''}$ curves, which additionally account for the stored energy of ferrite. The stored energy is the transformation strain energy and has been found to be around 400 J mol^{-1} [Bhadeshia, 1981b].

1.4.h Widmanstätten Ferrite, Acicular Ferrite and Overview of Transformations

Widmanstätten ferrite plates nucleate on austenite grain boundaries or on pre-existing ferrite allotriomorphs. The transformation occurs at a temperature below that of allotriomorphic ferrite but above bainite. The mechanism of transformation is displacive but the available driving force at this relatively high temperature is not enough to sustain growth without carbon partitioning. The substitutional atoms do not partition. The paraequilibrium growth rate is therefore controlled by diffusion of carbon in austenite, even though this transformation is considered as displacive. The cooperative, back-to-back growth of two mutually accommodating variants ensures that the strain energy of transformation is minimised to about 50 J mol^{-1}, thus allowing the transformation to proceed at a relatively small driving force. Widmanstätten ferrite has a wedge morphology. Plates of Widmanstätten ferrite tend to form in

packets of parallel variants, which hardly deflect cleavage cracks and hence can be detrimental to toughness [Ali and Bhadeshia, 1990]. It is frequently observed in welds but is less common in wrought products. It is very unusual in low-carbon steels [Tsuji *et al.*, 1997] and is more likely to form in large austenite grains.

A phase very similiar to bainite is *acicular ferrite*, but the two are microstructurally different in that the bainite plates nucleate on grain boundaries and grow in the form of sheaves of parallel plates whereas acicular ferrite plates nucleate intragranularly on non-metallic inclusions and grow radially in many different directions (Figure 1.15). Acicular ferrite is also favoured when the austenite grain size is large, i.e the grain boundary density is decreased or when the grain boundary is previously decorated with allotriomorphic ferrite [Ali and Bhadeshia, 1991]. The resulting chaotic microstructure gives a better toughness because cleavage cracks are deflected more frequently at the plate boundaries. The low carbon concentration of the vast majority of welding alloys prevents the formation of lower bainite. An experiment in which the carbon concentration was deliberately increased led to the first ever observation of 'lower acicular ferrite' [Sugden and Bhadeshia, 1989].

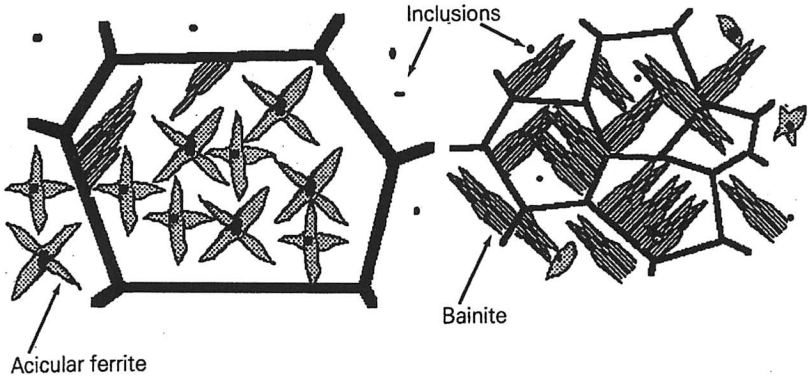

Fig. 1.15: Illustration of how the microstructure changes from one which is predominantly acicular ferrite, to another which is mostly bainitic as the austenite grain size is refined [Bhadeshia, 1992].

The classification of phase transformations according to their diffusive or displacive character by the displacive school is as shown in Figure 1.16. Amongst the papers which have concluded that bainite transforms by a displacive mechanism, the reader should consult: Bhadeshia and Edmonds, 1980; Bhadeshia, 1992; Wang and Yang, 1992; Tsuzaki *et al.*, 1994; Yamamoto

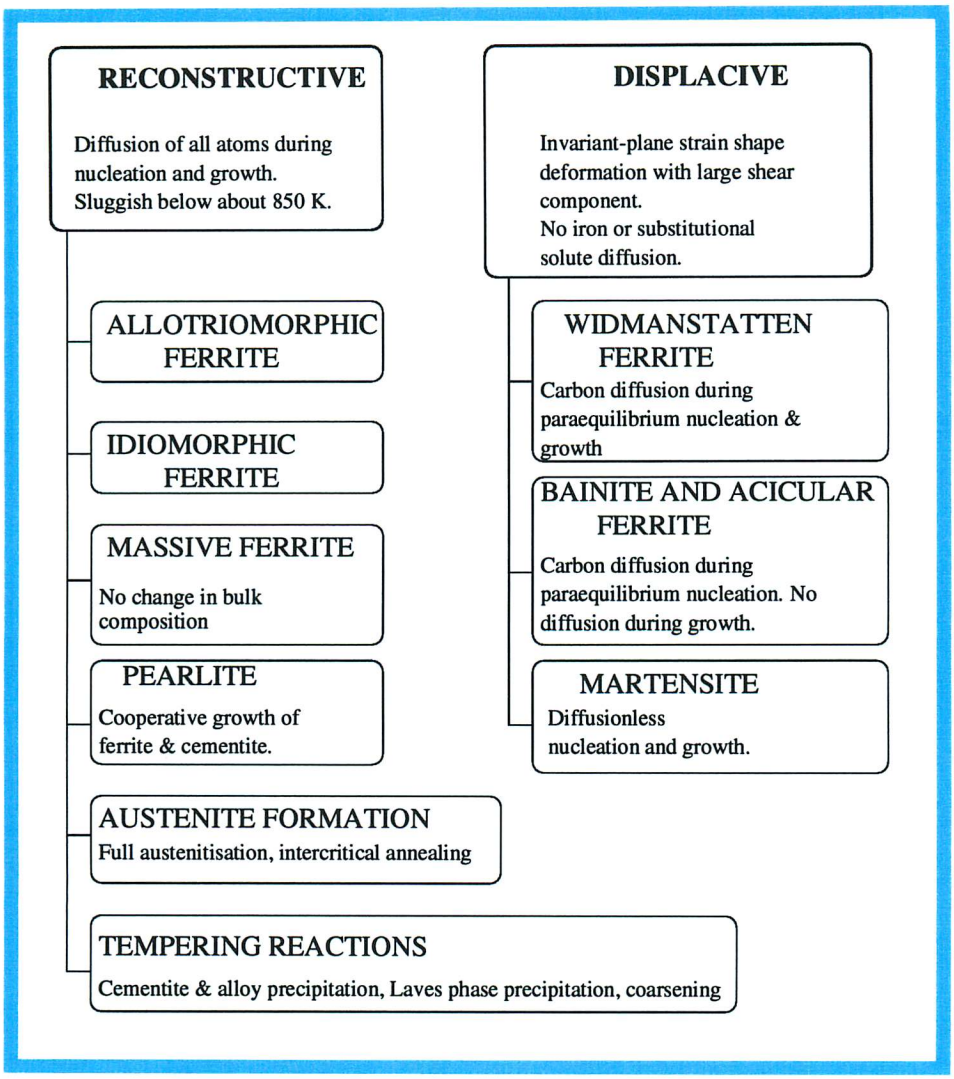

Fig. 1.16: Flow chart summarising the characteristics of transformations in steels [Bhadeshia, 2001].

et al., 1995; Zarei Hanzaki *et al.*, 1997; Jung *et al.*, 1997; Chang, 1999; Girault *et al.*, 1999; Jacques *et al.*, 1999.

1.4.i Unresolved Issues

Bhadeshia [1999b] identified four fundamental key areas in which progress still has to be made in order to gain an even better understanding of the bainite transformation.

- The measured growth rate of individual plates of bainite is far greater than expected from the theory of diffusion-controlled growth [Bhadeshia and Waugh, 1984]. It is clear that bainite forms with a large supersaturation of carbon, but the possibility of some interstitial diffusion cannot be entirely ruled out. There are a number of theories about this [Hillert, 1975; Agren, 1989; Olson *et al.*, 1990] but none of them are completely convincing for

reasons discussed in [Bhadeshia, 1992, page 167].

- There exists kinetic theory capable of estimating the fraction of bainite obtained during the isothermal transformation of austenite in steels where the reaction is not accompanied by the formation of carbides [Chester and Bhadeshia, 1997]. The autocatalytic nucleation that will be mentioned in Chapter 2 needs to be understood better in order to have some idea on the nature of the theory's fitting constants.
- There are no existing quantitative model for carbide formation during bainite transformation (or even during tempering of martensite!), and therefore the models must be inaccurate for the majority of industrial steels which contain carbides.
- There needs to be a better understanding of the effects of plastically deformed austenite on subsequent bainite formation since most of the industrial bainitic steels are produced by thermomechanical processes.

In the light of the work presented in this thesis on modelling of the bainite transformation in cooling conditions, the third issue regarding modelling of carbide formation should be tackled. Improvements are needed to better model nucleation at grain boundaries but also intra-granularly and to understand the influence of alloy chemistry on the potency of the various nucleation sites, this latter point including autocatalysis.

1.5 Characteristic Mechanical Properties of Bainitic Microstructures

Although it is not the purpose of this study to model mechanical properties, a rapid overview of the typical properties associated with bainitic microstructures is given here. Indeed, bainitic steels are used more and more extensively because they can offer a good combination of strength and toughness.

High-strength bainitic steels have not in the past been as successful as quenched and tempered martensitic steels, because the coarse cementite particles in bainite are detrimental to toughness. However, it is now known that the precipitation of cementite during bainitic transformation can be suppressed. This is done by alloying the steel with about 1.5 wt% of silicon, which has a very low solubility in cementite and greatly retards its growth. When silicon-alloyed steel is transformed into upper bainite, the carbon that is rejected into the residual austenite, instead of precipitating as cementite, remains in the austenite and stabilises it down to ambient temperature. The resulting microstructure consists of fine plates of bainitic ferrite separated by carbon-enriched regions of austenite, which has the following advantages of a composite material [Bhadeshia, 1998]:

- Cementite is responsible for initiating fracture in high-strength steels. Its absence is expected to make the microstructure more resistant to cleavage fracture and void formation.
- Bainitic ferrite is almost free of carbon, which is known to embrittle ferritic microstructures.
- The microstructure derives its strength from the ultrafine grain size of the ferrite plates (less than 1 μm in thickness), which determines the mean free slip distance. Grain refinement is the only method available for simultaneously improving the strength and toughness of steel.
- The ductile films of austenite which are intimately dispersed between the plates of ferrite have a crack-blunting effect. They further add to toughness by increasing the work of fracture as the austenite is induced to transform to martensite under the influence of the stress field of a propagating crack.
- The diffusion of hydrogen in austenite is slower than in ferrite. The presence of austenite can therefore improve the stress corrosion resistance of the microstructure.
- Steels with this microstructure can be obtained without the use of any expensive alloy addition. All that is required is that the silicon concentration should be large enough to suppress cementite.

However, 'blocky' regions of austenite between the sheaves of bainite transform into high-carbon martensite under the influence of stress. This untempered, hard martensite embrittles the steel. The volume fraction of such regions can be decreased and their stability to martensitic transformation increased by shifting the T_0' curve of the phase diagram to higher carbon content. This can be achieved by appropriate solute additions [Bhadeshia, 1998].

Microstructures of mixed bainite and martensite have a peak in the curve of the strength as a function of the volume fraction of martensite [Young and Bhadeshia, 1994]. Indeed, when bainite forms, it enriches the residual austenite with carbon, so that the strength of the subsequent martensite increases. In addition, during its deformation, the strength of the bainite is enhanced via plastic constraint by the surrounding stronger martensite.

1.6 Summary

According to the ferrite growth mechanism involved, a phase transformation can be classified as either a reconstructive or a displacive transformation, the mechanisms of which have been discussed. A flow chart summarising the characteristics of the different transformation products and their mechanisms is shown on Figure 1.16.

The widely acknowledged characteristic features of the bainite transformation, *i.e.* the absence of redistribution of substitutional chemical elements, the shape deformation, the mechanical stabilisation and the incomplete-reaction phenomenon show beyond doubt that bainite is a displacive transformation. However, there still remain a few critical issues that are unresolved, some of which are an obstacle to better modelling of the transformation. The typical advantageous mechanical properties of a bainitic microstructure have been mentioned.

Chapter 2

Existing Isothermal Models

2.1 Introduction

The existing models for the rate of isothermal transformation to bainite are described in this chapter. It is important before trying to develop a model for continuous cooling to make sure that the isothermal model on which calculations are based is accurate. The discussion will show that good agreement with isothermal experimental data can already be achieved by several models, even if empirical constants have to be used to hide some of the physics which are not understood.

Firstly, the Johnson, Mehl, Avrami and Kolmogorov approach (JMAK) is introduced. It allows a description of most precipitation and recrystallization kinetics, as it reproduces experimental sigmoidal curves. Two examples of such recent studies [Matsuzaki and Bhadeshia, 1999; Quidort, 1999] will be given here. This approach requires the separate estimation of the nucleation and growth rates for the new phase.

An approach that is less descriptive and more physical comes with the displacive model of Bhadeshia *et al.* Its fundamentals as well as successive improvements will be explained in detail here. This model is, to date, the more complete and physical. It will be adapted for the first time to continuous cooling conditions according to the incrementation method described in Chapter 3.

In section 2.6, the factors influencing the bainite transformation are presented with a particular emphasis on the effects of chemical composition, austenite grain size and cooling rate. They are presented here because they are well known effects and provide easy ways of checking that the model predicts the right trends.

2.2 General Isothermal Models

2.2.a Equations for Representing Solid-State Isothermal Transformation Behaviour

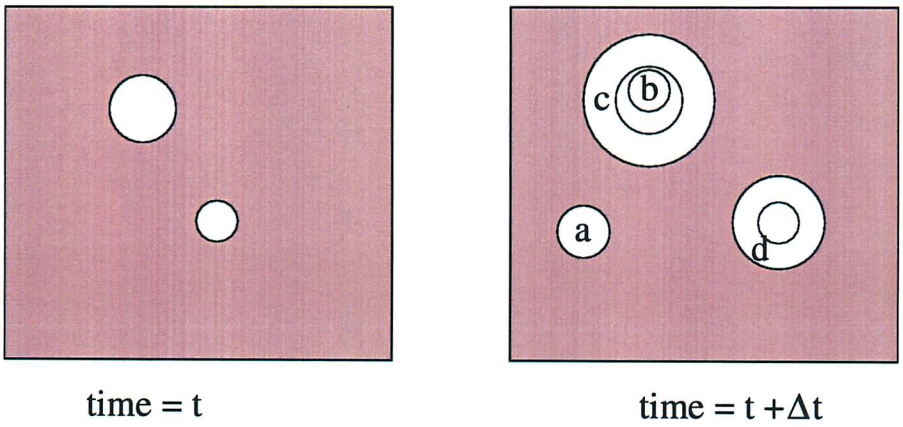

Fig. 2.1: Illustration of the concept of extended volume: two precipitate particles have nucleated together and grown to finite size in time t: new regions c and d are formed as original particles grow, but a and b are new particles, of which b has formed in a region which is already transformed.

A model for a single transformation begins with the calculation of the nucleation and growth rates using classical theory, but an estimation of the volume fraction requires impingement between particles to be taken into account. This is generally done using the extended volume concept of Johnson, Mehl, Avrami and Kolmogorov [described in Christian, 1975], as illustrated in Figure 2.1. Suppose that two particles exist at time t; a small interval Δt later, new regions marked a, b, c and d are formed assuming that they are able to grow unrestricted in extended space whether or not the region into which they grow is already transformed. However, only those components of a, b, c and d which lie in previously untransformed matrix can contribute to a change in the real volume of the product phase (identified by the subscript '1') so that:

$$dV_1 = \left(1 - \frac{V_1}{V_s}\right) dV_1^e \tag{2.1}$$

where it is assumed that the microstructure develops randomly. The superscript e refers to the extended volume, V_1 is the volume of phase 1 and V_s is the total volume of the sample. Multiplying the change in extended volume by the probability of finding untransformed regions has the effect of excluding regions such as b, which clearly cannot contribute to the real change in volume of the product. This equation can easily be integrated to obtain the real volume fraction:

$$\frac{V_1}{V_s} = 1 - \exp\left\{-\frac{V_1^e}{V_s}\right\} \tag{2.2}$$

Consider the nucleation process. A particle does not form the instant a sample reaches the transformation temperature, but there is an incubation period τ. Thus, the volume ω_t of a particle is given by

$$\omega_t = \frac{4\pi}{3} G^3(t-\tau)^3 d\tau \qquad (t > \tau) \tag{2.3}$$

$$\omega_t = 0 \qquad (t < \tau) \tag{2.4}$$

where G is a growth rate assumed to be constant, t is the time defined to be zero at the instant when the sample reaches the isothermal transformation temperature (convention also used in this work for the experimental study of isothermal transformations) and the growing particle is assumed to be spherical. The extended volume of phase 1 is given by:

$$dV_1^e = \omega_t I V_s \, d\tau \tag{2.5}$$

i.e.

$$V_1^e = \frac{4\pi V_s}{3} \int_{\tau=0}^{t} G^3 I (t-\tau)^3 d\tau \tag{2.6}$$

Using equation 2.5, equation 2.2 can be integrated assuming that the nucleation rate I is constant. This leads to the familiar Avrami equation [Avrami, 1940]:

$$v_1 = \frac{V_1}{V_s} = 1 - \exp\left(-\frac{\pi}{3} G^3 I t^4\right) \tag{2.7}$$

This equation can also describe other phenomena such as recrystallisation kinetics [Medina and Mancilla, 1996] and is written in a more general form as

$$v_1 = 1 - \exp(-kt^n) \tag{2.8}$$

The parameter k is known to depend on the temperature and transformation mechanism, i.e. it depends on the nucleation and growth rates. The time exponent n is sometimes considered constant over the temperature range where a unique transformation mechanism operates. In the case of equation 2.7, the time exponent is 4, but if growth is diffusion-controlled, *i.e.* the particle dimension increases with $t^{0.5}$, then the time exponent becomes $\frac{5}{2}$. Alternatively, for growth at a constant rate, beginning from a fixed number of sites (*i.e.* no nucleation), the time

exponent can be shown to have a value of 3. The time exponent can therefore be used as an indicator to the mechanism of growth.

By rearranging Equation 2.8. and taking the logarithm twice, the following equation is obtained:

$$\ln\{\ln[\frac{1}{(1-v_1)}]\} = \ln(k) + n\ln(t) \tag{2.9}$$

The values of k and n can then be determined from the intercept and slope of $\ln\{\ln[\frac{1}{(1-v_1)}]\}$ vs. $\ln(t)$ plot.

In practice, there are many cases where several transformations occur together. In the case of two phases 1 and 2, only phase 1 formed in untransformed γ will contribute to the real volume of 1. On average a fraction $\left(1 - \frac{V_1+V_2}{V_s}\right)$ of the extended volume will be in previously untransformed material. It follows that the increase in real volume of 1 is given by an equation corrected from equation 2.1:

$$dV_1 = \left(1 - \frac{V_1 + V_2}{V_s}\right) dV_1^e \tag{2.10}$$

and similarly for phase 2:

$$dV_2 = \left(1 - \frac{V_1 + V_2}{V_s}\right) dV_2^e \tag{2.11}$$

where the increase of extended volumes of the two phases are given by:

$$dV_1^e = \frac{4}{3}\pi G_1^3 (t-\tau)^3 I_1 V_s \, d\tau \tag{2.12}$$

$$dV_2^e = \frac{4}{3}\pi G_2^3 (t-\tau)^3 I_2 V_s \, d\tau \tag{2.13}$$

Generally V_1 will be some complicated function of V_2 and it is not possible to integrate these expressions analytically to find the relationship between the real and extended volumes. Numerical integration is straightforward and offers the opportunity to change the boundary conditions for nucleation and growth as transformation proceeds, to account for the change in the matrix composition during the course of reaction. This method was applied successfully to the modelling of the carbide precipitation sequence in power plant steels by Robson and Bhadeshia [1997], and to the modelling of three simultaneous transformations (allotriomorphic ferrite, pearlite and Widmanstätten ferrite) in steels by Jones and Bhadeshia [1997]. It can in principle be applied to any number of simultaneous reactions.

2.2.b An Example of the use of the JMAK Equation for Bainite

From here onwards, the subscripts '1' and '2' are suppressed as bainite is studied in isolation. For example, v_1 become v. A more general expression of the JMAK equation is as follows:

$$v(t) = 1 - \exp\left[-\int_0^t I(\tau)V(t,\tau)d\tau\right] \tag{2.14}$$

where $v(t)$ is the fraction of bainite at time t, I is the nucleation rate per unit volume at time τ, and $V(t,\tau)$ is the volume, at time t, of the bainite nucleated in the time interval between τ and $\tau + d\tau$. I is the derivative of the number density of nucleation sites with respect to time, which is proportional to S_v, the number density of sheaf nucleation sites per unit volume. S_v is inversely proportional to the austenite grain size d_γ. $I(\tau)$ can therefore be written:

$$I(\tau) = \frac{C_1 N_0 \nu}{d_\gamma}\exp(-\nu\tau) \tag{2.15}$$

where N_0 is the initial number density of nucleation sites per unit of grain boundary area, C_1 is a constant and ν is a frequency that represents the rate at which individual sites become nuclei.

The formulation of $V(t,\tau)$ depends on the characteristics of the development of bainite sheaves. For steels with rapid growth, it is assumed that each nucleus is associated with a fixed volume of transformation. The growth rate does not feature explicitly in the kinetic equations and $V(t,\tau)$ can be written as:

$$V(t,\tau) = C_2 d_\gamma^3 \tag{2.16}$$

where C_2 is another constant. In the other case where growth is slower and particles are rapidly nucleated, the volume can be described in terms of a constant growth rate as follows:

$$V(t,\tau) = C_3(t-\tau)^3 \tag{2.17}$$

where C_3 is a constant. Substituting Equations 2.15 and 2.16 or 2.17 in Equation 2.14 and expanding the term $\exp(-\nu\tau)$ for early stages of transformation (t small), the following relationship is derived:

$$v(t) = 1 - \exp(-C_4 d_\gamma^m t^n) \tag{2.18}$$

which is similar to equation 2.8. This treatment for bainite was proposed by Matsuzaki and Bhadeshia [1999] in order to study the influence of austenite grain size (Section 2.6.c). To determine $v(t)$, they used dilatometric data and the relationship:

$$v(t) = \frac{\frac{\Delta L}{L_0}(t)}{\frac{\Delta L}{L_0}(max)} \tag{2.19}$$

where $\frac{\Delta L}{L_0}(t)$ is the relative length change at transformation time t and $\frac{\Delta L}{L_0}(max)$ the maximum length change. Indeed, it was demonstrated that the linear relation between the volume fraction of bainite and the corresponding relative length change is preserved up to a volume fraction of at least 0.7 [Takahashi and Bhadeshia, 1989]. The values Matsuzaki and Bhadeshia found for m and n using the method of equation 2.18 are given in section 2.6.c. Although they were able to explain the different forms of fraction transformed versus time curves as a function of austenite grain structure, their analysis is unable to predict the different kinds of behaviour observed.

Similar kinetic equations of the Avrami type were developed by several authors [Bhadeshia, 1982; Krüger, 1993; Donnay *et al.*, 1995]. Fang *et al.* derived n values for lower bainite (n between 1.0 and 1.2) and for upper bainite (n between 1.2 and 1.7) in two alloys [Fang *et al.*, 1997; Lee, 1999].

2.2.c The Isothermal Model due to Quidort [1999]

In a recent study, and following a rather similar approach, Quidort [1999] developed a model for bainite kinetics in isothermal or continuous cooling conditions. The model for continuous cooling transformation is presented in Chapter 3.4. The isothermal model takes account of both nucleation and growth, whereas in the Bhadeshia *et al.* model (sections 2.3, 2.4 and 2.5), a nucleus transforms instantly into a sub-unit of fixed volume making it unnecessary to deal with the growth process.

The following equation is the well known equation for the development of spherical precipitates:

$$v = 1 - \exp\left(-\frac{\pi}{3}G^3 I t^4\right)$$

and is the same as equation 2.7. I is the constant nucleation rate per unit volume and G is the isotropic and constant growth rate. The coefficient n is here equal to 4 (1 from the nucleation term and 3 for three-dimensional growth). For bainite, Quidort chose $n = 2$, assuming that

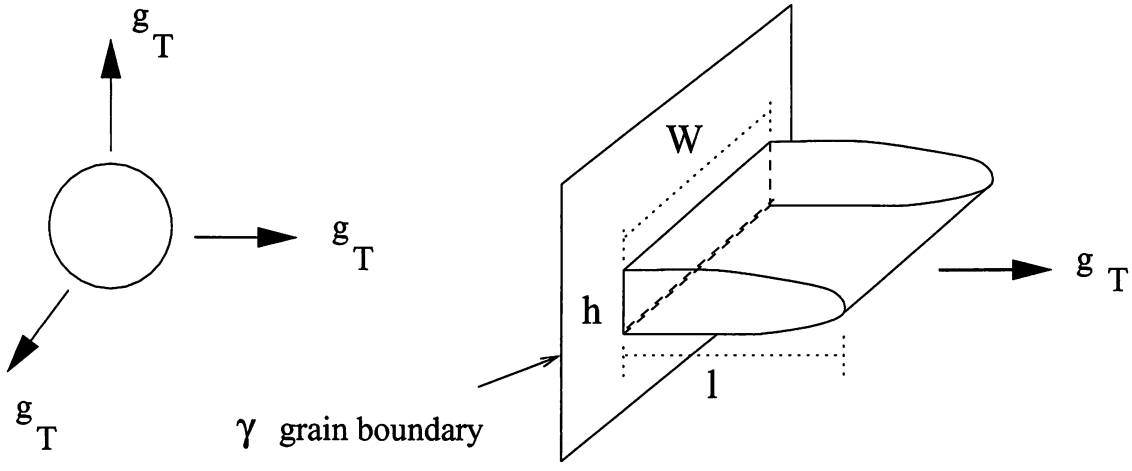

Fig. 2.2: Illustration of the link between the Avrami exponent n and the growth geometry. For the diagram on the left, $n = 4$, and for the diagram on the right, the value of n is taken as 2, although h and w are finite [Quidort, 1999].

the growth of a sub-unit is essentially only possible in one direction, represented by the arrow on Figure 2.2.

The extended volume $V^e(t)$ at time t is generally calculated using the equation

$$V^e(t) = \int_{t_o}^{t} (\text{number of units nucleated during } d\tau) * (\text{volume of unit nucleated at } \tau) d\tau \tag{2.20}$$

The volume transformed for each sub-unit is proportional to g_T, the lengthening rate of a sub-unit. The bainite volume, using the formalism of equation 2.2 is easily shown to be equal to:

$$V(t) = 1 - \exp\ (-V^e(t)) \tag{2.21}$$

To calculate the lengthening rate, Quidort assumed paraequilibrium and used the Trivedi [1970] model with a correction factor to match experimental results better. The Trivedi model is for diffusion-controlled growth of parabolic plates and relates the austenite carbon supersaturation to the 'Péclet number' which in turn depends on the plate-tip curvature and growth speed of a forming plate. For nucleation, Quidort used an activation energy inversely proportional to the square of the maximum driving force available for nucleation, as is the case in classical nucleation theory ($G^* \propto \Delta G_m^{-2}$). Bhadeshia, on the other hand uses a proportionality relationship ($G^* \propto \Delta G_m$), as in martensite nucleation theory.

The overall isothermal transformation kinetics obtained by Quidort are of the form:

$$\xi(t) = 1 - \exp\left[-K_1 \exp(-K_2 Q_c^\gamma / RT) g_T (t-\tau)^2\right] \tag{2.22}$$

where R is the universal gas constant and Q_c^γ is the activation energy for the diffusion of carbon in austenite. Quidort's model contains 3 empirical constants K_1, K_2 and K_3 (determined graphically), different for each steel, with K_3 included in the expression of τ, the incubation time for the transformation. This incubation time is defined as the average time at which the nuclei reach a critical size and start to grow into the new phase. Model predictions for a Fe-0.5C-0.7Mn-0.29Cr wt% steel were in good agreement with experimental results.

2.3 The General Theory of the Bainite Transformation

2.3.a The Thermodynamic Parameters

Consider austenite of composition $\bar{x}$ at temperature T_1 (Figure 2.3.a). Its free energy G can decrease if it decomposes into a mixture of ferrite and carbon-enriched austenite. At a fixed temperature, the minimum or the equilibrium free energy lies on a line which is a common tangent to the free energy curves of both phases. The equilibrium compositions of ferrite and austenite, namely $x^{\alpha\gamma}$ and $x^{\gamma\alpha}$ are given by the points where the common tangent touches the respective free energy curves. The decrease in free energy associated with the decomposition is largest when the compositions of the ferrite and the austenite are $x^{\alpha\gamma}$ and $x^{\gamma\alpha}$ respectively.

The free energy change associated with the equilibrium decomposition of one mole of austenite $\Delta G^{\gamma\rightarrow\gamma'+\alpha}$, can thus be obtained by a common tangent construction. Considering two similar triangles in Figure 2.3.a, it can be shown that the same free energy change expressed per mole of ferrite is given by ΔG_1, which is $\Delta G^{\gamma\rightarrow\gamma'+\alpha}$ divided by $(x^{\gamma\alpha} - \bar{x})$ / $(x^{\gamma\alpha} - x^{\alpha\gamma})$, the ferrite mole fraction.

The amount of product formed during nucleation is very small and as such has little influence on the composition of the residual austenite. In the limiting case, it can be said that the points representing the compositions of the initial austenite and the residual austenite coincide with each other so that the line AB becomes a tangent to the austenite free energy curve at the original composition $\bar{x}$ (Figure 2.3.b). The free energy change accompanying the formation of one mole of ferrite nuclei of composition x_α is then given by ΔG_2. The value of ΔG_2 depends on the choice of the ferrite nucleus composition and attains a maximum value of ΔG_m when the nucleus composition is x_m^α. As shown in Figure 2.3.b, this is obtained by drawing a tangent to the ferrite free energy curve which is parallel to the tangent AB.

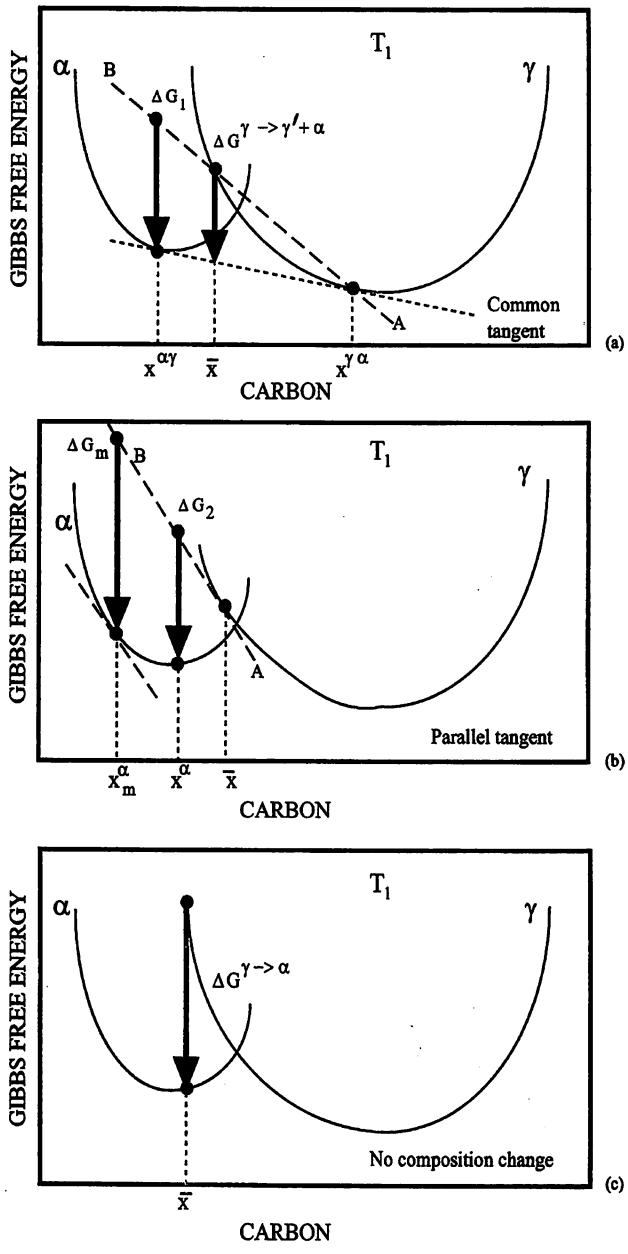

Fig. 2.3: Geometrical illustration of the chemical free energy change associated with nucleation and growth of ferrite from austenite of composition $\overline{x}$ [Bhadeshia, 1992].

Finally, the free energy change $\Delta G^{\gamma \rightarrow \alpha}$ for a transformation in which there is no change in the chemical composition, is obtained by the difference in the free energies of austenite and ferrite at the appropriate composition (Figure 2.3.c).

2.3.b The T_0 Criterion

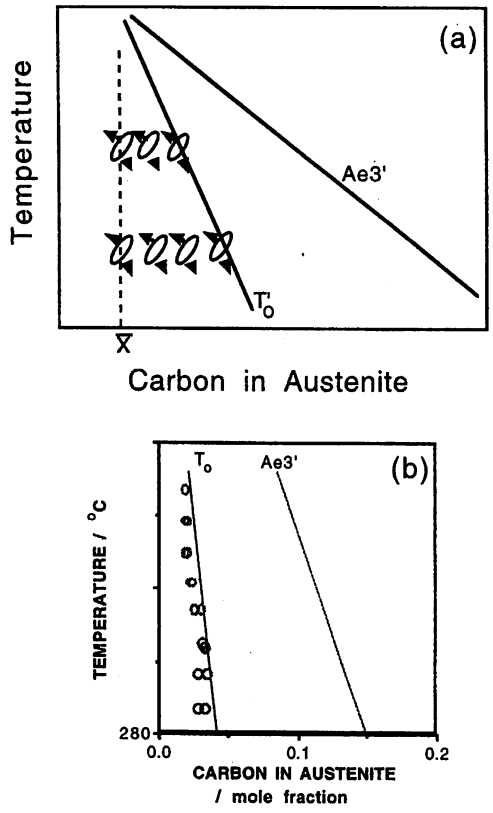

Fig. 2.4: (a) Illustration of the incomplete reaction phenomenon. During isothermal transformation, a plate of bainite grows without diffusion, then partitions its excess carbon into the residual austenite. The next plate therefore has to grow from carbon-enriched austenite. This process continues until diffusionless transformation becomes impossible when the austenite composition eventually reaches the T_0 boundary. (b) Experimental data showing that the growth of bainite stops when the austenite carbon concentration reaches the T_0 curve (Fe-0.43C-3Mn-2.12Si wt% alloy) [Bhadeshia, 1982].

Successive bainite sub-units grow from carbon-enriched austenite with decreasing driving force [Chang and Bhadeshia, 1995]. This continues until the carbon concentration of austenite reaches T_0 when the driving force for composition-invariant transformation drops to zero and the reaction stops (Figure 2.4). The locus of T_0 temperatures as a function of the carbon concentration on the Fe–C phase diagram is called the 'T_0 curve'. This curve is shifted to still lower temperatures to account for 400 J mol^{-1} of the stored energy due to the shape deformation [Bhadeshia, 1981b]; the locus is then designated the T_0' curve. A study of the thickness of austenite films lying between parallel bainitic ferrite sub-units for several alloys has indeed shown that transformation stops at T_0', and not at T_0 nor when paraequilibrium is

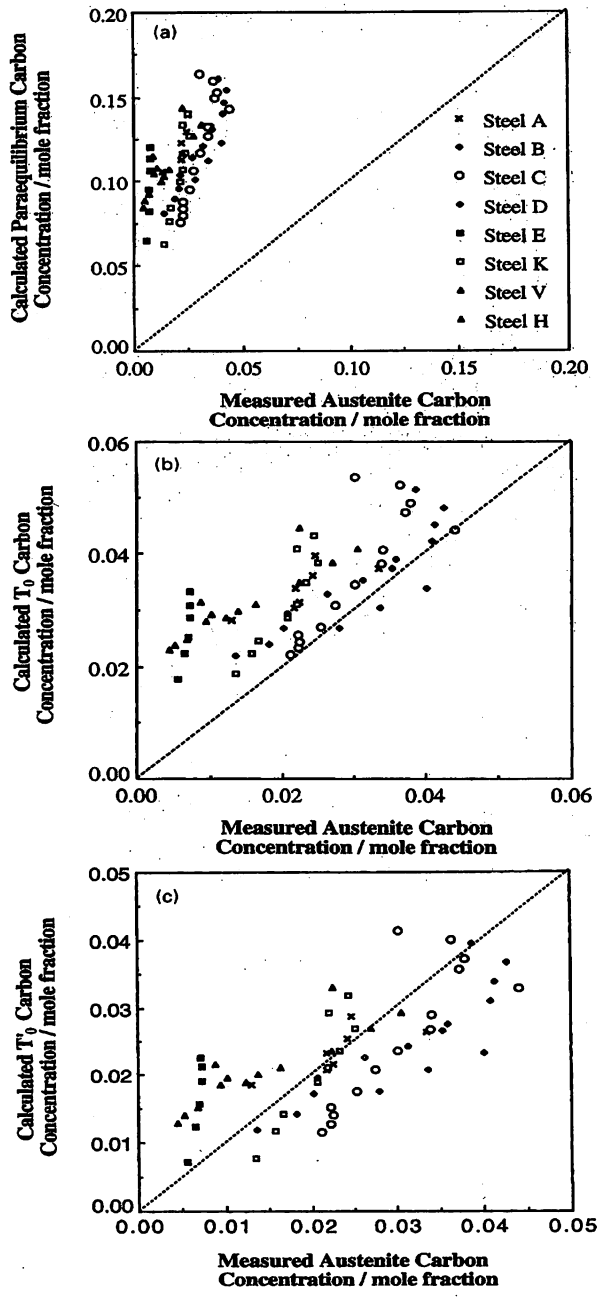

Fig. 2.5: Measured carbon concentration of austenite at point where transformation to bainite stops versus calculated concentration for various conditions [Chang and Bhadeshia, 1995].

reached (Ae_3') (Figure 2.5). Because of this observation, the model developed in the present study uses the T_0' curve as the locus where transformation stops.

The phenomenon is known as the 'incomplete reaction phenomenon' because the reaction stops before austenite reaches its equilibrium concentration given by the Ae_3 phase boundary. Owing to the negative slope of the T_0 curve, the maximum volume fraction of bainite that can

form at any temperature increases with decreasing temperature.

If the initial average carbon composition of the alloy is reduced, more bainite forms according to the lever rule and vice-versa. Another way of forming more bainite is to shift the T_0 curve to higher C-contents by altering the substitutional solute content. This cannot be done with austenite stabilising elements (e.g. Mn or Mo) which shift the T_0 curve to lower carbon concentrations [Wang and Yang, 1992].

If the 400 J mol^{-1} of stored energy in bainite is reduced by plastic deformation of the surrounding austenite, then a higher bainite volume fraction should form [Chester and Bhadeshia, 1997]. The observation that, in fact, in certain alloys the reaction ceases at a lower austenite carbon content than T_0' could indicate that transformation stops when the nucleation of bainite becomes impossible.

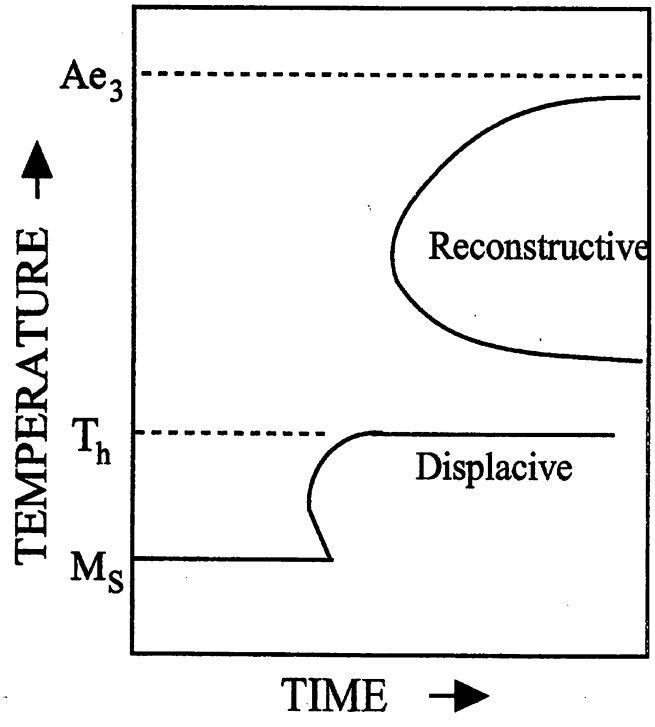

Fig. 2.6: A schematic TTT diagram showing the two C-curves and the T_h temperature [Bhadeshia, 1992].

2.3.c Universal Nucleation Function

In the case where the C-curves for reconstructive and displacive transformations in a TTT diagram do not overlap, the lower C-curve has a characteristic flat top which represents the highest temperature T_h at which displacive transformation to ferrite can take place (Figure 2.6). This transformation-start temperature must be controlled by nucleation which is more difficult than growth, because of the disproportionate amount of energy spent in creating a new interface around a small particle. An analysis of the magnitude of the free energy change available at T_h provides useful clues to the mechanism of transformation and gives an indication of the amount of driving force necessary for nucleation to occur at a detectable rate.

Steven and Haynes [1956] measured the T_h temperatures for a wide range of low-alloy steels. All of these steels exhibited two distinct C-curves. For each of these steels, the driving force available at T_h was calculated assuming two possible nucleation mechanisms - (i) nucleation without the partitioning of any of the solute atoms including carbon ($\Delta G^{\gamma\rightarrow\alpha}$) and (ii) nucleation with paraequilibrium carbon partitioning (ΔG_m) [Bhadeshia, 1981]. The results of the analysis are plotted in Figure 2.7. and reveal some important facts. Firstly, the nucleation of Widmanstätten ferrite or bainite occurs with the partitioning of carbon atoms since the alternative hypothesis of diffusionless nucleation would lead to an increase in the free energy for some of the cases illustrated. Secondly, all the points, whether they correspond to Widmanstätten ferrite or to bainite lie on the same straight line in Figure 2.7.b.

Therefore, the nucleation mechanisms of Widmanstätten ferrite and bainite are considered to be identical: a potential nucleus can develop into either phase depending on whether or not an adequate driving force is available for the growth of bainite at the transformation temperature concerned. On this basis, it is possible to define a universal nucleation function of temperature G_N which is applicable to all steels. In a given steel, nucleation first becomes possible at a detectable rate below a temperature W_s (the Widmanstätten ferrite-start temperature), at which the magnitude of the maximum nucleation free energy change ΔG_m (nucleation with paraequilibrium carbon partitioning) for the steel exceeds that given by G_N:

$$G_N = B_1 T_h - B_2 \tag{2.23}$$

For the best fit line, the values of B_1 and B_2 have been found to be 3.637 J mol^{-1}K^{-1} and 2540 J mol^{-1} respectively, when T_h is expressed in °C [Ali and Bhadeshia, 1990].

Although the above treatment appears empirical, it has been interpreted in terms of martensite nucleation theory [Bhadeshia, 1981; Bhadeshia, 1992]. The nucleation rate per unit volume depends on the activation energy G^*:

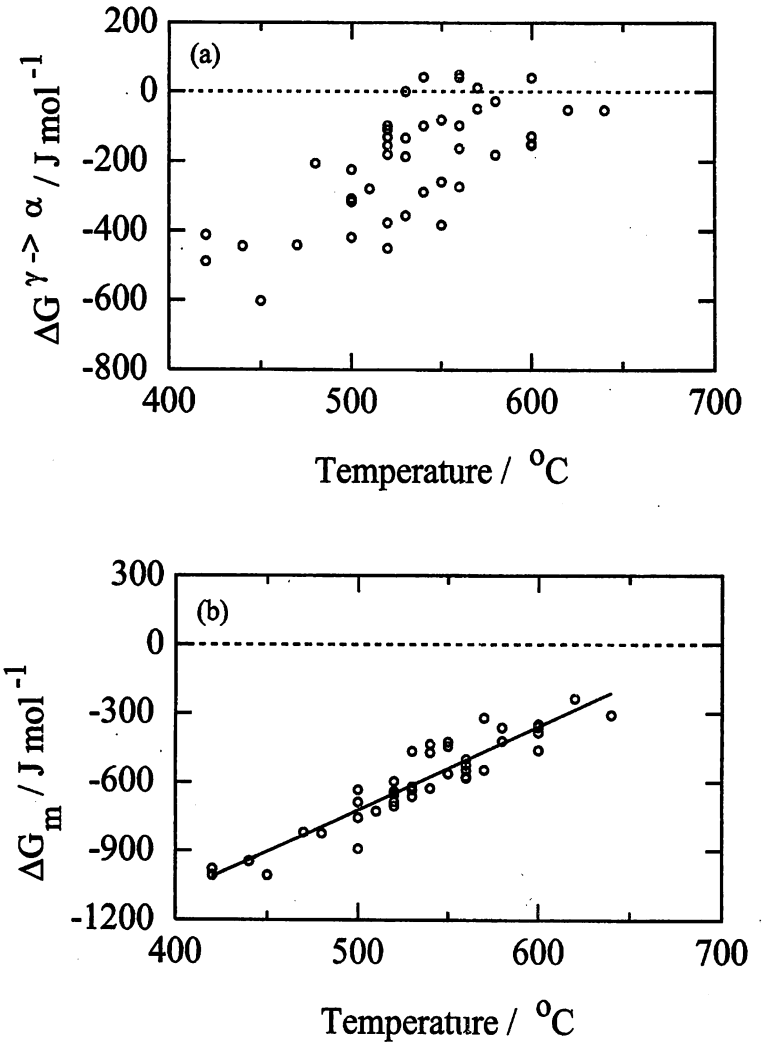

Fig. 2.7: The driving force for nucleation for a variety of steels at their respective T_h temperatures. The driving force was calculated assuming (a) diffusionless nucleation ($\Delta G^{\gamma \rightarrow \alpha}$) and (b) paraequilibrium redistribution of carbon (ΔG_m) [Bhadeshia, 1981].

$$I \propto \nu \exp\{-G^*/RT\} \tag{2.24}$$

The activation energy G^* for the nucleation of bainite is known to be directly proportional to the driving force for transformation, $G^* \propto \Delta G_m$. This is consistent with the theory for martensite nucleation, although it is required that carbon should partition into the austenite during bainite nucleation. On the other hand, in the classical nucleation theory where a new phase forms by a random structural and composition fluctuation in the parent phase, $G^* \propto \Delta G_m^{-2}$. Such a relation cannot explain the behaviour obtained for Widmanstätten ferrite and bainite.

2.3.d Growth of the Nucleus

It was pointed out earlier that both Widmanstätten ferrite and bainite appear to grow from the same nucleus and that the nucleation rate becomes appreciable when

$$\Delta G_m \leq G_N \tag{2.25}$$

The nucleus can develop into Widmanstätten ferrite (i.e., $T_h = W_s$) if the driving force for paraequilibrium growth exceeds the stored energy of Widmanstätten ferrite, which has been estimated to be 50 J mol^{-1} [Ali and Bhadeshia, 1990]:

$$\Delta G^{\gamma \rightarrow \gamma' + \alpha} \leq 50 \text{ J mol}^{-1} \tag{2.26}$$

Sometimes, the curve corresponding to ΔG_m crosses the G_N line twice (while the condition of Equation 2.26 is satisfied), which means that at some temperature below W_s, there is a region where no Widmanstätten ferrite can form.

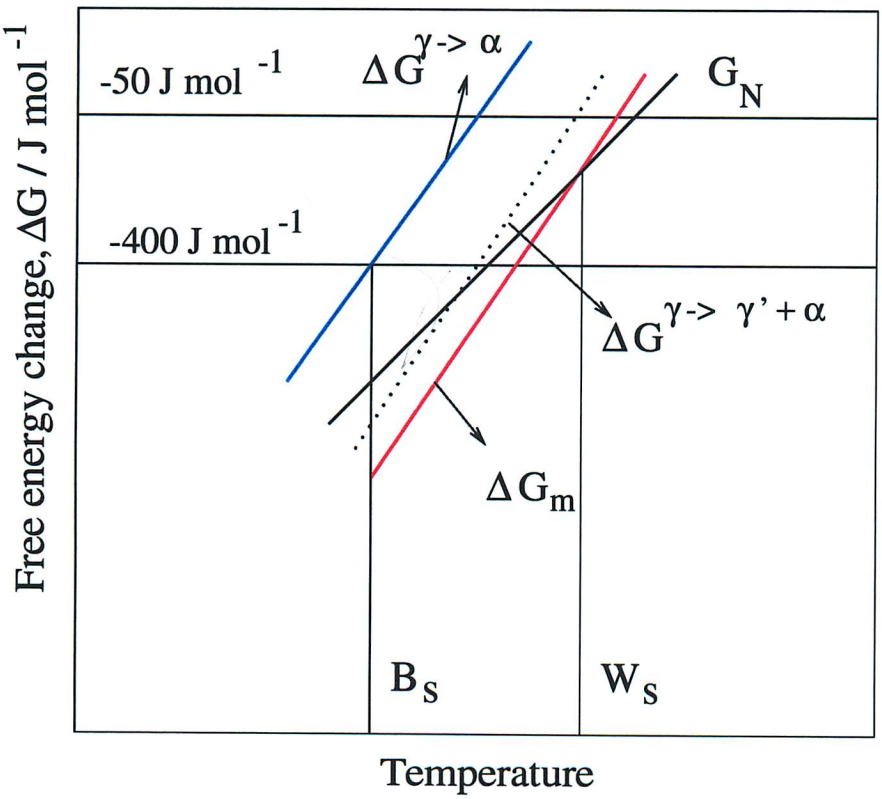

Fig. 2.8: Diagram illustrating the definition of the W_s and B_s temperatures based on available driving force for nucleation and growth [Bhadeshia, 1981].

Alternatively, if the driving force for diffusionless growth is sufficient to allow for 400 J mol^{-1} of the stored energy of bainite [Bhadeshia, 1981b], then transformation to bainite takes place and T_h is identified with the bainite start temperature B_s,

$$\Delta G^{\gamma \rightarrow \alpha} \leq 400 \text{ J mol}^{-1} \tag{2.27}$$

The Widmanstätten ferrite-start temperature W_s, or the bainite-start temperature B_s, is defined as the highest temperature at which both the nucleation and the growth criteria for the respective phase are first satisfied (Figure 2.8).

2.3.e The Nucleation Rate

At any temperature the rate of nucleation per unit volume is related to the activation energy by an Arrhenius type equation:

$$I = B_3 \exp\left\{\frac{-G^*}{RT}\right\} \tag{2.28}$$

where B_3 is a constant related to the density of potential nucleation sites and to an attempt frequency. Expanding G^* to account for its linear dependence on the driving force, we get:

$$I = B_3 \exp\left\{-\frac{B_4 + B_5 \Delta G_m}{RT}\right\} \tag{2.29}$$

where B_4 and B_5 are constants. At $T = T_h$, $\Delta G_m = G_N$; the nucleation rate I_{T_h} is then given by:

$$I_{T_h} = B_3 \exp\left\{-\frac{B_4 + B_5 G_N}{RT_h}\right\} \tag{2.30}$$

At their respective T_h temperatures, two steels A and B have identical nucleation rates: $I^A_{T_h} = I^B_{T_h} = I_{T_h}$. Combining equations 2.23 and 2.30, this gives $B_4 = B_2 \times B_5$. The nucleation rate can therefore be written as:

$$I = B_3 \exp\left\{-\frac{B_4}{RT} - \frac{B_4 \Delta G_m}{B_2 RT}\right\} \tag{2.31}$$

2.4 Rees and Bhadeshia Model

2.4.a Description

The general theory of bainite transformation described previously was applied by Bhadeshia [1982] to model the bainite transformation kinetics, with subsequent modifications by Rees and Bhadeshia [1992]. The model is limited to upper bainite and to steels where cementite precipitation is retarded due to alloying with elements like silicon, aluminium or chromium.

The bainite plates first nucleate on austenite grain boundaries. The initial nucleation rate is given by equation 2.31. The density of nucleation sites, B_3, is related to the austenite grain size:

$$B_3 = \frac{1}{d_\gamma B_3'} \tag{2.32}$$

where d_γ is the austenite grain size and B_3' is an empirical constant. The inverse of the grain size is related to the amount of austenite grain surface per unit volume.

The dislocation debris generated by the shape deformation stop plate growth even before it encounters an austenite grain boundary. The transformation proceeds further by autocatalytic nucleation of new plates at the tips of the old ones [Oblak and Hehemann, 1967]. This results in a sheaf like structure (Figure 1.13). The plates, once nucleated, grow very rapidly to consume a given volume of austenite before they are halted [Barford and Owen, 1961; Oblak and Hehemann, 1967; Bhadeshia and Edmonds, 1980]. The overall transformation kinetics are thus controlled by nucleation rather than by growth. The nucleation rate due to autocatalysis was assumed to be proportional to the existing bainite volume fraction [Bhadeshia, 1982]. The total nucleation rate per unit volume was written as:

$$I_b = I(1 + \beta\theta_b\xi) \quad \text{or} \quad I_b = I(1 + \beta v) \tag{2.33}$$

where β is an autocatalysis constant and ξ is the volume fraction (v) of bainite normalised with respect to the maximum fraction θ_b possible at a given temperature:

$$\xi = v/\theta_b \tag{2.34}$$

Austenite is enriched in carbon as the reaction progresses, reducing the driving force for transformation. The free energy for nucleation, ΔG_m, was assumed to vary linearly with the extent of reaction from its initial value of ΔG_m^o to the final value of G_N according to:

$$\Delta G_m = \Delta G_m^o - \xi(\Delta G_m^o - G_N) \tag{2.35}$$

The form of equation 2.35 assumes that the nucleation and growth criteria of transformation fail simultaneously so that $\Delta G_m = G_N$ when $\xi = 1$. The autocatalysis factor β was modelled as a function of the average carbon content of the steel, $\overline{x}$:

$$\beta = \lambda_1(1 - \lambda_2\overline{x}) \tag{2.36}$$

where λ_1 and λ_2 are empirical constants and $\overline{x}$ is the mean carbon concentration of the steel in mole fraction. Thus autocatalysis is less effective in higher carbon steels where a significant build-up of carbon at the transformation interface inhibits autocatalytic nucleation of new plates. When the steels are considered individually, $\beta = \lambda_1$.

Consider austenite of volume V_γ undergoing transformation to bainite. The extended volume of bainitic ferrite that forms between time τ and $\tau + d\tau$ is given by:

$$dV^e = I_b V_\gamma u d\tau \tag{2.37}$$

where u is the volume of a single bainite plate. The change in real volume is related to that in extended volume by [Christian, 1975]:

$$dV = (1 - \xi)dV^e \tag{2.38}$$

This gives:

$$dV = (1 - \xi)V_\gamma u I_b d\tau \tag{2.39}$$

Writing this in terms of volume fraction v while remembering that $v = \theta_b\xi$, we get

$$\theta_b d\xi = (1 - \xi)u I_b d\tau \tag{2.40}$$

Substituting for nucleation rate I_b gives the differential equation for the overall transformation rate:

$$d\xi = \frac{uB_3}{\theta_b}(1 - \xi)(1 + \beta\theta_b\xi) \times \exp\left[\frac{-B_4}{RT}\left(1 + \frac{\Delta G_m^o}{B_2}\right) + \Gamma_2\xi\right]d\tau \tag{2.41}$$

where Γ_2 is given by

$$\Gamma_2 = \frac{B_4(\Delta G_m^o - G_N)}{B_2 RT} \tag{2.42}$$

Equation 2.41 was solved analytically to give the time to form a certain volume fraction of bainite [Rees and Bhadeshia, 1992].

The above model has four empirical constants, namely $B_3^{'}$, B_4, λ_1 and λ_2. The model was optimised using bainite transformation kinetics data due to Bhadeshia [1982] to determine the best-fit values of these empirical constants. The chemical compositions of the steels used in the analysis are given in Table 2.1. The best-fit values of the constants after optimisation are given in Table 2.2.

Alloy	C	Si	Mn	Ni	Cr	Mo	V
Fe-Mn-Si-C	0.22	2.03	3.0	0.00	0.00	0.00	0.00
Fe-Ni-Si-C	0.39	2.05	0.00	4.08	0.00	0.00	0.00
300 M	0.44	1.74	0.67	1.85	0.39	0.83	0.09

Table 2.1: The composition (wt%) of the steels used for the optimisation of the Rees and Bhadeshia model [1992]. The bainite transformation kinetics of these alloys were first studied by Bhadeshia [1982].

Dataset	$B_3^{'}/u$, $\mathrm{m^{-1}s}$	B_4, $\mathrm{J\,mol^{-1}}$	λ_1	λ_2
Fe-Mn-Si-C	3.876×10^7	1.925	4.756	0.00
Fe-Ni-Si-C	2.028×10^7	2.907×10^4	90.822	0.00
300 M	1.231×10^7	3.767×10^4	141.66	0.00
Combined data	3.390×10^7	2.065×10^4	139.00	25.46

Table 2.2: The best fit values of the empirical constants of the Rees and Bhadeshia model [1992].

2.4.b Limitations of the Rees and Bhadeshia Model

As stated previously, the Rees and Bhadeshia model has a number of empirical assumptions. The bainite plate volume, u, is not considered explicitly. Measurements of bainite plate thickness indicate that it varies with the composition of the steel [Chang and Bhadeshia, 1996]. The model does not take into account this variation and treats the plate thickness as an empirical constant along with the nucleation site density.

The effect of autocatalytic nucleation is modelled empirically in Equation 2.33. The optimised value of the autocatalysis factor β seems unrealistically high in some cases (*e.g.*, it is 141 for alloy 300M). This was considered not to be consistent with the observed sheaf structure.

With such a high value of β, the sheaf is expected to be much thicker than is actually obtained since the observed structure indicates that each existing plate can nucleate only about 3 or 4 plates. Another inconsistency with the autocatalysis factor is that when all the alloys are considered together, β is assumed to decrease linearly with increasing carbon concentration of the steel (Equation 2.36). However, when the data for individual alloys are treated separately, the optimum values of β indicate exactly the opposite trend. This is particularly true for alloys in Table 2.1.

The best-fit value of the empirical constant B_4 varied by 4 orders of magnitude from alloy to alloy which is not justified as B_4 should be independent of alloy composition. Moreover, the assumption in equation 2.35 that the chemical free energy change associated with nucleation (ΔG_m) varies linearly with the extent of reaction ξ from its initial value ΔG_m^o to G_N is not valid, except in a few special cases.

2.5 The Singh and Bhadeshia Model

2.5.a Bainite Plate Volume

There is no physical model which can predict the bainite plate thickness, given the steel composition and the transformation temperature. Therefore, a quantitative model was developed by Singh and Bhadeshia [1998b] using neural network analysis. The experimental data on the thickness of bainite plates in high-silicon steels published by Chang and Bhadeshia [1996] were used for the purpose of training the network. The thicknesses for other alloys were measured and constituted the training dataset for the analysis. For a given alloy, the predicted plate thickness increased with transformation temperature (Figure 2.9). This is because strong austenite or large driving force (at low temperatures) result in finer plates, the former because there is a larger resistance to interface motion and the latter because an increased nucleation rate leads to microstructural refinement. The conclusion is that temperature, does not, in its own right, seem to have a significant effect on the bainite plate thickness over the range 260-460°C.

The plate thickness predicted by the neural network model was used as an input to the kinetics model. Considering an oblate spheroid shape of the bainite plates with a constant radius to thickness ratio over the entire transformation range, the volume of the plate was modelled as being proportional to the cube of its thickness, a_b:

$$u = \alpha_p a_b^3, \qquad \alpha_p = \text{constant} \tag{2.43}$$

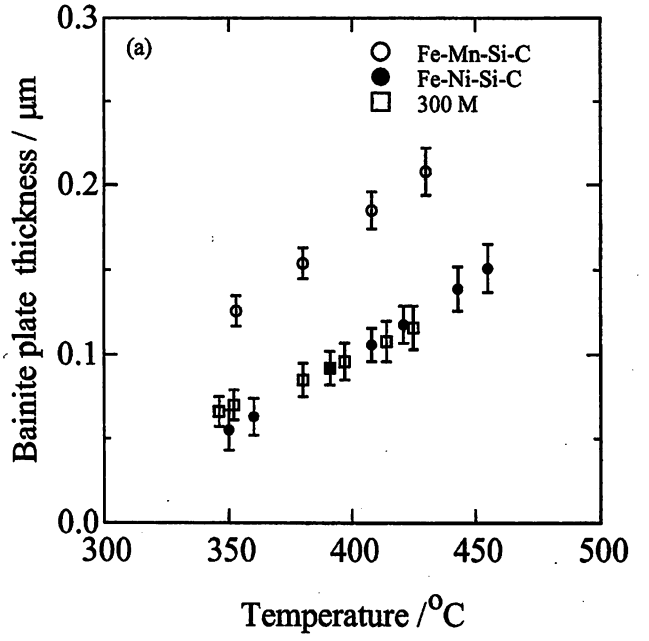

Fig. 2.9: Bainite plate thickness predicted by the neural network model for alloys in the Rees and Bhadeshia study [Singh, 1998a].

2.5.b Autocatalysis

An attempt was made to formulate the effect of autocatalysis on the total nucleation rate based on the actual mechanism of the development of the sheaf structure. Details of the calculations are not given here. It was assumed that at a fixed temperature, ΔG_m remains constant over the entire extent of transformation, *i.e.* from $\xi = 0$ to $\xi = 1$. After calculations, the autocatalysis factor was found to vary from 1.4 to 3.5, which is compatible with the observed sheaf structure.

2.5.c New Expression of the Nucleation Rate I_b

The following equation was used as an alternative to equation 2.32:

$$N_V^0 = \frac{B_6}{d_\gamma} \tag{2.44}$$

where N_V^0 is the initial density of nucleation sites. The initial nucleation rate is:

$$I = N_V^0 \ \nu \ \exp\left\{\frac{-G^*}{RT}\right\} \tag{2.45}$$

where $\nu = k_b T/h$ is a frequency factor (k_b is the Boltzmann constant and h is the Planck constant). From equation 2.31, the activation energy for nucleation, G^*, is given by:

$$G^* = B_4\left\{1 + \frac{\Delta G_m}{B_2}\right\} \tag{2.46}$$

In equation 2.33, the total nucleation rate per unit volume I_b was taken to be proportional to the volume v of bainite already formed and the proportionality constant was β, the autocatalysis factor. The new approach of Singh and Bhadeshia suggests that I_b, including the effect of autocatalysis is given by:

$$I_b = N_V^T\ \nu\ \exp\left\{\frac{-G^*}{RT}\right\} \tag{2.47}$$

where N_V^T is the total density of nucleation sites at time τ, equal to the sum of the initial density N_V^0 and the number of plates formed by autocatalysis during the time τ, which is taken to be proportional to the initial nucleation rate I:

$$N_V^T = N_V^0 + \beta I \tau \tag{2.48}$$

Combination of equations 2.45 and 2.48 with equation 2.47 gives

$$I_b = I\left[1 + \beta\ \tau\ \nu\ \exp\left(-\frac{G^*}{RT}\right)\right] \tag{2.49}$$

Substituting equation 2.49 into Equation 2.40, the following kinetic equation is easily obtained

$$\frac{d\xi}{dt} = (1-\xi)\frac{\nu}{C}\exp\ \left(\frac{-G^*}{RT}\right)\left[1 + \beta t\nu\ \exp\ \left(\frac{-G^*}{RT}\right)\right] \tag{2.50}$$

where the constant C is

$$C = \frac{\theta_b d_\gamma B_6^{'}}{u}\ \text{ and }\ B_6^{'} = \alpha_p \frac{B_6}{2} \tag{2.51}$$

2.5.d New Empirical Constants Values

The new model also has four empirical constants namely $B_6^{'}$, B_4, λ_1 and λ_2. The best fit values of the constants for individual alloys as well as for all the alloys taken together are shown in Table 2.3.

2.5.e Error in this Development

In reviewing the theory it was noticed that the term $\beta I d\tau$ really represents a change in the number density of nucleation sites in *extended space*. The real change should have been obtained by multiplying the term by $(1-\xi)$:

Dataset	B_6', m^{-2}	B_4, J mol^{-1}	λ_1	λ_2
Fe-Mn-Si-C	3.845×10^{-25}	4.469×10^4	2.203	0.00
Fe-Ni-Si-C	1.945×10^{-25}	8.407×10^4	1.865	0.00
300 M	2.432×10^{-23}	7.147×10^4	1.416	0.00
Combined data	3.845×10^{-25}	3.805×10^4	4.932	45.158

Table 2.3: The best fit values of the empirical constants after optimisation of the new model [Singh, 1998a].

$$dN_V^T = (1-\xi)\ dN_V^e = (1-\xi)\ \beta\ N_V^T\ \nu\ \exp\left\{\frac{-G^*}{RT}\right\} d\tau \tag{2.52}$$

which after integration gives the following equation for N_V^T which implies a modification of equation 2.48:

$$N_V^T = N_V^0\ \exp\left[\beta\ \nu\ \exp\left(\frac{-G^*}{RT}\right) \int_{\tau=0}^{\tau=t} (1-\xi) d\tau\right] \tag{2.53}$$

2.5.f Further Modifications to Account for Grain Size Effect

Singh and Bhadeshia [1998b] argued that the temperature corresponding to the top of the lower C-curve of the *TTT* diagram which gives the Widmanstätten ferrite or the bainite transformation-start temperature should depend on the austenite grain size. This has been proved experimentally for bainite transformation taking the example of an Fe-0.27C-2.01Si-2.16Mn-2.07Ni wt% alloy. Further evidence was provided by analysing the data reported in literature. The universal nucleation function G_N was modified in the light of this result with the new function taking into account the grain size effect. The dependence of G_N on temperature has also been modified.

With the new G_N function, the number of empirical constants in the bainite kinetics model described above can be reduced from 4 to 3.

2.6 Factors Influencing the Bainite Transformation

2.6.a Austenite Enrichment in Carbon

Carbon has a large effect on the range of temperature over which upper and lower bainite occur. The B_s temperature is depressed by many alloying elements but carbon has the greatest influence, as indicated by the following popular empirical equation [Steven and Haynes, 1956]:

$$B_s(^\circ\mathrm{C}) = 830 - 270\mathrm{C} - 90\mathrm{Mn} - 37\mathrm{Ni} - 70\mathrm{Cr} - 83\mathrm{Mo} \tag{2.54}$$

where the concentrations are all in wt%. The above equation is valid for steels containing 0.1 to 0.55 carbon, 0.1-0.35 silicon, 0.2-1.7 manganese, 0.0-5.0 nickel, 0.0-3.5 chromium and 0.0-1.0 molybdenum (in wt%).

Carbon has a much larger solubility in austenite than in ferrite, and is a very powerful austenite stabiliser which leads to a general retardation of reaction kinetics. The fraction of carbides to be found in the final microstructure increases in proportion to the carbon concentration, so that the concentration must be kept below about 0.4 wt% to ensure reliable mechanical properties. We have already seen that an increase in carbon makes it easier for lower bainite to form because it becomes more difficult for plates of supersaturated bainitic ferrite to decarburize before the onset of cementite precipitation.

When enough bainite forms without the interference of carbides (e.g., in silicon-rich steels), it enriches the austenite in carbon so that the martensite formation can be prevented (dramatic drop in M_s) on cooling to ambient temperatures. The austenite enrichment can thus be determined readily by the difference in predicted and measured M_s [Barnes *et al.*, 1995]. This is assuming that all regions of austenite have been enriched by the same amount. This is rather unlikely in a morphology where blocky austenite and films of austenite trapped between bainite sub-units coexist. If one measures the carbon enrichment in a certain austenite area, it is likely not to represent the average enrichment because the result is too high: only regions of austenite with the highest carbon-content have been retained [Minote *et al.*, 1996].

Austenite films between bainitic ferrite sub-units are limited in size by the carbon diffusion field around the sub-units. The T_0 criterion implies that this austenite must have a composition in carbon higher than the carbon content at T_0. The more carbon is rejected into these films, the larger they are in a Si steel where carbide precipitation is prevented (Figure 2.10). However, if carbide precipitation occurs, there is removal of carbon from austenite in a way similar to that by which the films of austenite isolate excess carbon from the reacting bulky regions of austenite [Rees and Bhadeshia, 1992]. This leads to the idea that modelling carbide formation

between sub-units (this is yet to be done) could be done by an approach similar to the one used for the modelling of austenite films. Carbide formation occurs at least after a bainite sub-unit formation and not alternatively. The reverse is true for inverse bainite in hypereutectoid steels where cementite forms first. In hypoeutectoid steels, therefore, carbide precipitation is not a fundamental characteristic but a secondary effect of the bainite transformation.

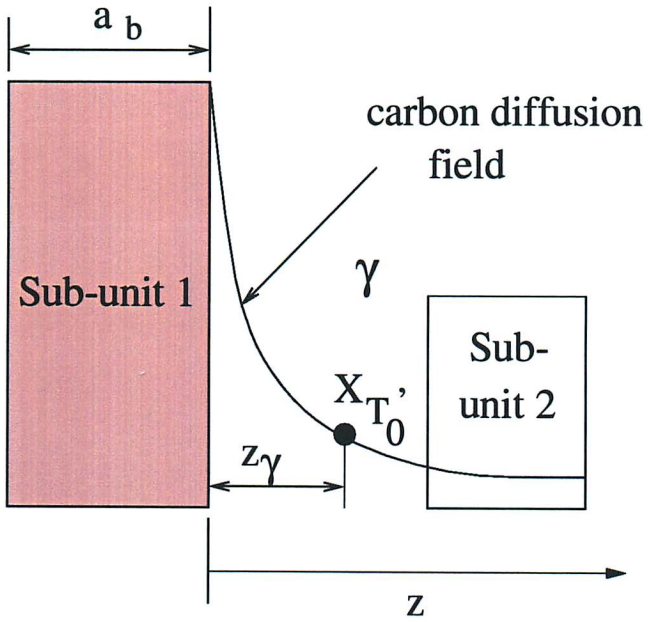

Fig. 2.10: Schematic diagram of the method used in estimating the thickness of austenite films: sub-unit 1 forms first, and sub-unit 2 is allowed to approach it to point where $x_\gamma \leq x_{T_0'}$ (distance of this point from sub-unit 1 is denoted z_γ) [Chang and Bhadeshia, 1995].

More retained austenite in the form of films can be obtained in upper bainite because more carbon has been partitioned into it [Jung *et al.*, 1997]. Carbon is trapped in the films because the solubility of carbon in austenite is higher than in ferrite.

One study showed that the retained austenite volume fraction as well as elongation go through a maximum near 400°C [Zarei Hanzaki *et al.*, 1995]. The smaller the initial austenite grain size, the smaller the bainite packet size and the smaller the regions of retained austenite trapped in between [Zarei Hanzaki *et al.*, 1997]. More retained austenite is thus obtained because these numerous trapping areas do not transform subsequently to lower bainite or martensite on cooling like blocky austenitic regions do.

2.6.b Role of Alloying Elements and Microalloying

It has been found that both dissolved niobium in austenite and free boron are prerequisites for granular bainite formation which is predominant in continuous cooling, although some authors challenge this since granular bainite can be obtained in steels without these solutes [Wang and Kao, 1993]. A critical boron content is necessary to achieve the desired bainitic transformation and the associated strengthening effect. This critical concentration increases with carbon content. A higher carbon content is found to promote allotriomorphic ferrite formation. Carbon might diminish the effect of boron for bainitic transformation due to the formation of boron carbides and/or the depletion of dissolved niobium in austenite.

Niobium is known to increase hardenability, possibly by its segregation to austenite grain boundaries, when in solid solution. It accelerates transformation when in precipitated form (lowers hardenability) [Rees *et al.*, 1995]. The solubility product relationship allows the calculation of the temperature at which all niobium can enter solid solution:

$$\log_{10}([\mathrm{Nb}][\mathrm{C}]) - 0.248[\mathrm{Mn}] = 1.8 - \frac{6770}{T} \tag{2.55}$$

where [Nb], [C] and [Mn] are the concentrations of niobium, carbon and manganese respectively (in wt%), and the temperature T is in K.

Zarei Hanzaki *et al.* [1997] have shown that promoting Nb(CN) precipitation by a change in thermomechanical processing (TMP) conditions results in a decrease in the volume fraction of retained austenite. This is attributed to a reduction of niobium in solid solution and therefore to a decrease in parent austenite stability.

Silicon inhibits the formation of cementite in which it has negligible solubility. In addition, Quidort [1999] studied a series of alloys with increasing silicon and showed that an addition of 1 wt% silicon not only suppresses cementite precipitation but decreases the rate of reaction by a factor of about three (Figure 2.11). Quidort also proposed that the increased kinetics when cementite particles can form is because the latter remove carbon from the transformation tip along the interface so that more carbon can diffuse out of the sub-unit, thereby giving it a faster growth rate. This proposed mechanism is illustrated on Figure 2.12. The absence of coarse cementite is generally good for toughness. Cementite also precipitates very slowly with high amounts of aluminium [Thomson, 1998].

Nickel has very little influence on cementite precipitation. Quidort showed that the effect of nickel reported in the literature is greater than expected from thermodynamic considerations of its austenite stabilising character. He suggested that a solute drag effect for nickel at the

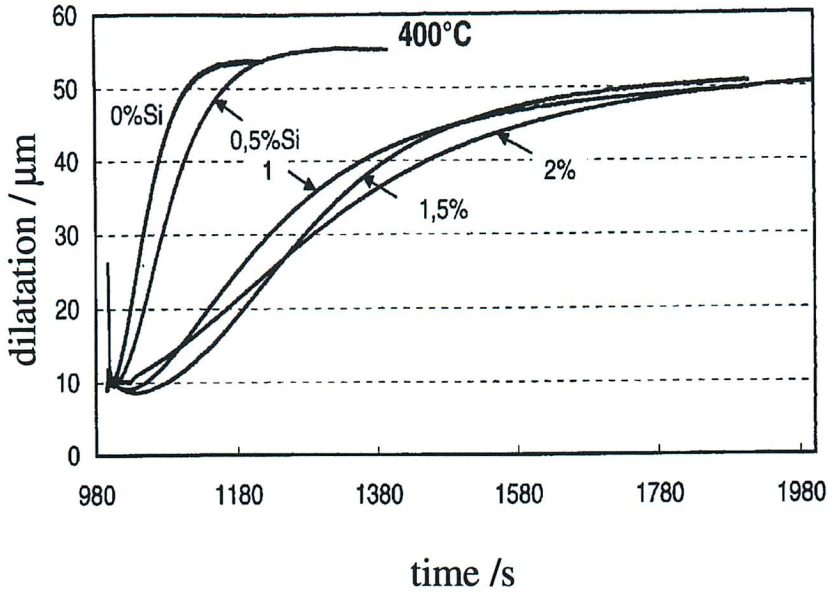

Fig. 2.11: Dilatometric data associated with the isothermal transformation at 400°C of the series of alloys Fe-0.5C-5Ni wt% with Si content from 0 to 2 wt%. There is a marked decrease in the kinetics when increasing the silicon content from 0.5 to 1 wt% [Quidort, 1999].

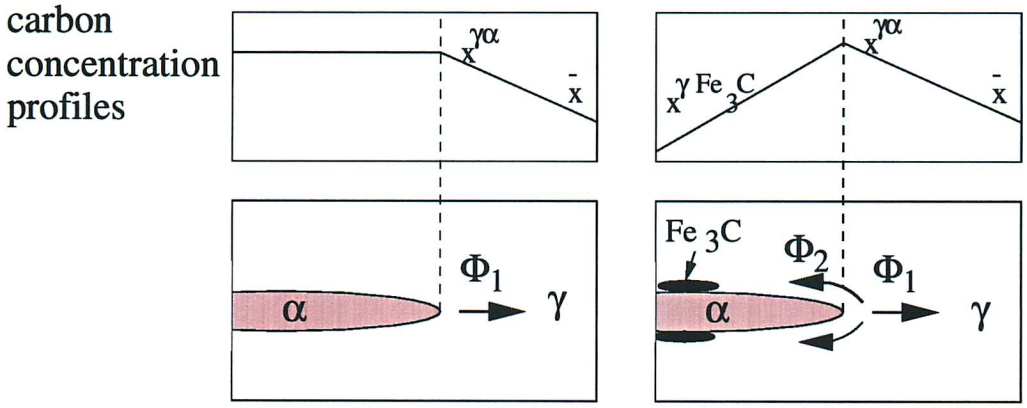

Fig. 2.12: Schematic illustration for the suggested process that allows acceleration of transformation when cementite is present in the microstructure [Quidort, 1999]. Φ_1 and Φ_2 are carbon fluxes.

interface is probable. The addition of 0.2 wt% molybdenum results in a marked decrease in the transformation temperatures at all cooling rates [Barnes *et al.*, 1995].

In plain carbon steels, the bainitic reaction is kinetically shielded by the ferrite and pearlite reactions which commence at higher temperatures and shorter times (Figure 2.13.a), so that in continuously cooled samples bainitic structures are difficult to obtain. Even using isothermal

transformation, difficulties arise if, for example, the ferrite reaction is particularly rapid. The addition of metallic alloying elements usually results in the retardation of the ferrite and pearlite reactions. In addition, the bainite reaction is depressed to lower temperatures. This often leads to a greater separation of the reactions, and the TTT curves for many alloys show much more clearly separate C-curves for the pearlite and bainitic reactions (Figure 2.13.b). However, it is still difficult to obtain a fully bainitic microstructure, even with an appropriate range of cooling rates because of its proximity to the martensite reaction.

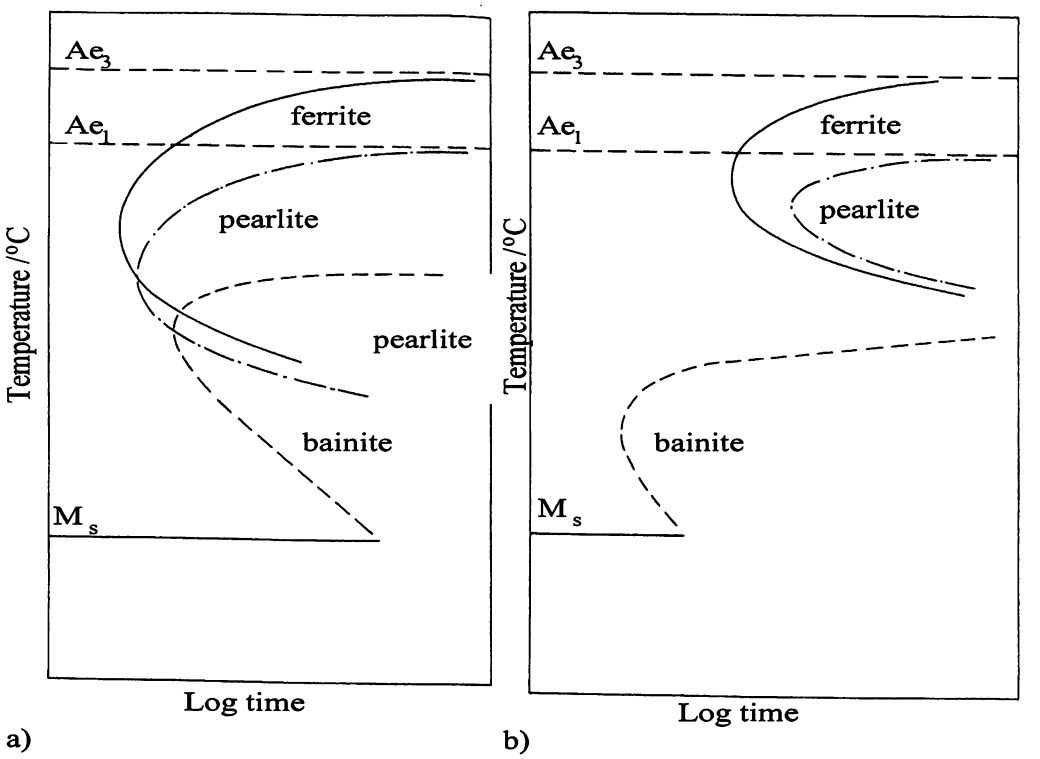

Fig. 2.13: Effect of alloying elements on the bainite reaction TTT curves. Schematic diagram for; a) a plain carbon steel; b) for a low alloy steel with contents in metallic alloying elements such as to produce a greater separation of the reactions [Irvine and Pickering, 1957].

Boron increases bainitic hardenability by shifting the allotriomorphic ferrite nose to the right [Irvine and Pickering, 1957]. A very effective way of isolating the bainite reaction in low carbon steels has been found by adding about 0.002 wt% soluble boron to a 0.5 wt% Mo steel. Boron can be used in interstitial free (IF) steels to considerably improve their mechanical properties apart from deep drawing which is what they are made for. A high level of manganese slows down the bainite transformation [Rees and Bhadeshia, 1992].

The extent of the bainite transformation can be so high in low carbon steels –where there

are almost no carbides– as to make the sheaf structure indistinct [Chang and Bhadeshia, 1995]. The segregation of carbon atoms at dislocations in bainitic ferrite can prevent the carbon atoms from precipitating explaining the higher than expected carbon concentration in bainitic ferrite [Bhadeshia and Waugh, 1982].

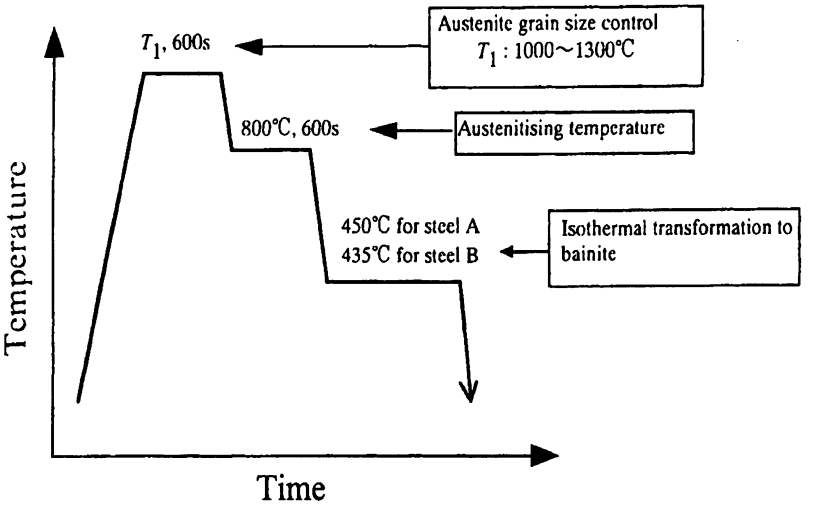

Fig. 2.14: Heat treatment used in the Matsuzaki and Bhadeshia study [1999].

2.6.c Influence of Austenite Grain Size

The slope of austenite volume fraction versus temperature during bainite transformation was found by some authors [Krielaart and van der Zwaag, 1998] to be less abrupt for larger grain sizes using a method based on differential scanning calorimetry. Thus, the rate of transformation seems to decrease when the austenite grain size increases [Zarei Hanzaki *et al.*, 1997]. But contradictory results have been obtained. Barford and Owen [1961] reported that the reaction rate was accelerated by decreasing the grain size, because of an increase in the number density of grain boundary nucleation sites. Umemoto *et al.* [1982a] reported similar results and proposed an equation that describes the grain size dependence of overall kinetics. Davenport [1941] argued that the grain size had no appreciable effect upon the transformation kinetics. By contrast, Graham and Axon [1959] suggested that because the growth of a bainite plate is resisted by the matrix, a smaller austenite grain size must retard growth. These apparently contradictory studies have yet to be rationalized.

In an interesting study, Matsuzaki and Bhadeshia [1999] investigated the effect of austenite grain size in isolation. After the usual isothermal holding at temperatures in the range 1000-1300°C, they maintained the samples to a constant temperature of 800°C for 10 min (Figure

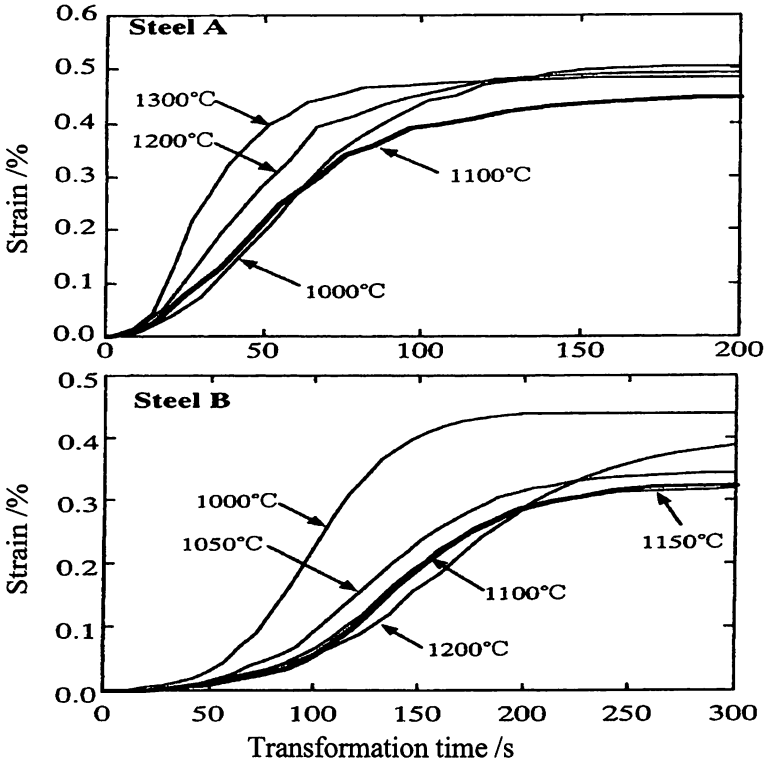

Fig. 2.15: Effect of maximum heating temperature on development of strain during isothermal formation of bainite [Matsuzaki and Bhadeshia, 1999].

2.14) before going to the isothermal test temperature. This rules out any influence of other factors, such as dissolution of chemical elements that can happen at high temperatures and still affect the transformation if the specimen is quickly quenched to the test temperature.

They indeed found faster kinetics as the austenite grain size is increased for a Fe-0.12C-2.03Si-2.96Mn wt% steel (named A) and slower kinetics as the grain size is increased for a Fe-0.96C-0.21Si-0.38Mn wt% steel, named B. This is illustrated on Figure 2.15. Moreover, using the formalism of Section 2.2.b., they found that steel A had its m coefficient (in equation 2.18) equal to 1.00 whereas for steel B, m was equal to -1.24. They concluded that steel A has a very fast growth rate with respect to its nucleation rate and that steel B has a fast nucleation rate but a slow growth rate. Different steels can therefore develop various bainite morphologies as shown in Figure 2.16. Steels A and B in the Matsuzaki and Bhadeshia study have nothing to do with alloys A, B and C used in the present study.

The Widmanstätten ferrite-start temperature W_s increases with increasing austenite grain size [Ali and Bhadeshia, 1991]. At the same time, B_s is not affected much because of the sheaf structure. The small effect of the austenite grain boundary on the growth of bainite seems to indicate that the transformation is indeed displacive [Yamamoto *et al.*, 1995].

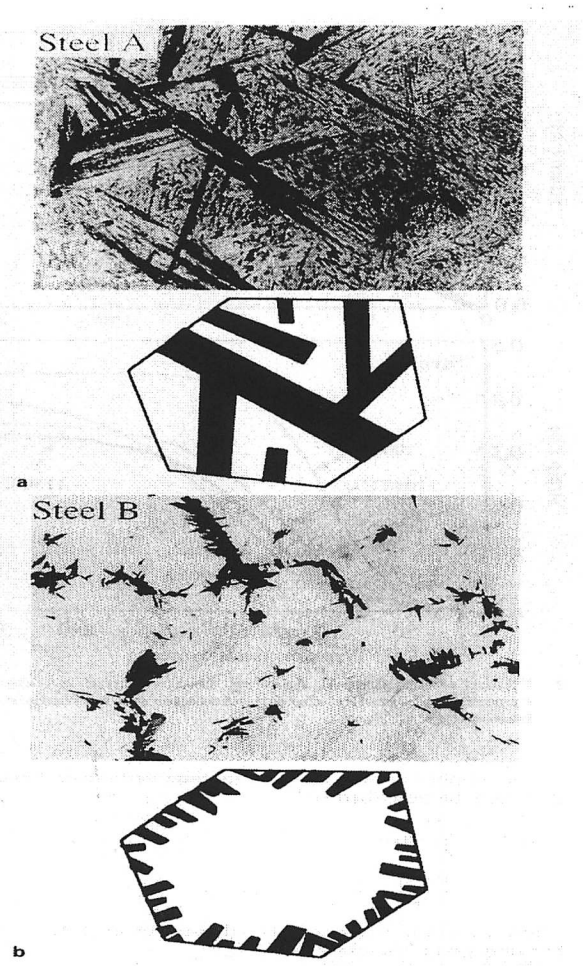

Fig. 2.16: Observed (optical, × 100) and schematic morphology of bainite sheaves at early stages of isothermal transformation in a) steel A with maximum heating temperature $T_1 = 975°C$ and b) steel B with $T_1 = 1000°C$ [Matsuzaki and Bhadeshia, 1999].

2.6.d Cooling Rate and Isothermal Transformation Temperature

An increase in the cooling rate makes the transformation-start temperature decrease, independently of the transformation product considered [Manohar *et al.*, 1996]. This can be accompanied by an acceleration of the progress of transformation (time between the beginning and the end of transformation) [Manohar *et al.*, 1996].

For isothermal experiments, the bainite transformation kinetics can be faster at lower temperatures because of the higher driving force (the ultimate fast transformation is martensite, which is limited by the speed of sound) but not necessarily (Chapter 4). The amount of bainite formed is also larger which reflects the validity of the T_0 criterion [Ali and Bhadeshia, 1990], although this would also happen if austenite could reach its equilibrium concentration given by Ae_3. Decreasing the isothermal transformation temperature also decreases the sheaf and

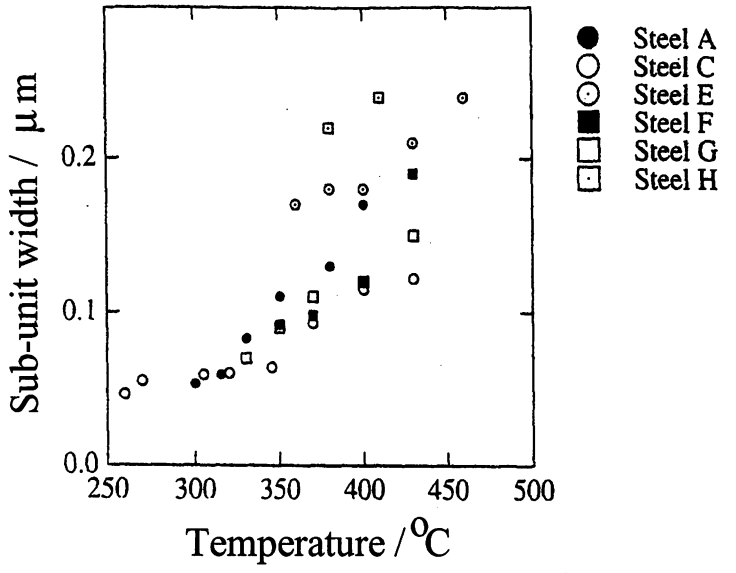

Fig. 2.17: The variation in bainite sub-unit thickness as a function of transformation temperature [Chang and Bhadeshia, 1995]. A variation in the transformation temperature also causes a change in the austenite strength and the chemical driving force. Thus, the variation illustrated is not due to the effect of temperature alone.

sub-unit width, as shown on Figure 2.17 [Barnes *et al.*, 1995; Zarei Hanzaki *et al.*, 1995; Singh and Bhadeshia, 1998b] as well as the number of sub-units per sheaf [Singh and Bhadeshia, 1998b].

2.7 Summary

A variety of mechanism-based, general and descriptive 'Avrami-type' models have been presented in this chapter. The models seem to have the ability to make accurate predictions during isothermal transformation.

The model based on a displacive transformation mechanism is powerful and can cover a large range of alloy chemical compositions. The bainite and Widmanstätten-start temperatures are predicted by thermodynamic criteria that all steels must verify. Some empiricism is introduced to account for the effects of autocatalysis and to match the predicted and measured nucleation rates for a wide variety of steels. The model requires the use of 3 or 4 empirical constants. Each sub-unit, once nucleated, is supposed to achieve its final size 'instantly' so that there is no need to consider the growth rate as is the case in some other approaches.

Chapter 3

Transition from Isothermal to Anisothermal Conditions

The purpose of this chapter is to review methods for obtaining anisothermal reaction rates from the theory for isothermal transformation. The general theory of transformation kinetics is confined largely to isothermal reactions, but there have been several attempts to predict the course of a non-isothermal reaction from a set of isothermal transformation curves determined either experimentally or by using a kinetic model. The idealized problem is thus to calculate the anisothermal $X-t$ curves from the isothermal $X-t$ curves and some given $t-T$ relation. In this chapter, the generic variable X is used to represent the volume fraction of a forming phase, irrespective of its nature or formation mechanism. T is the temperature and t the time. X ranges from 0 to 1. The variable ξ, which also varies from 0 to 1, represents the normalised bainite volume fraction (equation 2.34). It is not used here because it is reserved for bainite throughout this work.

3.1 The Method of Increments

The cooling curve is divided in small isothermal steps, with the increments of transformation summed progressively as the temperature decreases (Figure 3.1). Thus, if X_0, X_1 and X_2 are the fractions formed at T_0, T_1 and T_2 respectively, we have:

$$X_1 = X_0 + dX_1 \quad \text{and} \quad X_2 = X_1 + dX_2 \tag{3.1}$$

where dX_1 and dX_2 are the increments in fraction at T_1 and T_2.

The model used in this study was developed over the years by Bhadeshia *et al.* The overall isothermal transformation rate to bainite is obtained by modifying equation 2.50 to use the expression of autocatalysis as originally defined by Rees and Bhadeshia (equation 2.33) and is given by the following relationship:

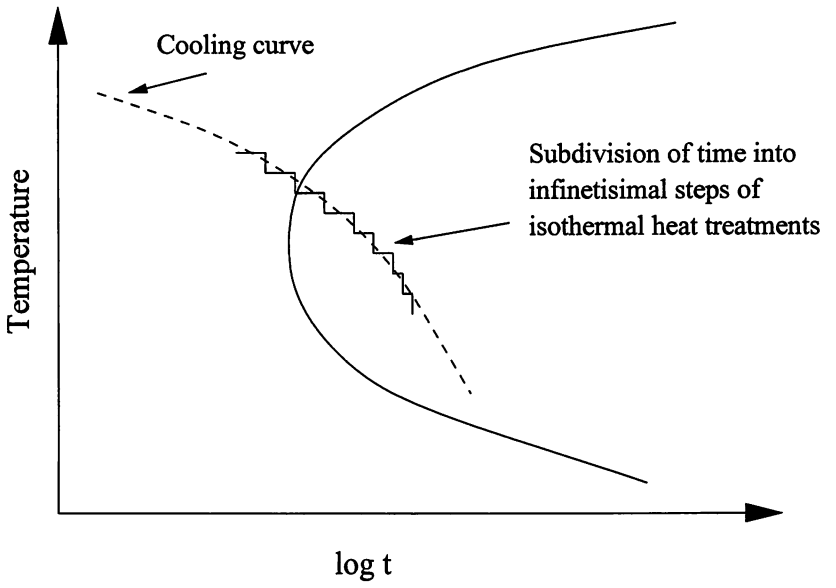

Fig. 3.1: Schematic illustration of the division of the cooling curve into small isothermal segments.

$$\frac{d\xi}{dt} = (1-\xi)\frac{\nu}{C}\exp\left(\frac{-G^*}{RT}\right)\left[1+\beta v\right] \tag{3.2}$$

where v is the bainite fraction. The significance of the other symbols has been explained in Chapter 2. The reasons for this change in the autocatalysis function as given by the Singh and Bhadeshia model are explained in chapter 6.

In the present study, the method of equation 3.1 was used in conjunction with equation 3.2 for the prediction of the bainite volume fraction.

3.2 The Concept of Additivity

The increment method described above carries no assumptions about the form of the kinetic equation. An alternative, more restricted method due to Scheil [1935] is known as the 'additivity rule'. Difficulties in treating non-isothermal reactions are mainly due to the independent variations of growth and nucleation rate with temperature. The problem is tractable only when the instantaneous transformation rate can be shown to be a function solely of the amount of transformation and the temperature [Christian, 1965].

Consider the simplest type of non-isothermal reaction, obtained by combining two isothermal treatments. The assembly is transformed at temperature T_1 where the kinetic law is $X = f_1(t)$ for a time t_1, and is then suddenly transferred to a second temperature T_2. If

the reaction is additive, the course of the transformation at T_2 is exactly the same as if the transformed fraction $f_1(t_1)$ had all been formed at T_2. Thus if t_2 is the time taken at T_2 to produce the same amount of transformation X_1 as is produced at T_1 in a time t_1, we have $f_1(t_1) = f_2(t_2)$, and the course of the whole reaction is

$$X = f_1(t) \quad \text{for} \quad (t < t_1)$$

$$X = f_2(t_2 + (t - t_1)) \quad \text{for} \quad (t > t_1) \tag{3.3}$$

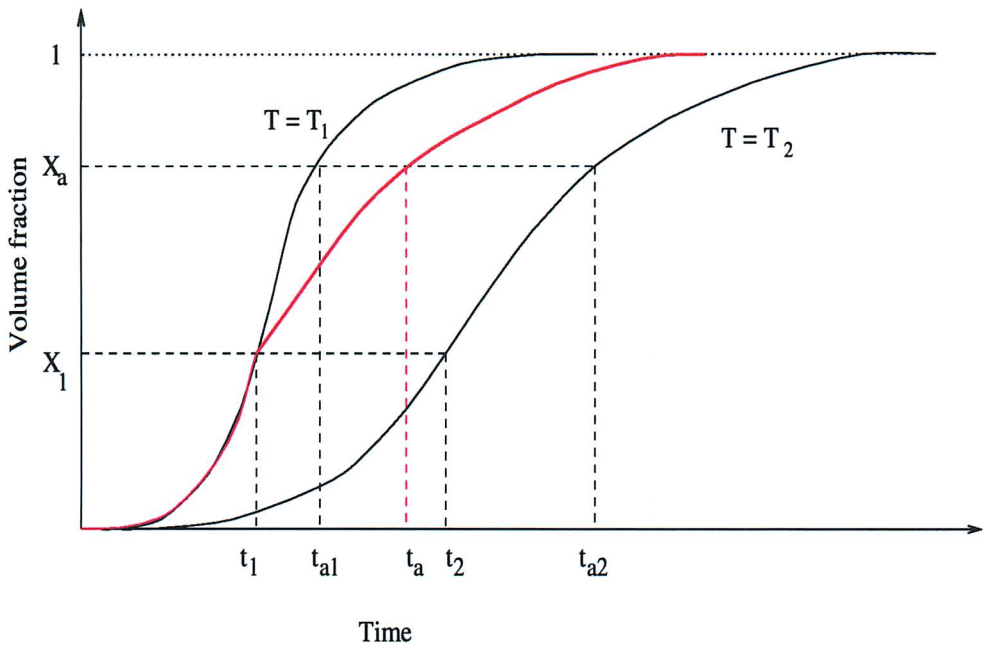

Fig. 3.2: Schematic representation of the additivity principle [after Lusk and Jou, 1997]. The red transformation curve corresponds to transformation at T_1 until the time t_1. At this time, the temperature is suddenly changed to T_2. When the reaction is additive, the curve readily adopts the shape of the transformation curve recorded at T_2 for the same fraction X_1.

Suppose that t_{a1} is the time taken to produce a fixed amount of transformation X_a at T_1, and t_{a2} is the corresponding time to produce the same amount of transformation at T_2. Then in the composite process above, an amount X_a of transformation will be produced in a time t_a with

$$t_a = t_{a2} - (t_2 - t_1) \tag{3.4}$$

if the reaction is additive (Figure 3.2). The time t_a can be defined as the solution of the following equation of t:

$$\frac{t_1}{t_{a1}} + \frac{(t - t_1)}{t_{a2}} = 1 \tag{3.5}$$

An additive reaction thus implies that the total time to reach a specified stage of transformation is obtained by adding the fractions of the time to reach this stage isothermally until the sum reaches unity. The generalization of equation 3.5 to any time-temperature path is clearly

$$\int_0^t \frac{dt}{t_a(T)} = 1$$

which can also be written:

$$\int_0^t \frac{1}{t_a(T)} \frac{dt}{dT} dT = 1 \tag{3.6}$$

where $t_a(T)$ is the time to reach the fraction X_a isothermally at T and t is the time to reach X_a for the non-isothermal reaction.

3.3 Conditions for Validity of the Additivity Rule

3.3.a Analytical Proof of Equation 3.6 [Christian, 1965b]

Equations 3.3 will be true if the reaction rate depends only on X and T, that is only on the state of the assembly, and not on the thermal path by which it reached that state [Christian, 1965b]. An analytical proof of equation 3.6 also follows from this statement. Christian considered a transformation for which the instantaneous reaction rate can be written:

$$\frac{dX}{dt} = \frac{h(T)}{j(X)} \tag{3.7}$$

where $h(T)$ and $j(X)$ are respectively functions only of temperature and transformed fraction. He went on to demonstrate that when the above separation into a ratio (or indeed a product) of two independent functions can be done, the reaction considered is additive. His original proof is reproduced below. From equation 3.7

$$\int h(T)dt = \int j(X)dX = J(X) \tag{3.8}$$

for any transformation path. This equation is equivalent to

$$X = F\left\{\int h(T)dt\right\} \tag{3.9}$$

and in particular for an isothermal transformation

$$X = F\left\{h(T)t\right\} \tag{3.10}$$

According to equation 3.10 , the fraction transformed at a fixed temperature is dependent only on the time and on a single function of the temperature. This function $h(T)$ might specify the growth rate or the diffusion coefficient, for example. Transformations at different temperatures then differ only in the time scale, as assumed in asserting the identity of equations 3.4 and 3.5. Reactions of this type are called isokinetic, after Avrami [1939, 1940]. Avrami defined an isokinetic reaction by the condition that the nucleation and growth rates are proportional to each other: the two processes have the same temperature dependence. Following Cahn [1956a], however, Christian took equation 3.9 as a more general definition of an isokinetic reaction. He showed that an isokinetic reaction is additive in the sense defined by equation 3.6. From equation 3.8 it can be seen that

$$h(T) = J(X_a)/t_a(T) \tag{3.11}$$

and on substituting into equation 3.7

$$t_a(T)(dX/dt) = J(X_a)/j(X) \tag{3.12}$$

Christian then considered the integral

$$\int_0^t \frac{dt}{t_a(T)} = \int_0^X \frac{dX}{t_a(T)(dX/dt)} = \frac{J(X)}{J(X_a)} \tag{3.13}$$

This gives the relation between the time t and the fraction transformed for the whole non-isothermal reaction, and is the general expression of the concept of additivity. In particular, if $X = X_a$, equation 3.13 reduces to equation 3.6.

3.3.b Discussion

In general, reactions with more than one temperature dependent parameter, for example the nucleation and growth rates, will not be additive. Consider the simplest type of cooling transformation, obtained by combining two isothermal treatments at temperatures T_1 and T_2 (where $T_1 > T_2$). Assume that the ratio of the nucleation rate I to the growth rate G is larger at the lower temperature T_2. When specimens are transformed at each temperature to

the same fraction X_0, the microstructures are presumably like those schematically shown in Figure 3.3. At temperature T_1 where the nucleation rate is slow and the growth rate is fast, the microstructure will consist of a small number of large size nodules. While at temperature T_2 where the nucleation rate is fast and the growth rate is slow, the microstructure will consist of a large number of small size nodules [Umemoto *et al.*, 1982a].

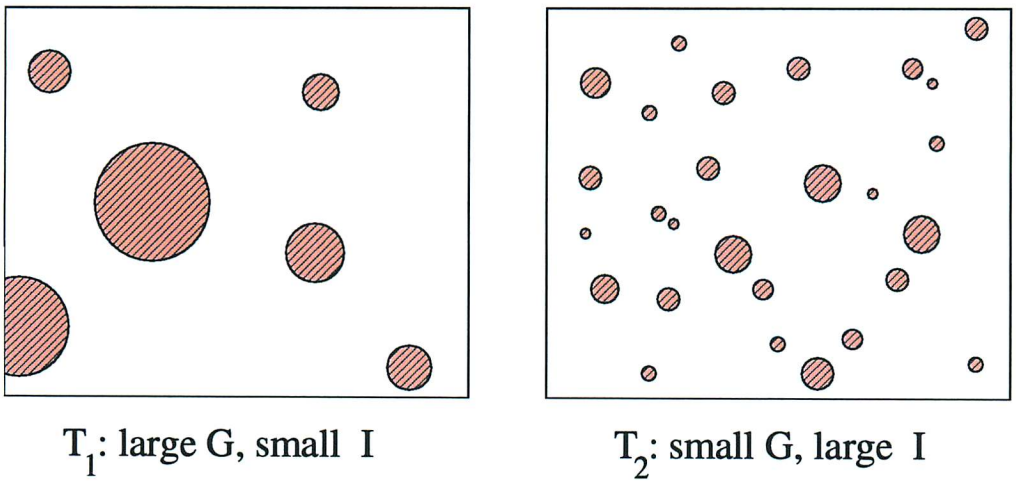

Fig. 3.3: Schematic microstructures: a) with large growth rate and small nucleation rate. b) with small growth rate and large nucleation rate [Umemoto *et al.*, 1982a].

Suppose that the specimen is transformed at the higher temperature T_1 to fraction X_0 and is then suddenly cooled to T_2. When transformation is continued at T_2, the progress of transformation of the specimen initially transformed at T_1 should be considered to be slower than that transformed at T_2 from the beginning, since the former has smaller total growing interface area per unit volume than that of the latter. The additivity rule will not hold in this case. This situation is schematically illustrated on Figure 3.4.

Umemoto *et al.* proposed that the transformed fractions become additive when one of the following three circumstances is satisfied:

(i) One is that the ratio of the nucleation rate to the growth rate is constant with temperature. According to Avrami [1939], the factors which govern the tendency of the growth nuclei to grow out of the germ nuclei are similar to those which govern further growth, i.e. the variation of I and G with external conditions may be expected to be similar.

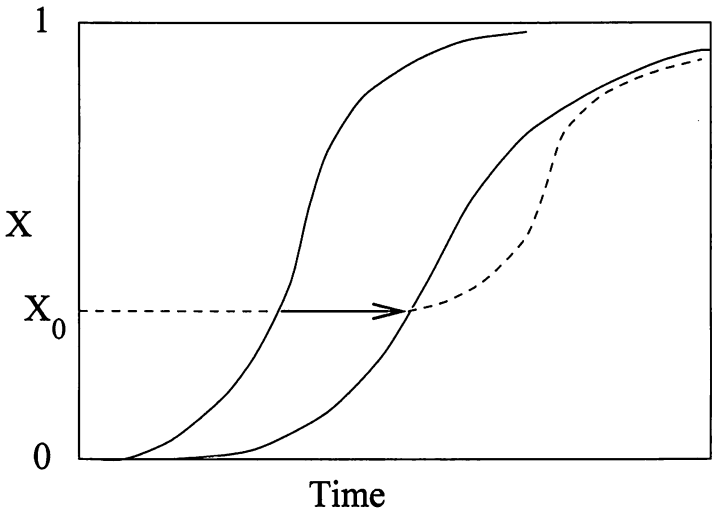

Fig. 3.4: Schematic representation of delay of transformation and deviation from the additivity rule. The specimen is initially held at T_1 for transformation to X_0, whereupon it is cooled suddenly to T_2; the subsequent transformation will be delayed as shown by the broken line because here the additivity rule does not apply [Umemoto *et al.*, 1982a].

$$\frac{I}{G} = \text{constant} \tag{3.14}$$

(ii) Second is when all the nuclei have been formed early in the reaction and the progress of transformation is controlled only by their growth. This condition is called 'site saturation' [Cahn, 1956a]. If the growth rate at any instant then depends only on the temperature, the reaction is additive [Umemoto *et al.*, 1983]. It has indeed been shown that for the case of grain boundary surface, edge and corner nucleation, the expected interval in undercooling from the initiation of nucleation to site saturation is small [Cahn, 1956a]. Kuban *et al.* [1986] suggested a condition for additivity based on early site saturation and related to the time for completion of one half of the transformation, $t_{0.5}$, in the case of pearlite. They concluded that for a reaction where nucleation is confined to grain boundaries, edges or corners, the rate of the reaction becomes insensitive to the nucleation rate when:

$$\frac{Gt_{0.5}}{d_\gamma} < 0.5 \tag{3.15}$$

In many reactions on cooling, the nucleation rate is determined mainly by an Arrhenius type equation with an activation energy which decreases more than

linearly with temperature [Christian, 1965]. This gives a rapidly increasing nucleation rate as the under-cooling (or supersaturation) increases. The growth rate in contrast, is controlled by an activation energy which is nearly independent of temperature, and hence the rate decreases as the temperature decreases. These opposing factors give an overall transformation rate which first increases and then decreases again as the temperature falls, leading to the C-curves characteristic of so many TTT diagrams. At sufficiently low temperatures, the nucleation rate may be so large that the nucleation sites saturate early in the reaction. The growth rate alone then controls the overall reaction rate. Kuban *et al.* [1986], proposed that a reaction is additive provided that the growth of the first 20% transformed subsequently exceeds about 75% of the total transformation. This criterion was referred to as 'effective site saturation'.

(iii) The third is when the growth of the new phase is very fast but ceases when the new phase reaches a limiting size. In such a case, the progress of transformation is controlled only by the nucleation of the new phase. This condition is often named as 'growth limited'.

A restriction applies [Cahn, 1956a] for diffusion-controlled precipitation reactions, in order that the rule for additivity holds: the bulk of the reaction must occur at temperatures where the composition of the equilibrium phases are relatively constant, *i.e.* at large degrees of undercooling [Christian, 1965b], where the solvus boundary becomes increasingly steep and approaches a vertical line. A change in the equilibrium composition with temperature will produce deviations, not only because the same volume of precipitate may not correspond to the same fraction of completion X, but also because a sudden change in the equilibrium concentrations will make the material which previously had been close to equilibrium, suddenly undersaturated or supersaturated.

3.3.c Geometrical Criteria

Before using complex kinetic equations to check whether any of the above criteria apply, it is possible to carry out a bi-isothermal test as well as the corresponding two isothermal tests to check that the bi-isothermal transformation curve behaves as on Figure 3.2 or that adding the increments of fraction formed at the two transformation temperatures gives a value of the fraction close to 1 (equation 3.5).

Todinov derived a method based on simple geometrical considerations. This method, schematically represented on Figure 3.5 is explained in detail in [Todinov, 1998]. For the reaction to be additive, the tangents to all isothermal kinetics curves, at points corresponding to the same quantity transformed, must intersect at a common point lying on the x-axis.

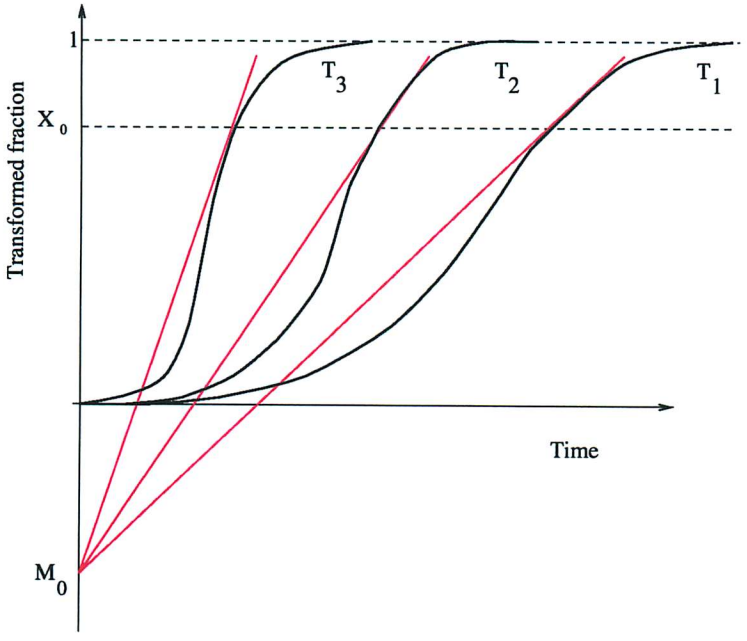

Fig. 3.5: Geometrical condition for additivity in the sense of Scheil. The tangents to points corresponding to the same quantity transformed X_0 intersect at the point M_0 lying on the x-axis [Todinov, 1998].

In a paper on the crystallization kinetics of high-density polyethylene, Chew *et al.* [1989] observed that isothermal transformation curves of $X(t,T)$ vs. log (t) can be brought into coincidence simply by shifting each curve by a distance along the time axis (Figure 3.6). This superposition can be regarded as being a necessary condition for the application of the additivity rule.

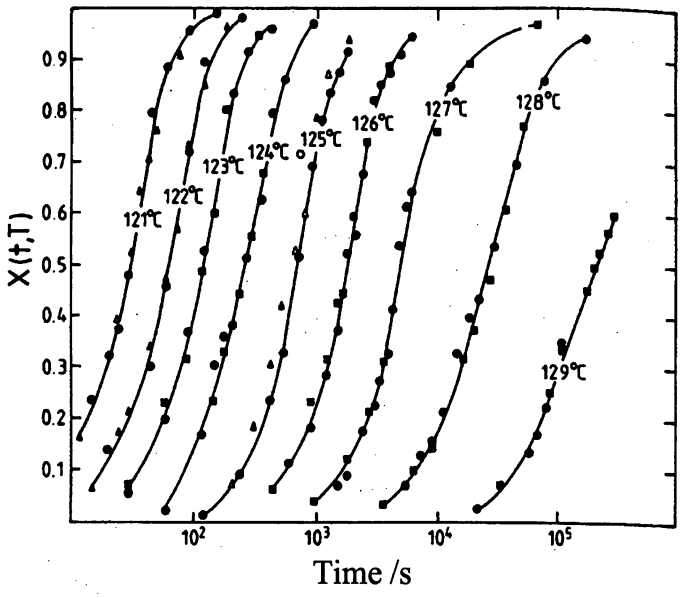

Fig. 3.6: Fraction of transformation $X(t,T)$ vs. time for various crystallization temperatures [Chew *et al.*, 1989].

3.3.d Limitations

The conventional TTT curve, which is determined from experiments, inherently contains an initial temperature transient which arises prior to attaining the isothermal conditions. This initial transient exists, at least in part, within the decomposition range, causing a shift of the TTT curve to longer times, away from its ideal position (Figure 3.7). Hence, determination of the transformation-start time using an experimental TTT curve and the additivity principle often results in an over-prediction of the start of transformation [Pham *et al.*, 1995, Lee *et al.*, 1998].

The concept of an 'ideal' (Pham *et al.* al., 1995) or 'true' (Wierszyllowski, 1992) TTT curve is introduced to account for the fractional incubation time consumed during cooling to the test temperature. The ideal TTT curve is considered to depend only on the steel composition and its austenite grain size prior to the transformation. This TTT curve can only be generated if an infinitely rapid initial cooling rate is applied to reach each isothermal temperature, but this is an impossible requirement.

The following equation relates the observed start time during an isothermal transformation t_s to the incubation time τ_t for the ideal TTT curve:

$$t_s = \tau_t + \int_{T_t}^{T_e} \left[1 - \frac{\tau_t}{\tau(T)}\right] \frac{dT}{Q(T)} \tag{3.16}$$

τ_t should be used instead of t_s as t_a in equation 3.6 to correct the error introduced by not

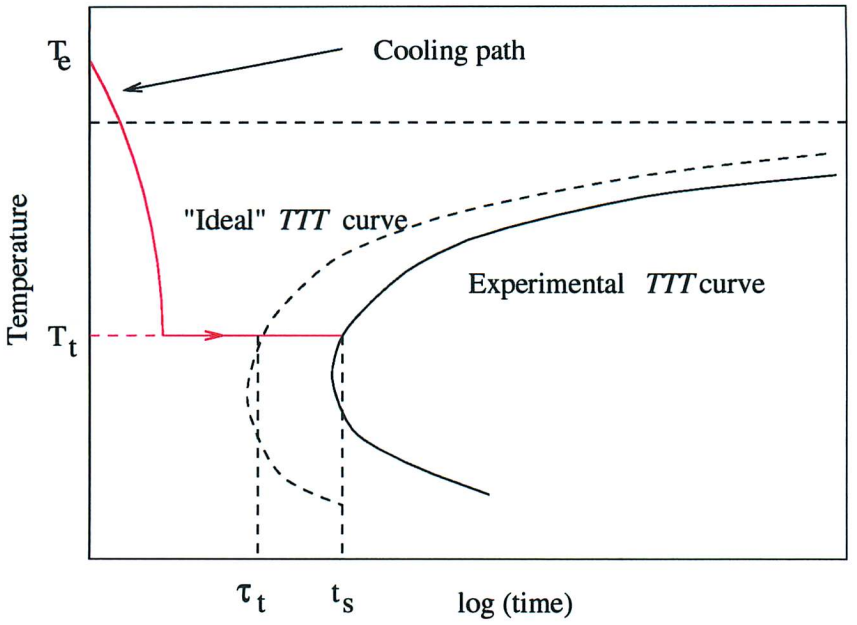

Fig. 3.7: Schematic illustration of the relationship between the ideal and the experimental incubation time at temperature T_t [Pham *et al.*, 1995].

using the ideal TTT curve. $Q(T)$ is the cooling rate.

In their study, Lee *et al.* showed that ideal TTT diagrams could be derived by the experimental data of TTT and CCT diagrams using numerical methods. Conversely, they showed that the ideal TTT diagram can be used to predict TTT or CCT diagrams [Lee *et al.*, 1998].

3.4 Results of Previous Studies on the Additivity Rule

An extensive range of studies was carried out by Umemoto *et al.* regarding the use of the additivity rule, notably on the pearlite and bainite transformations.

Mathematical Method for the Application of the Additivity Rule

They presented the following rate law for pearlite transformation considering the effect of austenite grain size d_γ (which is included in the constant C in equation 3.2):

$$X = 1 - \exp\ [-k(T)t^n/d_\gamma^m] \tag{3.17}$$

where the exponent m depends on the type of nucleation site. m is equal to 0, 1, 2, and 3 for random nucleation in the matrix, nucleation on grain surfaces, on grain edges and on grain corners, respectively.

From equation 3.17, the time $t_a(T)$ to reach a volume fraction X_a at T can be written:

$$t_a(T) = \left[\frac{d_\gamma^m}{k(T)} \ln \frac{1}{1 - X_a}\right]^{1/n} \tag{3.18}$$

Remembering that the cooling rate $Q(T)$ is $-\frac{dT}{dt}$, and substituting equation 3.18 in equation 3.6, we get:

$$\frac{1}{\left[d_\gamma^m \ln \frac{1}{1-X_a}\right]^{1/n}} \int_{T_2}^{T_1} \frac{k(T)^{1/n}}{Q(T)} dT = 1 \tag{3.19}$$

and rearranging about X:

$$X_a(T) = 1 - \exp\left[-\frac{1}{d_\gamma^m}\left\{\int_{T_2}^{T_1} \frac{k(T)^{1/n}}{Q(T)} dT\right\}^n\right] \tag{3.20}$$

This is the general equation which expresses the transformed fraction at temperature T during cooling from temperature T_1 to T_2. When the cooling rate is constant, equation 3.20 is simplified further. Note that the integral goes from T_2 to T_1 due to the $-$ sign in the cooling rate.

A similar reasoning can be used for the bainite transformation, if a different rate law than equation 3.17 is used. But it is important in order to use this method that the reaction be additive. This can be checked *a posteriori* by comparing predicted and experimental results. If they are in good agreement, the additivity rule is valid for the reaction studied. If they show poor agreement, the problem can arise from the rate law being inappropriate or from the additivity rule not being valid.

The complete isothermal model proposed by Quidort was presented in Section 2.2.c. Quidort assumed that the bainite transformation is additive, arguing that the carbon diffusion gradient near the growing interface adapts very quickly to a change in temperature. It is easy to transpose his model for continuous cooling conditions. The formalism is the same as above (equations 3.17 to 3.20).

His model predictions for a Fe-0.5C-0.7Mn-0.29Cr wt% steel agree reasonably well with experimental results as shown on Figure 3.8.

3.4.a Additivity Rule and the Pearlite Transformation

Using the additivity rule, Umemoto *et al.* [1983] made an attempt to predict the cooling transformation over the entire range of the pearlite reaction from the isothermal transformation kinetic data. The steel used in their study was a 1 wt% Ni commercial eutectoid steel. The progress of pearlite transformation during isothermal holding and continuous cooling was

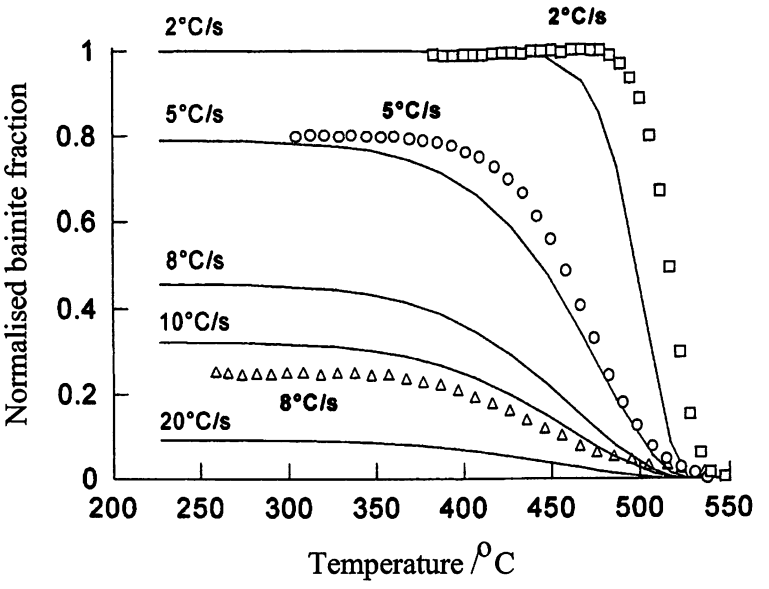

Fig. 3.8: Comparison of predicted and experimental results for a Fe-0.5C-0.7Mn-0.29Cr wt% steel in continuous cooling conditions [Quidort, 1999].

measured by an automatic quench dilatometer. Since the C-curve in a TTT diagram is of parabolic shape, they approximated $k(T)$ as:

$$k(T) = \exp\{-a(T-b)^2 - c\} \tag{3.21}$$

and found an average value of n equal to 4.0. They found that the transformed fractions of pearlite appear to be additive, firstly because the change in the ratio of the nucleation to the growth rate $\frac{I(T)}{G(T)}$ as a function of supercooling was small, and secondly because the cooling transformation occurred nearly isokinetically when the cooling rate was slow or almost in the condition of site saturation when the cooling rate was fast. For the latter situation, the transformation occurs in a wider range of temperature with a large change in the ratio $\frac{I(T)}{G(T)}$. However, when the supercooling becomes large the value of $\frac{I(T)}{G(T)}$ becomes large, and the condition of site saturation is likely to occur. Cooling transformation curves calculated on the basis of the nucleation and growth process were close to the ones calculated with the additivity rule.

Verdi and Visintin [1987] also developed a model for the pearlite and martensite transformations during continuous cooling, taking into account recalescence. It is interesting to note that these authors engulfed both pearlite and bainite in the term 'pearlite' even though they acknowledged that the two products have different microstructures and form at different

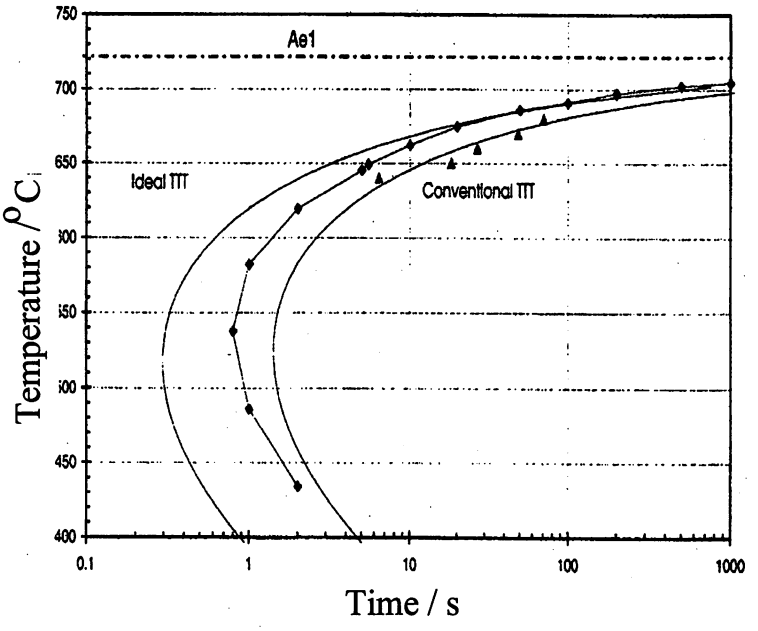

Fig. 3.9: The experimental TTT curves (points) compared with the conventional TTT curve for a eutectoid steel and the calculated ideal TTT. [Pham *et al.*, 1995].

temperatures.

Pham *et al.* [1995] calculated an ideal TTT curve (Figure 3.9). They found that the minimum transformation time is considerably shorter than that of the traditional TTT curve. The reason for this was explained earlier in this chapter. When using their ideal TTT curve to predict the start of transformation to pearlite by applying the additivity rule, they found good agreement between the measured and predicted results for continuous cooling conditions.

3.4.b Additivity Rule and the Allotriomorphic Ferrite Transformation

Lee [1999] derived a method for the determination of the kinetic parameters k and n of the Avrami equation from continuous cooling transformation data based on the concept of the additivity rule. He found that applying this method to the austenite $\rightarrow$ ferrite isothermal transformation data confirmed the validity of the method at the early stages of transformation, but not at the later stages.

Through the analysis of experimental results and diffusional growth model results, the author concluded that the time exponent n for the austenite to ferrite transformation is 1 at the early stages of transformation by two-dimensional growth of ferrite nuclei saturated at the austenite grain edge. However, n was gradually reduced to a value of 1/2 due to the impingement with neighbours. With n expressed as an appropriate function of transformed

fraction X, the values of k could be estimated independently of the cooling rate from the continuous cooling experimental data. A comparison of the author's results and calculated cooling transformation curves is shown in Figure 3.10.

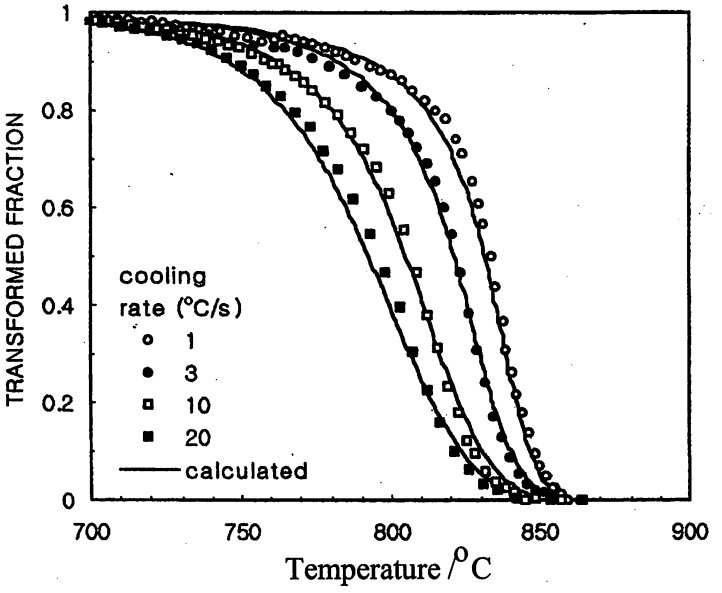

Fig. 3.10: Comparison of measured and calculated continuous cooling transformation curves. [Lee, 1999]

Hawbolt *et al.* [1981] found that the continuous cooling decomposition of austenite to ferrite, derived using isothermal data, constant n and assuming that the transformation is additive seriously underestimated the initial stages of the transformation in a Fe-0.09C-0.37Mn wt% steel, although the changing boundary conditions and associated carbon fluxes are quickly accommodated in a CCT test. Early site saturation at the austenite grain boundaries and the dependence of the subsequent transformation rate on temperature-dependent growth were shown to explain the additive behaviour that was nonetheless observed.

3.4.c Additivity Rule and the Bainite Transformation

Umemoto *et al.* studied the isothermal and continuous cooling transformation kinetics of bainite using an automatic quench dilatometer [1982a]. The steel used was Fe-0.99C-0.24Si-0.29Mn-1.39Cr wt%. They found that the overall isothermal bainite transformation kinetics were well expressed by a Johnson-Mehl-Avrami-Kolmogorov type equation and that the transformation rate decreased with an increase in the austenite grain size. The analysis of transformation kinetics and the optical microscope observations suggested that nucleation sites for bainite were both on grain boundaries and inside austenite grains. A value of m equal to 0.65

was found, compared with 1.76 for pearlite. This effect of austenite grain size on the rate of isothermal transformation to bainite was found to be smaller than that of pearlite.

They compared the observed cooling transformation kinetics with that predicted from the isothermal kinetic data (equations 3.17 to 3.20) and found that the transformed fractions were additive for the bainite transformation. They suggested that bainite falls in the third category of validity for the additivity rule, *i.e.* it is a growth-limited transformation. Bainite transformation proceeds with repeated nucleation and growth of basic sub-units, each attaining the limit size rapidly (Figure 3.11). Therefore, the overall rate is controlled by the nucleation rate, as proposed by Bhadeshia [Bhadeshia, 1992]. Umemoto *et al.* seem to be the only ones having studied the additivity rule with respect to the bainite transformation.

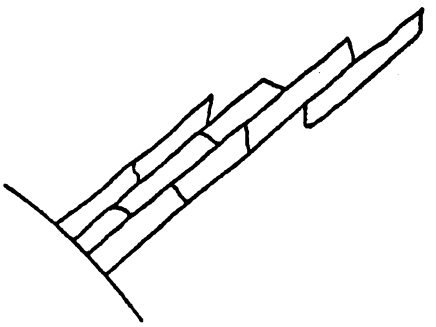

Fig. 3.11: Schematic illustration of the bainite structure produced by repeated nucleation of sub-units. Each of the sub-units rapidly attains a limited size and ceases to grow further, but nucleation and growth of another sub-unit takes place afresh [Umemoto *et al.*, 1982a].

3.4.d Additivity Rule and Precipitates

Park *et al.* [1992] used the additivity rule as a tool to predict the precipitation kinetics of Nb(CN) during continuous cooling in a Fe-0.07C-1.23Mn-0.20Si-0.04Nb wt% steel. It was found that the precipitation-start and finish times during continuous cooling were determined with 'reasonable' accuracy. Another study incorporating proeutectoid ferrite and precipitation of cementite both from austenite and ferrite was conducted by Enomoto [1994]. The additivity rule caused quite a large error in the transformations studied. From theoretical results, Enomoto concluded that the error occurred primarily due to the temperature variation of the local equilibrium solute concentration at the interphase boundary, and that the error was insensitive to the cooling rate and/or the magnitude of solute diffusivity.

3.5 Summary

The literature on the additivity principle has been reviewed. The principle has been discussed mathematically and in the context of nucleation and growth phenomena. Conditions for the validity of the additivity rule fall into three main categories: a constant nucleation to growth rate ratio, early site saturation and cases where the growth is rapid and the particles grow to a limiting size. The bainite reaction, with its displacive formation of successive sub-units is likely to fall into the third category.

It is always necessary to carry out experimental work to establish whether a reaction is additive. When the experimental variables X and T can be separated into two different functions in the expression of the kinetic rate law, it is theoretically correct to say that the reaction is additive. This is seldom true. For example, in equation 3.2, the activation energy G^* depends both on T and X, so the separation of variables is not strictly possible. For this reason, the simple, rigorous method of increments is used in the work presented in subsequent chapters.

Chapter 4

Alloy Selection and Experimental Procedures

4.1 Introduction

This chapter introduces the alloys used in the present study. The thermodynamic approach described in Chapter 2 allows the prediction of the important transformation temperatures for each alloy. The different heat treatments used to study the bainite transformation kinetics experimentally are then introduced. The dilatometry technique is presented together with the method used to calculate the experimental bainite fraction. This method used initially for isothermal transformations was adapted to the case of continuous cooling transformations. Finally, all the techniques used for microstructural characterisation of the transformed samples are described herein.

4.2 Alloy Selection

In the context of the present study, where a physical model for isothermal transformations is adapted for continuous cooling conditions, it is necessary to select alloys such that the bainite transformation can be studied in isolation. Several important rules of thumb must be satisfied:

- The alloys must have sufficient hardenability to avoid the formation of other constituents before the B_s temperature is reached. The hardenability should also be sufficient to slow down the transformation kinetics so that they can be observed in isothermal experiments.
- It is also important to try and prevent the formation of carbides. Existing physical models cannot cope with the added complexity associated with carbides. Carbide formation is regarded as a secondary process.

The first criterion is achieved with appropriate additions of chemical elements. For example, nickel, when present at concentrations of around 4 wt% is very beneficial. It stabilises the austenite and hence decreases the temperature domain of the bainite transformation. At lower

temperatures, the kinetics are slower and easier to monitor. Manganese and molybdenum are also used to enhance hardenability.

The second criterion can be achieved with the addition of silicon and/or aluminium. These two elements are known to have a very low solubility in cementite and therefore to suppress its formation. Cementite is the most common carbide in bainitic microstructures, unless long tempering heat treatments are used.

Carbon concentrations of 0.1 to 0.5 wt% are characteristic of many industrial steels. Carbon is the element with the most pronounced effect on hardenability. Niobium is introduced in some steels to form niobium carbides for controlled rolling. Other elements (phosphorous, sulphur, copper, tin and vanadium) are present in steel as impurities only at trace concentrations. All the concentrations are listed in Table 4.1, which details the compositions of the alloys used for this work.

Carbon concentrations were determined on a LECO apparatus, by measuring the concentration of CO_2 with an infra-red cell following oxygen combustion. Concentrations of other elements were measured by optical emission spectrometry with an argon plasma excitation source (ICP) after being put in acidic solution. The error bars associated with this technique for alloy B are included in Table 4.1.

Steel	C (wt%)	Mn (wt%)	Si (wt%)	Mo (wt%)	Ni (wt%)	Cr (wt%)	Nb (wt%)	Predicted B_s (°C)
A	0.158	1.432	0.327	0.226	0.064	0.564	0.003	**546**
B	0.365 ± 0.007	0.005 ± 0.003	2.019 ± 0.050	0.002 ± 0.0001	3.976 ± 0.042	0.013 ± 0.001	< 0.001 ± 0.005	**471**
C	0.186	0.002	1.994	0.002	4.114	0.016	0.002	**523**
Steel	P (wt%)	N_2 (wt%)	Al (wt%)	Cu (wt%)	V (wt%)	Ti (wt%)	B (wt%)	Predicted M_s (°C)
A	0.011	0.006	0.064	0.012	0.056	0.002	0.002	**420**
B	< 0.001 ± 0.0014	0	0.010 ± 0.0016	0.008 ± 0.0005	< 0.001 ± 0.0006	< 0.001 ± 0.002	0.002 ± 0.001	**332**
C	< 0.001	0	0.013	< 0.001	< 0.001	< 0.001	< 0.001	**405**

Table 4.1: Chemical composition (wt%) of steels A, B and C.

It will be seen in Chapter 5 that alloy A frequently develops a bainitic microstructure containing carbides. It does not therefore satisfy the second criterion cited above. It was nevertheless studied because of its commercial importance and to reveal the influence of carbides on the bainite transformation kinetics. Samples were taken from ingots that were hot-rolled. The alloy contains marked chemical segregation which manifests in the form of bands in the microstructure. These segregation bands originate during the solidification process with the formation of dendrites. During hot-rolling, regions of segregation are flattened and highly elongated parallel to the rolling direction. Regions of higher concentrations in substitutional elements tend to have a higher hardenability. Such regions hardly transform into bainite during the typical heat-treatments used here; instead they transform into martensite during subsequent cooling from the isothermal transformation temperature.

Alloys B and C are laboratory steels. With high silicon and nickel contents, they have microstructures similar to the ones of TRIP-assisted steels. The TRIP effect (transformation-induced plasticity), is a mechanically-induced martensitic transformation of metastable austenite. B and C are almost identical except for their carbon concentration, which, for B is double that of C. The expected absence of cementite in the microstructure should lead to a significant increase of the carbon content in residual austenite as the bainite transformation progresses, thereby stabilising it with respect to martensitic transformation. As a consequence, significant amounts of retained austenite are expected to be present at room temperature.

Samples of all alloys for dilatometry were machined after homogenisation in vacuum for 3 days at 1200°C. For alloy A, this homogenisation treatment did not totally eliminate the chemical segregation.

4.3 Transformation Temperatures

It was pointed out in Chapter 2 that both Widmanstätten ferrite and bainite grow from the same nucleus and that the nucleation rate becomes appreciable when

$$\Delta G_m \leq G_N \tag{4.1}$$

which is always the case on Figure 4.1 where ΔG_m is represented by the red curve on the right of the diagram and G_N is the solid black line.

The nucleus can develop into Widmanstätten ferrite (i.e., $T_h = W_s$) if the driving force $\Delta G^{\gamma \rightarrow \gamma' + \alpha}$ for paraequilibrium growth (dotted curve on Figure 4.1) exceeds, in absolute value, the stored energy of Widmanstätten ferrite which has been estimated to be 50 J mol^{-1} [Ali

and Bhadeshia, 1990]. If the driving force $\Delta G^{\gamma\rightarrow\alpha}$ (blue curve on the left of Figure 4.1) for diffusionless growth is sufficient to allow for 400 J mol^{-1} of the stored energy of bainite [Bhadeshia, 1981b], then transformation to bainite takes place and T_h is identified with the bainite-start temperature B_s.

The computer program MAP-STEEL-MUCG46 which implements these calculations was used to construct Figure 4.1.

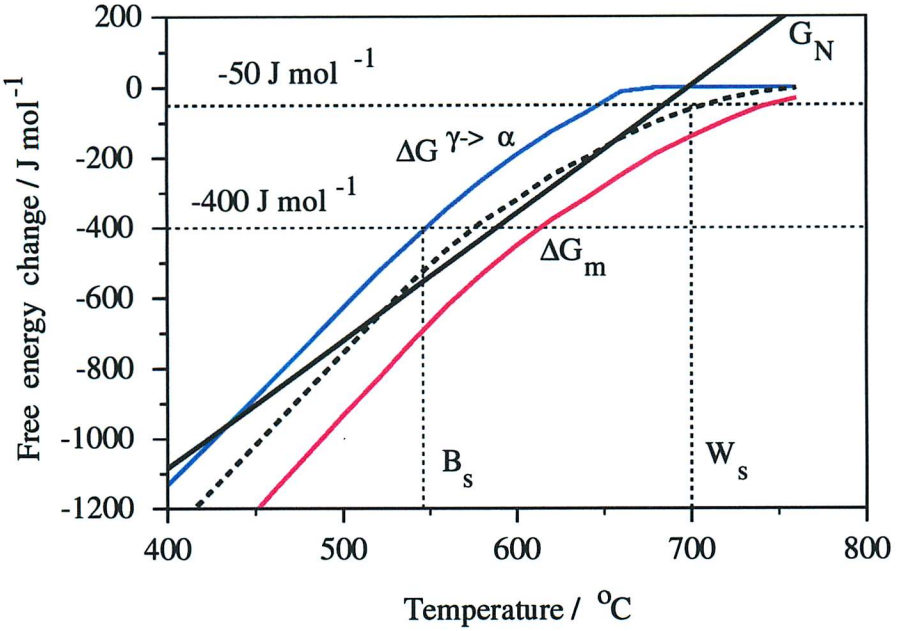

Fig. 4.1: Diagram illustrating the definition of W_s and B_s for alloy A based on available driving force for nucleation and growth. The black dotted curve represents $\Delta G^{\gamma\rightarrow\gamma'+\alpha}$.

From the thermodynamic considerations mentioned above, the transformation temperatures of alloy A were found to be: W_s = 700°C; B_s = 546°C and M_s = 420°C. Calculated values for alloys B and C are also listed in Table 4.1. For alloy A, the empirical relationship found by Steven and Haynes [1956], gives B_s = 598°C (equation 2.54).

MAP-STEEL-MUCG46 can also be used to estimate time-temperature transformation (*TTT*) diagrams based on thermodynamic and kinetic considerations with the chemical composition as the input. The calculated *TTT* diagram consists of two C-curves for the initiation of transformation. The higher C-Curve is for reconstructive reactions such as allotriomorphic ferrite and pearlite. The lower C-curve is for displacive reactions such as Widmanstätten ferrite, bainite and acicular ferrite (Figure 4.2).

Figure 4.3 illustrates how the shape of the bainite C-curve on a *TTT* diagram can in-

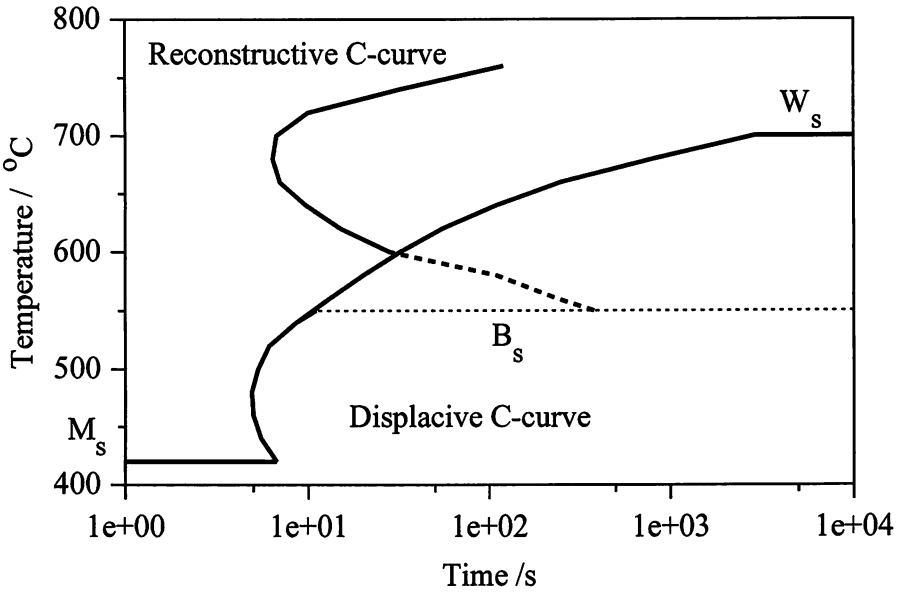

Fig. 4.2: *TTT* diagram illustrating the calculated reconstructive and displacive C-curves of alloy A.

fluence the way that isothermal transformation is slowed down or accelerated as temperature decreases between B_s and M_s. On Figure 4.3.a, a decrease in temperature leads to acceleration of the bainite kinetics. Figure 4.3.b shows the opposite effect and Figure 4.3.c shows that transformation kinetics can be relatively insensitive to temperature in the 'nose' region. The three cases can exist depending on the alloy tested. The situation of Figure 4.3.b leads to a characteristic **'cross-over'** of the kinetic curves, as curves for lower isothermal temperatures correspond to slower kinetics but higher limiting volume fractions.

4.4 Heat Treatments and Dilatometry

Once the approximate transformation temperatures of an alloy were estimated using the method described above, experiments were done to enable the study of the bainite transformation in isolation. Four types of heat treatment were used:

(i) An **isothermal** heat treatment where the specimen is austenitised and then cooled rapidly to a lower temperature situated between B_s and M_s where it is held for a specified time. The evolution of the microstructure can be studied by quenching before transformation is completed.

(ii) A **continuous cooling** heat treatment involves cooling the specimen at a constant appropriate cooling rate. The cooling rate must be rapid enough to avoid the reconstructive

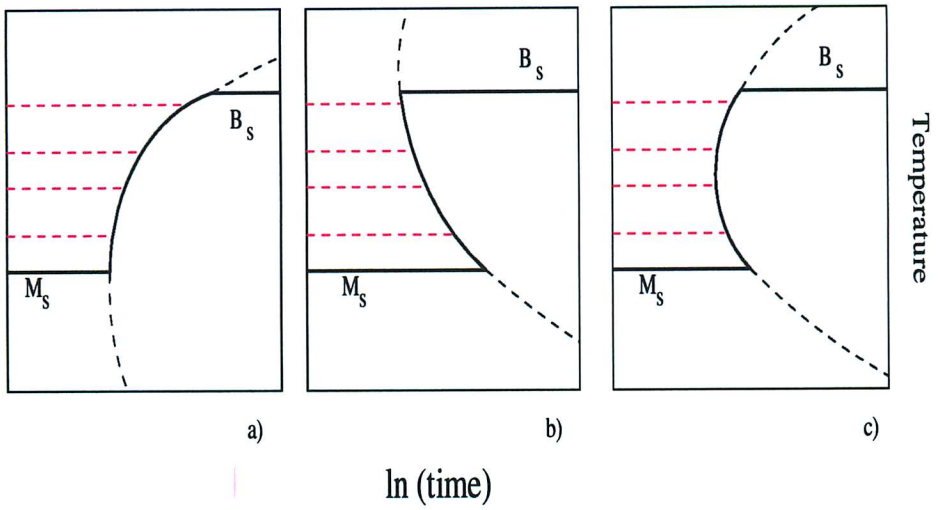

Fig. 4.3: Illustration of the influence of the position of the bainite C-curve in a TTT diagram on the kinetics of isothermal transformation: a) transformation starts earlier at lower temperatures; b) transformation starts later at lower temperatures; c) transformation is expected to start at similar times for all the temperatures.

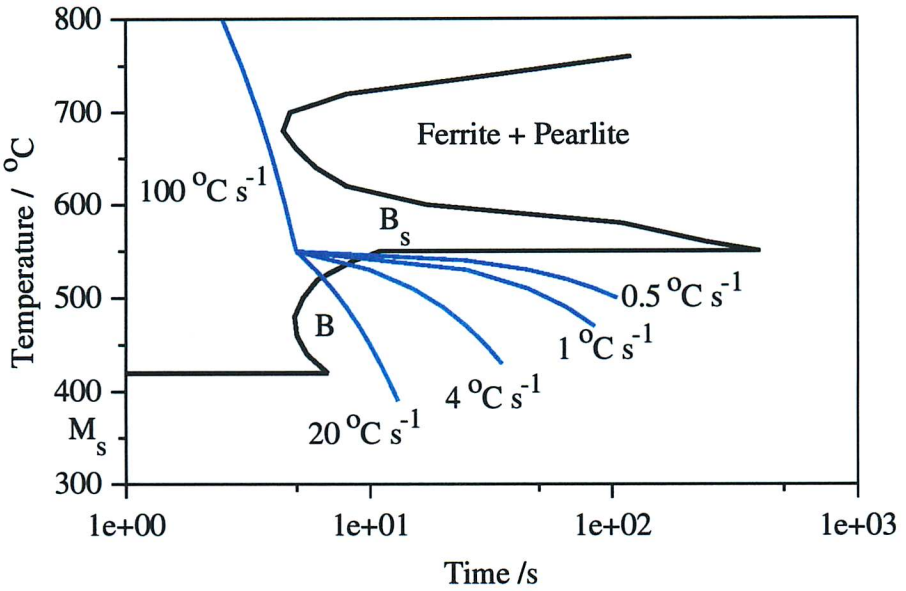

Fig. 4.4: CCT diagram illustrating the principle of the 'bi-slope' heat treatments (logarithmic scale). At first, a high cooling rate is used to avoid the ferrite and pearlite C-curves. Then, a wide range of cooling rates can be used to obtain bainite as the main microstructural constituent. The corresponding CCT diagram is only for illustration. It is not related to any of the alloys of the present study.

reactions but not so rapid that bainite does not form. Usually, the cooling rate 'window' is quite narrow, a few degrees per second, so preliminary tests are required.

(iii) An adaptation of the continuous cooling treatment enables bainite to be obtained more easily. This is the principle of a **bi-slope** experiment. At first, the sample is cooled rapidly down to a temperature just above B_s. Having avoided the reconstructive C-curve (allotriomorphic ferrite, pearlite), a wider range of cooling rates is permitted in order to obtain bainite. This is illustrated schematically on the *CCT* diagram of Figure 4.4.

(iv) Finally, **bi-isothermal** experiments are a succession of two isothermal heat treatments (Figure 4.5). The transition to the lower temperature must be operated when the fraction of bainite formed at the upper temperature is relatively small. This test, if continuous cooling is modelled as a succession of short isothermal steps (chapter 3), provides a way of checking the applicability of the additivity rule for a given alloy in the simplest of cases (two steps).

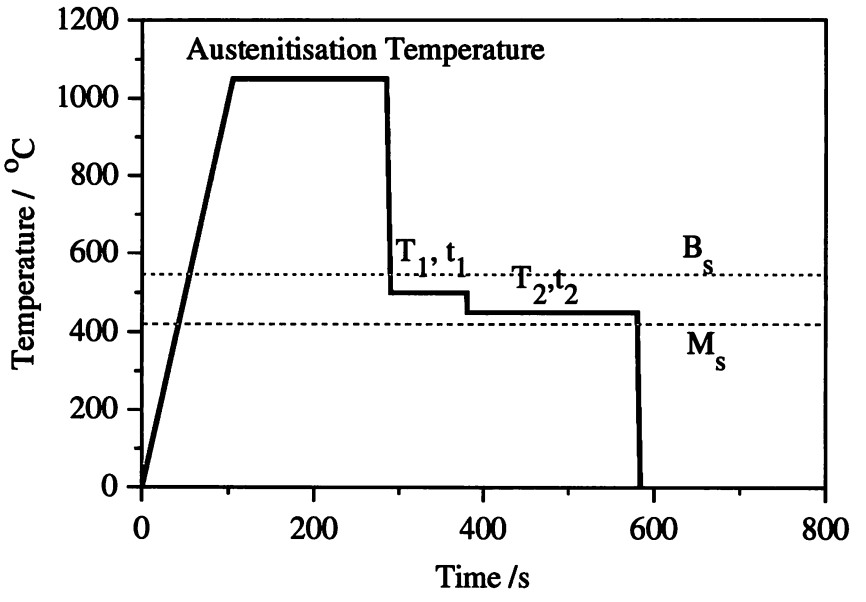

Fig. 4.5: Diagram illustrating the principle of a 'bi-isothermal' heat treatment (for alloy A). Such a heat treatment is designed to study the variations in bainite transformation rates at two different temperatures.

The THERMECMASTOR-Z thermomechanical simulator (THERMEC), manufactured by Fuji Electronic Industrial Co. Ltd., is a laboratory machine capable of simulating a specified thermal cycle (with deformation if required) on a small specimen, under accurate computer control. The temperature and diametrical dilatation of the specimen are measured and thus

the progress of a phase transformation within the material can be followed when it occurs in isolation.

A cylindrical specimen with dimensions 8 mm diameter × 12 mm length is placed in the THERMEC chamber (Figure 4.6) between two silicon nitride dies. The die holders are insulated from the dies by two mica discs. The upper die can be raised and lowered by a hydraulic ram to hold the sample in position. A platinum / platinum-10% rhodium thermocouple is spot-welded to the specimen in a central position, the contacts spaced approximately 1 mm apart. The accuracy of the temperature reading is ± 3°C whilst the variation along the specimen length is no more than ± 10°C, the 'coldest' region being near the dies [Shipway and Bhadeshia, 1995]. The diametrical dilatation of the sample is monitored using a He-Ne laser beam, which moves and scans with the ram to ensure the same location on the sample is measured throughout the experiment. The beam is positioned at the same height as the thermocouple on the sample to ensure that the temperature and dilatation measurements are for the same location.

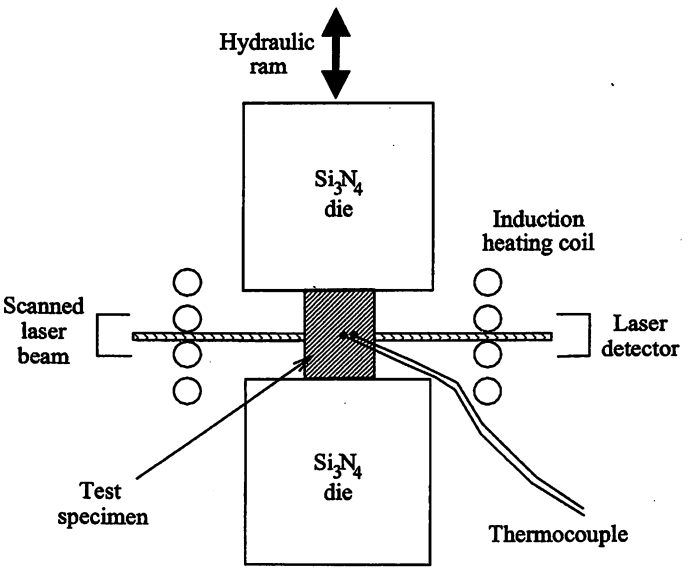

Fig. 4.6: Schematic layout of the vacuum chamber of the THERMEC thermomechanical simulator.

The accuracy of the dilatation reading is ± 1 μm. The sealed chamber is then pumped out to a vacuum of $\approx 10^{-2}$ Pa to prevent oxidation of the specimen. An inert gas (argon) atmosphere can also be introduced if required. Heating is provided by a water-cooled, high frequency induction coil which surrounds the sample. Cooling can be controlled using gas (He or N_2) or water, He being used in all these experiments. The thermal cycle is programmed

into a computer which then controls the process – the heating rate, cooling gas valves, *etc.* Time, temperature and dilatation data are recorded and can be stored on the computer for subsequent analysis.

Another plasto-dilatometer, the BÄHR DIL805 (BÄHR) was used at IRSID (France), so as to provide an insight on how different experimental results can vary when using two different equipments. Heating and cooling were performed with devices similar to the ones of THERMEC, the main difference being that BÄHR measures the length of the specimen and not the diameter. Its precision is of the order of 0.1 μm, ten times better than THERMEC. The specimen, in turn, is a cylinder of 4 mm diameter $\times$ 10 mm length. Both devices can achieve cooling rates of around 100°C s^{-1} with a solid specimen and 150°C s^{-1} with a hollow specimen.

Figure 4.7 shows an example of tests carried out on alloy C. The experimental kinetics as well as the delay times measured with the two devices are approximately similar. This becomes more evident on Figure 4.8, when the dilatations at the start of the transformation are all taken as zero. Due to the better accuracy of measurement, the curves obtained with BÄHR are smoother.

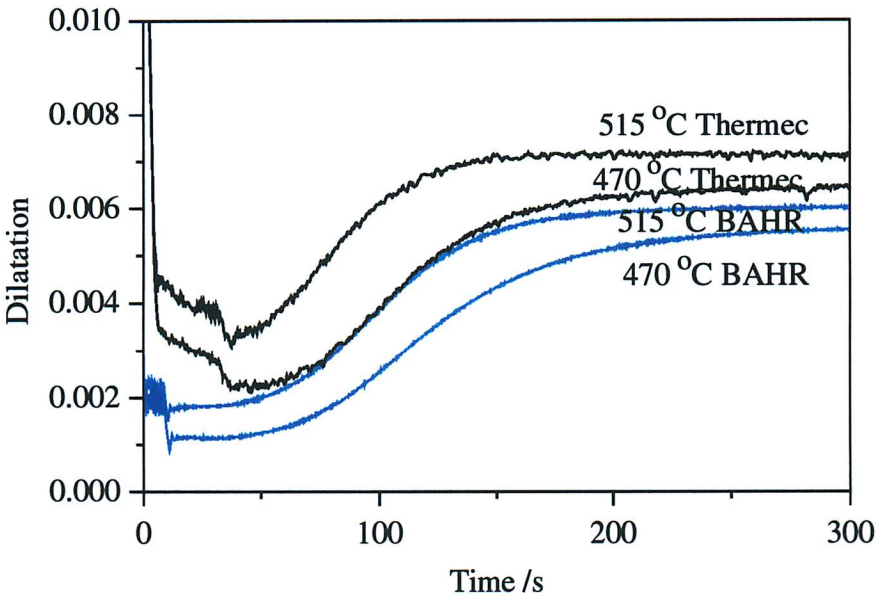

Fig. 4.7: Variation of the dilatation as a function of time for 2 sets of isothermal experiments (515 and 470°C) carried out on samples of alloy C on two different dilatometers. The black curves correspond to THERMEC and the blue curves to BÄHR.

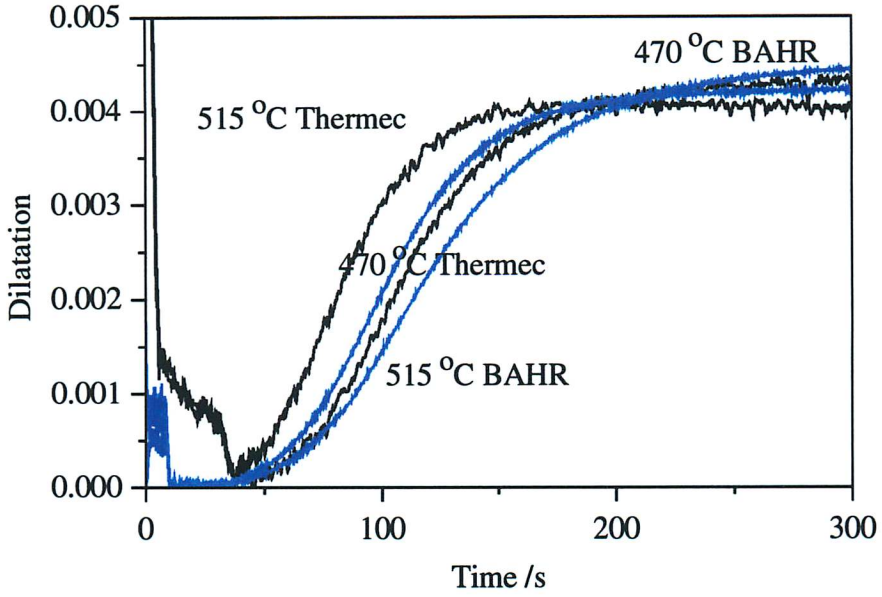

Fig. 4.8: Variation of the dilatation as a function of time for 2 sets of isothermal experiments (515 and 470°C) carried out on samples of alloy C on two different dilatometers. The black curves correspond to THERMEC and the blue curves to BÄHR. The curves are superimposed at the arbitrary zero-value for the start of transformation.

4.5 The Influence of the Equipment and of the Sample Size

Figure 4.8 shows that, using the THERMEC dilatometer, the dilatation decreases for about 35 s before an increase corresponding to the beginning of transformation is recorded. With the BÄHR dilatometer, the dilatation is stabilised in about 10 seconds and transformation can be detected earlier, because of the higher sensitivity of this instrument. Figure 4.8 also shows that for both instruments, the bulk of the transformation is happening at similar times.

Looking at the two 515°C tests on Figure 4.8, it appears that the curve corresponding to the THERMEC test lies significantly to the left of the curve for the BÄHR test. Data presented in Chapter 7 show that after 100 s, more bainite had formed (11 % in volume more) in the sample heat-treated in THERMEC, for a volume fraction of 0.35 instead of 0.24.

Figure 4.9 demonstrates that the differences cannot be entirely attributed to the equipment, as far as the time to stabilise the temperature to the isothermal transformation temperature is concerned. The THERMEC requires about 4 seconds more for stabilisation. After 7 s, the target temperature is reached. The regular oscillations for the BÄHR dilatometer originate from the temperature regulation when the He cooling valve is left open. This artefact can be suppressed.

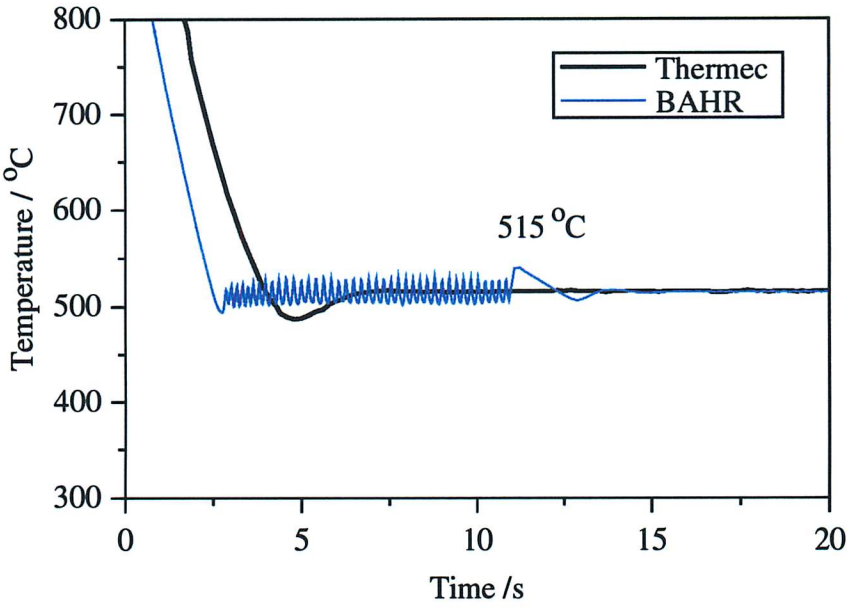

Fig. 4.9: Variation of the temperature as a function of time for the 515°C isothermal experiments carried out on samples of alloy C on two different dilatometers.

The 35 s corresponding to the decrease in dilatation are partly associated with the time that it takes for the whole of the THERMEC sample, which is bigger, to reach the desired temperature. The volume of a THERMEC sample is 0.96 cm^3, while the volume of a BÄHR sample is 0.4 cm^3.

Assuming that the thermal diffusivity α_{th} of the alloy is 5×10^{-6} m^2 s^{-1} and using the following relationship for the conduction of heat in solids:

$$\frac{\alpha_{th}\, t}{r^2} = 0.5 \tag{4.2}$$

where r is the radius of a cylinder. It would take $t = 0.4$ s in a BÄHR specimen (2 mm radius) for the temperature at the centre of the specimen to reach the isothermal temperature once it has been reached at the surface. For a THERMEC specimen (4 mm radius), this time would be 1.6 s. Heat conduction arguments alone therefore cannot explain a delay time of 35 s.

Similarly, Figure 4.10 shows that, with THERMEC, it takes about 3 s more to stabilise the temperature with a solid specimen than with a hollow specimen, for which heat transfers are maximised. Finally, Figure 4.11 shows that using the same sample for two consecutive tests on alloy A does not rule out the possibility of vastly different kinetics. The red and black curves represent tests for which the cooling rate was exactly the same above 480°C and yet they are not superimposed in that temperature domain. The transformation for the red curve

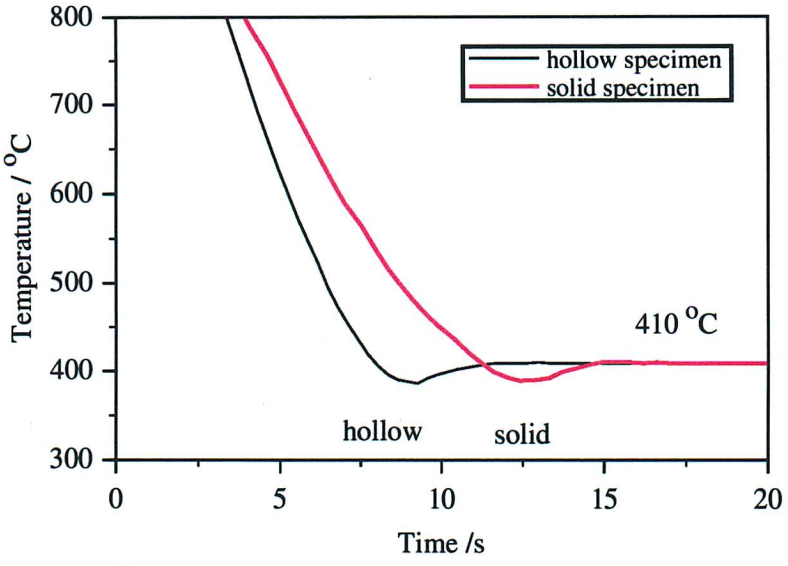

Fig. 4.10: Variation of the temperature as a function of time for the 410°C isothermal experiments carried out on samples of alloy C, one solid and one hollow, after austenitisation at 1200°C on THERMEC.

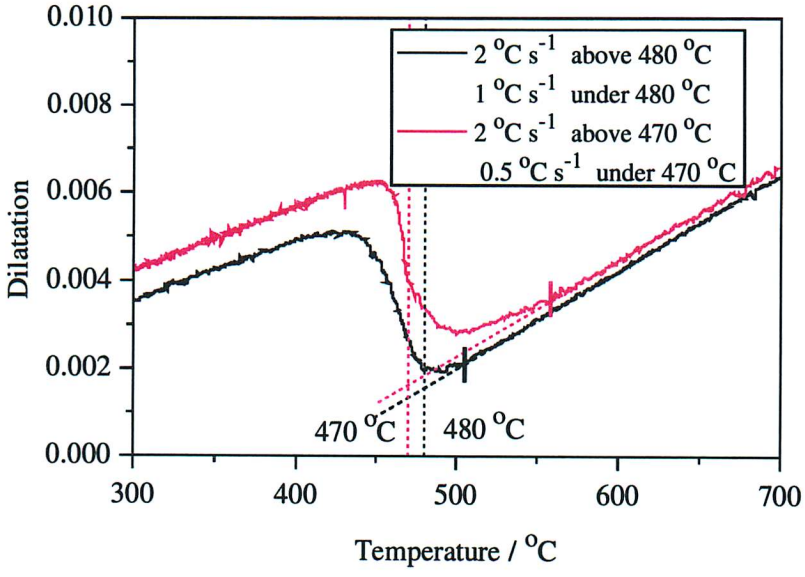

Fig. 4.11: Variation of the dilatation as a function of temperature for two bi-slope experiments carried out on the same sample of alloy A, after austenitisation at 1050°C on the THERMEC dilatometer. The cooling rate for the two tests is identical above 480°C and is equal to 2°C s^{-1}.

is shown clearly to start about 50°C higher than for the black curve. This is also illustrated in the plot of the bainite fractions, as will be shown on Figures 5.22.b and 5.22.d.

4.6 Method of Computation of the Transformed Bainite Fraction

When the change in dilatometric signal is associated only with one decomposition product of austenite and there is no change in the composition of the latter (which in turn can affect its density), the dilatational strain is directly proportional to the volume fraction transformed (equation 2.19):

$$v(t) = \frac{\frac{\Delta L}{L_0}(t)}{\frac{\Delta L}{L_0}(max)} \tag{4.3}$$

This method can only be used when the transformation is known to have achieved completion when $\frac{\Delta L}{L_0}(t) = \frac{\Delta L}{L_0}(max)$, *i.e.* $v(t) = 1$. With the high-silicon steels used, austenite is expected to become enriched in carbon, causing its stabilisation. The bainite transformation cannot then go to completion.

Because of this change in austenite composition, a different method was used to interpret the dilatometric data [Bhadeshia, 1982; Babu, 1991].

For bainitic transformation involving no precipitation of carbides, the following equation can be used to calculate v, the volume fraction of bainite [Bhadeshia, 1982; Bhadeshia *et al.*, 1991; Babu, 1991]:

$$\frac{\Delta L}{L_0} = \frac{1}{3}\frac{\Delta V_s}{V_{s0}} \simeq \frac{[2va_\alpha^3 + (1-v)a_\gamma^3 - a_{0\gamma}^3]}{3a_{0\gamma}^3} \tag{4.4}$$

where $\frac{\Delta L}{L_0}$ is the experimental strain recorded by dilatometry, V_{s0} is the initial total specimen volume and a_α and a_γ are the ferrite and austenite lattice parameters which are temperature dependent according to:

$$a_\alpha = \bar{a}_\alpha(1 + e_\alpha(T - 298)) \tag{4.5}$$

and

$$a_{0\gamma} = \bar{a}_{0\gamma}(1 + e_\gamma(T - 298)) \tag{4.6}$$

for austenite which is not enriched with carbon (subscript 0) and

$$a_\gamma = \bar{a}_\gamma(1 + e_\gamma(T - 298)) \tag{4.7}$$

when austenite enrichment is taken into account. $\bar{a}_\alpha$ and $\bar{a}_\gamma$ or $\bar{a}_{0\gamma}$ are the lattice parameters of ferrite and austenite at ambient temperature. Note that a_γ varies during the transformation even during an isothermal test, as the austenite is gradually enriched in carbon. The

new austenite composition (taking account of all solutes) is calculated from the initial austenite composition, the ferrite composition and the volume of ferrite already formed. Thermal expansion coefficients of ferrite and austenite, e_α and e_γ can be determined from simple dilatometric experiments.

The method can be used either for isothermal (Figure 4.12) or continuous cooling tests (Figure 4.13), with the segments in blue as examples of $\frac{\Delta L}{L_0}$ values.

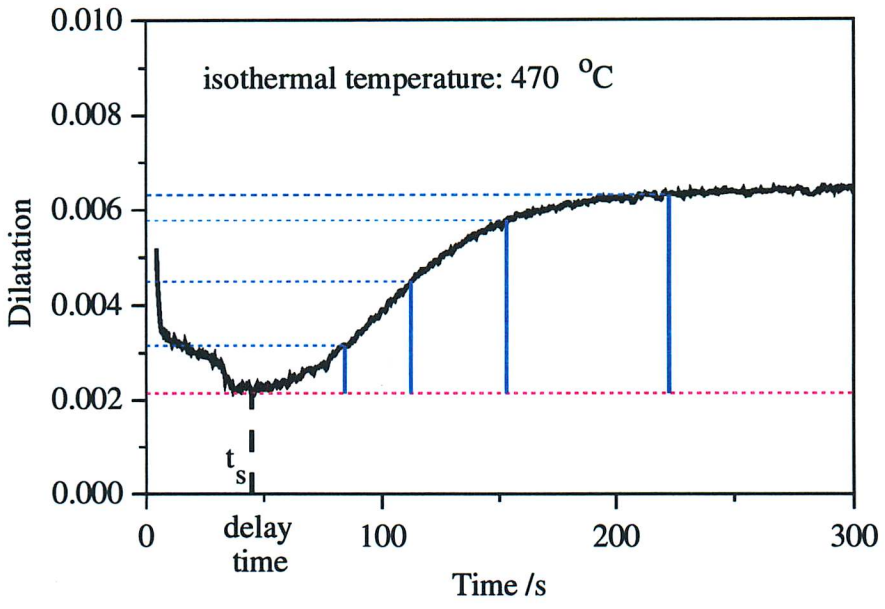

Fig. 4.12: Illustration of the dilatation values used for the calculation of the experimental bainite volume fraction in an isothermal experiment. In the case illustrated, alloy C was transformed at 470°C for 5 min, after austenitisation for 3 min at 1050°C.

On Figure 4.12, the dilatation is plotted from the point where the specimen temperature falls to the isothermal temperature. This time is used in this study as the origin of time for isothermal transformations. Because of the temperature regulation, oscillations around the isothermal temperature can happen before stabilisation (Figures 4.7 and 4.8 for BÄHR tests). It is noticeable that there is a significant delay before transformation starts. Dilatation curves have a sigmoidal shape that can be reproduced by a Johnson-Mehl-Avrami-Kolmogorov relationship.

Figure 4.14 shows the values of the measured bainite volume fractions v estimated with equation 4.4. Two curves are shown for each isothermal experiment. The curves that give the higher fractions use a value of $\bar{a}_\alpha$ equal to 2.871×10^{-10}m, and the lower curves are obtained with $\bar{a}_\alpha$ equal to 2.875×10^{-10}m. This illustrates how a very small variation in one

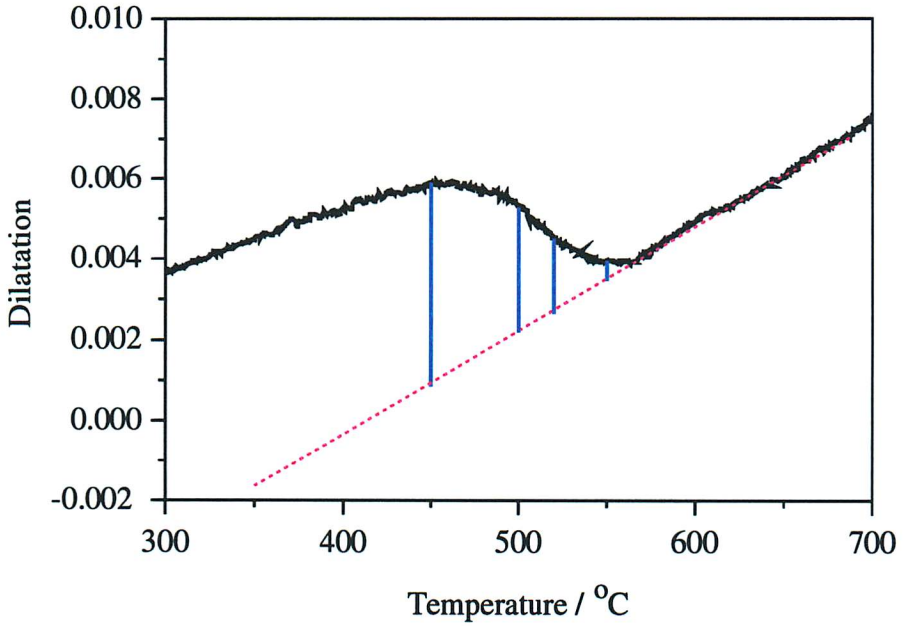

Fig. 4.13: Illustration of the dilatation values used for the calculation of the experimental bainite volume fraction in a cooling experiment. In the case illustrated, alloy A was continuously cooled at 1°C s^{-1}, after austenitisation for 5 min at 1200°C.

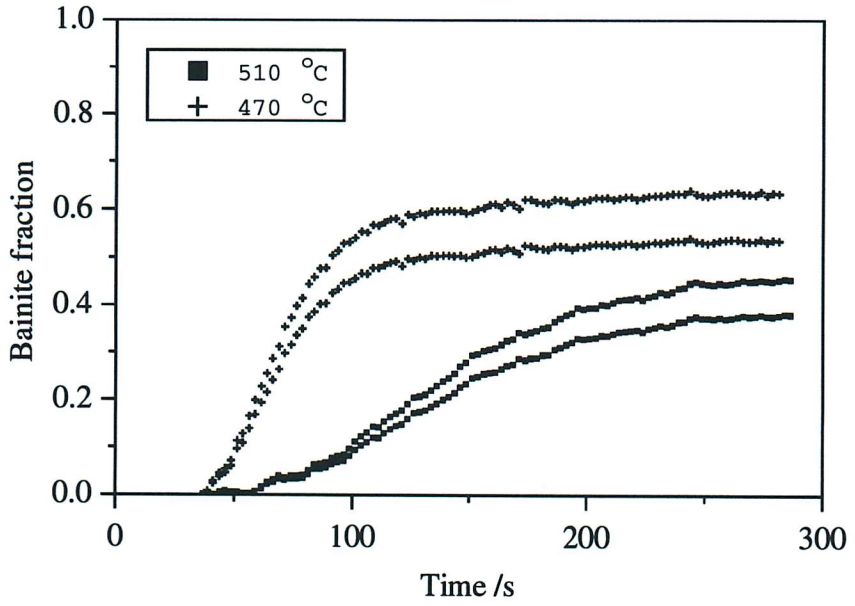

Fig. 4.14: Schematic illustration of the uncertainty of calculation of the bainite fraction using the method described in this chapter. The value of the spacing between the two curves can be taken as the error bar surrounding the measured value at the corresponding time.

of the parameters can have significant repercussions on the fraction calculated from the length change. The difference between the two curves can be taken as the error bar. It increases with the fraction transformed. In the example of Figure 4.14, the final difference between the two curves is 10% at 470°C and 7% at 510°C.

In the present work, the value $\bar{a}_\alpha$ was chosen as 2.871×10^{-10}m, which means that the experimental bainite fraction will be superior to the fraction calculated with a higher value. The error bar associated with the austenite thermal expansion coefficient also has repercussions on the measured bainite volume fraction.

4.7 Microstructural Characterisation

4.7.a Optical Microscopy

After being heat treated in the dilatometer, specimens were cut along their diameters in the central region, where the thermocouple was attached. They were then embedded in Bakelite and successively ground and polished down to 1 μm size. Optical micrographs were taken with a ZEISS AXIOPLAN2. The etchants used are listed in Table 4.2.

Name	Composition	Etching procedure	Specificity
NITAL	Ethanol + 2 to 5 % HNO_3	Immersion of sample for 5 to 10 seconds	Standard use
DINO	140 ml H_2O 100 ml H_2O_2 4 g $H_2C_2O_4$ 2 ml H_2SO_4 1.5 ml HF	Fresh solution Immersion of sample for 2-3 seconds HF must be handled in fume cupboard with goggles	For Si steels To reveal prior austenite grain boundaries
RABINOVITCH	100 ml H_2O + saturated $Na_2S_2O_3$ 1 to 2.5 g $Na_2S_2O_5$	Fresh solution Immersion for 30-120 s Surface becomes dark with blue reflections	Retained austenite appears white in Si steels

Table 4.2: Composition and conditions of use of etchants.

4.7.b Transmission Electron Microscopy (TEM)

For transmission electron microscopy, a number of 3 mm diameter circular rods were machined from the heat treated dilatometer samples of alloy A. A STRUERS ACCUTOM-5 cutting machine was used to remove thin discs of thicknesses around 150 μm. To obtain thin foils, an '800-grit' mechanical polishing paper was used to manually thin the specimens to a thickness of $\leq$ 50 μm with the aid of a specially designed holder and water as a lubricant. A twin-jet electropolisher was used in conjunction with a 5% perchloric acid-10% glycerol-85% ethanol solution at ambient temperature. Typical polishing conditions were 45 V and 25 mA. Imaging was performed in a JEOL 200CX instrument operating at 200 kV.

Carbon replicas can be more useful than thin foils in the identification of precipitates. Carbon replicas eliminate magnetic effects due to the ferrite matrix and enable a large area to be examined. The procedure followed to extract the replicas from surfaces prepared for samples for optical microscopy is as follows. Carbon was deposited in a vacuum of 10^{-5} torr onto the etched sample's surface. The deposited carbon layer was then cut into 2 mm square pieces to enable the removal of several small sections covering the whole area of the sample. Then the film was detached from the sample by electrolytic etching in a 5 % hydrochloric acid in methanol solution at 1.5 V. Each replica was washed in methanol and then in distilled water. Finally the replicas floating in distilled water were collected on 400 square mesh copper grids for examination in the transmission electron microscope.

4.7.c Vickers Macro-hardness

Macro-hardness tests were performed for all heat treated specimens. In some cases, to save material and ensure better experimental reproducibility, the same specimen was used for several tests. In that case, hardness measurements could only be carried out for the last heat treatment performed. The results can be compared to the values calculated using the following empirical equations [Blondeau, 1976]:

$$H_V(\text{martensite}) = 127 + 949\text{C} + 27\text{Si} + 11\text{Mn} + 8\text{Ni} + 16\text{Cr} + 21.\log Q \tag{4.8}$$

$$\begin{aligned} H_V(\text{bainite}) = {} & -323 + 185\text{C} + 330\text{Si} + 153\text{Mn} + 65\text{Ni} + 144\text{Cr} + 191\text{Mo} \\ & + (89 + 53\text{C} - 55\text{Si} - 22\text{Mn} - 10\text{Ni} - 20\text{Cr} - 33\text{Mo}).\log Q \end{aligned} \tag{4.9}$$

$$\begin{aligned} H_V(\text{ferrite/pearlite}) = {} & 42 + 223\text{C} + 30\text{Mn} + 12.6\text{Ni} + 7\text{Cr} + 19\text{Mo} \\ & + (10 - 19\text{Si} + 4\text{Ni} + 8\text{Cr} + 130\text{V}).\log Q \end{aligned} \tag{4.10}$$

where the concentrations are in wt% and the cooling rate Q is in °C per hour. The applicability of equations 4.8, 4.9 and 4.10 is for carbon concentrations between 0.1 and 0.5 wt% and for concentrations in silicon, manganese, nickel, chromium, molybdenum and vanadium lower than 1, 2, 4, 3, 1 and 0.2 wt% respectively (an additional condition being that Mn + Ni + Cr + Mo + V $\leq$ 5).

For samples containing a mixture of bainitic ferrite, martensite and little retained austenite, macrohardness values are expected to be higher for samples with a small fraction of bainite than for samples with a large fraction of bainite. Indeed, bainite is a softer phase than martensite; the latter retaining all its carbon.

4.7.d Determination of the Retained Austenite Fraction

The specific saturation magnetisation, σ_{Sat}, is used to assess the amount of retained austenite † present in a microstructure. Ferrite in all its forms is a ferromagnetic substance whereas austenite in low alloy steels is paramagnetic.

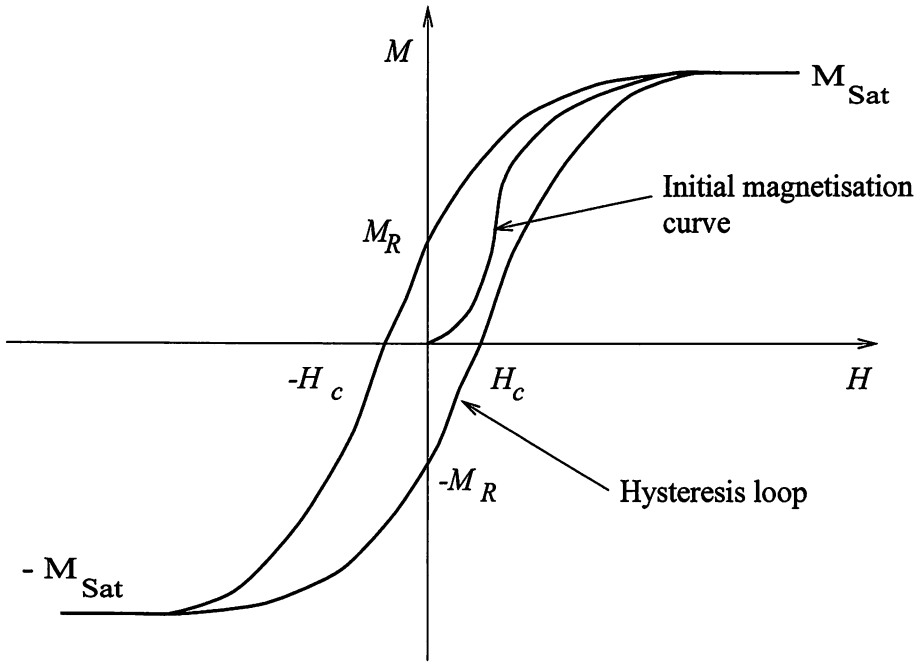

Fig. 4.15: Illustration of a typical hysteresis cycle for a ferromagnetic material, with the associated characteristic points.

A ferromagnetic substance shows the typical hysteresis cycle of Figure 4.15 when a magnetic field H of varying magnitude and sign is applied. The hysteresis cycle can be used to

† The term 'retained austenite' is used for austenite that remains in the microstructure at room temperature *i.e.* when the heat treatment is over. 'Residual austenite' refers to austenite during the heat treatment which can still undergo transformation.

determine the following important parameters:

- M_{Sat}, the saturation magnetisation, is the maximum magnetisation obtained by increasing the positive magnetic field.
- H_c, the coercivity, is then the field required to reduce the magnetisation to zero.
- After looping to saturation in the opposite direction (with a negative field), the remanent magnetisation M_R is the value of the magnetisation when the magnetic field has been reduced to zero.

The magnetic induction B is given by:

$$B = \mu_0(H + M) \tag{4.11}$$

where μ_0 is the permeability of vacuum. The specific saturation magnetisation σ_{Sat} can be measured accurately by putting a sample in a varying magnetic field, in a device named 'sigmameter'. A sigmameter measures the magnetic moment of a sample which is equal to its volume $\times$ its saturation magnetisation M_{Sat}. Since

$$M_{Sat} = \sigma_{Sat} \cdot \rho \tag{4.12}$$

where ρ is the density of the material, σ_{Sat} can be easily deduced from the measurement. For a given alloy composition, the measured values of σ_{Sat} increase linearly from zero in an entirely austenitic sample (paramagnetic) to a limit value for a fully ferritic reference sample (ferromagnetic). Hence the following simple relationship can be used to determine the volume percentage of retained austenite in a sample after heat treatment:

$$\%\gamma_R(sample) = 100\left[1 - \frac{\sigma_{Sat}(sample)}{\sigma_{Sat}(reference)}\right] \tag{4.13}$$

4.8 The Nucleation Rate

Figure 4.16 shows the variations for a Fe-0.43C-2.12Si-3.00Mn wt% steel of a quantity proportional to the nucleation rate according to the general theory of bainite transformation described in Chapter 2. The model predicts that the nucleation rate should increase slowly as the temperature is decreased and then much more rapidly as the temperature is decreased further in the martensite transformation range.

Detailed metallography was carried out in order to count the number of sheaves of lower bainite formed during isothermal holding of this alloy for several times at 363 and 273°C. For

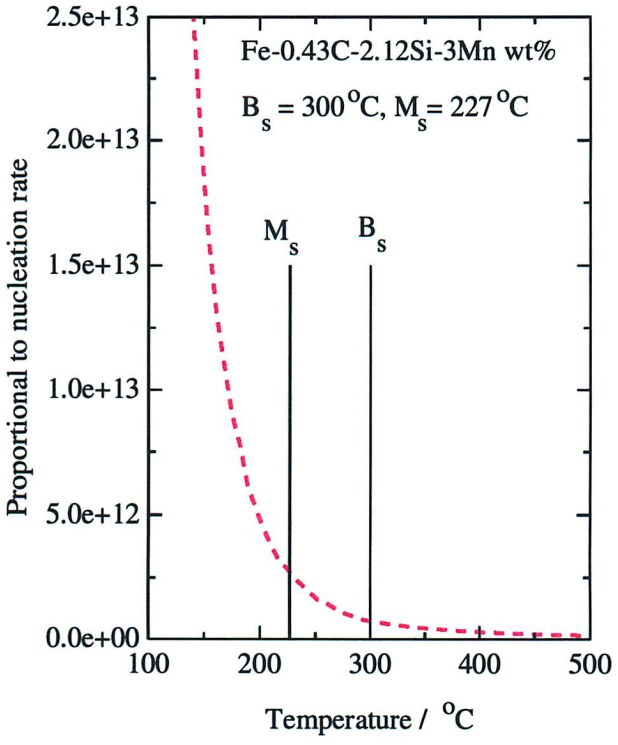

Fig. 4.16: Variation of a quantity proportional to the nucleation rate as predicted for a Fe-0.43C-2.12Si-3.00Mn wt% steel by the general theory of bainite transformation.

that purpose, the average number of sheaves observed on 10 different micrographs for each time and temperature was measured and the standard deviation was taken as the error bar. Lower bainite, because of an alloy carbon concentration $\geq$ 0.4 wt% [Bhadeshia, 1992], is the only form of bainite forming in this alloy. Its dark aspect caused by intra-lath carbides and the small dimensions of the sheaves makes lower bainite very easily distinguishable, and the counting of sheaves possible. Figure 4.17 is an example of a micrograph showing sheaves of lower bainite.

Counting results are given in Figure 4.18. Contrary to the predictions of MAP-STEEL-MUCG46, which gives B_s = 300°C for that alloy, sheaves of bainite were observed even at 363°C. The results show that the number of nucleated sheaves at a given temperature increases with holding time. The numbers counted at the two temperatures were, within the error bars, very similar, which does not permit a confirmation of the complete shape of the curve in Figure 4.16, as they are in the temperature zone where the increase is relatively slow. Access to lower temperatures is unfortunately limited by the onset of martensitic transformation.

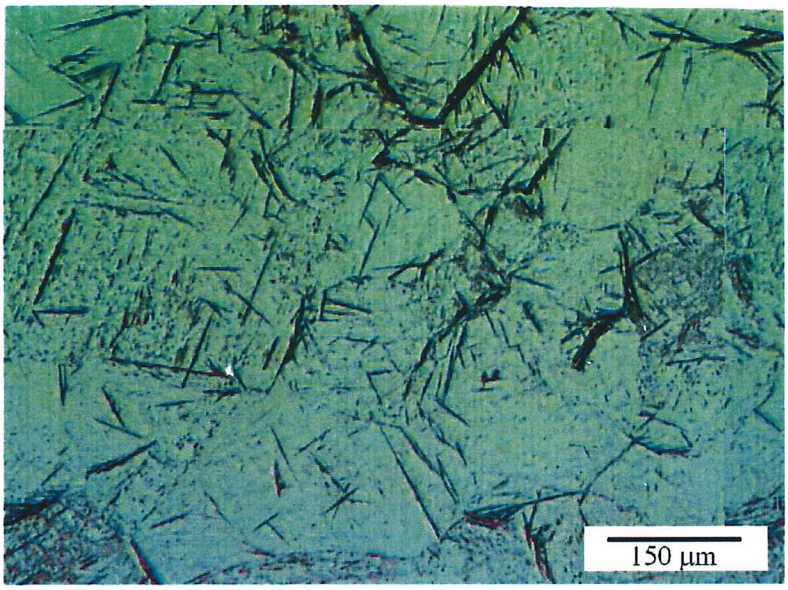

Fig. 4.17: Optical micrograph showing sheaves of lower bainite in a Fe-0.43C-2.12Si-3.00Mn wt% steel isothermally transformed at 273°C for 40 minutes after austenitisation at 1220°C. Etched in 3% Nital.

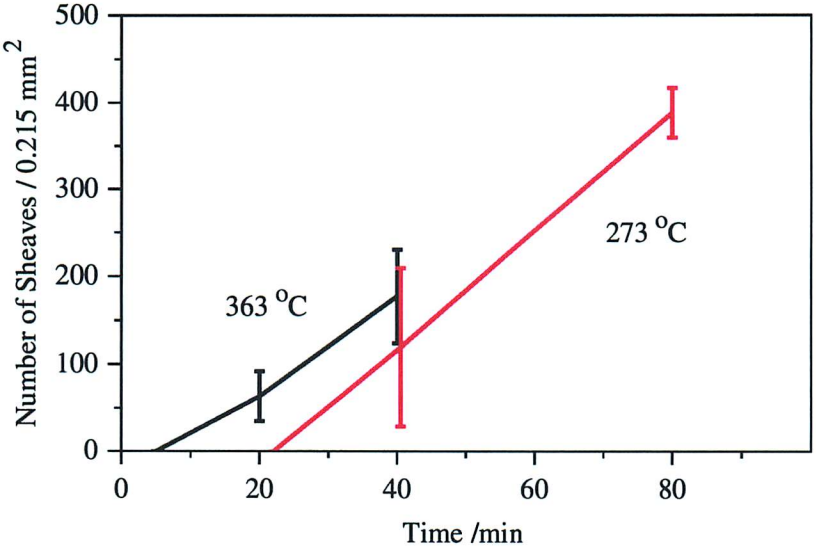

Fig. 4.18: Experimental results of counting lower bainite sheaves in a Fe-0.43C-2.12Si-3.00Mn wt% alloy.

4.9 Summary

The work presented in this Chapter has shown that for the bainite transformation to be observed in isolation, the experimental conditions must be chosen carefully. The estimation of the bainite-start transformation temperature by calculation is reasonable but preliminary tests are necessary before finding the 'bainite window'. There are four types of heat treatments used in the present study.

For a heat treatment to be selected for the study, the optical micrographs must show a mostly bainitic microstructure, with compatible values of macro-hardness. The increase in dilatation associated with the transformation must also be situated in or very close to the calculated bainite domain (between B_s and M_s).

A method for the determination of the experimental bainite volume fraction from dilatometric data was presented in this chapter. It was shown, however, that the uncertainty in the final transformed volume is expected to be around 10 volume percent. This is because small variations in lattice parameters induce significant variations in the bainite volume fraction.

Finally, an experimental method to assess the fraction of austenite retained in a microstructure thanks to a magnetic property was introduced. With the knowledge of both the experimental fractions of bainite and retained austenite, it is possible to infer the amount of martensite present in the microstructure (assuming no other than these three phases are present).

The next chapter presents experimental results for the bainite transformation in alloy A and the corresponding microstructures.

Chapter 5

Experimental Study of Alloy A

5.1 Introduction

Alloy A contains 0.33 wt% silicon, which is not a large enough concentration to suppress cementite precipitation. On the other hand, its carbon content, 0.16 wt% is relatively low, so it was not obvious whether carbides would form in the microstructure. The carbon concentration should be small enough to avoid lower bainite. The alloy is also useful because it is be easy to distinguish individual sheaves of bainite in austenite grains. It will be interesting to check in Chapter 6 whether the physical model, which does not take account of carbides, nevertheless delivers accurate predictions for alloy A.

It was mentioned in Chapter 4 that alloy A contains chemical segregation bands. These regions of different chemical compositions can manifest quite markedly in the microstructure. Even in a sample where the bainite transformation has reached its maximum extent of transformation (Figure 5.1), some areas consisting of many austenite grains transform only into martensite; these areas have the highest hardenability because of chemical segregation. However, the sample must be considered as a whole and since there appears no discontinuity on the dilatation curves during transformation, it is probable that the average kinetics are not affected much by banding.

A coherent colour code is used in this and all following chapters. Each colour is used to represent a different kind of data:

- *Black:* for experimental data collected on THERMEC and BÄHR and experimental or predicted transformation curves at the low temperature of a bi-isothermal test.
- *Red:* for experimental isothermal data collected on BÄHR (when plotted in a TTT diagram) and experimental or predicted transformation curve at the high temperature of a bi-isothermal test.
- *Blue:* for the experimental transformation curve of a bi-isothermal test.
- *Green:* for model predictions using constants fitted on isothermal data belonging to the same alloy.

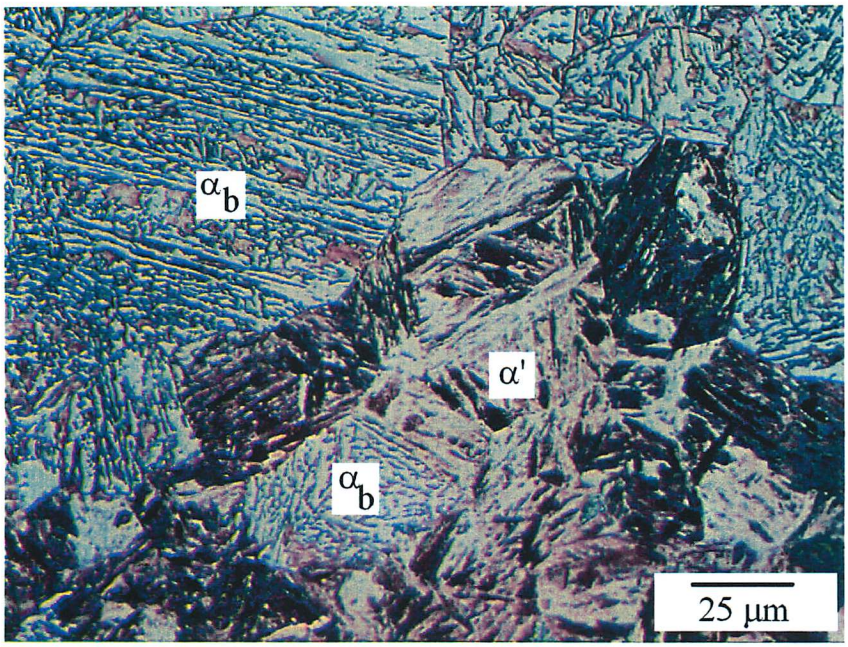

Fig. 5.1: Optical micrograph of alloy A isothermally transformed at 525°C for 5 min after austenitisation for 3 min at 1050°C (BÄHR). There is a very clear separation between entirely martensitic regions (darker contrast) and regions with a bainitic microstructure, including one at the bottom of the micrograph which is isolated. The latter also contains smaller areas of martensite (etched brown) between the sheaves. The symbols α_b and α' represent areas of bainite and martensite in all subsequent micrographs. Etched in 2% nital.

- *Yellow:* for model predictions using 'general' constants.
- *Magenta:* for experimental cooling data estimated in order to include bainite AND martensite.

5.2 Heat Treatments

The austenite grain sizes at the two austenitisation temperatures used (namely 1050 and 1200°C) were determined by the method of linear intercepts with the uncertainty expressed as a standard deviation. The values of the thermal expansion coefficients of alloy A are listed in Table 5.1. To measure the expansion coefficient of ferrite, THERMEC specimens were first tempered for one hour at 600°C to ensure an essentially ferritic microstructure. The length change data recorded during subsequent slow cooling from 600°C ($\simeq 4$°C s^{-1}) were analysed to estimate the expansivity. For austenite, length change data during heating from 850 to 1000°C, at a rate of 10°C s^{-1} in the austenite phase field, were analysed.

The experimental conditions which produced bainite as the first and main constituent on decomposition of the austenite are listed in Appendix 1.

Grain size at 1200°C (μm)	Grain size at 1050°C (μm)	Ferrite thermal expansion coefficient (K^{-1})	Austenite thermal expansion coefficient (K^{-1})
166 ± 18	26 ± 5	$(1.61 \pm 0.02) \times 10^{-5}$	$(2.46 \pm 0.02) \times 10^{-5}$

Table 5.1: Table listing the measured γ grain sizes of alloy A after austenitisation for 3 min at 1200 or 1050°C, and the measured values of the ferrite and austenite thermal expansion coefficients.

Although the experiments listed in Appendix 1 all produce bainite, small fractions of other high temperature transformation products were found to decorate the austenite grain surfaces before the bainite-start temperature was reached, in the case of the large austenite grain size samples. This is apparent on the micrograph of Figure 5.2. The heat treatment applied to that specimen was slow cooling at 2°C s^{-1} above B_s followed by quenching. Very little if any bainite could form as a consequence of this heat treatment.

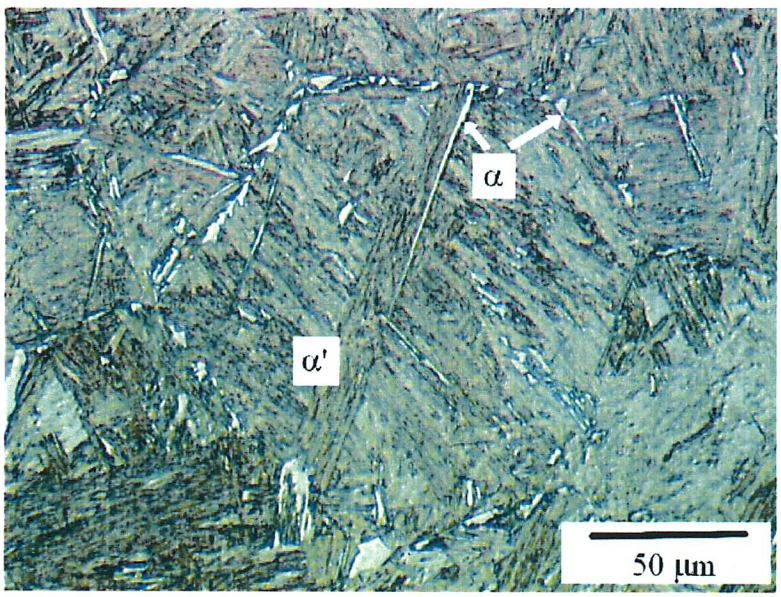

Fig. 5.2: Optical micrograph of alloy A with a large γ grain size of 166 μm after austenitisation at 1200°C (THERMEC). Continuously cooled at 2°C s^{-1} above 546°C (the value of B_s) followed by quenching. The symbol α represents areas of allotriomorphic ferrite in all subsequent micrographs. Etched in 3% nital.

It is well known that large austenite grain sizes can promote the development of Widmanstätten ferrite [Jones and Bhadeshia, 1997]. Another grain boundary phase, allotriomorphic ferrite is also present in microstructures associated with the large γ grain sizes.

It is very likely that the formation of grain boundary phases affects the process of nucleation of bainite which also occurs mainly at grain boundaries. Since it is necessary for bainite to be studied in isolation, large austenite grain sizes were avoided in the present work. A plot of experimental results for the large γ grain size is given in Figure 5.3. By comparison with Figure 5.4, it seems that the kinetics are accelerated by the presence of prior grain boundary phases.

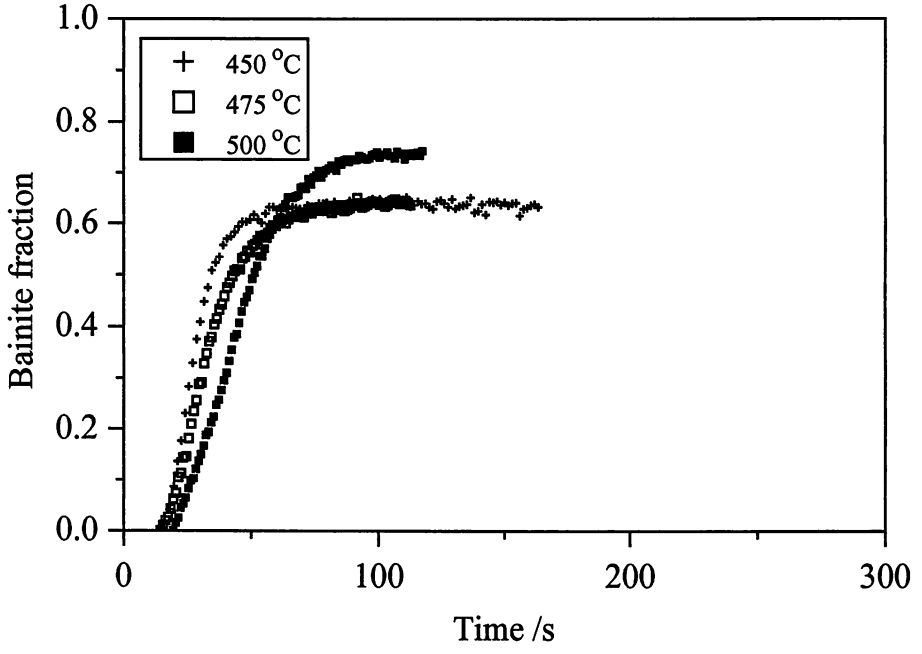

Fig. 5.3: Isothermal transformation data (THERMEC) for alloy A with 166 μm γ grain size (austenitised at 1200°C) for a variety of isothermal transformation temperatures.

5.3 Isothermal Treatments

Figures 5.4.a and 5.4.b show the experimental isothermal kinetics of alloy A with the small austenite grain size for a variety of temperatures covering the bainite transformation range. As shown in Chapter 4 for alloy C, when using THERMEC, there is a period of about 35 s during which the dilatation keeps decreasing and no transformation takes place. For experiments done on BÄHR, the smaller sample volume enables this delay to be reduced. Moreover, the BÄHR dilatometer is ten times more sensitive than THERMEC and transformation becomes detectable almost as soon as the isothermal temperature is reached. The time $t = 0$ is taken as the time at which the isothermal temperature is reached for the first time during the quench preceding isothermal holding.

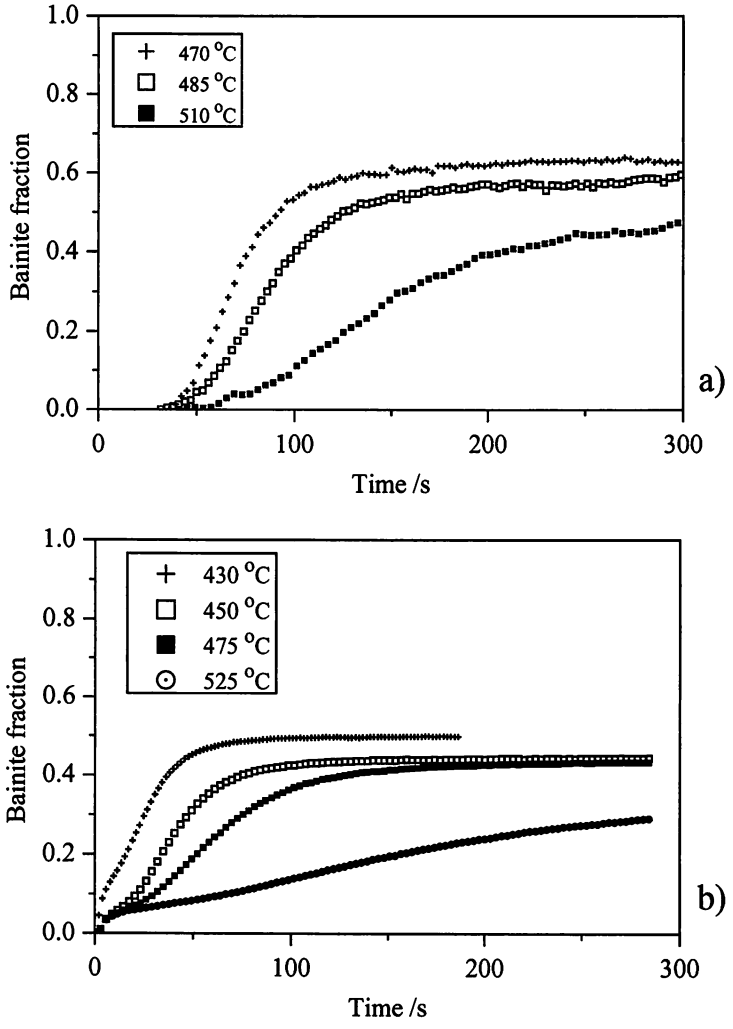

Fig. 5.4: Isothermal transformation data for alloy A with 26 μm γ grain size (austenitised at 1050°C) for a variety of isothermal transformation temperatures. a) with THERMEC; b) with BÄHR.

For the curves illustrated in Figure 5.4.b, the transformation starts abruptly, before slowing down at a fraction of around 0.05. Such a phenomenon is not observed in tests performed with the THERMEC. Although the transformation rates for both sets of curves are similar, maximum volume fractions obtained with the BÄHR dilatometer are smaller than those obtained with THERMEC. Indeed, the maximum fraction for 470°C with THERMEC is 0.63 while the maximum fraction for 475°C with BÄHR is 0.43 and the 430°C test gives a fraction of 0.50.

Alloy A complies with the incomplete reaction phenomenon. Transformation reaches a higher limiting fraction (which is less than required by equilibrium) as the isothermal transformation temperature is decreased.

Figures 5.5.a and 5.5.b were plotted using the data of Figures 5.4.a and 5.4.b. Figure 5.5.b uses a logarithmic time scale as in conventional *TTT* diagrams. The points in red correspond to the BÄHR tests and the points in black to the THERMEC tests. It appears that the time necessary to go from a fraction of 0.1 to 0.4 increases as the temperature increases. Although the two sets of points corresponding to the two dilatometers correlate well, the reaction rates recorded on THERMEC, *i.e.* the time taken to complete the reaction not accounting for the initial delay period, were larger than their BÄHR counterparts. This is illustrated by the black dotted lines being closer together than the red ones.

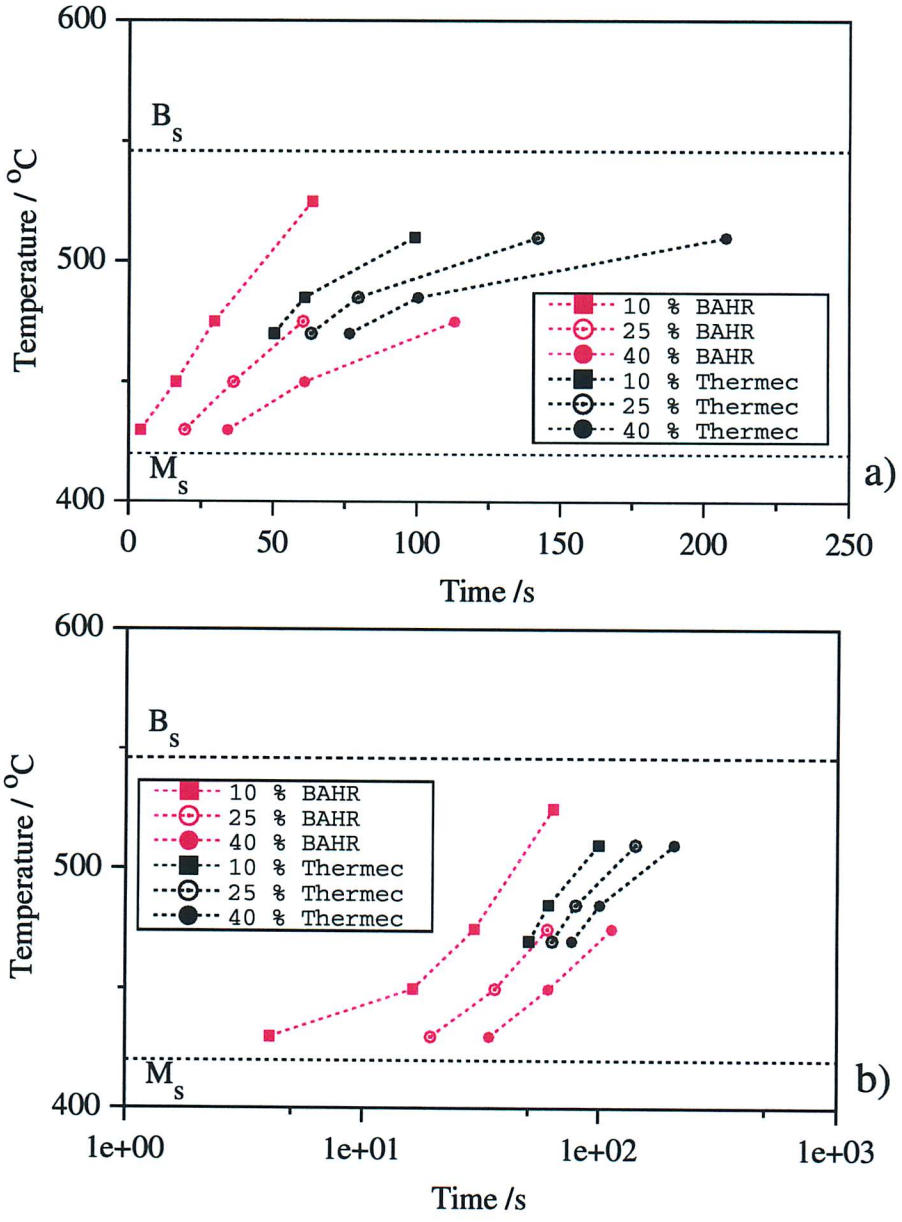

Fig. 5.5: Experimental *TTT* diagram of alloy A obtained with BÄHR (red) and THERMEC (black) isothermal experiments. a) linear time scale; b) logarithmic time scale.

Figure 5.6 is a micrograph of alloy A isothermally transformed at 475°C for 3 hours in which bainite appears with an irregular shape. Some sheaves are seen in their longitudinal direction while most of them are seen in their cross section. Carbides are not observed, but confirmation of this is needed at higher magnifications with the use of transmission electron microscopy. The space between bainitic sheaves is filled with martensite, which appears brown. Some grain boundaries have developed a small fraction of a dark phase, probably pearlite, which had enough time to develop during the long holding time.

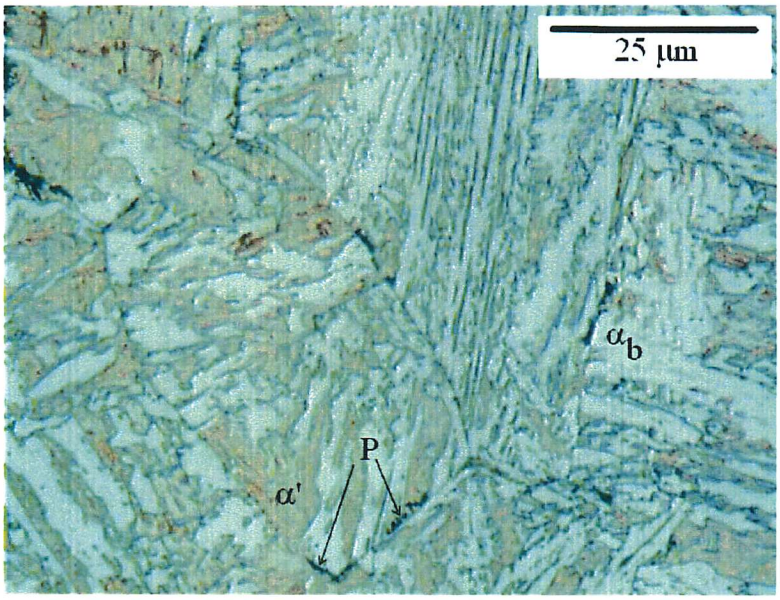

Fig. 5.6: Optical micrograph of alloy A transformed isothermally at 475°C for 3 h after austenitisation for 3 min at 1050°C ($d_\gamma = 26$ μm, THERMEC). White regions represent bainite, with the brown-etching martensite occupying the remaining space. Due to the prolonged heat treatment, pearlite had time to develop at some grain boundaries and corners. The symbol P represents areas of pearlite in all subsequent micrographs. Etched in 3% nital.

5.4 Interrupted Quenching Experiments and Study of Expansivities

5.4.a Interrupted Quenching Experiments

An isothermal experiment can be interrupted by a quench in order to study the progress of the bainite transformation. Figure 5.7 shows the recorded variation of dilatation as a function of time for samples of alloy A isothermally held at 450°C for 13, 25, 36 and 50 s before quenching. The heat treatments were performed on the BÄHR dilatometer. Figure 5.7 shows that after quenching starts and induces a decrease in length, the dilatation increases sharply

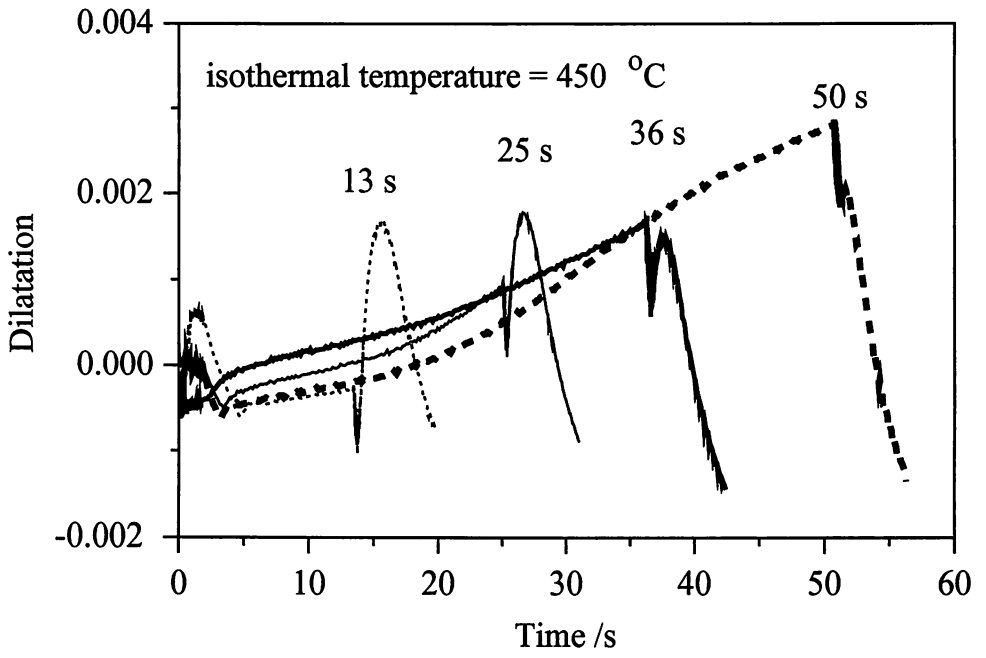

Fig. 5.7: Interrupted quenching data (BÄHR) for alloy A with 26 μm austenite grain size (austenitised at 1050°C) at various isothermal holding times.

when the martensite transformation takes place. As the holding time increases, more bainite is formed and the amount of martensite decreases.

Figure 5.8 shows that in the sample that was held at 450°C for only 13 s, sheaves of bainite started developing inside the central grain.

The micrograph of Figure 5.9 shows the microstructure of the sample that was held at 450°C for 50 s. All grains are mostly filled with bainite. The way that bainite sheaves develop within individual grains can be seen clearly in the central grains, with martensite forming upon quenching. Vickers hardness data for these treatments are given in Appendix 1 (Table 1). The trend is that hardness decreases as the isothermal transformation time is increased, indicating that there is an increased bainite fraction in the microstructure.

A plot of the dilatation as a function of the temperature was used to determine the M_s temperature for each of the four treatments above. The results appear in Table 5.2. The martensite-start temperature is increased by about 20°C for the largest bainite fractions. This suggests that there is less carbon in residual austenite when the fraction of bainite is high. The most likely explanation is that carbides remove carbon from the austenite. This phenomenon might only be noticeable when the fraction of bainite is large, since the precipitation occurs as a secondary event during the transformation. Carbon is known to stabilise austenite with respect to martensite.

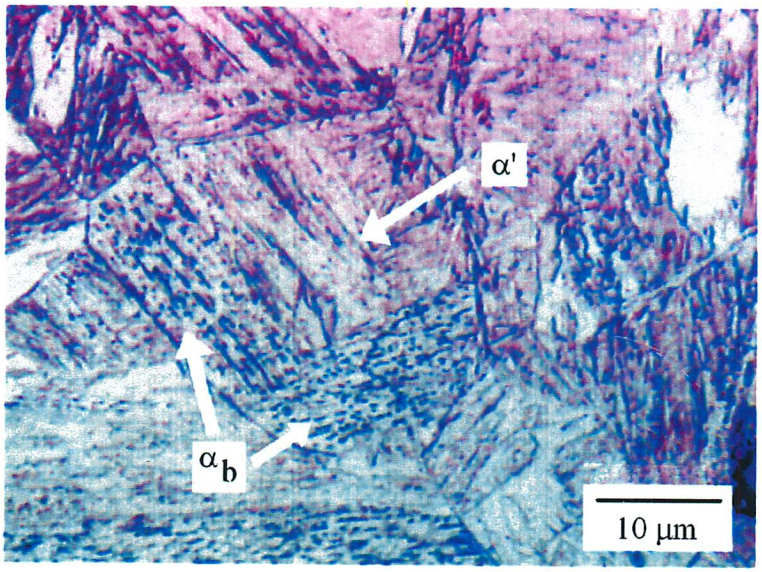

Fig. 5.8: Optical micrograph of alloy A isothermally transformed at 450°C for 13 s followed by quenching (BÄHR), after austenitisation for 3 min at 1050°C. Etched in 2% nital.

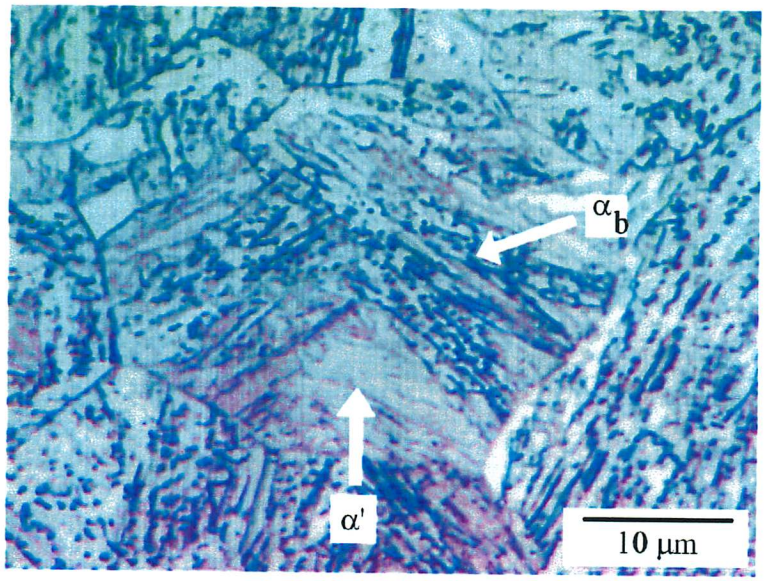

Fig. 5.9: Optical micrographs of alloy A isothermally transformed at 450°C for 50 s followed by quenching (BÄHR), after austenitisation for 3 min at 1050°C. Etched in 2% nital.

Assuming that the increase in martensite-start temperature is only caused by a variation in carbon concentration and using the empirical relationship due to Andrews [1965]:

$$M_s\ (°C) = 539 - 423C - 30.4Mn - 17.7Ni - 12.1Cr - 7.5Mo \qquad (5.1)$$

Time of isothermal holding	13 s	25 s	36 s	50 s
M_s (°C)	378	376	398	395

Table 5.2: Table listing the martensite-start temperatures recorded for the interrupted quenching treatments on alloy A. Samples were austenitised for 3 min at 1050°C and held at 450°C for various times before quenching.

where the concentrations are all in wt%, a decrease of 42.3°C of the value of M_s corresponds to an enrichment of 0.1 wt%. In this case, it is found that a M_s temperature of 378°C corresponds to a carbon concentration of 0.255 wt% in residual austenite. At this point, there is already a significant enrichment of residual austenite. 398°C corresponds to a carbon concentration of 0.21 wt%, *i.e.* a difference of 0.045 wt% with the original composition $\bar{x}$. It can therefore be inferred that as the bainite transformation proceeds, forming carbides requires more carbon than is rejected from the plates of bainitic ferrite.

The maximum bainite fraction obtained during a test can be related to the residual austenite carbon enrichment by equation 6.1 (Chapter 6). In alloy A, for example, 0.255 wt% of carbon in residual austenite corresponds to a limiting bainite fraction of 0.42, if there is no carbide precipitation. The value of M_s for the isothermal test interrupted after 25 s is consistent with a bainite fraction of 0.4. Evaluating the carbon enrichment of residual austenite *via* the maximum bainite fraction is interesting but caution must be used in doing so. It is well known that carbon redistribution is not homogeneous: large areas of residual austenite between sheaves are less enriched on average than small areas between bainitic sub-units.

5.4.b Variation in Expansivities as Reaction Progresses

The thermal expansion coefficient of pure austenite (Table 5.1) is markedly larger than its counterpart for pure ferrite. As the face-centred cubic austenite progressively transforms into the body-centred cubic ferrite (either bainitic ferrite α_b or martensite α'), the expansivity of the mixture decreases and reaches the value for pure ferrite when all the austenite has transformed. This is illustrated schematically on Figure 5.10, for two typical heat treatments.

- For an isothermal heat treatment (Figure 5.10.a), the sample is quenched from T_γ down to a temperature $T_{iso} < B_s$. There is therefore no transformation to bainite during that segment of the heat treatment. Ample time is allowed at the transformation temperature so that transformation to bainite can reach completion and the dilatation its maximum value before the second quench. The progressive decrease in thermal expansion coefficient

indicates that significant martensite transformation is taking place, even if there is no apparent sudden rise in dilatation on the curve.

- When slow cooling is interrupted by quenching (Figure 5.10.b), bainite continues to form which explains why the dilatometric signal does not decrease immediately below T_{quench}. When martensitic transformation starts at a depressed value of the M_s temperature, a rapid increase in dilatation is observed as long as the amount of martensite that forms is large. Otherwise, martensite transformation can only be detected by monitoring the total expansion coefficient as on Figure 5.10.a.

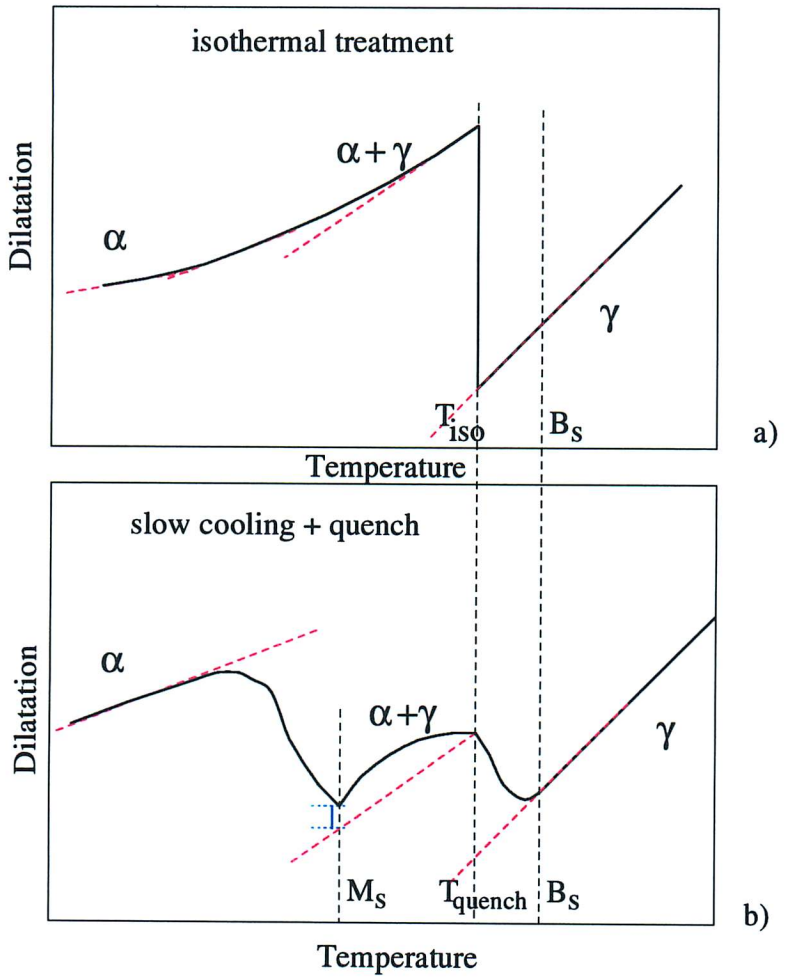

Fig. 5.10: Schematic illustration of the variation of the dilatometric signal during two typical heat treatments: a) isothermal transformation at T_{iso} below B_s followed by quench during which there is no appreciable 'bump' associated with martensite transformation; b) slow cooling above and below B_s followed by a quench at T_{quench} before enough bainite could form to suppress the 'bump' associated to martensite. The symbol α here represents both bainitic ferrite α_b and martensite α', which have the same e_α and e_γ.

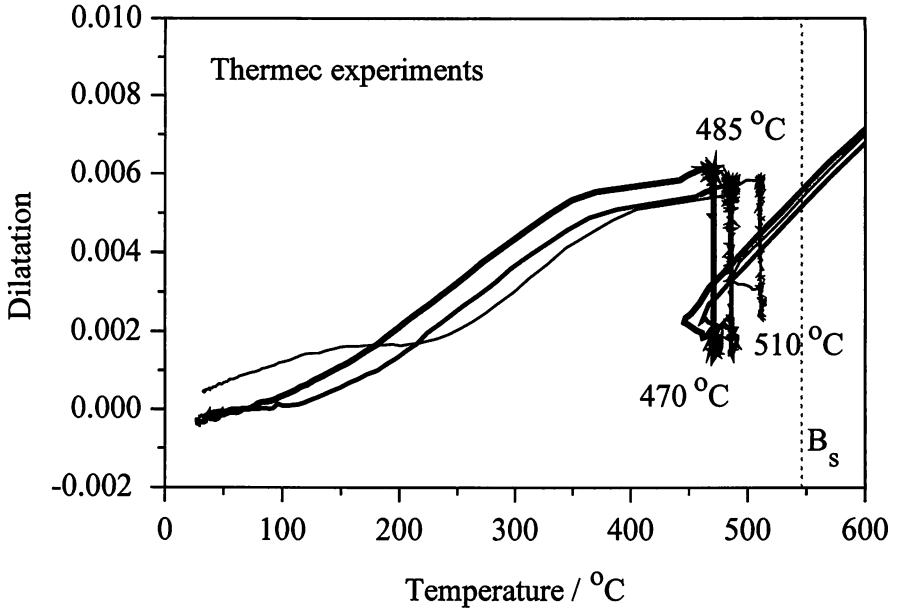

Fig. 5.11: Variation of the dilatometric signal before, during and after isothermal heat treatments carried out on THERMEC on alloy A. The samples were austenitised at 1050°C.

Figures 5.11 and 5.12 show that a 'bump' for martensite is only observed on the curve for the THERMEC test at 510°C with a significant decrease in M_s from the thermodynamic value calculated to be 420°C. All the curves show a decrease in slope as the fraction of residual austenite in the microstructure decreases with temperature.

On Figures 5.13 and 5.14, which correspond to the case of Figure 5.10.b, the dilatometric curves were superposed before the start of transformation in order to compare changes in dilatation amplitudes. When the fraction of bainite increases, less martensite forms and the M_s temperature is progressively depressed. This remark about M_s is not verified for the experiment where quenching starts at 500°C (Figure 5.14). It is possible that carbide precipitation leading to less carbon enrichment has taken place.

Carbides were visible on optical micrographs after interrupted quenching experiments at 450°C (Figures 5.8 and 5.9), although not on similar micrographs after isothermal holding for 3 h at 475°C (Figure 5.6) and for 5 min at 525°C (Figure 5.1). This is similarly evident on the microstructures shown in Figure 5.15. The top micrograph shows bainite without any apparent carbide precipitation at the magnification used after the sample was slowly cooled down and then quenched from 476°C. On the other hand, when the quench took place at 452°C, bainite with precipitates was observed. There might therefore be a transition in bainite morphology seen as a possible way of explaining the difference in kinetics (transformation rate) in the 500 / 450°C bi-isothermal experiment (details to follow).

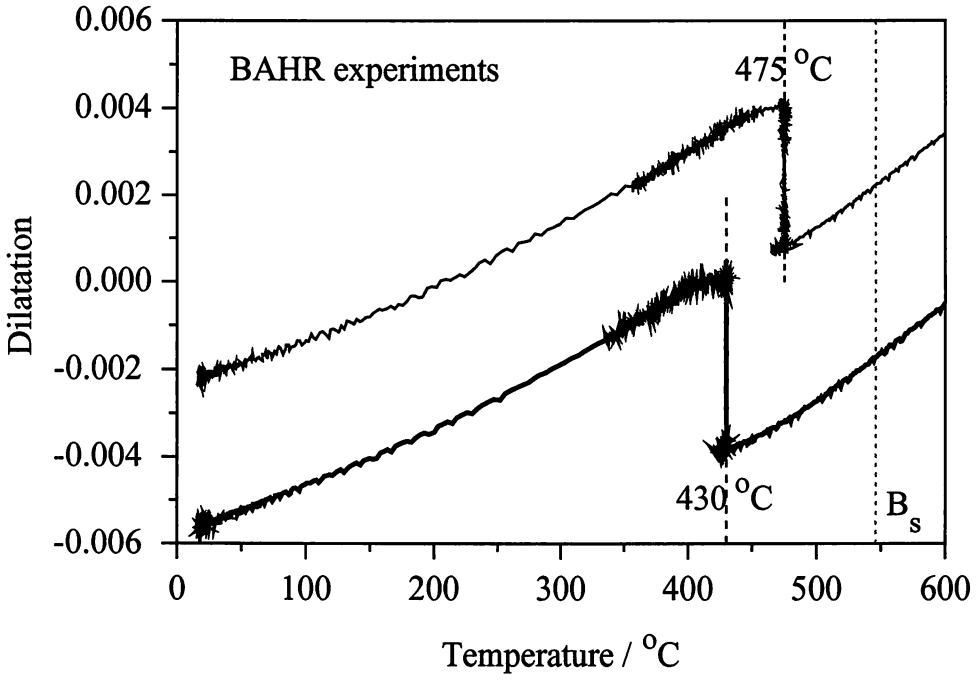

Fig. 5.12: Variation of the dilatometric signal before, during and after isothermal heat treatments carried out on BÄHR on alloy A. The samples were austenitised at 1050°C.

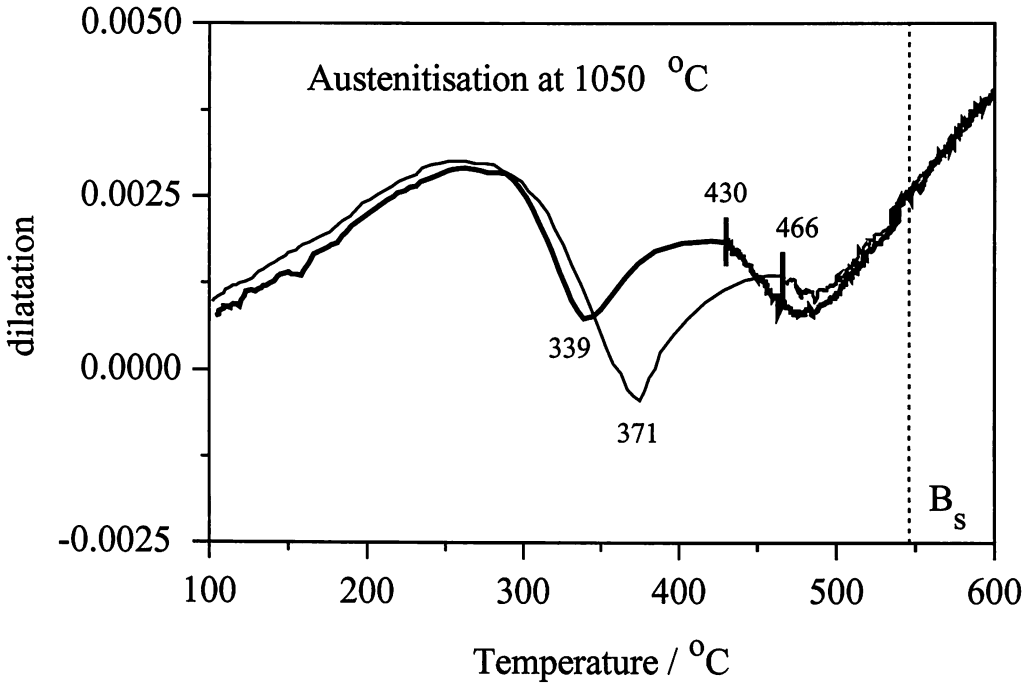

Fig. 5.13: Variation of the dilatometric signal during the following heat treatments using the THERMEC simulator: slow cooling at 2°C s^{-1} above 466 and 430°C followed by quenching. The samples were austenitised at 1050°C.

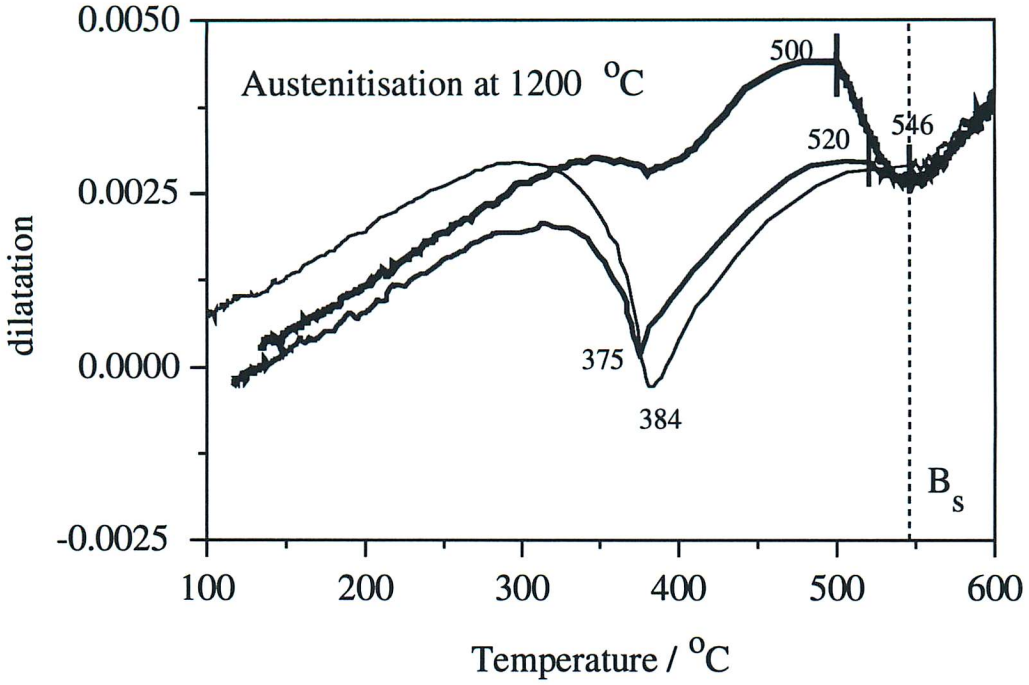

Fig. 5.14: Variation of the dilatometric signal during the following heat treatments using the THERMEC simulator: slow cooling at 2°C s^{-1} above 546, 520 and 500°C followed by quenching. The samples were autenitised at 1200°C.

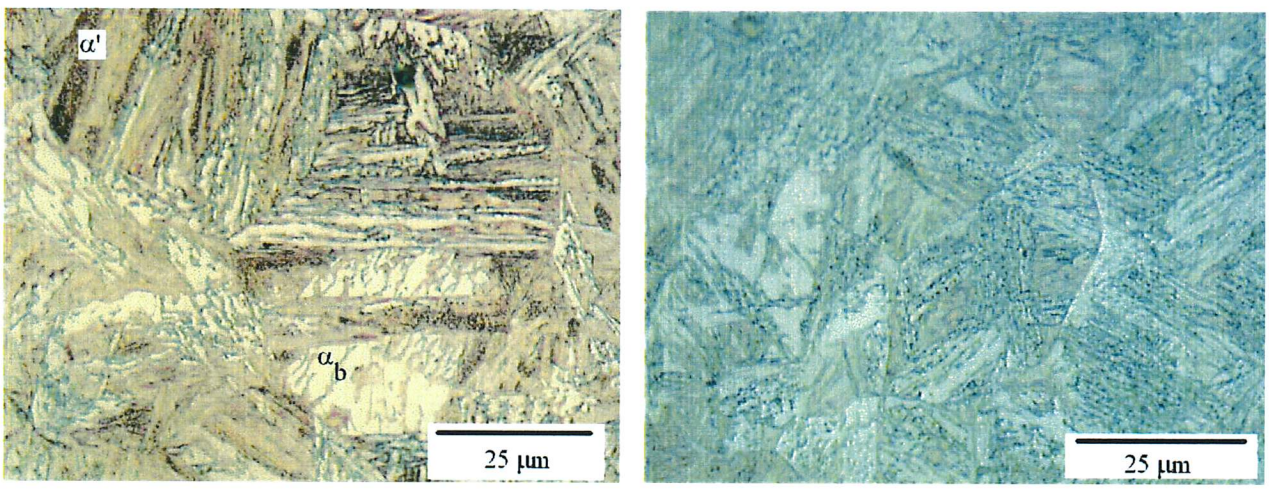

Fig. 5.15: Optical micrographs of alloy A cooled at 2°C s^{-1} above a temperature T_{quench} at which quenching starts. Top micrograph: T_{quench} = 476°C; bottom micrograph: T_{quench} = 452°C. Etched in 3% nital. The samples were austenitised at 1050°C (THERMEC).

5.5 Transmission Electron Microscopy Characterisation (TEM)

Transmission electron microscopy was performed using carbon replicas for the experiments listed in Table 5.3. The aim was to assess whether there is a transition from a microstructure which is mostly carbide-free at high transformation temperatures to one which contains many carbides at lower transformation temperatures.

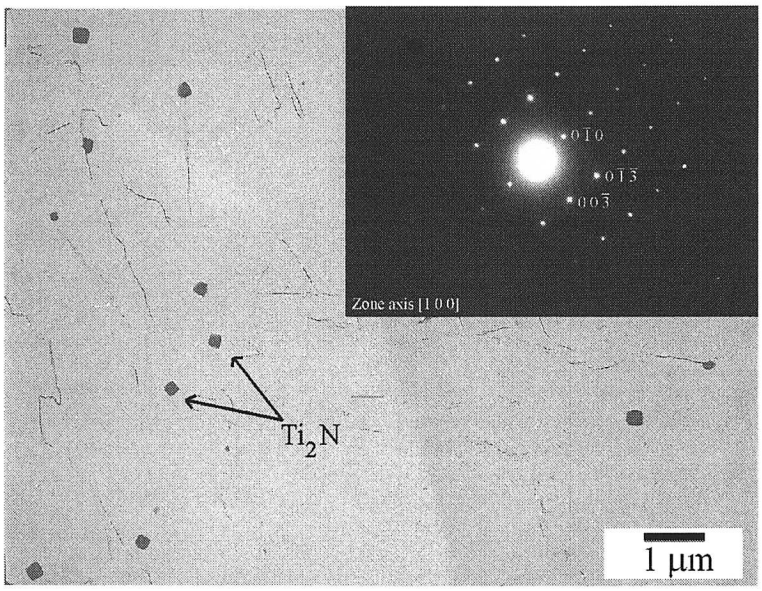

Fig. 5.16: Ti_2N precipitates observed in a carbon replica of alloy A isothermally transformed at 525°C for 5 min. Inset: electron diffraction pattern of one of the Ti_2N precipitates observed.

Experiment type	T_γ°C	Details	Hardness HV 20 kg load	γ_R %	Equipment
Isothermal	1050	525°C for 5 min	366		BÄHR
		475°C for 3 h	310	1	THERMEC
		430°C for 5 min			THERMEC

Table 5.3: Summary of isothermal heat treatments in Alloy A which were chosen for TEM characterisation and associated values of hardness and retained austenite content (where available).

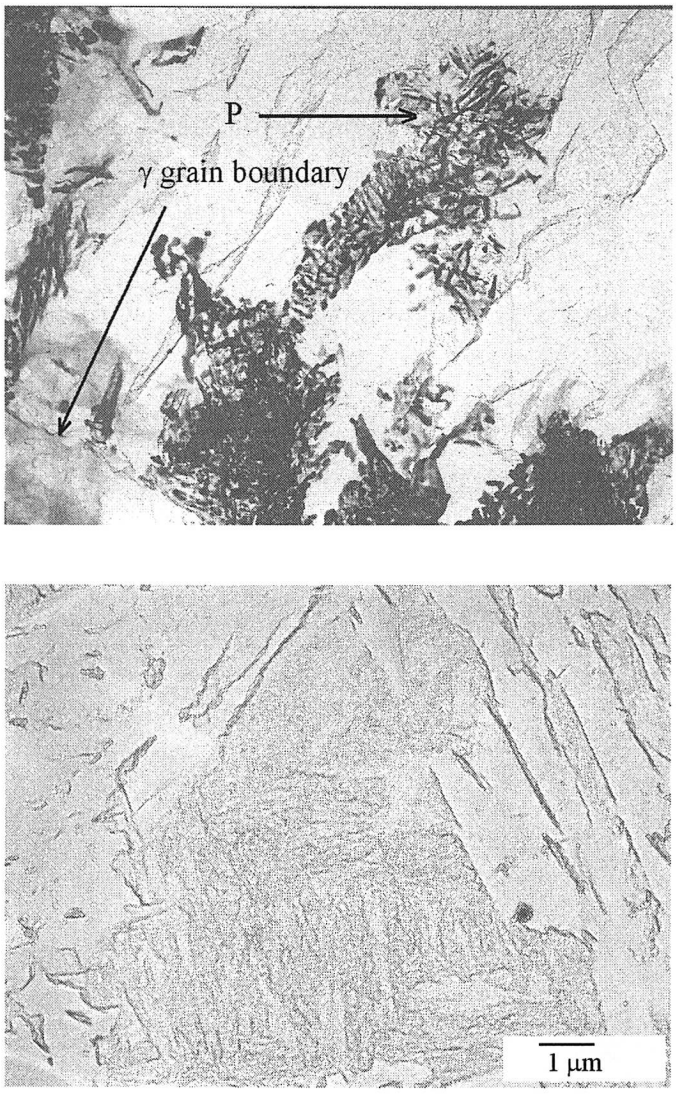

Fig. 5.17: TEM micrographs of a carbon replica from a sample of alloy A isothermally transformed at 475°C for 3 h. Top: colonies of pearlite developing near an austenite grain boundary. Bottom: martensite and bainite regions.

5.5.a Sample Transformed at 525° C for 5 min

Only one type of precipitate was found in alloy A transformed at 525°C for 5 min. The precipitates of Ti_2N were of cubic shape and irregularly dispersed in the microstructure (Figure 5.16). There was no evidence of carbides.

5.5.b Sample Transformed at 475° C for 3 h

Similarly, carbides were not observed in the sample transformed at 475°C for 3 h. The long heat-treatment enabled the formation of pearlite near the austenite grain boundaries (Figure 5.17). The bottom micrograph of Figure 5.17 shows a martensitic area between regions of bainitic ferrite, away from grain boundaries.

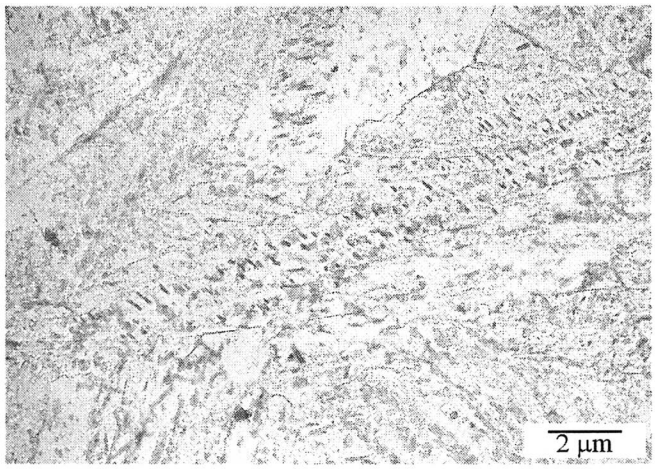

Fig. 5.18: TEM micrograph of a carbon replica from a sample of alloy A isothermally transformed at 430°C for 5 min showing carbides that are all similarly oriented in the centre of the picture.

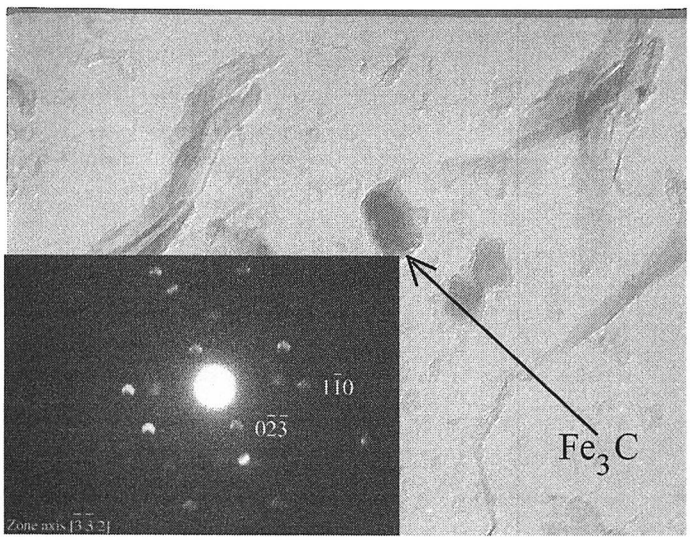

Fig. 5.19: TEM micrograph of a carbon replica from a sample of alloy A isothermally transformed at 430°C for 5 min showing a Fe_3C precipitate. Inset: electron diffraction pattern of this precipitate.

5.5.c Sample Transformed at 430° C for 5 min

On the sample transformed at 430°C for 5 min, many carbides were observed in the bainitic regions, mostly aligned (Figure 5.18), confirming the optical observations made in previous sections. Although lower bainite is unlikely to form in this alloy, the observations made here are inconclusive as to whether the carbides form between bainitic sub-units or within them. The replica technique makes the observation of carbides easy but there is not enough contrast to distinguish the bainitic sub-units as with thin foils.

A diffraction pattern of one of the precipitates (Figure 5.19) shows it is cementite (Fe_3C).

5.6 Bi-isothermal Experiment

Alloy A was held at 500°C for 100 s before being cooled quickly (in about 2 s) to the lower temperature of 450°C with the THERMEC dilatometer. The experiment was designed as the simplest way of checking whether the reaction is additive. Separate full isothermal treatments at the two temperatures were also carried out for comparison. Figure 5.20.a shows the decrease in dilatation associated with the change in temperature. It is apparent that transformation kinetics are faster at 450°C than at 500°C. The dilatation is effectively plotted only when the temperature reaches 500°C. The test was stopped when the dilatation stabilised at its maximum value.

Figure 5.20.b shows the evolution of the measured bainite fraction in the two isothermal and in the bi-isothermal tests. The origin of time was taken to be as the start of isothermal holding, so the bi-isothermal curve is shifted to the left compared with Figure 5.20.a. It can be seen that it takes a few seconds before the transformation adopts the rate corresponding to 450°C. To analyse data, it is assumed that the transformation is put on hold until the experimental dilatation is found to increase again. In reality, though, the transformation is not interrupted and some of it is hidden behind the dilatation decrease as the temperature is lowered. The maximum fraction will therefore be under-predicted, which is illustrated by the bi-isothermal curve not quite reaching the same extent of transformation as the test entirely carried out at 450°C.

Figure 5.20.c is the same as Figure 5.20.b but smoothing of the curves was done 6 times. The curves were smoothed by replacing each point by the average value corresponding to 3 points: the point itself as well as the points situated immediately before and after it. Unfortunately, the smoothing algorithm always gets rid of a few points at the beginning of transformation, which explains why early portions of the curves have disappeared.

In Chapter 3, the following equation was introduced as a condition for additivity:

$$\frac{dX}{dt} = h(T)/j(X) \tag{5.2}$$

where X is the transformed fraction and h and j are separate functions of the temperature and fraction respectively. It follows that if $\frac{dX}{dt}$, the transformation rate, is plotted versus X for two isothermal heat treatments on the same alloy, the shape of the curves should be similar, and corresponding to the function h for the reaction to be additive.

This implies that for a bi-isothermal experiment, the reaction rate must quickly adapt to the new temperature and become the same as if all the reaction had taken place at that

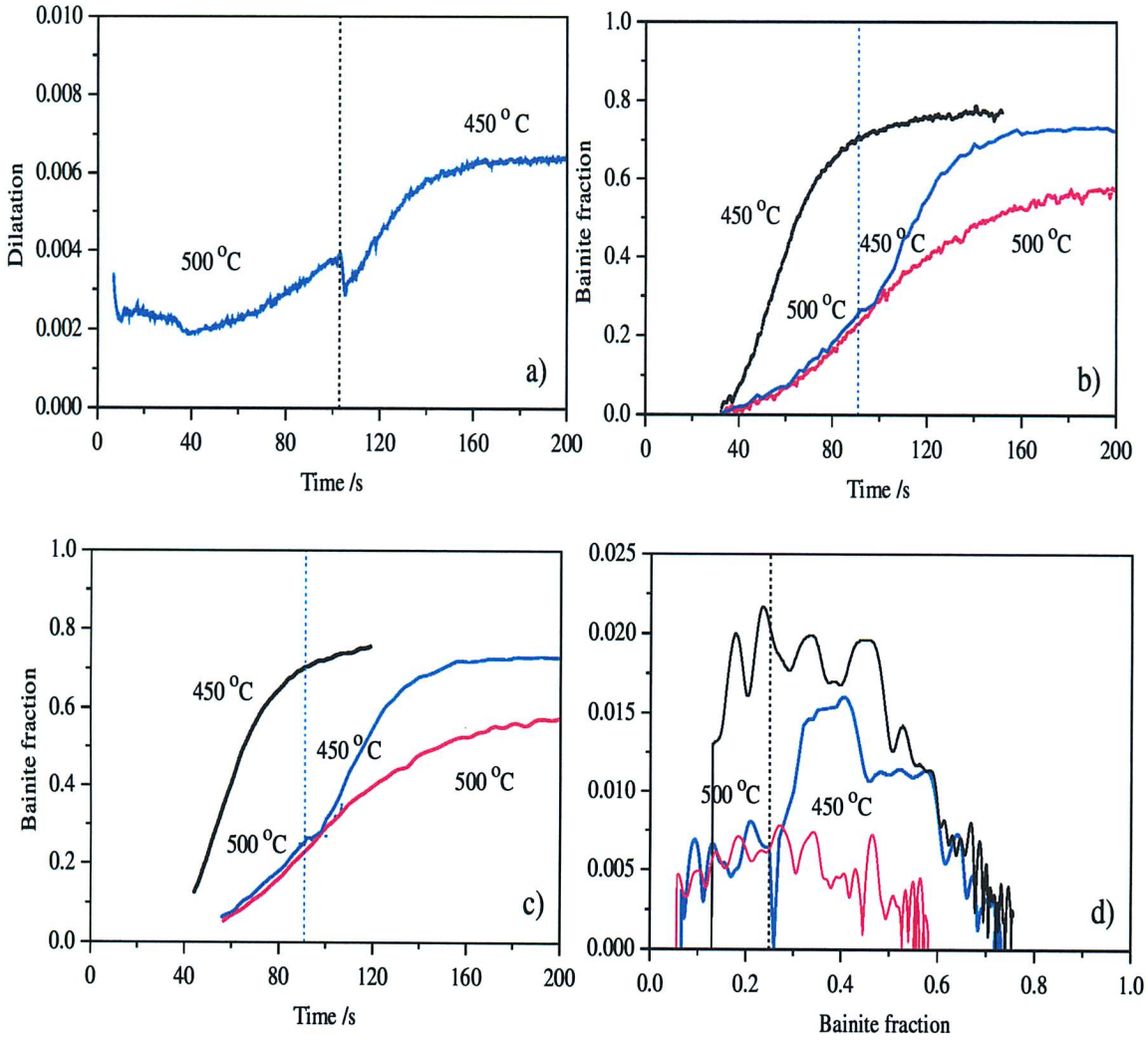

Fig. 5.20: a) Variation of the dilatation for the bi-isothermal experiment on alloy A (THERMEC). The plot starts once the temperature becomes lower than 500°C. b) Evolution of the experimental bainite volume fraction determined from isothermal data (THERMEC) for alloy A with 26 μm γ grain size (austenitised at 1050°C) at 500°C (red curve) and 450°C (black curve) as well as for the bi-isothermal experiment (blue curve). c) Similar curves to b) but they were smoothed 6 times. d) Variation of the experimental transformation rate as a function of the transformed bainite fraction. The curves were also smoothed 6 times.

temperature. This is clearly what happens in Figure 5.20.d, and which can also be seen on Figures 5.20.b and 5.20.c. Therefore, the bainite reaction is additive in alloy A.

5.7 Cooling Experiments

5.7.a Continuous Cooling

With the small value of d_γ, only one constant cooling rate, namely 1°C s^{-1}, was found capable of producing a bainitic microstructure. The experimental bainite fractions associated with two separate tests (showing the reproducibility for two different samples) are plotted on Figure 5.21.

Once the bulk of the transformation has taken place, the fraction becomes stabilised to a plateau value. The method described in Chapter 4 for the determination of the experimental fraction can only be used for bainite; it is not valid for martensite which inherits the carbon content of the austenite. Some transformation to martensite is expected to take place, leaving only a small fraction of retained austenite (compatible with experimental measurements), especially because the presence of carbides removes most of the carbon necessary to stabilise austenite with respect to martensite down to ambient temperature. A method to measure the fraction of martensite formed from experimental dilatation data is introduced in Chapter 8.

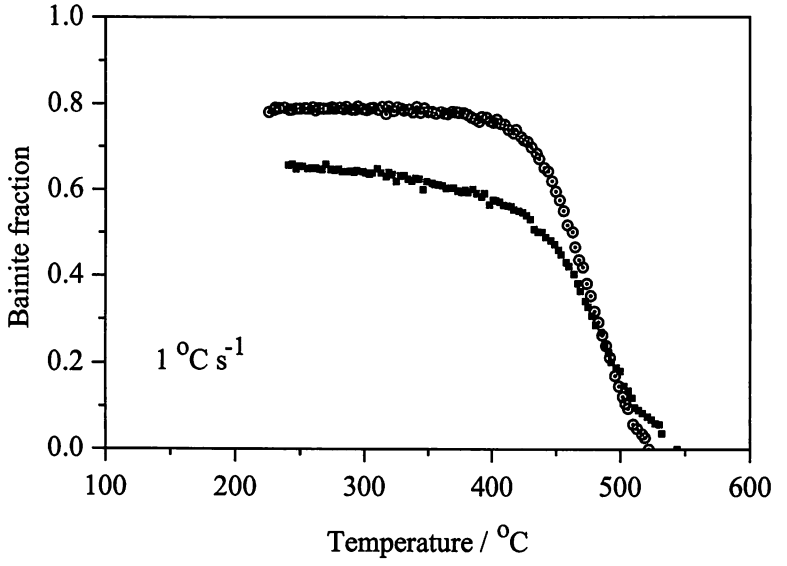

Fig. 5.21: Experimental continuous cooling transformation data for alloy A with 26 μm γ grain size (austenitised at 1050°C) cooled at 1°C s^{-1} (THERMEC).

5.7.b Bi-slope Experiments

Bi-slope experiments, the principle and the advantages of which were explained in Chapter 4, were carried out in order to obtain other bainite transformation data. Such data are plotted on Figure 5.22. Whatever the conditions used, the slopes of the curves are quite similar, so

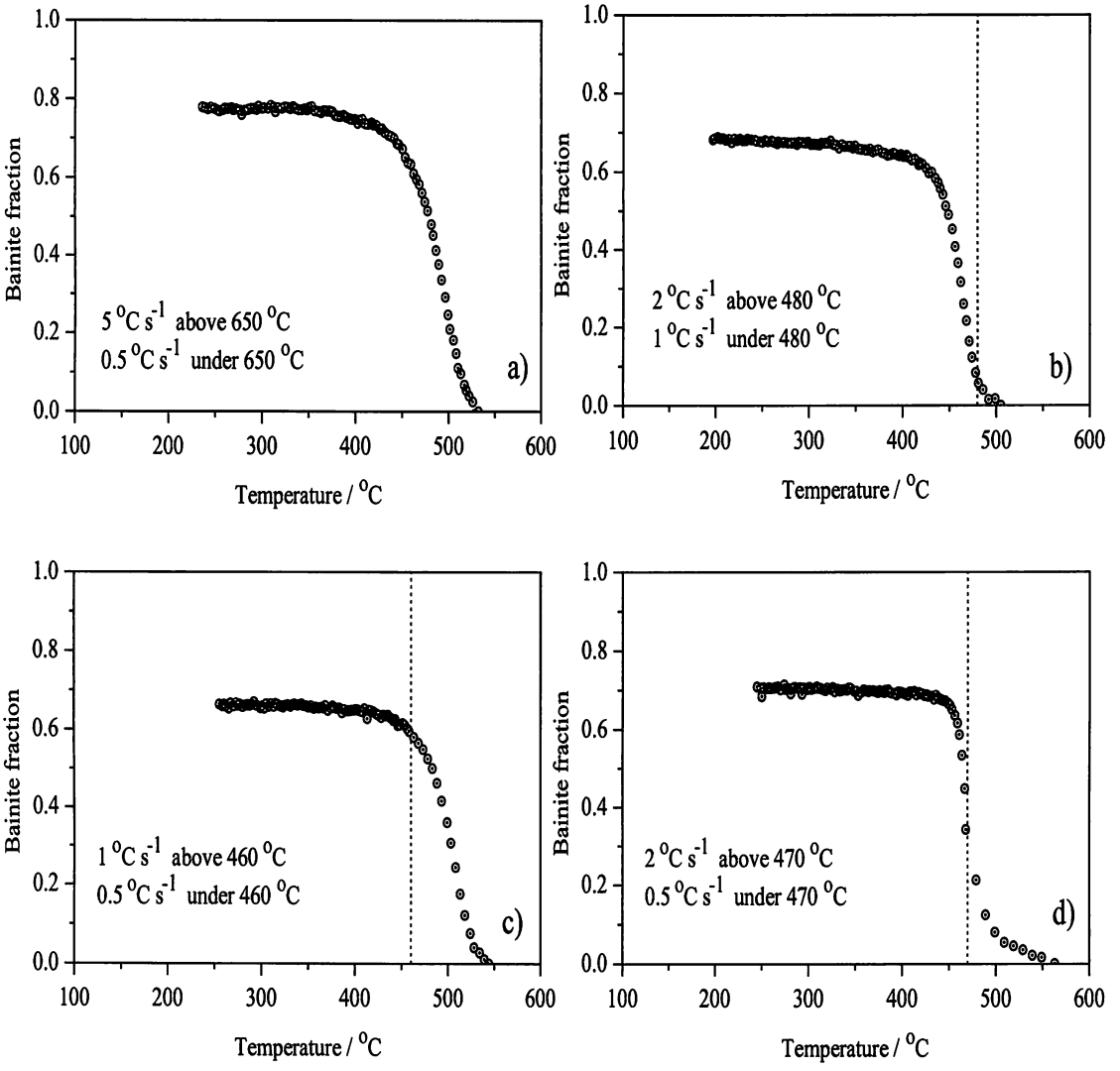

Fig. 5.22: Bi-slope transformation data for alloy A with 26 μm γ grain size (austenitised at 1050°C) cooled at: a) 5°C s^{-1} above 650°C and 0.5°C s^{-1} under 650°C; b) cooled at 2°C s^{-1} above 480°C and 1°C s^{-1} under 480°C; c) cooled at 1°C s^{-1} above 460°C and 0.5°C s^{-1} under 460°C; d) cooled at 2°C s^{-1} above 470°C and 0.5°C s^{-1} under 470°C.

are the final bainite volume fractions, between 0.66 and 0.78. The temperature at which the cooling rate is changed is represented in each case by a vertical dotted line.

It can be seen that depending on the cooling rate used, the transformation-start temperature varies from about 500 to 565°C, although the same sample was used to produce the results of Figures 5.22.b to 5.22.d. This is again a reproducibility issue, as in all cases the majority of the reaction took place between 500 and 450°C.

5.8 Retained Austenite

The 'Rabinovitch' etchant was used to reveal retained austenite γ_R. Bainite and martensite cannot be distinguished as they etch with the same blue or brown contrast. Figure 5.23 shows a micrograph of alloy A cooled at 2°C s^{-1} above 500°C and then quenched, where the amount of retained austenite was found by the sigmametry method to be 9%. The micrograph seems to be in approximate agreement with that value.

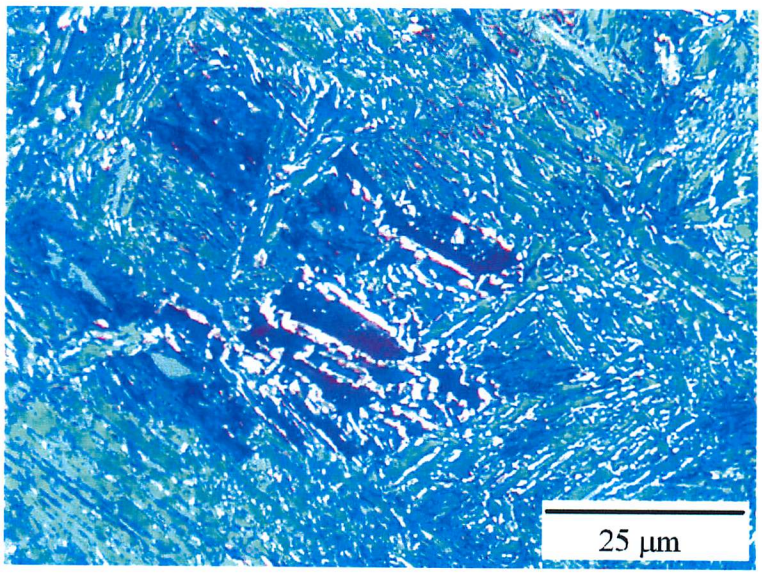

Fig. 5.23: Optical micrograph of alloy A cooled at 2°C s^{-1} above 500°C and then quenched (THERMEC). The Rabinovitch etching method reveals retained austenite in white.

The analysis of other sigmametry results compiled in Appendix 1 (Tables 1 and 2) leads to the following interpretation:

- The bi-slope experiments show that with increasing bainite fractions in the early stages of transformation and at high enough temperatures, the lack of carbide precipitation leads to a greater volume fraction of retained austenite.
- Isothermal transformation data with the large austenite grain size show that at low isothermal transformation temperatures, where many carbides are formed, there is a decrease in the amount of retained austenite down to zero for 450 and 425°C. This is because the formation of carbides prevents carbon from enriching the austenite.

However, caution must be applied in analysing the sigmametric data, as there are not enough measurements to be totally confident about the trends. Water-quenched martensitic samples were found by this method to be totally free of retained austenite.

5.9 Conclusions

Alloy A was chosen for study because of its commercial importance and the fact that the kinetics and limiting bainite fractions are markedly influenced by the isothermal transformation temperature. Carbides form in the alloy at low temperatures despite its low carbon content, which makes it very easy to observe the sheaves of bainite in individual grains. The presence of carbides removes carbon from the residual austenite, making it less stable and more likely to transform into martensite. This is echoed by two observations: the increase in martensite-start temperature for high fractions of bainite and also the decrease in the amount of retained austenite observed by sigmametry. Carbides are absent from the microstructures obtained by transformation at higher temperatures. When carbides are present, it is not clear which form of bainite they accompany, upper or lower bainite. Lower bainite seems unlikely with the relatively low carbon content of alloy A.

Experiments with the large austenite grain size of 166 μm, although they produce microstructures that are mostly bainitic, were discarded because of the prior formation of allotriomorphic ferrite and Widmanstätten ferrite.

It was demonstrated that alloy A complies with the additivity rule.

The following chapter will show how predictions made by the physical model compare to the experimental kinetics. The emphasis will be on the predictions of anisothermal kinetics using model constants derived from the corresponding isothermal experimental data.

Chapter 6

Model Predictions for Alloy A

6.1 Introduction

There were two primary aims to this work. The first was to demonstrate that with a suitable choice of the four adjustable constants in the equation representing the kinetics of the bainite reaction, it is possible to reproduce accurately the measured isothermal transformation data.

The second objective was to use these very same constants derived from the isothermal data, in combination with the model, to attempt a prediction of anisothermal transformation data.

6.2 Determination of Fitting Constants

6.2.a Using the Singh and Bhadeshia Model

An experimental database containing the bainite volume fraction v, maximum volume fraction θ_b, temperature T, time t, grain size d_γ and average carbon content $\bar{x}$ for all isothermal transformation data was assembled. The origin of time was chosen as that at which the isothermal transformation temperature is reached. For each experiment, 99 points separated by the same time interval were selected according to the procedure described on Figure 4.12. Points before the time where a detectable amount of transformation is measured, *i.e.* during the delay time were given a bainite fraction equal to zero.

In addition to these measured data, the database also included the calculated values of the driving force ΔG_m, the bainite plate-thickness a_b and the maximum bainite volume fraction θ_b defined by the T_0' criterion. Then, an iterative process was carried out. Starting with arbitrarily chosen values of the fitting constants, the constants were progressively modified in order to minimise an error represented by $\sum[v_p - v_m]^2$, where v_p and v_m denote the predicted and measured bainite fractions respectively. Such a method gives equal weight to all the points, as opposed for example to $\sum[\frac{v_p - v_m}{v_m}]^2$ which gives undue importance to points for small fractions.

Sets of constant for the isothermal experiments on alloy A on the two equipments were determined and are listed on the first two lines of Table 6.1. The physical model developed by Singh and Bhadeshia [1998a, equation 2.50] was used for the calculation of v_p.

Alloy	Set of Constants	B_6', m^{-2}	B_4, $J\,mol^{-1}$	λ_1	λ_2	Opt. Error
A	isothermal THERMEC	7.156×10^{-16}	1.510×10^{5}	8.479	0	34.31
A	isothermal BAHR	2.420×10^{-19}	1.006×10^{5}	2.793	0	3.31

Table 6.1: Individual constants for alloy A using the Singh and Bhadeshia model.

In this model, B_6' is the constant allowing the nucleation rate to vary with d_γ, the two quantities being inversely proportional to each other (equations 2.44 and 2.51). B_4 is used in the expression of the proportionality between the activation energy for nucleation G^* and the driving force as follows from equation 2.31:

$$G^* = B_4\left\{1 + \frac{\Delta G_m}{B_2}\right\}$$

Finally, λ_1 and λ_2 are factors describing the autocatalysis phenomenon. β, the autocatalysis factor varies with the mean carbon molar fraction of the alloy (equation 2.36):

$$\beta = \lambda_1(1 - \lambda_2\bar{x})$$

When fitting constants are determined for one alloy in isolation, the value of λ_2 must be set to zero since there is no $\bar{x}$ dependence.

The THERMEC tests database originally contained experimental data for the small austenite grain size (austenitisation at 1050°C) and for the large austenite grain size (austenitisation at 1200°C). It was shown in Chapter 5 that the large grain size data should not be used, because of the formation of austenite grain-boundary phases before bainite starts to form. The search for constants was therefore restricted only to the data associated with the small austenite grain size. Using these constants, the predicted curves represented by the solid green lines on Figure 6.1 were obtained. Although the maximum bainite fractions agree well, it is clear that the Singh and Bhadeshia model cannot reproduce experimental curves properly.

The start of the calculated curves is always too abrupt, which means that to minimise the error, the subsequent kinetics are notably slower than the measured ones.

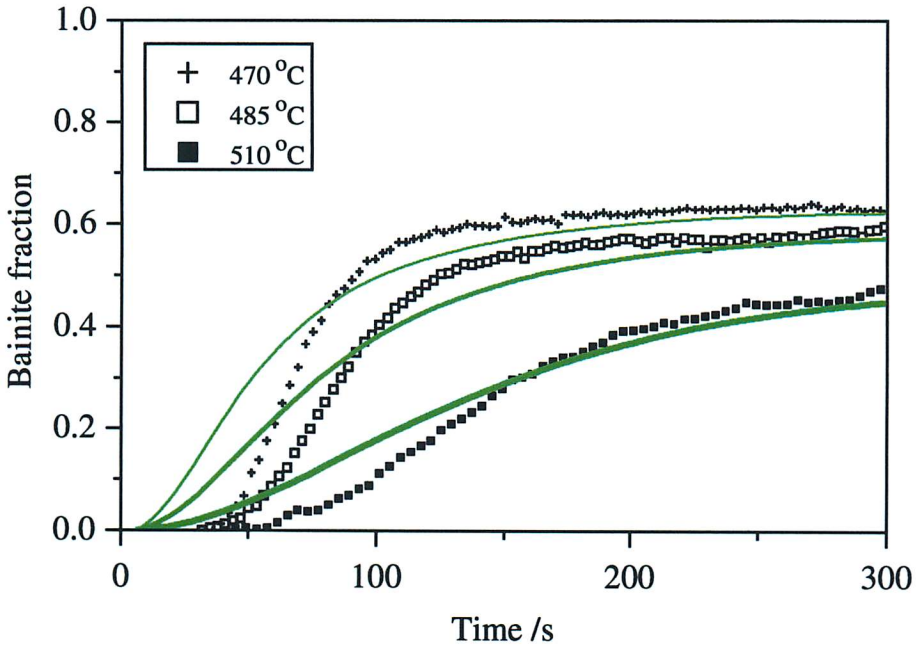

Fig. 6.1: Isothermal transformation data (THERMEC) for alloy A with 26 μm γ grain size (austenitised at 1050°C) at various temperatures compared with predictions (green curves) using constants fitted on the same data, *i.e.* on the first line of Table 6.1. and with the origin of time as the time when the isothermal temperature is attained.

Figure 6.2 shows that the Singh and Bhadeshia model is not flexible enough to take into account the delay time. When the constants are fitted only on experimental data such that $v_m < 0.1$, the start of the predicted 485°C curve is in accordance with the experiment but the subsequent kinetics are far too slow (dotted curve). Many attempts to find appropriate constants other than best fit values failed to reproduce the essential features of the experimental curves.

6.2.b Back to Autocatalysis as Modelled by Rees and Bhadeshia

The modifications made by Singh and Bhadeshia to the previously developed Rees and Bhadeshia model aimed to obtain more realistic values of the autocatalysis factor β. Indeed, they found values of λ_1 comprised roughly between 1.5 and 5 (Table 2.3) compared to the values of λ_1 found by Rees and Bhadeshia that could in some cases be two orders of magnitude larger (Table 2.2). It seems more probable that 2, 3 or 4 plates can nucleate next to an existing one by autocatalysis than 200!

However, an estimation of the term $\beta\tau\nu \exp(-\frac{G^*}{RT})$ shows that this term is 10 to 15 orders of magnitude larger than unity, as the value of $\nu = \frac{kT}{h}$ is equal to 1.55×10^{13} for a temperature

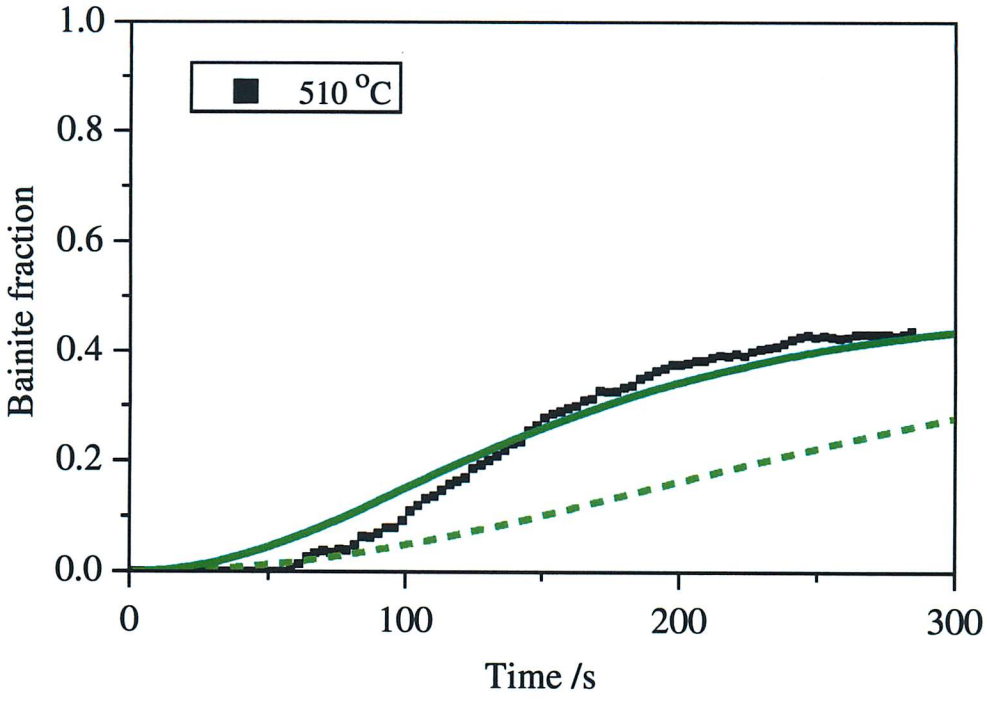

Fig. 6.2: Isothermal transformation data (THERMEC) for alloy A with 26 μm γ grain size (austenitised at 1050°C) at 510°C compared with predictions (green curves) using constants arbitrarily chosen to try and provide a good fit.

T equal to 470°C. Therefore, in the Singh and Bhadeshia model the initial nucleation rate is increased by 10 to 15 orders of magnitude due to autocatalysis only!!! This is clearly not physically possible.

The Singh and Bhadeshia model was kept, with the exception of autocatalysis for which βv replaced $\beta \tau \nu \exp(-\frac{G^*}{RT})$ in equations 2.49 and 2.50 as in equation 2.33. Constants derived by the same procedure as before but with this modification were determined for each set of experiments on each alloy. The values of the new constants for alloy A are listed in Table 6.2. It was demonstrated by fitting constants on the single THERMEC test at 485°C, that this model is indeed capable of reproducing a measured transformation curve, even when there is a large delay time (Figure 6.3). **The Singh and Bhadeshia model with the autocatalysis concept of Rees and Bhadeshia was therefore used in this work.**

A comparison of Tables 2.2 and 6.2 show that the values of λ_1 found in this study are similar to those previously determined. Although, a 'reasonable' value of 2.27 is found for the BAHR tests, larger values of λ_1 for the THERMEC tests are counterbalanced by lower values of the constant B_6' which also intervenes in the expression of the nucleation rate I_b. Therefore, it can be argued that it is a combination of the two, and not only λ_1, that represents autocatalysis.

Alloy	Set of Constants	B_6', m^{-2}	B_4, $J\,mol^{-1}$	λ_1	λ_2	Error
A	THERMEC, austenitisation at 1050	8.585×10^{-9}	1.377×10^5	202.35	0	0.061
A	BAHR, austenitisation at 1050	7.708×10^{-8}	1.351×10^5	2.27	0	0.063
A	combined data	1.444×10^{-8}	1.285×10^5	26.82	0	0.764

Table 6.2: Values of the constants for the modified Singh and Bhadeshia model fitted on isothermal transformation data for alloy A.

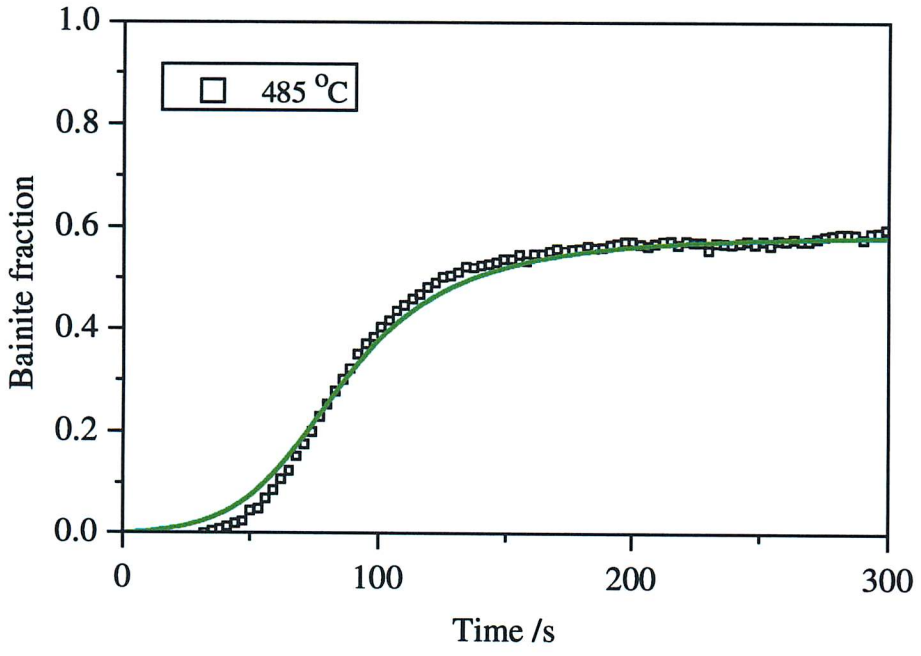

Fig. 6.3: Isothermal transformation data (THERMEC) for alloy A with 26 μm γ grain size (austenitised at 1050°C) at 485°C compared with predictions (green curves) using constants fitted on the same unique experiment.

6.3 Isothermal Transformation

The predicted kinetics for isothermal transformation at 470, 485, and 510°C using the modified model are plotted as the green curves on Figure 6.4.a (THERMEC tests). The thicker the green line, the lower the transformation temperature. This convention will be kept throughout the work. The predictions successfully reproduce the delay time and the slow start of reaction.

For the BAHR tests (Figure 6.4.b), higher maximum fractions are obtained than during the experiments.

Using predictions results of Figures 6.4.a and 6.4.b, the section of the predicted *TTT* diagram of alloy A corresponding to bainite was plotted in a similar way as in Figure 5.5 (Figure

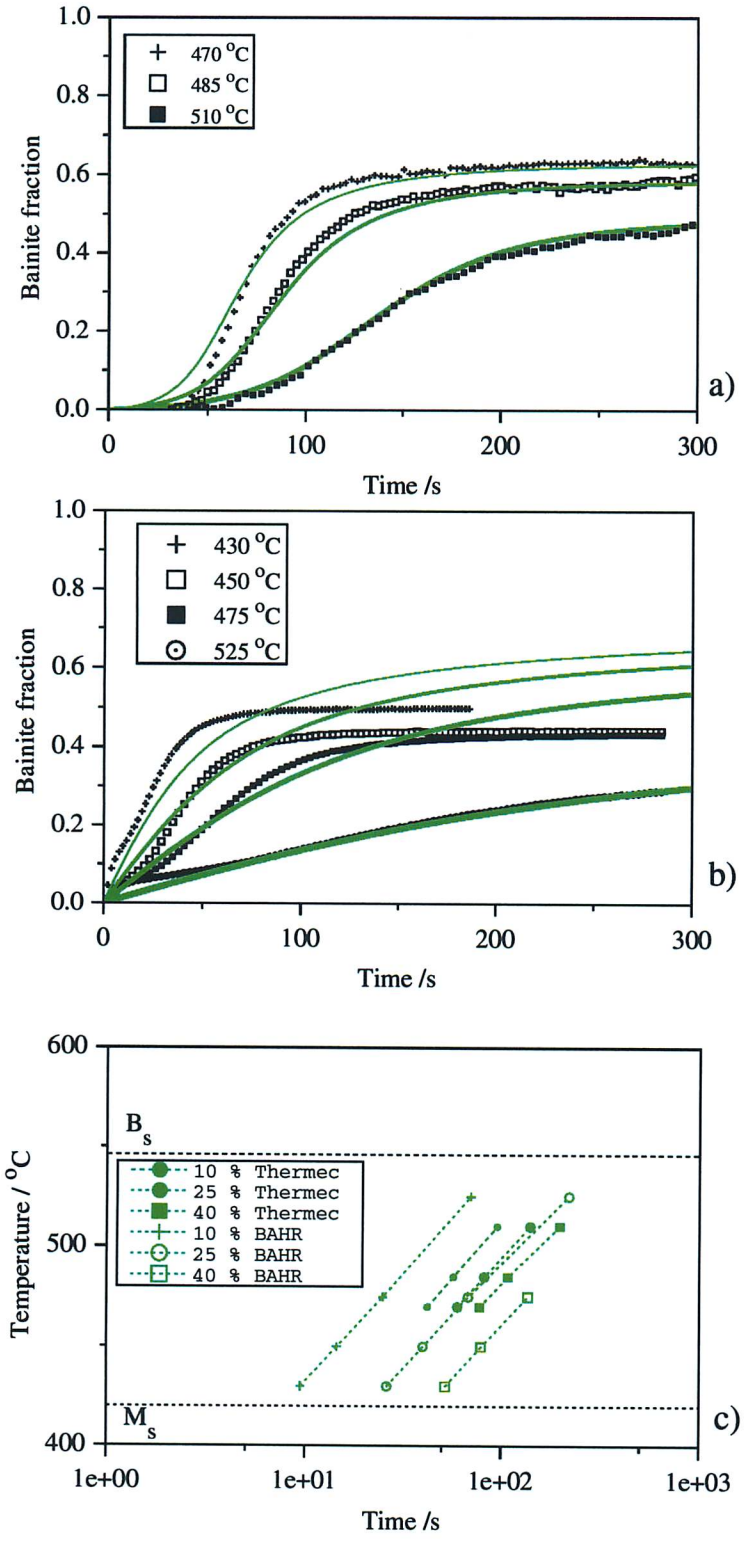

Fig. 6.4: Isothermal transformation data for alloy A with 26 μm γ grain size (austenitised at 1050°C) at various temperatures compared with predictions (green curves) using constants fitted on the same data. a) THERMEC tests; b) BÄHR tests; c) Predicted TTT diagram of alloy A obtained with BAHR and THERMEC fitting constants with a logarithmic time scale.

6.4.c). The lines corresponding to the THERMEC and BÄHR experiments have similar slopes, indicating a similar dependency of kinetics with respect to the transformation temperature. The lines linking all the points for 10, 25 and 40 % transformed are parallel in this logarithmic plot, indicating that the predictions follow sigmoidal curves by which the transformed fraction can be expressed as a function of the logarithm of time.

Table 6.3 summarises the above discussion. A positive value of 'difference' means that the predicted maximum fraction is larger than the experimental one. The agreement in maximum fractions is much better for THERMEC experiments.

Transformation temperature (°C)	**Equipment**	**Measured** θ_b	**Calculated** θ_b	**Difference**
510	THERMEC	0.44	0.45	0.01
485	THERMEC	0.56	0.57	0.01
470	THERMEC	0.63	0.62	-0.01
525	BAÄHR	0.29	0.39	0.10
475	BAÄHR	0.43	0.61	0.18
450	BAÄHR	0.44	0.67	0.23
430	BAÄHR	0.50	0.70	0.20

Table 6.3: Summary of measured and calculated values of θ_b in isothermal heat treatments which gave bainite as the main constituent in Alloy A.

Figure 6.5 confirms the fact that for a majority of experiments, the predicted kinetics are slightly slower, *i.e.* the calculated times are larger than the measured ones. This is noticeable on Figure 6.4.b. Only a few points are on the right of the 45-degree line, which means that the faster experimental kinetics have caught up with those predicted.

A knowledge of the measured value of θ_b allows the computation of the carbon content x_γ of enriched austenite at transformation completion using the following relationship:

$$\bar{x} = v\, x_\alpha + v_\gamma\, x_\gamma \tag{6.1}$$

where $\bar{x}$ and x_α are the average alloy carbon concentration and the ferrite carbon content respectively. The value of the latter is assumed to be equal to 0.02 wt%. v and v_γ (or 1 - v) are the bainite and austenite volume fractions respectively. In Figure 6.6, the values of

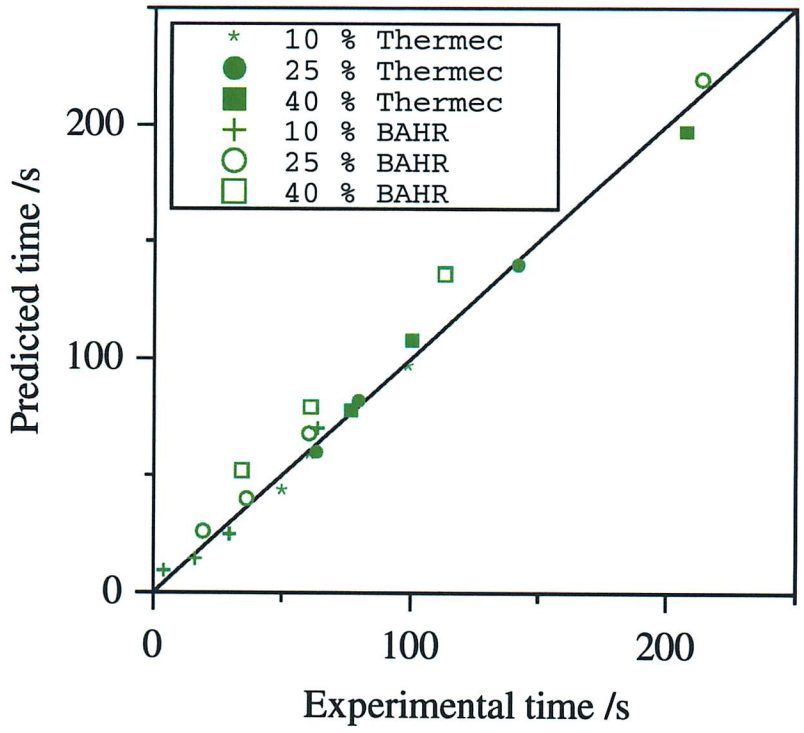

Fig. 6.5: Comparison of the predicted and experimental isothermal transformation times for 10, 25 and 40 % transformed for both sets of experiments (BAHR and THERMEC)

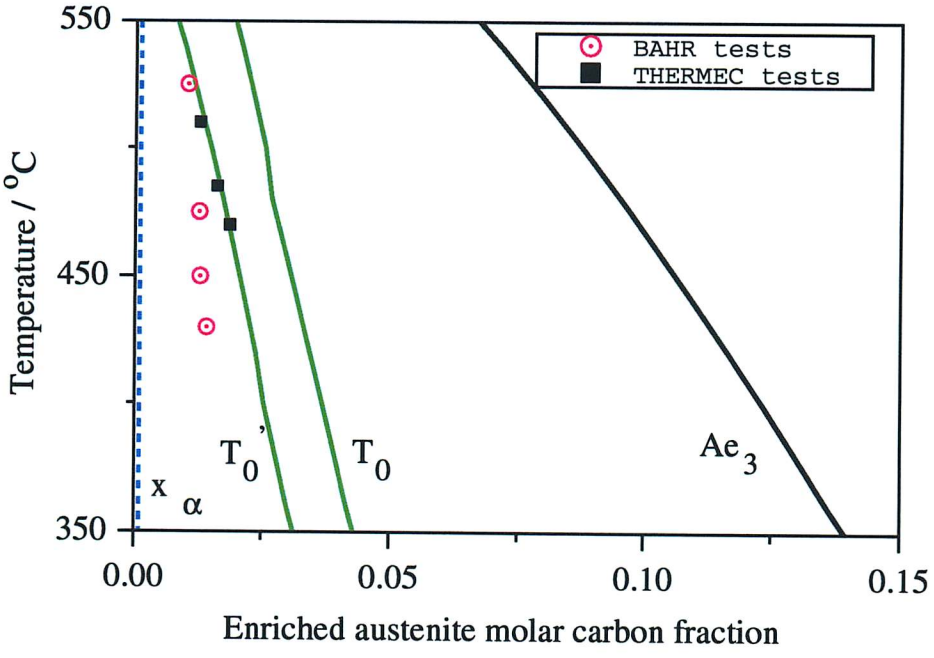

Fig. 6.6: Comparison of the values of enriched austenite carbon content (mole fraction) for the tests carried out with BAHR and THERMEC with the T_0 and T_0' lines calculated with thermodynamic criteria.

x_γ are plotted for comparison against the T_0, T_0' and Ae_3 lines, calculated with the program MAP-STEEL-MUCG46.

The points associated with THERMEC experiments show a very good match with the T_0' line. Points associated with BAHR tests are not following that line, showing a smaller variation of the limiting bainite fraction with temperature and are markedly less than expected. It is important to note that all predictions were made using the T_0' criterion. For this alloy, the choice seems judicious. Using the T_0 criterion would have lead to a vast overestimation of all θ_b values. For isothermal transformation temperatures lower or equal to 450°C, it was shown in Chapter 5 that bainite is accompanied by carbides which have formed as a secondary process. The removal of carbon from residual austenite should allow transformation to progress further than given by the T_0' curve but since the agreement shown in Figure 6.4.b is still reasonable, it must be concluded that the carbides have precipitated in the films of austenite between bainite plates; rather than in the blocky austenite which is available for transformation to bainite.

6.4 Bi-isothermal Transformation

Figure 6.7.a shows the predicted dilatation associated with the bi-isothermal experiment. The prediction was made using the same constants as in the previous section. At the end of the 500°C part, a dilatation almost equal to the one in the experiment was attained, but at a slower rate. The dilatation change associated with the drop in temperature only is predicted very well. At the lower temperature, the predicted kinetics resume at a rate equal to that measured. The agreement with the final dilatation is also very good.

Comparison of predicted and experimental volume fractions was then carried out. The experimental blue curve on Figure 6.7.b was produced using the rigorous method described in Chapter 4 (with $\bar{a}_\alpha$ equal to 2.871×10^{-10}m). With this method, but this time using the predicted dilatation of Figure 6.7.a instead of the experimental dilatation as an input, the dotted green curve in Figure 6.7.b is obtained. It was shown in Chapter 4 that the use of this particular ferrite lattice parameter can lead to an overestimation of the bainite fraction. This can be seen as the solid green line obtained with the physical model gives a lower fraction, the difference being 12 in percentage of volume fraction, value which can be taken as an error bar. The measured θ_b value lies between the two values.

The red and black curves on Figure 6.7.b are the predicted kinetics for the transformations at 500 and 450°C respectively. The predicted bi-isothermal reaction rate adapts readily to the predicted rate at 450°C after the change. This is also clearly visible on Figure 6.7.c.

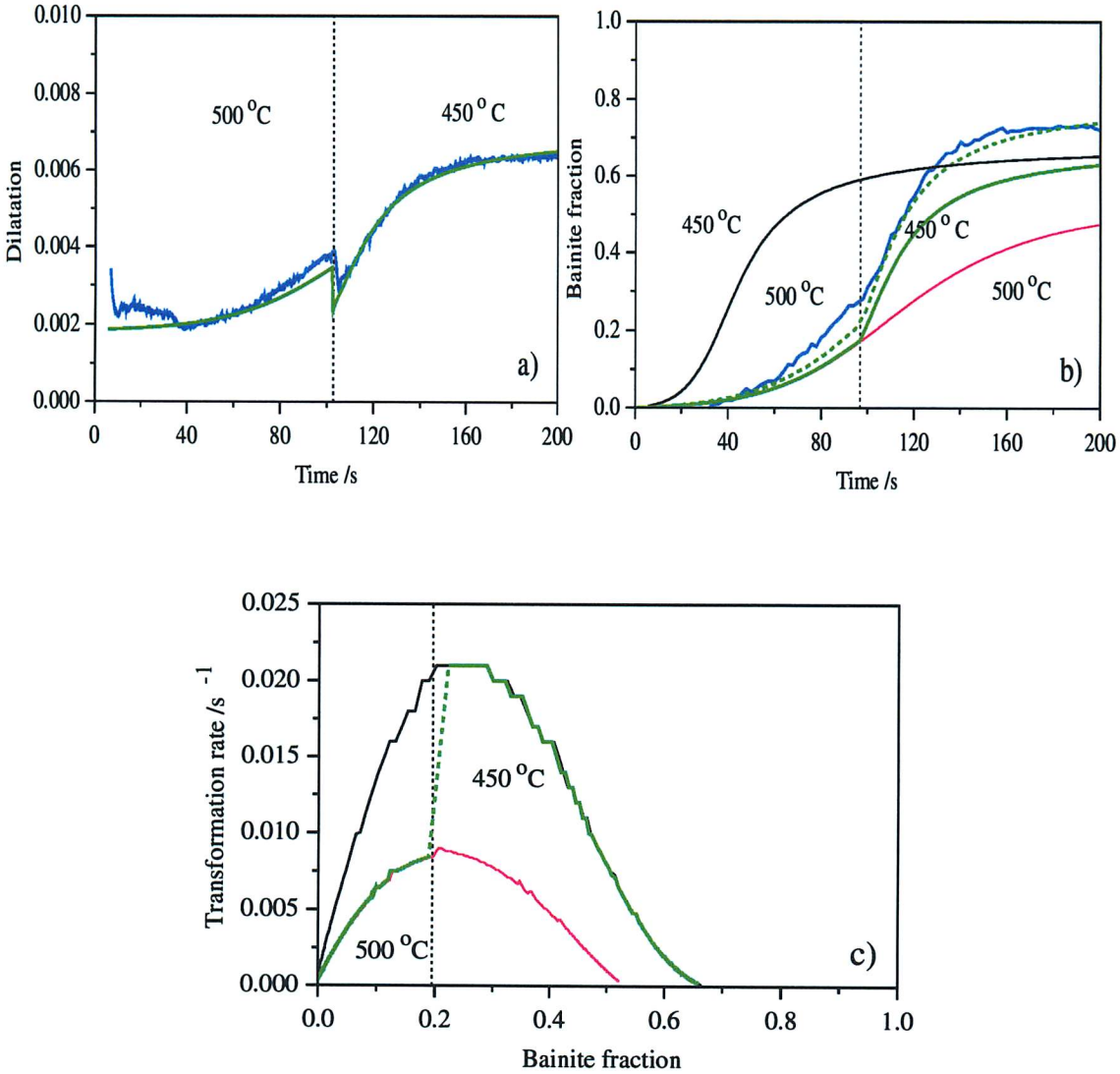

Fig. 6.7: a) Predicted dilatation of alloy A during the bi-isothermal heat-treatment (green curve) compared with the experimental dilatation of the bi-isothermal test (in blue). The predictions use the first line of constants for alloy A in Table 6.2. b) Evolution of the bainite fraction in alloy A during the bi-isothermal heat treatment compared with the predicted volume fractions for the bi-isothermal and isothermal experiments at 500 (red curve) and 450°C (black curve). The dotted green curve is calculated with $\bar{a}_{\alpha}$ equal to 2.871 $\times$ 10^{-10}m using the predicted dilatation, which is itself calculated from the predicted volume with equation 4.4. c) Variation of the predicted transformation rates as a function of the transformed bainite fraction for the isothermal as well as bi-isothermal tests. The same colour code applies throughout.

6.5 Cooling Experiments

Figures 6.8 and 6.9 compare the measured and predicted curves in anisothermal conditions. The solid green curves corresponds to the predictions made using the constants fitted on all the THERMEC and BÄHR isothermal tests ('combined data' in Table 6.2) for alloy A, whereas yellow curves use constants fitted on all the experiments on the three alloys (last line of Table 7.3). They are provided for the purpose of comparison and it will be seen that they generally offer a lesser degree of agreement with experimental data than the green lines so will not be plotted in Chapter 7.

6.5.a Continuous Cooling

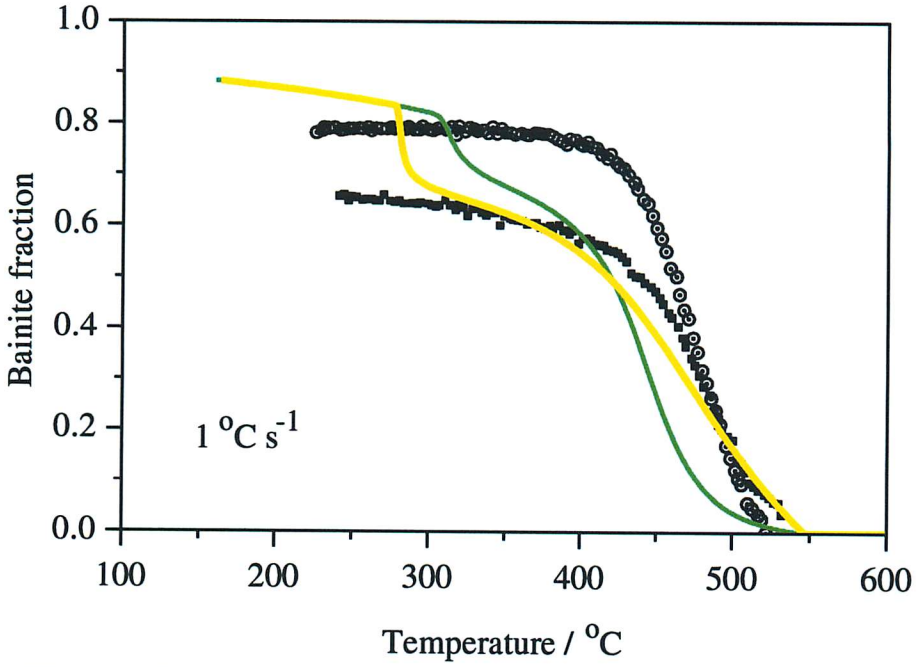

Fig. 6.8: Comparison between the measured and calculated continuous cooling transformation data (THERMEC experiments) for alloy A with 26 μm γ grain size (austenitised at 1050°C) cooled at 1°C s^{-1}.

It can be seen on Figure 6.8 that the slope of the green curve is similar to the slopes of the experimental curves. Therefore, the transformation rate is predicted well. However, there are two main sources of error in the predictions:

(i) The model predicts that transformation starts just under the B_s temperature, which is 546°C for alloy A, but in most cases the early portions of the measured curves are more abrupt. The slow start predicted by the model is not found experimentally.

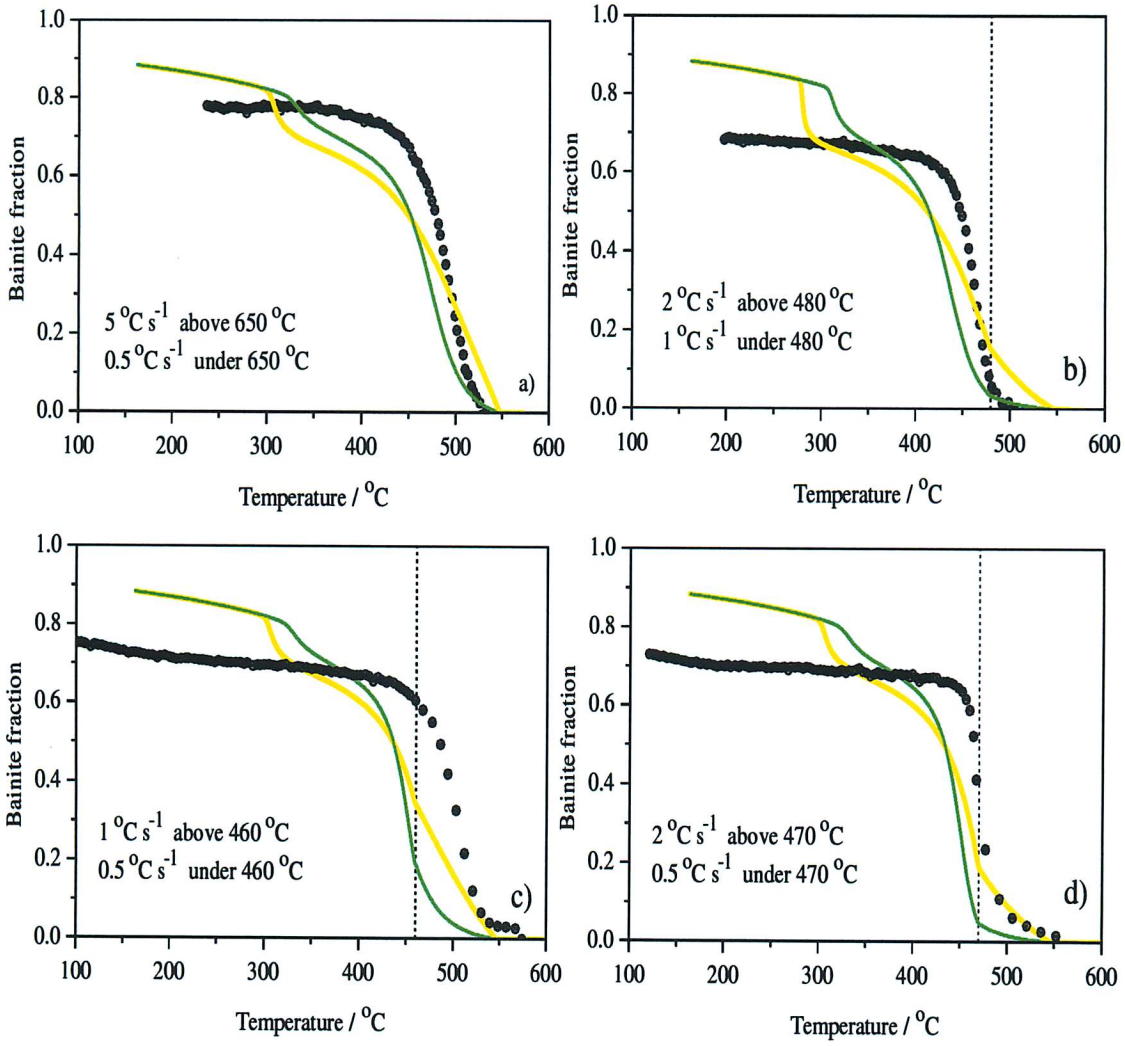

Fig. 6.9: Comparison between the measured and calculated continuous cooling transformation data (THERMEC experiments) for alloy A with 26 μm γ grain size cooled at: a) 5°C s^{-1} above 650°C and 0.5°C s^{-1} under 650°C; b) 2°C s^{-1} above 480°C and 1°C s^{-1} under 480°C; c) 1°C s^{-1} above 460°C and 0.5°C s^{-1} under 460°C; d) 2°C s^{-1} above 470°C and 0.5°C s^{-1} under 470°C.

(ii) The two calculated curves become superposed below around 280°C. This is because below that temperature, with both sets of constants, the value of θ_b is reached at each temperature. There continues to be a slow steady increase of the predicted bainite fraction as temperature decreases to follow values of volume fraction corresponding to the T_0' line (Figure 6.6). The model assumes that austenite carbon enrichment continues until the line is reached. This means that martensite formation is predicted as impossible as the martensite-start temperature of residual austenite is progressively decreased by stabilisation, eventually becoming markedly lower than room temperature. Experimental curves,

however, show that the bainite fraction increases slowly below about 400°Cand martensite was found in almost all the microstructures albeit in small quantities. This is further evidence of the fact that carbides are removing carbon from the austenite, which in turn becomes more prone to martensitic transformation.

6.5.b Bi-slope Experiments

The previous two points are also valid when the comparisons are made between measured and calculated kinetics in bi-slope experiments (Figure 6.9). The measured maximum fractions are all comprised between 0.66 and 0.78. For the reason mentioned above, calculations always overestimate these figures.

A plot similar to the one of Figure 6.5 is reproduced on Figure 6.10. This plot illustrates the fact that the predicted temperature for a given bainite fraction is almost always lower than its experimental counterpart, *i.e.* the points lie on the right of the 45-degree line. Given that the measured and predicted transformation rates are similar, the predicted curves are just shifted by 10 to 50 °C with respect to the measured curves, and the predictions are reasonably good.

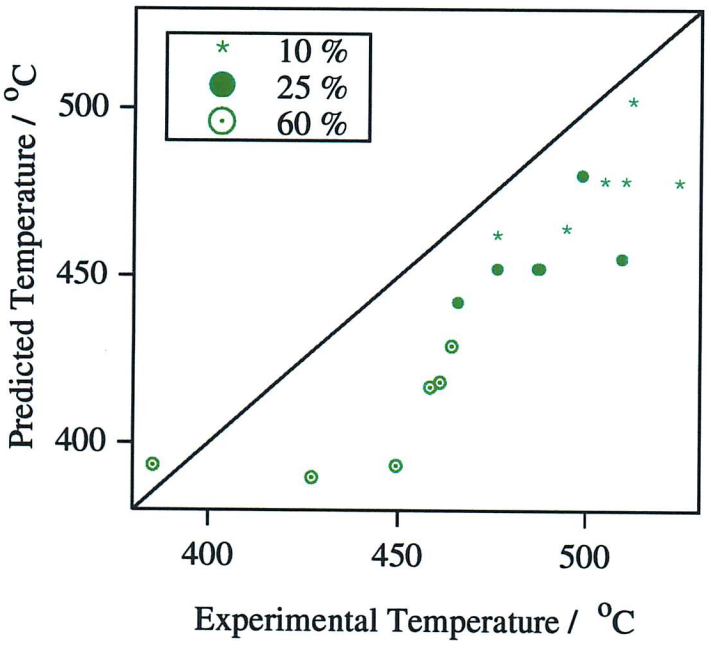

Fig. 6.10: Comparison of the predicted and experimental temperatures for transformed fractions of 10, 25 and 60 % for THERMEC cooling experiments on alloy A.

6.6 Conclusions

It has been demonstrated that theory for isothermal transformation to bainite, together with an economical set of parameters derived from isothermal transformation data, can be used to estimate the anisothermal kinetics reasonably well for a particular steel designated alloy A, apart from a shift in temperature.

Using a simple bi-isothermal test, it has been shown that the additivity principle works for alloy A. This test was particularly meaningful as there is a marked transition in the bainite transformation kinetics between a mode in which no carbides are formed (at high temperatures) and one, at lower temperatures, where carbide precipitation is observed even though the silicon concentration in the alloy is low.

In the presence of carbides, transformation to bainite was expected to reach a higher fraction. Nevertheless, the reasonable agreement with the T_0' line was preserved. It has been proposed that the carbides must have precipitated in the thin films of austenite between bainitic sub-units, rather than in the blocky austenite regions where they would have had greater influence over the overall transformation kinetics.

It has also been demonstrated that the Singh and Bhadeshia model greatly exaggerates the role of autocatalysis, so much so that it becomes impossible to properly represent a sigmoidal curve. The new model therefore incorporates the expression of autocatalysis used in the Rees and Bhadeshia model, which had been discarded by Singh and Bhadeshia.

Chapter 7

Model Predictions for Alloys B and C

7.1 Introduction

The extensive study of the bainite transformation kinetics in Alloy A (Chapters 5 and 6) demonstrated that for that particular alloy, isothermal experiments can be used to estimate non-isothermal transformation kinetics (Figure 6.9).

Similar work, but for alloys B and C is presented in this chapter. These alloys, due to a high level of silicon, can form bainite without cementite. Therefore, residual austenite becomes enriched with carbon as the reaction progresses and hence is stabilised with respect to martensitic transformation. A greater quantity of austenite can then be retained down to ambient temperature, but the enrichment may not be enough to prevent the formation of some martensite. A typical microstructure of this kind is presented on Figure 7.1. Brown-etching plates of hard martensite have formed in austenite islands. When the regions are wide enough, softer martensite with less distinct contours is also formed. The two types of martensite appear on the micrograph of Figure 7.1. Figure 7.2 shows regions of hard martensite highlighted with the Rabinovitch etchant. Martensite and bainite appear in blue or brown contrast, with austenite in white.

Steel	C (wt%)	Mn (wt%)	Si (wt%)	Mo (wt%)	Ni (wt%)	Cr (wt%)	Nb (wt%)
B	0.365	0.005	2.019	0.002	3.976	0.013	< 0.001
C	0.186	0.002	1.994	0.002	4.114	0.016	0.002

Table 7.1: Chemical composition (wt%) of steels A, B and C.

Alloys B and C have similar compositions, apart from their carbon concentrations (Table 7.1). Alloy B contains 0.36 wt% carbon and alloy C 0.19 wt%. Their predicted TTT diagrams are plotted on Figures 7.3 and 7.4. Due to its higher carbon content, B has lower B_s and

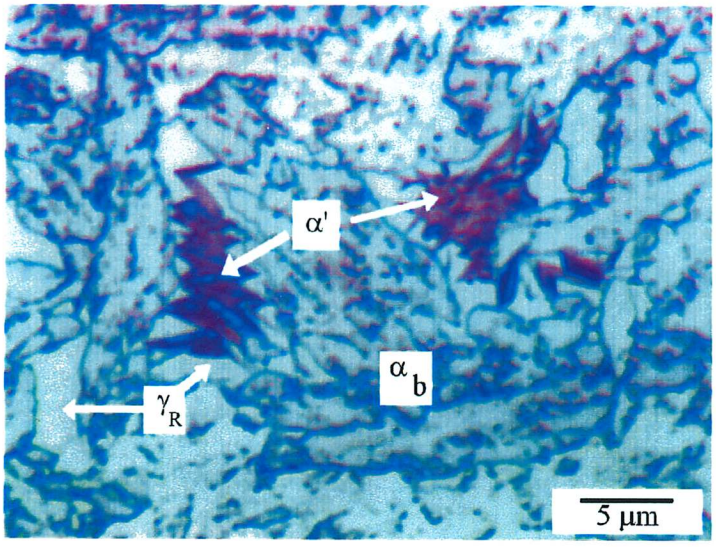

Fig. 7.1: Optical micrograph of alloy B with the large austenite grain size, isothermally held at 460°C for 20 min (THERMEC). The symbol γ_R represents areas of retained austenite in all subsequent micrographs. Etched with 2 % nital.

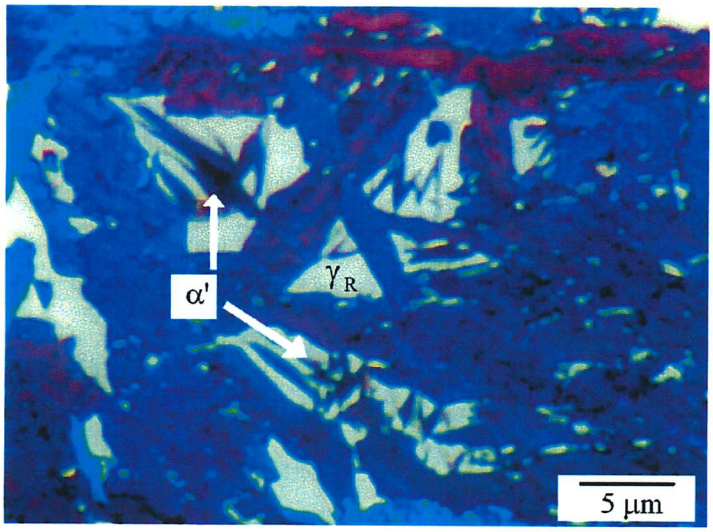

Fig. 7.2: Optical micrograph of alloy B with the large austenite grain size, isothermally held at 460°C for 20 min (THERMEC). The Rabinovitch etching method reveals retained austenite in white.

M_s temperatures than C, and a relatively higher hardenability, characterised by a shift of both C-curves on the *TTT* diagram to longer times. The calculated displacive C-curves of the two alloys would be essentially superposable, but the domain of bainite formation is in the lower part of the C-curve for alloy B whereas it is situated near the nose of the C-curve for alloy C. From such simple considerations, one can expect the rate of transformation to be relatively indifferent to the transformation temperature for alloy C, whereas it could decrease with temperature for alloy B.

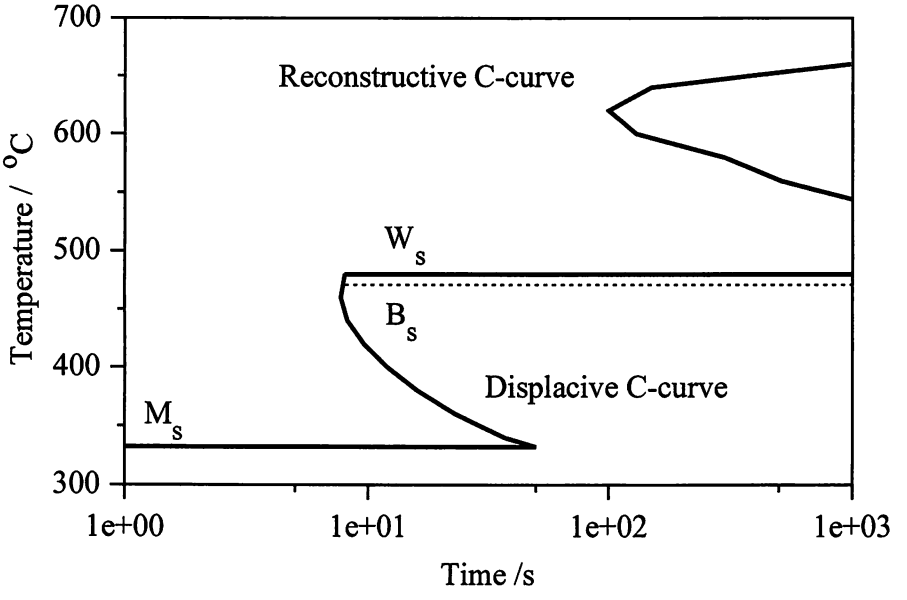

Fig. 7.3: *TTT* diagram illustrating the calculated reconstructive and displacive C-curves of alloy B. The curves represent the time required to initiate transformation.

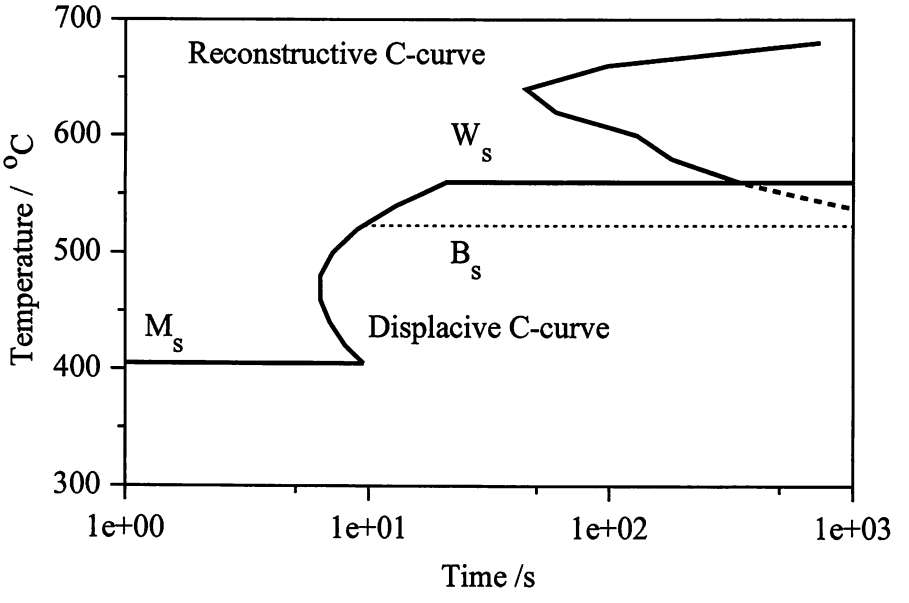

Fig. 7.4: *TTT* diagram illustrating the calculated reconstructive and displacive C-curves of alloy C. The curves represent the time required to initiate transformation.

7.2 Heat Treatments and Analysis

Alloys B and C have sufficient hardenability: at appropriate cooling rates, they do not transform to unwanted phases. However, in the case of alloy B with the small austenite grain size, the range of cooling rates where bainite was the major constituent was found experimentally to be quite small. A 1°C s^{-1} cooling rate produced some allotriomorphic ferrite whereas a 2°C s^{-1} cooling rate produced mostly martensite. It was decided therefore to focus on cooling transformations after austenitisation at 1200°C.

Grain sizes as well as the thermal expansion coefficients of alloys B and C, measured with the procedure described in Chapter 5 are given in Table 7.2. Summaries of heat treatments producing predominantly bainitic microstructures for alloys B and C are provided in Appendix 1 (Tables 3 and 4).

Alloy	d_γ at 1200°C (μm)	d_γ at 1050°C (μm)	e_α (K^{-1})	e_γ (K^{-1})
B	296 ± 63	57 ± 8	$(1.50 \pm 0.02) \times 10^{-5}$	$(2.29 \pm 0.02) \times 10^{-5}$
C	198 ± 52	66 ± 28	$(1.51 \pm 0.02) \times 10^{-5}$	$(2.33 \pm 0.02) \times 10^{-5}$

Table 7.2: Table listing the austenite grain sizes of alloys B and C after austenitisation for 3 min at 1200 or 1050°C, and values of ferrite and austenite thermal expansion coefficients.

Various sets of fitting constants were determined to be used for model predictions in the present chapter. They are given in Table 7.3.

7.3 Isothermal Transformations

Isothermal tests were carried out at different temperatures, with two different austenite grain sizes on the two dilatometers. To ensure that within one series, the tests performed on one equipment with a given d_γ are comparable and because of the limited amount of material available, it was necessary to use the same sample throughout the series to minimise the reproducibility errors. Transformation curves for an isothermal heat treatment carried out on two equipments with two different samples (Figures 4.7 and 4.8) can be separated by as much as 20 or 30 s on the time axis, while the reaction rates, characterised by the slopes of the curves are similar.

Even using the same sample twice for exactly the same heat treatment does not imply that the corresponding curves are superposed and in one case of continuous cooling, a difference of

Alloy	Set of Constants	B_6', m^{-2}	B_4, J mol^{-1}	λ_1	λ_2	Error
B	THERMEC, aust. at 1050°C	9.453×10^{-10}	1.147×10^{5}	742.06	0	1.780
B	THERMEC, aust. at 1200°C	3.375×10^{-10}	1.011×10^{5}	3658.3	0	1.354
B	BÄHR, aust. at 1050°C	1.065×10^{-10}	7.011×10^{4}	215.83	0	1.219
B	combined data	2.448×10^{-9}	7.554×10^{4}	1.999	0	13.90
B	combined data ($0.2 < \xi < 0.8$)	1.425×10^{-9}	8.398×10^{4}	287.21	0	6.06
C	THERMEC, aust. at 1050°C	7.783×10^{-12}	4.861×10^{4}	139.36	0	0.34
C	THERMEC, aust. at 1200°C	2.835×10^{-10}	8.347×10^{4}	698.01	0	0.11
C	BÄHR, aust. at 1050°C	1.032×10^{-12}	3.437×10^{4}	240.66	0	0.17
C	combined data	4.474×10^{-11}	4.649×10^{4}	5.23	0	7.63
A+B+C	combined data	9.962×10^{-8}	1.276×10^{5}	8.01×10^{-11}	1.246×10^{-6}	38.30

Table 7.3: Values of the constants for the modified Singh and Bhadeshia model fitted on isothermal transformation data for alloys B and C, and the constant values using combined data for the three alloys A, B and C together.

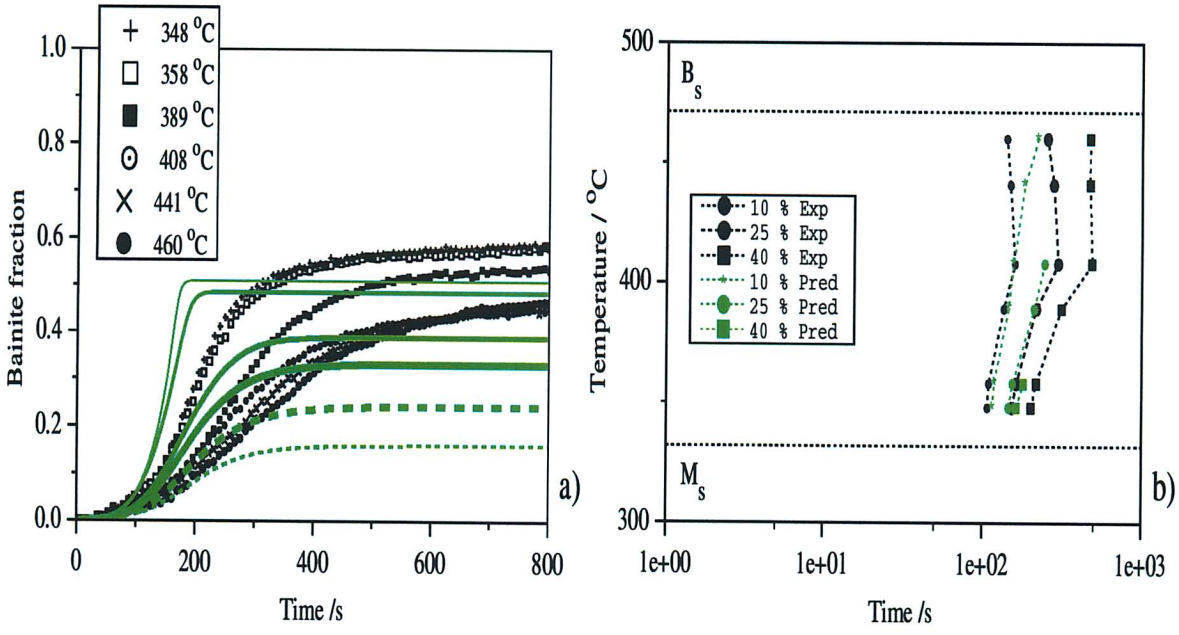

Fig. 7.5: a) Isothermal transformation data (THERMEC) for alloy B with 57 μm γ grain size at various temperatures compared with predictions (green curves) using constants fitted on the same isothermal data. b) TTT diagram of alloy B obtained using experimental (black points) and predicted data (green points).

50°C in the measured B_s was observed (Figure 4.11). Such considerations must be borne in mind when it is observed that one test in a series does not follow the general trend.

7.3.a Alloy B

For alloy B, the larger time scale of Figures 7.5 to 7.8 is evidence that the bainite transformation rates are slower than for alloys A and C, as expected from its higher hardenability.

With the exception of the 408°C test, it is found that the reaction rates for the tests carried out with the THERMEC and the small austenite grain size decrease and transformation becomes slower when temperature is increased, corresponding to the situation of Figure 4.3.a. Figure 7.5.a shows that the measured values of θ_b systematically exceeded their counterparts calculated with the T_0' criterion. There is less than 0.2 volume fraction difference between the maximum quantities of bainite measured at the variety of temperatures.

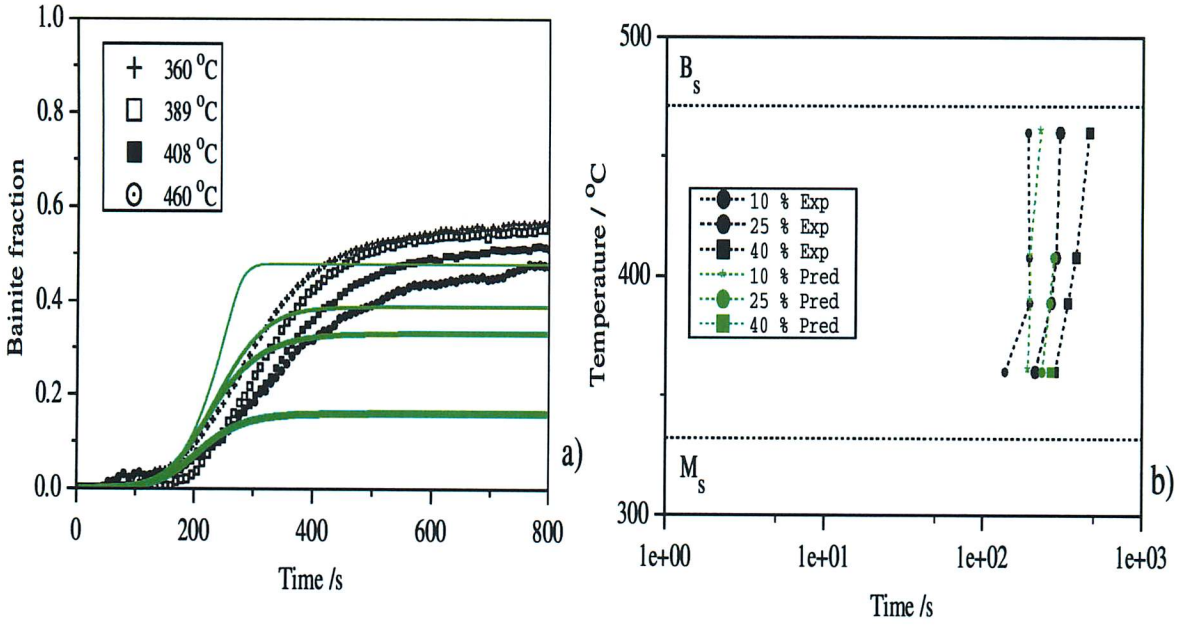

Fig. 7.6: a) Isothermal transformation data (THERMEC) for alloy B with 296 μm γ grain size at various temperatures compared with predictions made by using constants fitted on the same isothermal data. b) TTT diagram of alloy B obtained using experimental (black points) and predicted data (green points).

This contrasts with the large differences in θ_b values expected from the T_0' criterion. As a unique sample was used for all isothermal tests represented on Figure 7.5, it was neither possible to do hardness measurements nor optical counting for each transformation temperature

to confirm such a small variation in θ_b.

A possible explanation may be that the increase in austenite strength as temperature decreases prevents the formation of more bainite [Mujahid and Bhadeshia, 1993]. Indeed, plastic relaxation may become more difficult and the stored energy of bainitic ferrite may increase.

The discrepancies in θ_b lead to difficulties when attempting to fit the experimental data to theory hence the large optimisation error of 1.78 in Table 7.3, as opposed to the much smaller value of 0.06 found for alloy A (Table 6.2), where measured and calculated values of θ_b were in excellent agreement.

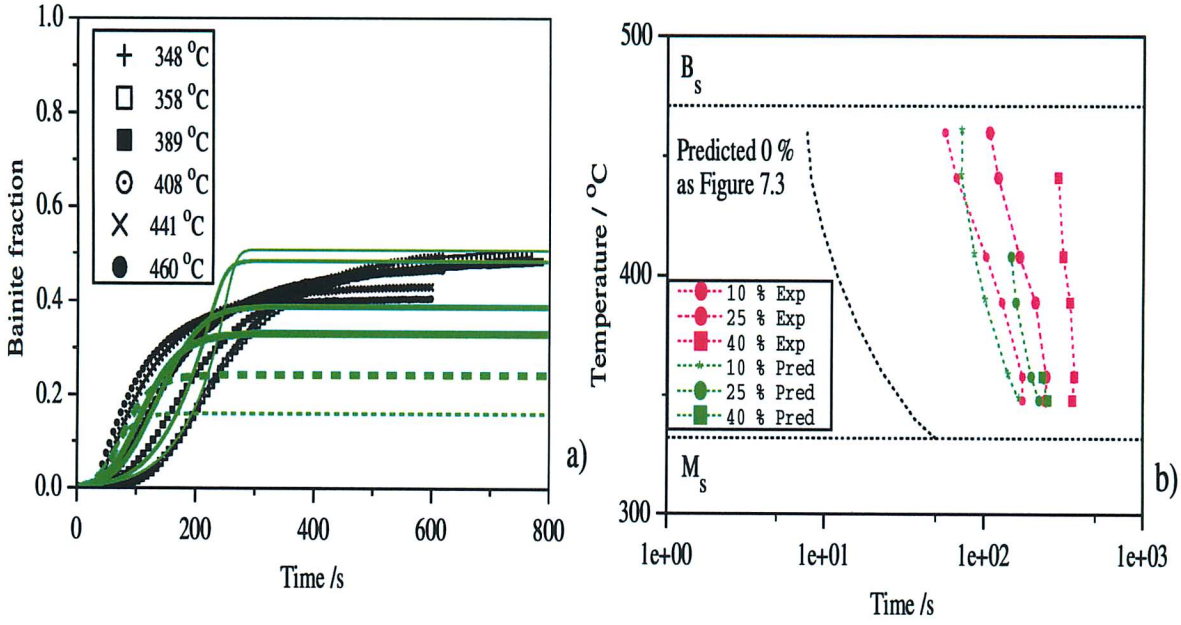

Fig. 7.7: a) Isothermal transformation data (BÄHR) for alloy B with 57 μm γ grain size at various temperatures compared with predictions (green curves) using constants fitted on the same isothermal data. b) TTT diagram of alloy B obtained using experimental (red points) and predicted data (green points).

The same trends were observed for THERMEC tests with the large austenite grain size. The four measured transformation curves as well as the limiting fractions of Figure 7.6.a are very similar. Reaction rates are slightly smaller and less sensitive to a change in temperature than for the small austenite grain size. In that respect, the TTT curve of Figure 7.6.b corresponds to the case represented on Figure 4.3.c.

Figure 7.7 shows that tests carried out on alloy B with the BÄHR dilatometer are charac-

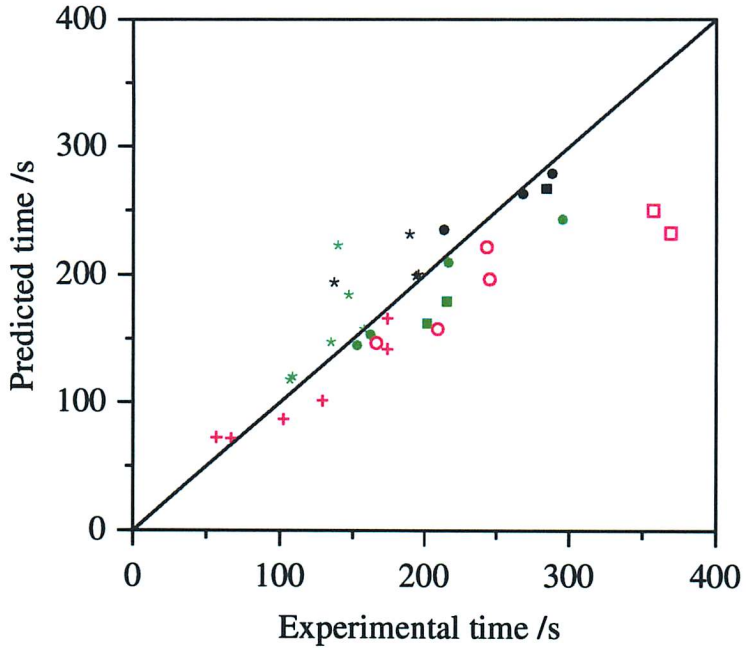

Fig. 7.8: Comparison of the predicted and experimental isothermal transformation times for alloy B and transformed fractions of 10, 25 and 40 % for all experiments. BÄHR tests are represented by red points. THERMEC tests with the small and large austenite grain size are represented by green and black points respectively.

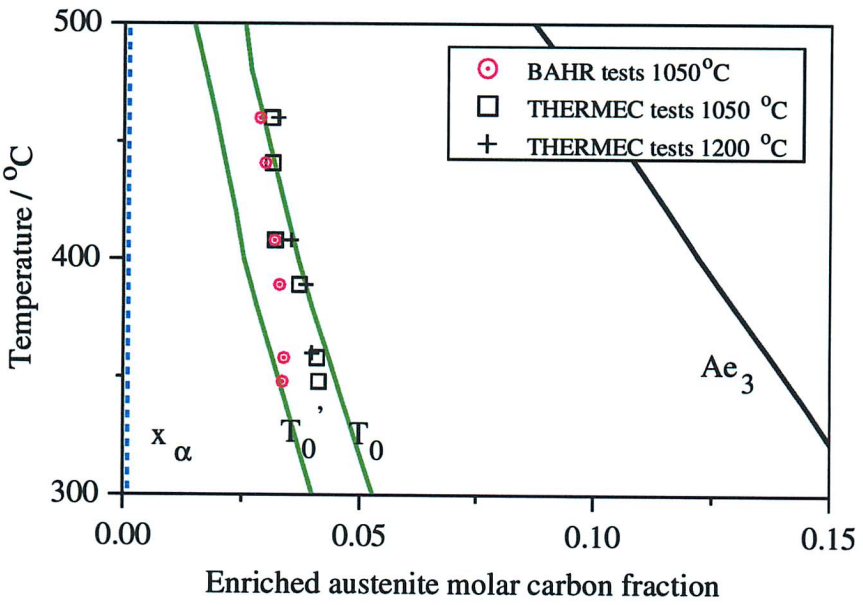

Fig. 7.9: Comparison of the values of enriched austenite carbon content (mole fraction) for the tests carried out on BÄHR and THERMEC on alloy B with the T_0 and T_0' lines predicted with thermodynamic criteria.

teristic of the case of Figure 4.3.b where there is a 'cross-over' of the measured transformation curves. As opposed to the THERMEC tests results obtained in the same conditions (Figure 7.5), a decrease in temperature results in an increase in the rates of reaction. Such differences in behaviour depending on the equipment used can only be attributed to different sample volumes or compositional variations from one sample to the other. Nevertheless, even if the difference is small, the measured values of θ_b increase with a decrease in temperature, as is observed in all cases for this alloy. After fitting, the model was able to reproduce this cross-over as demonstrated by the green curves on Figure 7.7.a.

The calculated TTT diagram of alloy B represented on Figure 7.3 shows that a cross-over of isothermal transformation curves for this alloy was expected, but the C-curve plotted is for 0 % transformation. The austenite grain size is not included in the calculations and the shape of the experimental C-curves for bainite is expected to vary with d_γ. Moreover, experimental C-curves represent points where the transformation becomes detectable and therefore correspond to transformed volume fractions probably closer to 0.05 than 0.

The comparison of calculated and measured times needed to form 10, 25 and 40% of bainite is presented on Figure 7.8. Points are equally spread around the 45-degree line of perfect match, with the exception of two points. This is a clear confirmation that the model has the flexibility to reproduce the data it was fitted on and the situation would be even better, were it not for the problem of maximum bainite fractions θ_b.

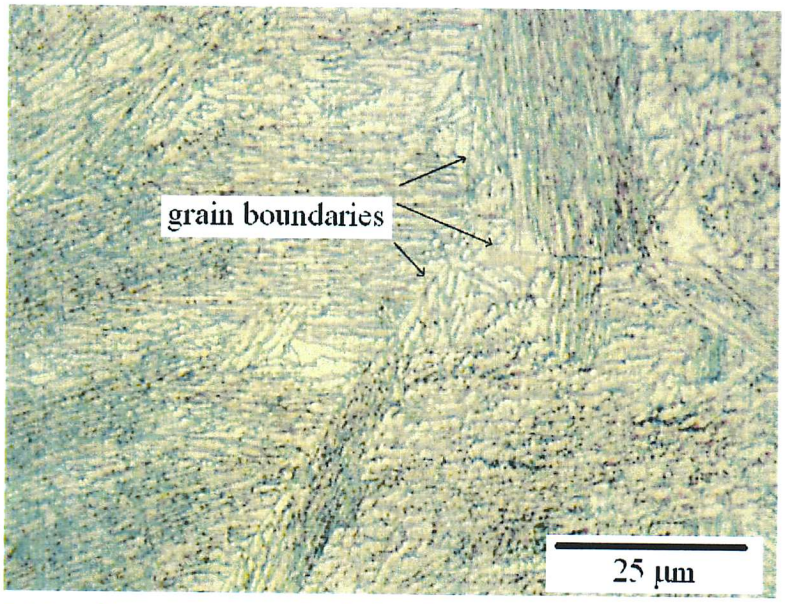

Fig. 7.10: Optical micrograph of alloy B with 296 μm γ grain size, isothermally held at 389°C for 20 min (THERMEC). Etched with 2 % nital. The austenite grain boundaries are annotated.

Figure 7.9 shows that the residual austenite carbon contents determined from the measured values of θ_b are always larger than expected with the T_0' criterion but the values are closer to the T_0' line as the temperature decreases. As before, it is suggested that in that case austenite may be stronger at lower temperatures, leading to a stored energy that increases and becomes closer to 400 J mol^{-1}. It would be interesting to vary the stored energy as a function of temperature, as proposed by Mujahid and Bhadeshia [1993].

Figure 7.10 shows the very fine bainitic microstructure of a sample of alloy B held for 20 min at 389°C (HV = 379).

7.3.b Alloy C

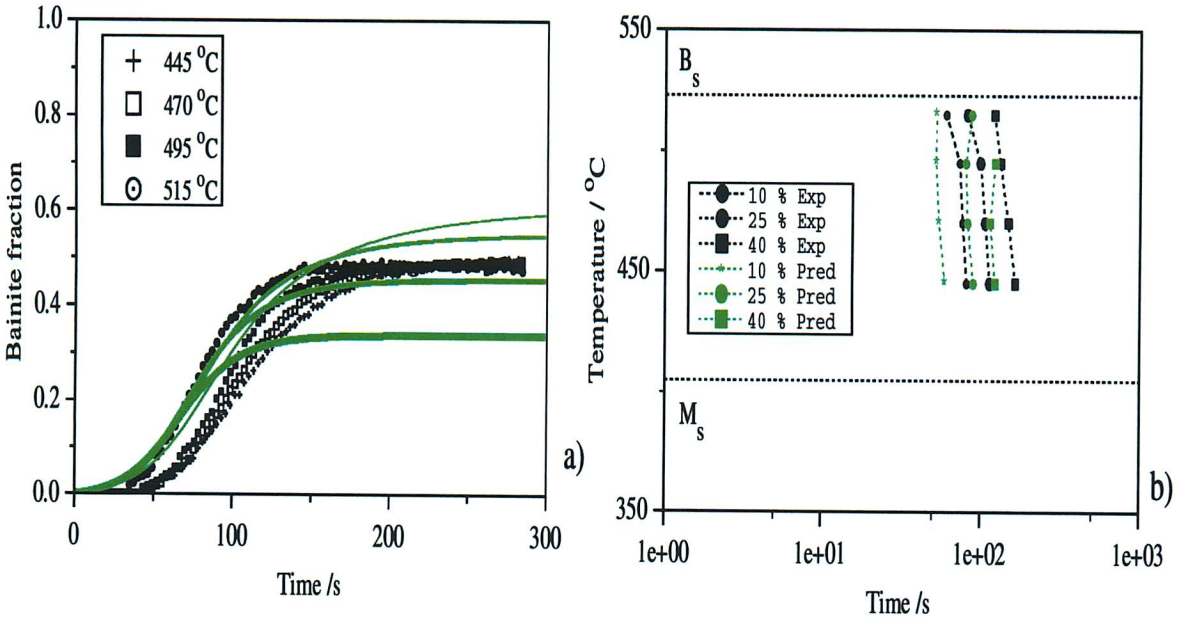

Fig. 7.11: a) Isothermal transformation data (THERMEC) **for hollow specimens** of alloy C with 66 μm γ grain size at various temperatures compared with predictions (green curves) using constants fitted on the same data. b) TTT diagram of alloy C obtained using experimental (black points) and predicted data (green points).

Similar experimental work was carried out for alloy C and substantial reaction only occurred after some 50 to 100 s at the isothermal transformation temperatures (Figures 7.11 to 7.13). The observations are similar to the ones made for alloy B:

- There is little variation in the measured values of θ_b. Once again, the proposed explanation is a possible increase in the stored energy as temperature decreases.

- The fact that the limiting fractions do not change much with the transformation temperature contributes again to the significant optimization errors of Table 7.3.

Two interesting remarks can be made concerning this alloy. Firstly, Figure 7.12 when compared with Figure 7.11 indicates that transformation is faster with the larger austenite grain size, without the possibility of the change of instrument being the cause. This is contrary to conventional knowledge which implies that a larger austenite grain size should lead to increased hardenability and was not observed for alloy B.

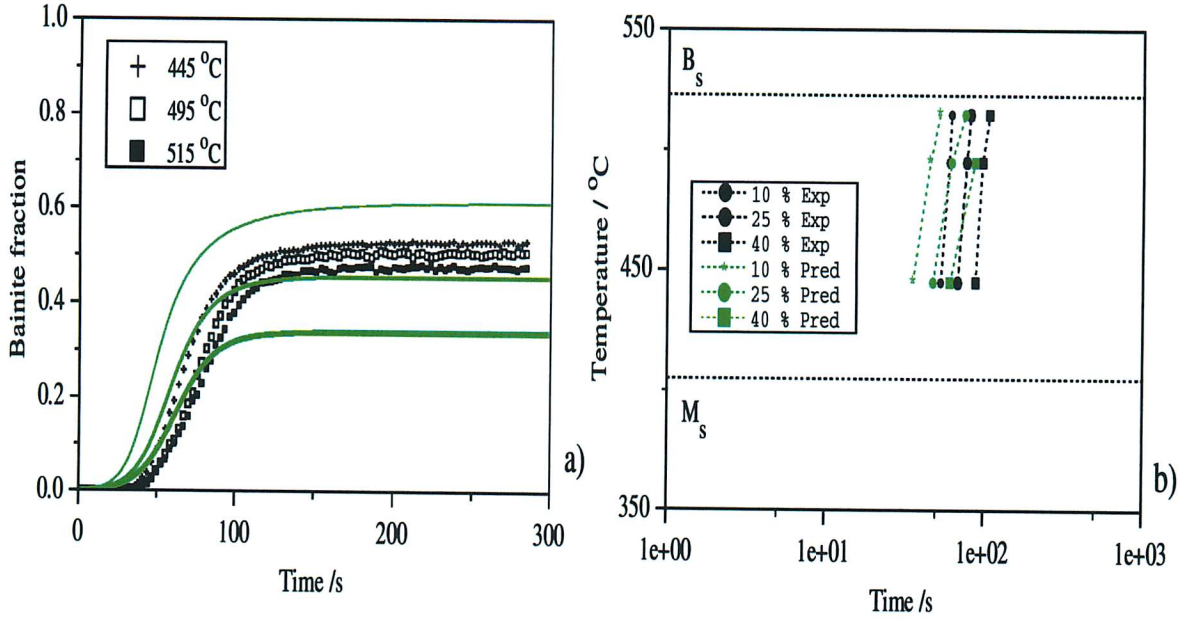

Fig. 7.12: a) Isothermal transformation data (THERMEC) **for hollow specimens** of alloy C with 198 μm γ grain size at various temperatures compared with predictions (green curves) using constants fitted on the same isothermal data. b) TTT diagram of alloy C obtained using experimental (black points) and predicted data (green points).

Secondly, it is worth looking carefully at Figure 7.15 in parallel to Figure 7.9. The value of the enriched austenite carbon content of alloy C is, at a given temperature, significantly lower than that of alloy B. The two alloys only differ by their carbon content.

Finally, on Figure 7.14, all of the points but one are situated to the right of the 45-degree line of perfect agreement. This reflects the fact that the measured times are larger than those predicted.

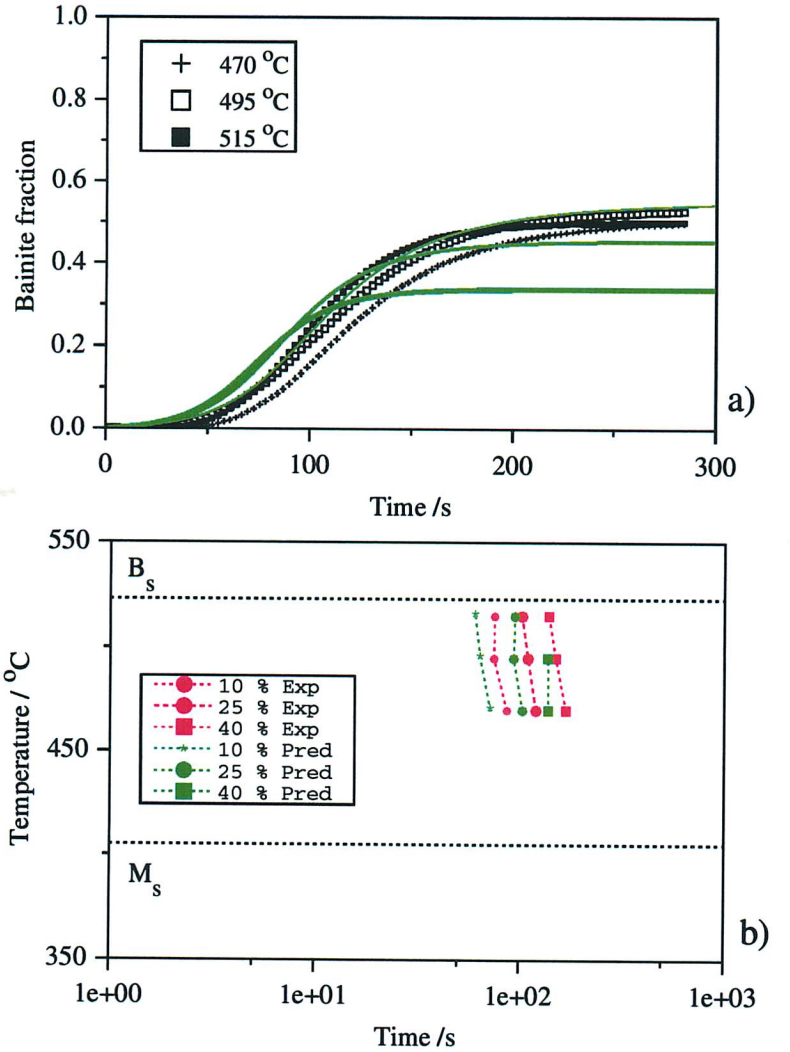

Fig. 7.13: Isothermal transformation data (BÄHR) for alloy C with 66 μm γ grain size at various temperatures compared with predictions (green curves) using constants fitted on the same isothermal data. b) TTT diagram.

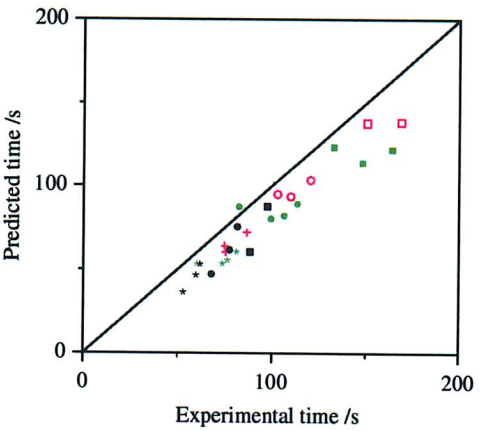

Fig. 7.14: Comparison of the predicted and experimental isothermal transformation times for alloy C and fractions of 10, 25 and 40 %. BÄHR (red points), THERMEC with small and large d_γ by green and black points.

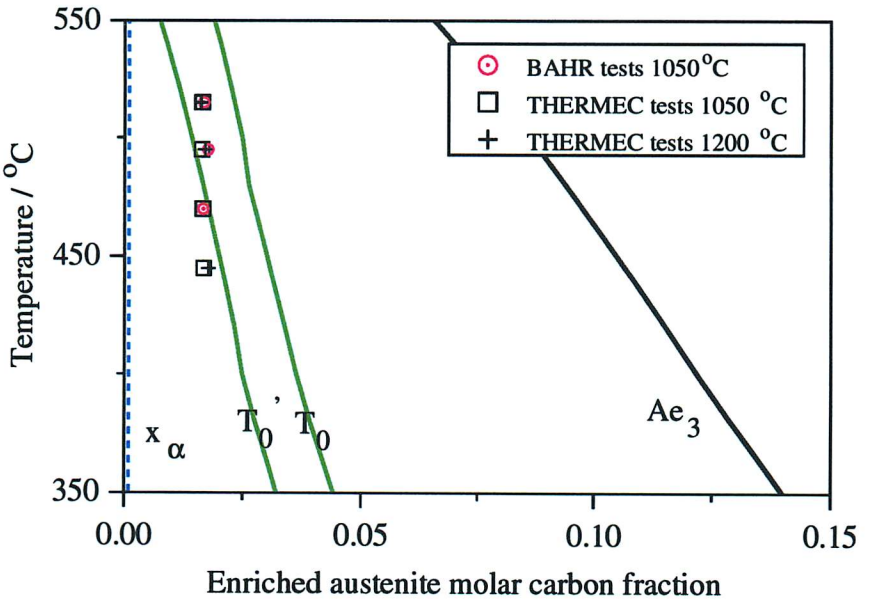

Fig. 7.15: Comparison of the values of enriched austenite carbon content (mole fraction) for the tests carried out on BÄHR and THERMEC on alloy C with the T_0 and T_0' lines predicted with thermodynamic criteria.

7.4 Bi-isothermal Transformation

Bi-isothermal experiments for alloys B and C were carried out after austenitisation at 1200°C, *i.e.* for austenite grain sizes of 296 and 198 μm respectively.

7.4.a Alloy B

Figures 7.16.a and 7.16.b show that there is no major difference in the measured reaction rates at 410 and 360°C. The alloy readily adopts the new rate after the decrease in temperature and reaches the same volume fraction as the isothermal transformation that took place entirely at 360°C. However, the fitting giving Figure 7.5.a was not perfect and the calculated dilatation or fraction at the end of the 410°C step is notably larger than its measured counterpart. The poor agreement between the predicted and experimental curve is therefore due to errors in fitting to the isothermal data.

As was demonstrated on Figure 6.7 for alloy A, the difference between the two predicted curves on Figure 7.16.b can be interpreted as the error bar in the prediction. Situated within this error bar, the measured θ_b value is well reproduced by the model.

7.4.b Alloy C

Figures 7.17.a and 7.17.b show that because of a reproducibility problem, the bi-isothermal transformation starts after a longer delay time than the two isothermal transformations. The

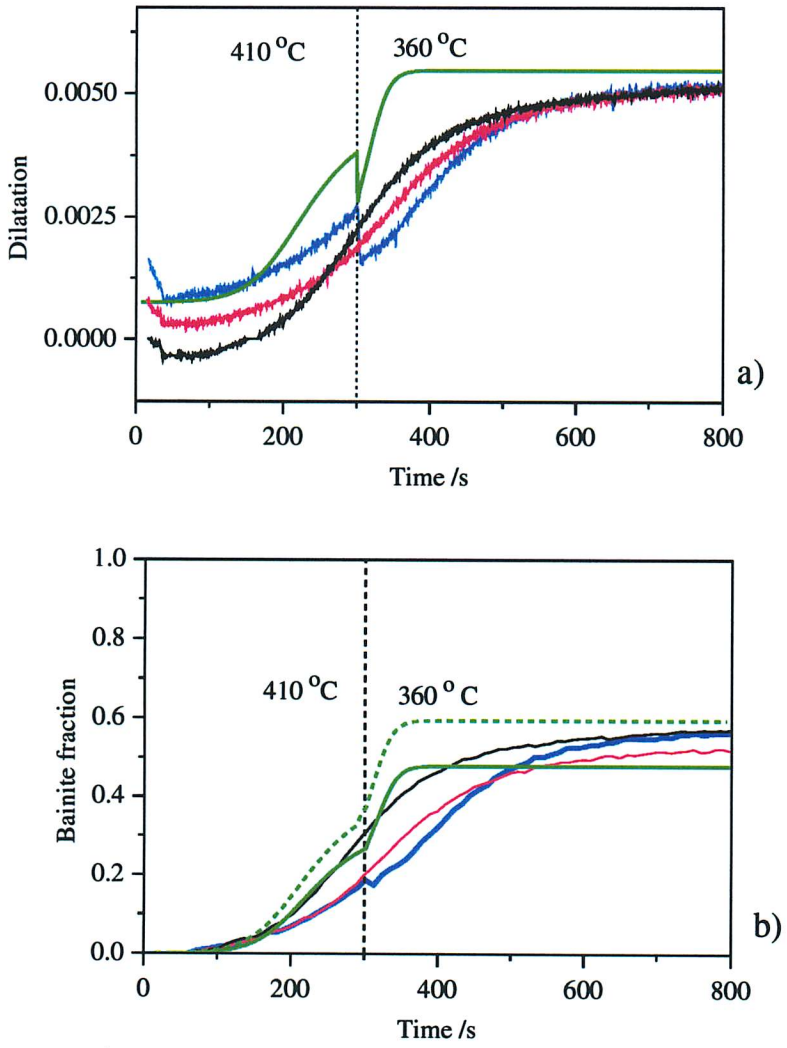

Fig. 7.16: a) Predicted dilatation of alloy B during the bi-isothermal heat treatment (green curve) compared with the corresponding experimental dilatations (in blue), and the isothermal tests at 410 (red curve) and 360°C (black curve). The predictions use the second line of constants in Table 7.3. b) Predicted evolution of the bainite fraction in alloy B during the bi-isothermal heat treatment compared with the experimental volume fractions for the bi-isothermal and isothermal experiments. The same colour code applies. The dotted green curve is calculated with $\bar{a}_\alpha$ equal to 2.871×10^{-10}m using the predicted dilatation with equation 4.4.

difference is about 15 s. As a consequence, the fraction achieved at the change of temperature is smaller than expected. As for alloy B, the reaction rates are not very sensitive to the temperature, even more so for alloy C. It is difficult to notice a change in the measured transformation rate.

It is not understood why a smaller bainite volume fraction is attained during the bi-isothermal test than during the two isothermal tests. Figure 7.18 shows the microstructure of

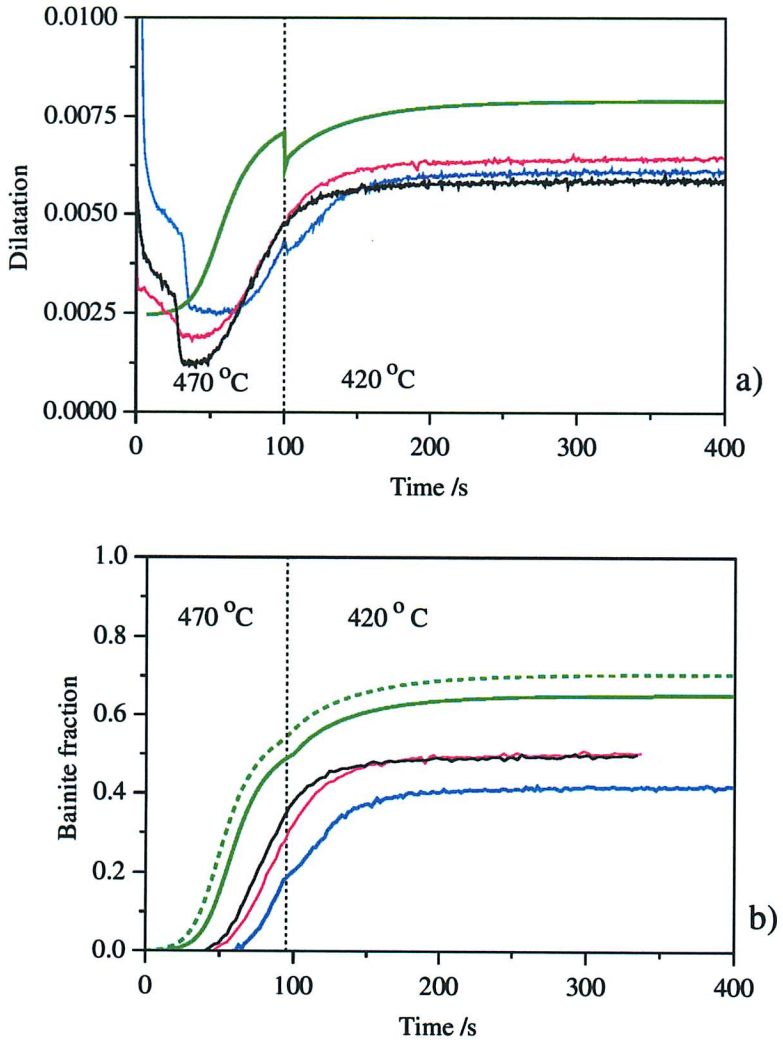

Fig. 7.17: Results of the bi-isothermal experiment carried out on alloy C, with the same colours as in Figure 7.16.

the transformed sample, with some plates of martensite visible in the centre of the picture.

7.5 Cooling Experiments

Extreme care must be taken to select appropriate cooling rates which form bainite as the first and major constituent in the microstructure. If the cooling rate is too high, a microstructure which is mostly martensitic is obtained.

For the purpose of comparison, Figure 7.19 shows a fully martensitic microstructure in alloy C, with its 'feathery' microstructure. With too low a cooling rate, phases such as Widmanstätten ferrite or allotriomorphic ferrite are obtained (Figure 7.20). Nodules of pearlite are sometimes observed at austenite grain corners (Figure 7.21, top) although the main constituents are bainite and martensite. Nevertheless, the experiment is of little use in studying

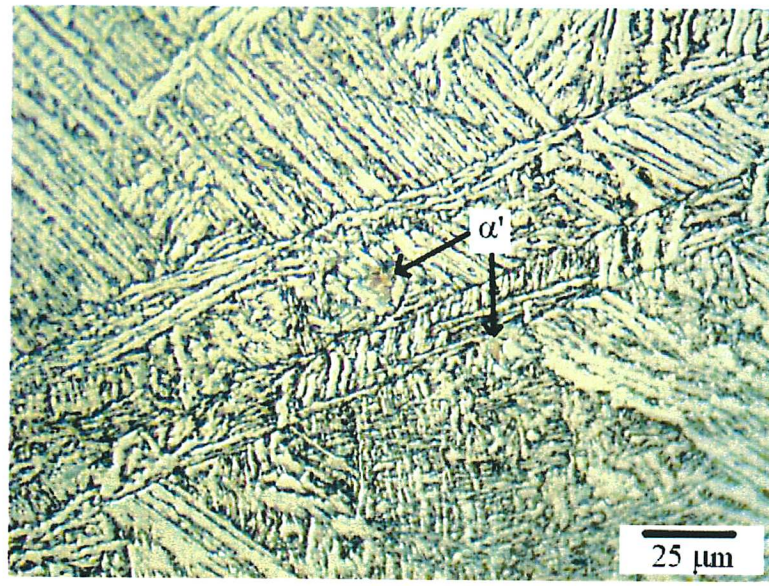

Fig. 7.18: Optical micrograph of alloy C with 198 μm austenite grain size, held at 470°C for 100 s and at 420°C for 500 s (THERMEC). Etched in 2 % nital.

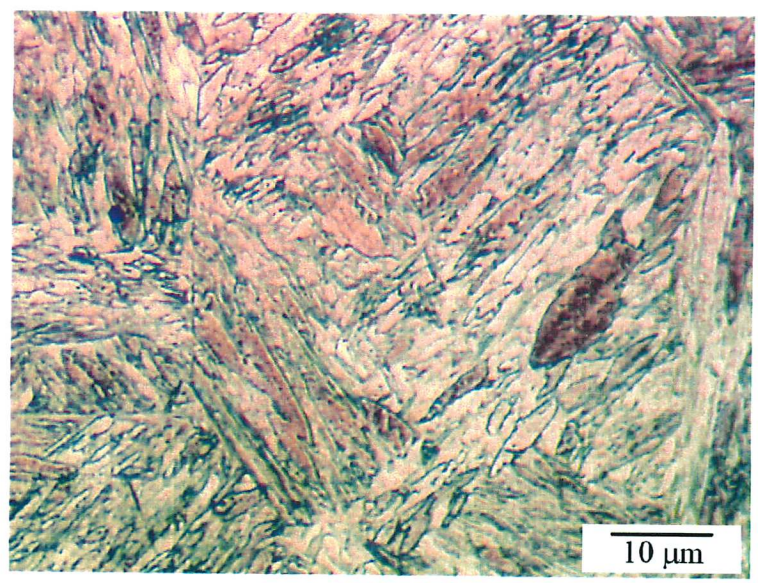

Fig. 7.19: Optical micrograph of alloy C with 198 μm γ austenite grain size, quenched to obtain a fully martensitic microstructure (THERMEC). Etched in 2 % nital.

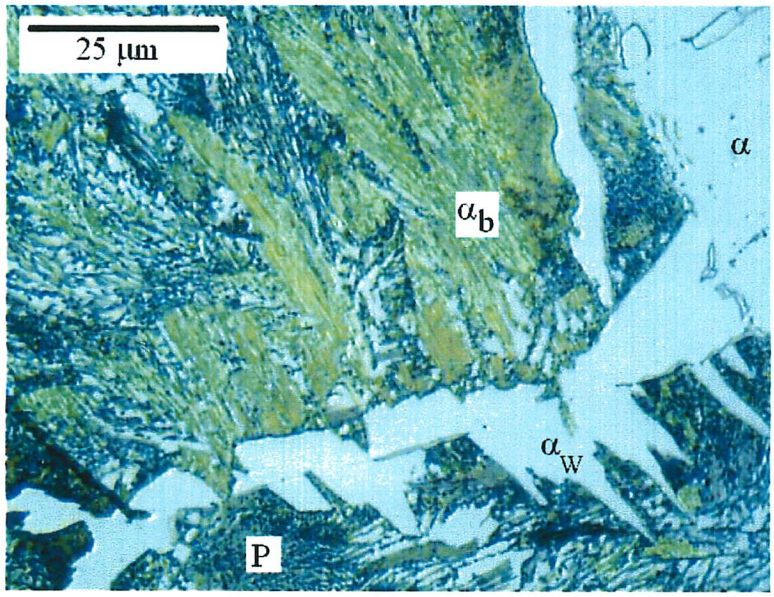

Fig. 7.20: Optical micrograph of alloy B with 296 μm austenite grain size, continuously cooled at 0.5 °C s^{-1} from 1200°C (HV = 296) with THERMEC. The symbol α_W represents Widmanstätten ferrite. Etched in 2 % nital.

the kinetics of bainite in isolation. Two other microstructures of the same sample are shown to illustrate the following:

- Austenite is locally enriched in carbon partitioned from bainite; these regions do not transform into martensite. Figure 7.21 (middle) shows bainite sheaves; the individual bainite plates cannot be seen at this magnification. Some martensite has formed between the sheaves. The sheaves are nevertheless surrounded by a thin layer of retained austenite.
- Figure 7.21 (bottom) shows sheaves of lower bainite that have developed from austenite which was enriched by the previous formation of the surrounding upper bainite. Lower bainite etches dark as it contains intra-lath carbides. Subsequently, martensite has formed from the residual austenite. Thin films of retained austenite etching white are also seen clearly on this microstructure at the interface upper bainite/martensite.

Since it was not possible to obtain bainite in alloy B with a small austenite grain size by continuous cooling transformation, only the large austenite grain size was used. Only bi-slope heat treatments were used for alloy C in order to cover a wider range of cooling rates and yet avoid any transformation above B_s.

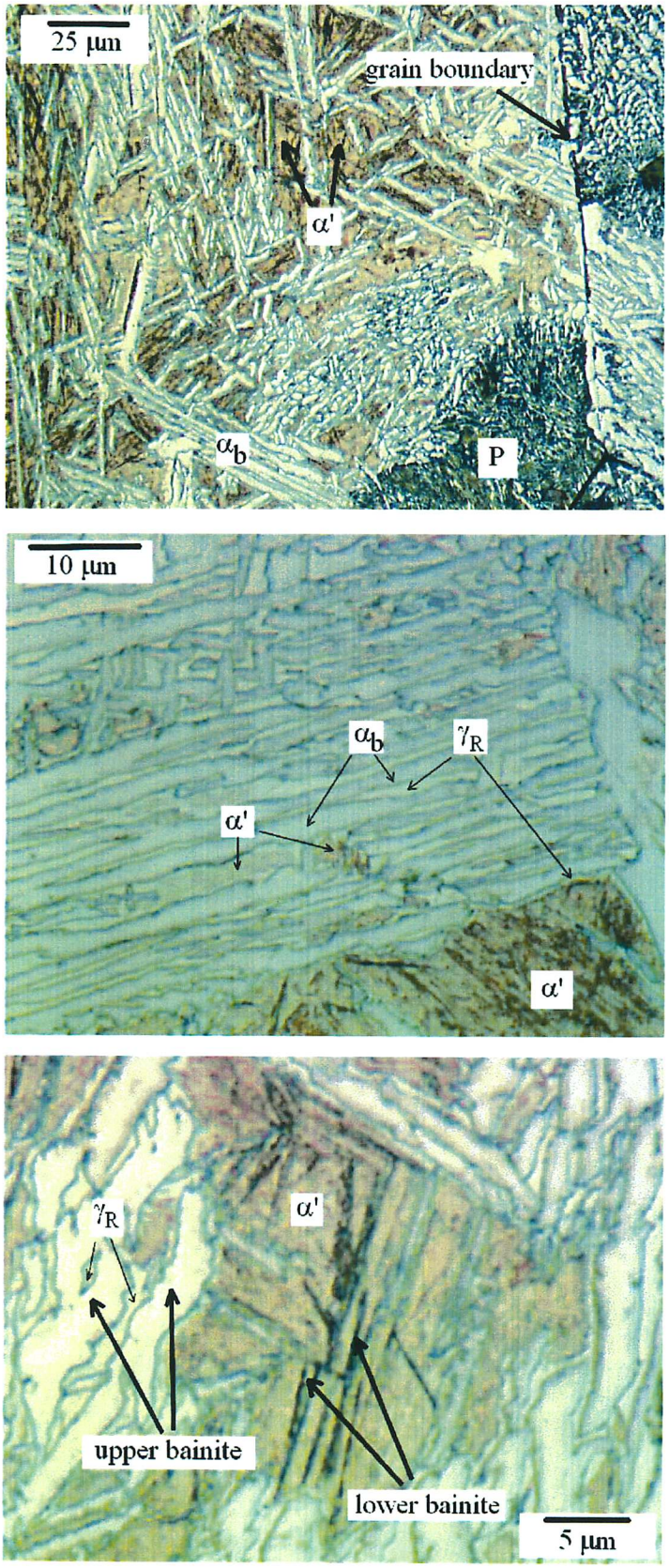

Fig. 7.21: Optical micrographs of alloy B with 296 μm γ austenite grain size, continuously cooled at 0.5°C s^{-1} from 1200°C (HV = 296) with THERMEC. Etched in 2 % nital.

7.5.a Alloy B

Figure 7.22 shows the variation of the measured bainite fraction in alloy B during continuous cooling at 1°C s^{-1} and various bi-slope experiments compared with the calculated transformation curves. Calculated curves were obtained after fitting constants were derived from intermediate portions of the isothermal curves, with $0.2 < \xi < 0.8$. Calculated reaction rates using constants fitted on all the data were found to be too small and are not plotted here.

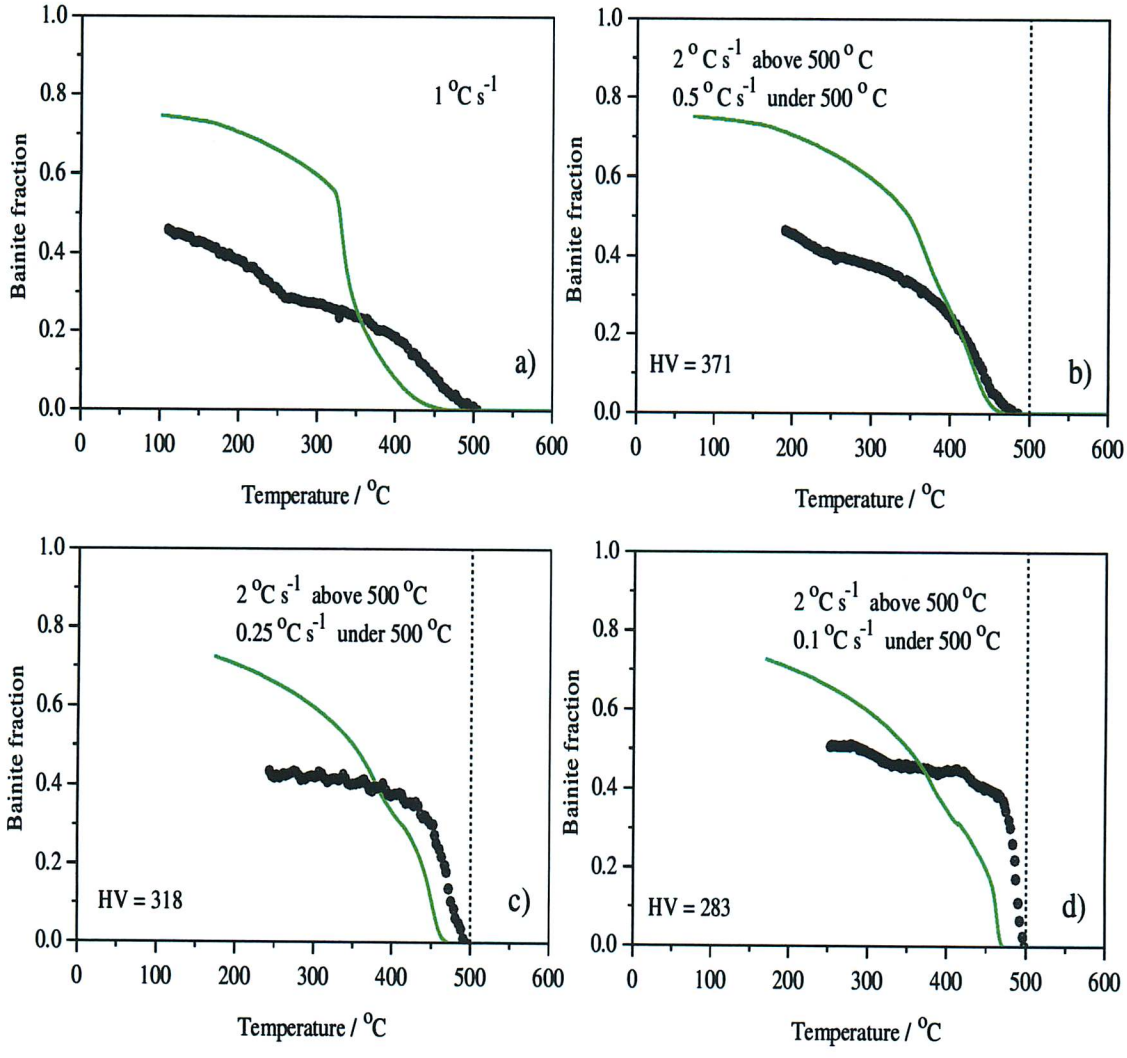

Fig. 7.22: Comparison between the measured and calculated cooling transformation data (THERMEC experiment) for alloy B with 296 μm γ grain size (austenitised at 1200°C) and cooled at various cooling rates. The dotted line represents the temperature at which the cooling rate changes during a bi-slope experiment. Solid green curves use constants from the fifth line of Table 7.3 ($0.2 < \xi < 0.8$).

The bainite transformation illustrated on Figure 7.22.a seems to occur at an almost constant rate even at low temperatures as austenite is progressively enriched and stabilised. The model predicts that martensite formation is not possible in that situation.

Caution must be exercised when interpreting measured transformation curves. Below M_s, bainite is often found to continue forming at a steady rate (Figures 7.22 and 7.24). This is because it is assumed that the corresponding dilatation increase is produced by the bainite transformation. However, it may be entirely due to martensite, in which case the bainite fraction should remain constant. Alternatively, there might even be a mixture of the two phases forming simultaneously. This will be analysed in more details in Chapter 8.

In the early stages of transformation, the calculated transformation rates are similar to the measured ones. But bainite transformation is found to start at around 500 °C, while the calculated value of B_s is 471 °C. This results in a shift between the calculated and measured curves. As the cooling rate under 500 °C decreases, bainite has more time to form and therefore experimental curves appear steeper. The maximum volume fraction is itself not influenced by the cooling rate and remains close to 0.5. However, the data in Appendix 1 (Table 3) show that the hardness decreases from 371 to 283, indicating that the bainite volume fraction increases, which is confirmed by Figure 7.23. It can therefore be concluded that there is a large error bar on the measured bainite fraction in continuous cooling conditions.

The calculated transformation curves of figures 7.22.b, c and d exhibit a secondary acceleration at volume fractions of 0.3 to 0.4 and temperatures below about 400°C. It is thought that the origin of this phenomenon may be the rapid increase in nucleation rate (Figure 4.16) that is happening under the M_s temperature of the alloy studied in Chapter 4. A similar increase could happen at temperatures above the calculated M_s temperature of alloy B, which is 332 °C. Such a dramatic increase does not seem to be observed experimentally.

Under temperatures of about 300 to 350°C, the calculated bainite fraction is limited to a value given by the T_0' criterion, independently of the set of fitting constants used, as shown on Figure 6.9 when yellow and green curves become superposed.

From the experimental data, it is inferred that martensite and retained austenite must account for about 50 % of the final microstructure, which is difficult to assess microscopically, except at a very large magnification.

Figure 7.23 (top, middle, bottom) show the microstructures corresponding to Figure 7.22.b, c and d respectively. Microstructures comprise mostly of upper bainite, martensite and retained austenite.

The contours of upper bainite sheaves appear more and more irregular, with thicker

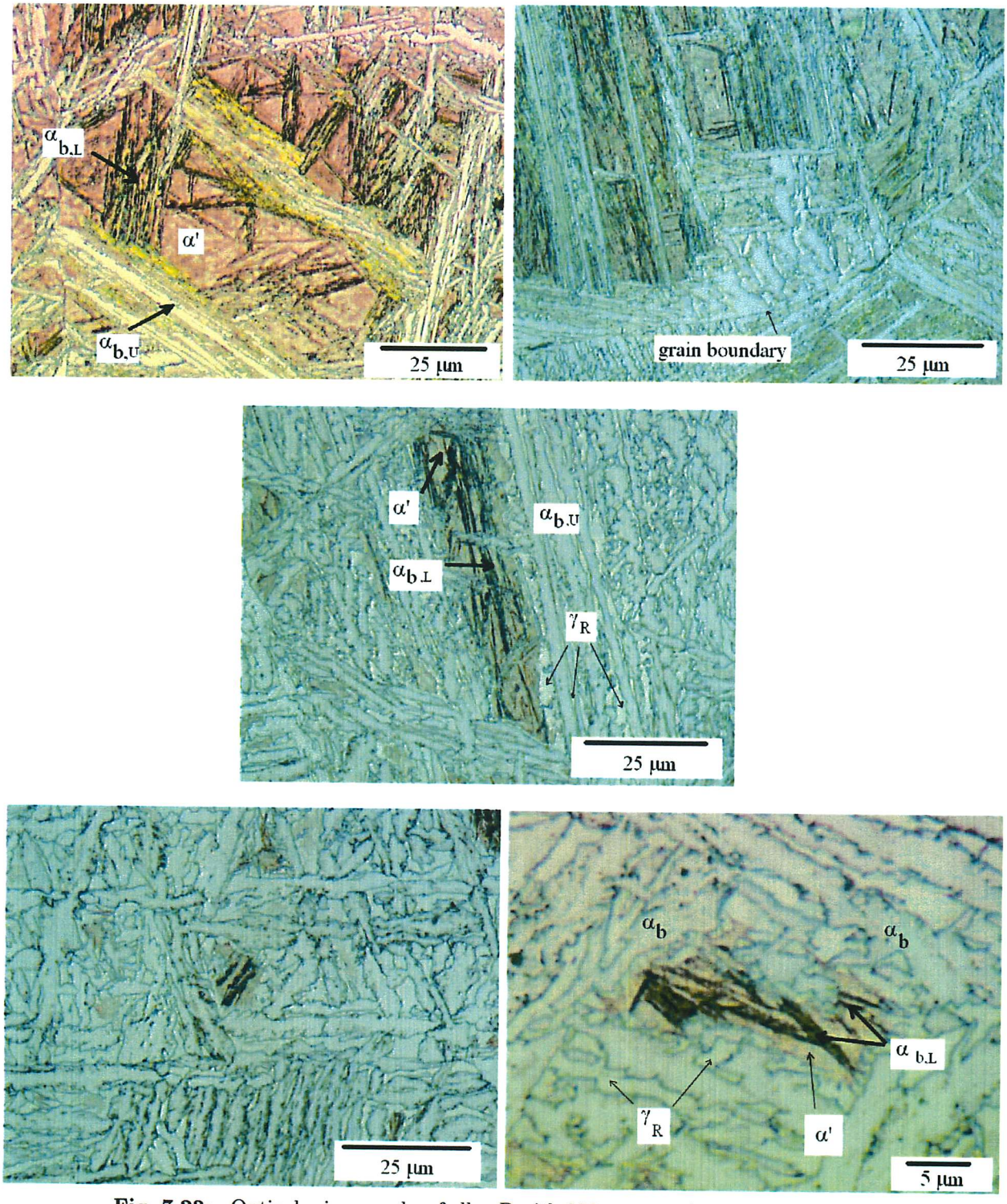

Fig. 7.23: Optical micrographs of alloy B with 296 μm γ grain size, cooled at 2°C s^{-1} above 500°C and at: top): 0.5°C s^{-1} under 500°C; middle): 0.25°C s^{-1} under 500°C; bottom): 0.1°C s^{-1} under 500°C(with THERMEC). The symbols $\alpha_{b,L}$ and $\alpha_{b,U}$ represent lower and upper bainite respectively. Etched in 2 % nital.

sheaves as the cooling rate decreases. This is because, with a slow cooling rate, the majority of bainite forms in the high temperature region of the bainite range. The bottom micrographs are in that respect, similar to that of Figure 7.1, which corresponds to isothermal holding at 460°C for 20 min. Sheaves of lower bainite etching dark are visible in all of these micrographs.

Figure 7.23 (bottom) shows a highly magnified region where lower bainite has formed. Between the sheaves of upper bainite, there is a large volume fraction of retained austenite, which could be compatible with a total bainite fraction of 0.5 given that retained austenite exists also within the sheaves between individual sub-units but cannot be resolved using optical microscopy.

Overall, the main reason why the anisothermal transformation data cannot be reproduced accurately is that the model cannot be properly fitted to isothermal data for alloy B.

7.5.b Alloy C

For this alloy, predictions using constants fitted on all isothermal data were used in the case of a small austenite grain size (ninth line of Table 7.3) but constants for large austenite grain sizes experiments were the ones determined for the corresponding experiments (seventh line of Table 7.3). Indeed, it was shown that the bainite transformation kinetics are faster for the large austenite grain size.

The comparison of the measured and calculated transformation kinetics of alloy C yields similar observations as for alloy B (Figures 7.24.a to 7.24.f). However, the carbon concentration of alloy C is only half the one of alloy B. Therefore, it is expected that austenite enrichment may not be sufficient to ensure stabilisation of residual austenite to ambient temperature. This is visible on Figure 7.24.d on which the measured bainite fraction reaches a plateau under 400 °C. A plateau is also present on calculated curves for the experiments carried out with the small austenite grain size, meaning that bainite transformation ceased and that martensite transformation took over (Figures 7.24.d to 7.24.f). According to the model, a larger γ grain size leads to a smaller nucleation rate, the two quantities being inversely proportional (equation 2.44). Therefore, if the same fitting constants are used, the calculated transformation rate is reduced. This is the reason why no plateau is observed on the calculated curves of Figures 7.24.a to 7.24.c.

Figure 7.24.a shows that for a cooling rate of 0.5°C s^{-1} under 460°C, both predicted and experimental curves show a slowing down of the bainite transformation at around 400°C. The two measured curves indicate that there is a lack of reproducibility between tests and therefore a large error bar on the measured bainite value. The curve showing the highest bainite volume

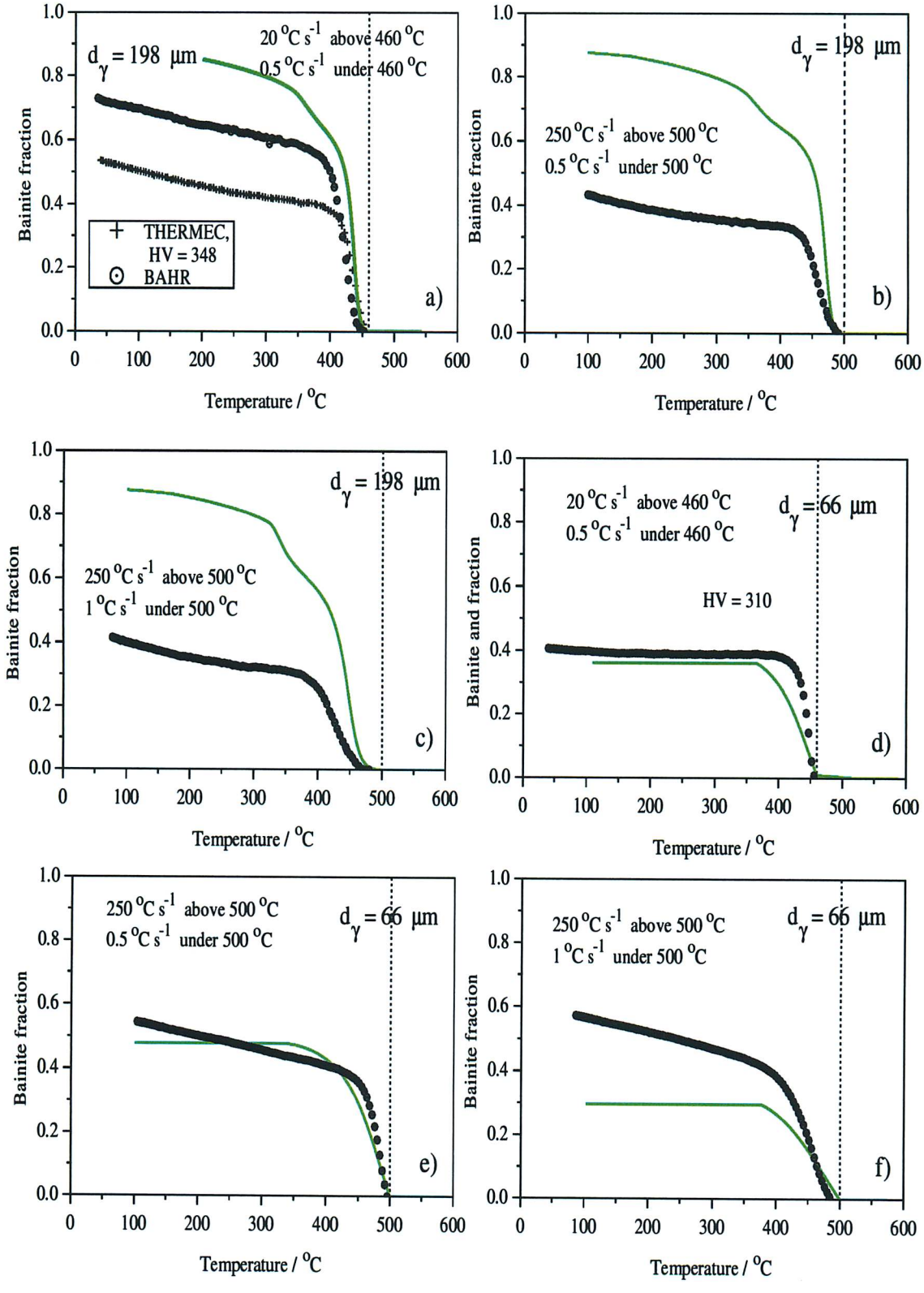

Fig. 7.24: Comparison between the measured and calculated cooling transformation data (BÄHR experiment unless otherwise stated) for alloy C with 198 or 66 μm γ grain size at various cooling rates. Dotted black lines represent the temperature at which the cooling rate is changed during a bi-slope experiment.

fraction was obtained with THERMEC using a hollow specimen.

Figure 7.25 is the corresponding microstructure, consisting mostly of upper bainite but also of some sheaves of lower bainite visible in the centre of the micrograph. Some regions have a slight shade of brown, suggesting that there is a significant amount of martensite in between the bainite laths.

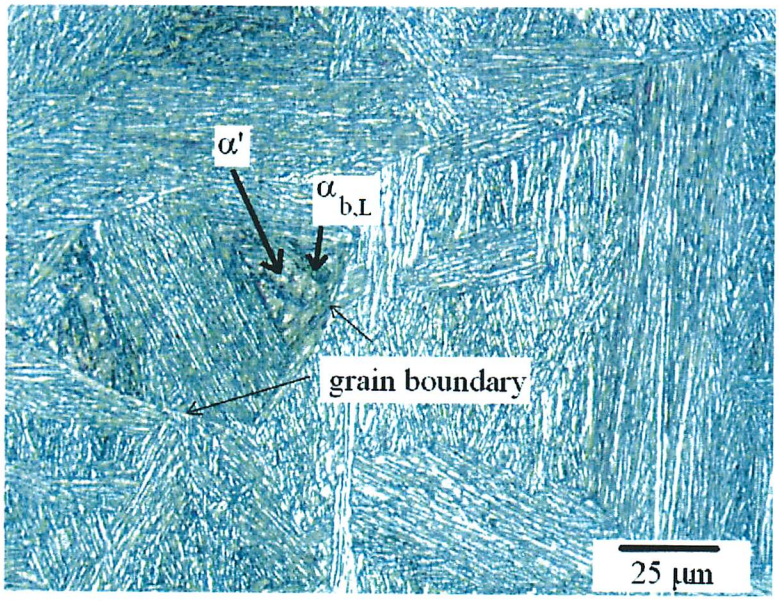

Fig. 7.25: Optical micrograph of alloy C with 198 μm γ grain size, cooled at 20°C s^{-1} above 460°C and at 0.5°C s^{-1} under 460°C (BÄHR). Etched in 2 % nital.

7.6 Conclusions

An important experimental observation is that although all alloys exhibit the incomplete reaction phenomenon, in which the maximum volume fraction of bainite θ_b is far smaller than expected from paraequilibrium, the observed values of θ_b are not exactly consistent with the T_0 or T_0' boundary. In practice, θ_b approaches values consistent with the T_0 curve at high temperatures but agrees better with the T_0' curve at lower temperatures. Whereas this does not influence the interpretation of the transformation mechanism, the measured θ_b as a consequence becomes insensitive to the transformation temperature.

On the other hand, the kinetic theory assumes that the shape deformation is elastically accommodated, with reaction stopping at the T_0' boundary. Therefore, the error in fitting experimental data to theory can be large. What is needed really is a theory which allows a more precise calculation of the stored energy as a function of the strength of austenite, its

elastic modulus, driving force and temperature. This may explain why θ_b is insensitive to temperature, plastic relaxation being easier at higher temperature.

An interesting observation which is consistent with calculated TTT curves for 0 % transformation is that the rate of reaction can decrease or remain insensitive to temperature depending on the disposition of the B_s temperature with respect to the C-curve for displacive transformations.

A distinct feature of continuous cooling transformation to bainite is that it is possible to completely avoid the formation of martensite. With an appropriate slow cooling rate, the enrichment of austenite with carbon can continuously keep the M_s temperature below the actual temperature. This could be useful in practice since high carbon, untempered martensite can be harmful to the toughness.

There are some puzzling and as yet unexplained observations regarding the effect of austenite grain size on transformation kinetics. It appears that in some cases a large d_γ accelerates transformation, which is contradictory to expectations from hardenability theory. Matsuzaki and Bhadeshia [1999] explained this in terms of the amount of volume that each nucleus is able to grow into, the volume being larger when nucleation sites are sparse (as with large d_γ). However, in the present study, this remains a speculation since there was no time to undertake the detailed investigation carried out by Matsuzaki.

Chapter 8

Measuring the Martensite Fraction

8.1 Introduction

A new method is introduced in this chapter which takes into account the formation of martensite when analysing experimental dilatation data. The dilatation data have previously only been used to deduce the bainite fraction, exploiting the lattice parameters of carbon-free bainitic ferrite and carbon-enriched residual austenite. It was the intention here to show that the measured martensite fractions are compatible with the observed microstructures. Indeed, a knowledge of both bainite and martensite fractions can permit the retained austenite fraction to be deduced by difference.

8.2 Calculation of the Experimental Martensite Volume Fraction

The program MAP STEEL DILAT takes into account the gradual enrichment of residual austenite as the bainite volume fraction increases and carbon partitions into the austenite. Martensite, on the other hand, inherits the chemical composition of the parent phase so the analysis of dilatometric data must be different.

It is assumed that the composition of the residual austenite is homogeneous throughout a sample during cooling experiments. With this assumption, martensite is expected to form uniformly at all locations within the austenite when M_s of the residual austenite becomes higher than the actual temperature at this point. It is also assumed that the bainite transformation then stops altogether as martensite is kinetically favoured. Naturally, there is no change in the chemical composition of the austenite once its M_s temperature is reached.

The method is the same as for bainite (Chapter 4). At a temperature generally chosen as the M_s temperature of the alloy, the new lattice parameters of austenite and ferrite, now having the same fixed carbon concentration are calculated and substituted to their former values in equation 4.4. Naturally, the values of the lattice parameters are still temperature-dependent (equations 4.5 and 4.7).

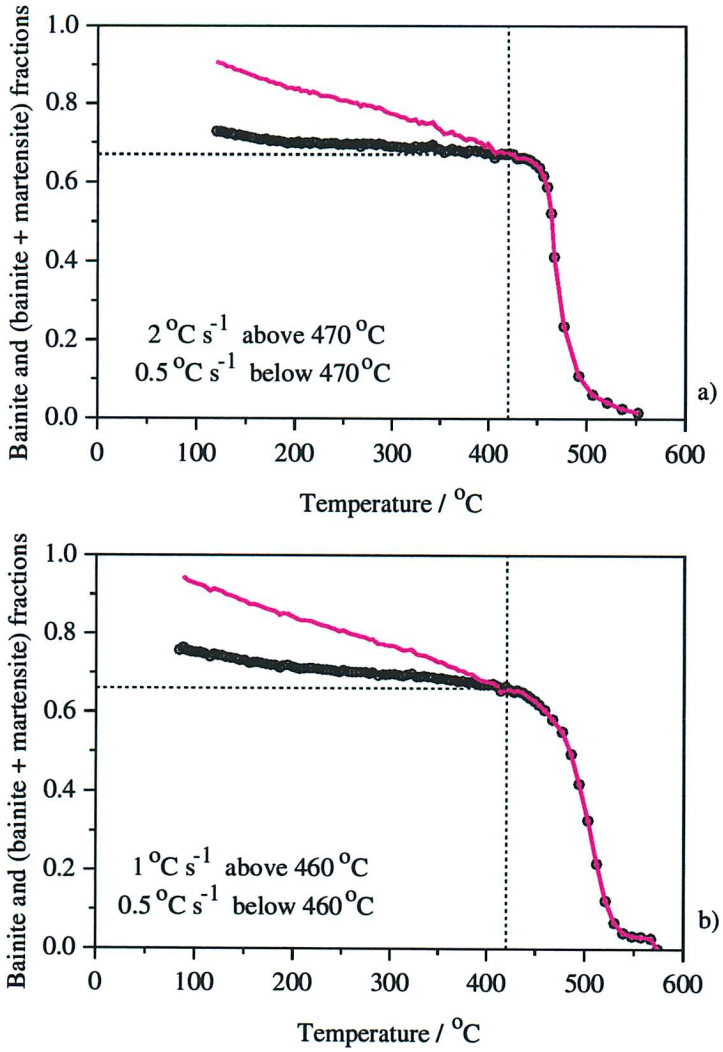

Fig. 8.1: Comparison between the measured bainite fraction (black points) and the measured (bainite + martensite) fraction (magenta curve) for bi-slope transformation data on alloy A. The alloy, with 26 μm austenite grain size, was cooled at: a) 2°C s^{-1} above 470°C and at 0.5°C s^{-1} under 470°C; b) 1°C s^{-1} above 460°C and at 0.5°C s^{-1} under 460°C. Martensite can start forming at temperatures below 420 °C, the M_s temperature for this alloy represented by the dotted line.

Figures 8.1 to 8.3 show the magenta curves corresponding to the new analysis for selected experiments on alloys A, B and C. The black points are the experimental data, assuming that all the transformation is bainitic. Black dotted lines represent the bainite volume fraction if the bainite reaction stopped altogether at the vertical dotted line.

From these figures, the following points can be inferred:

(i) The method used previously analysed the dilatometric data as if the increase below the vertical dotted line was due uniquely to bainite. When the same increase is assumed to

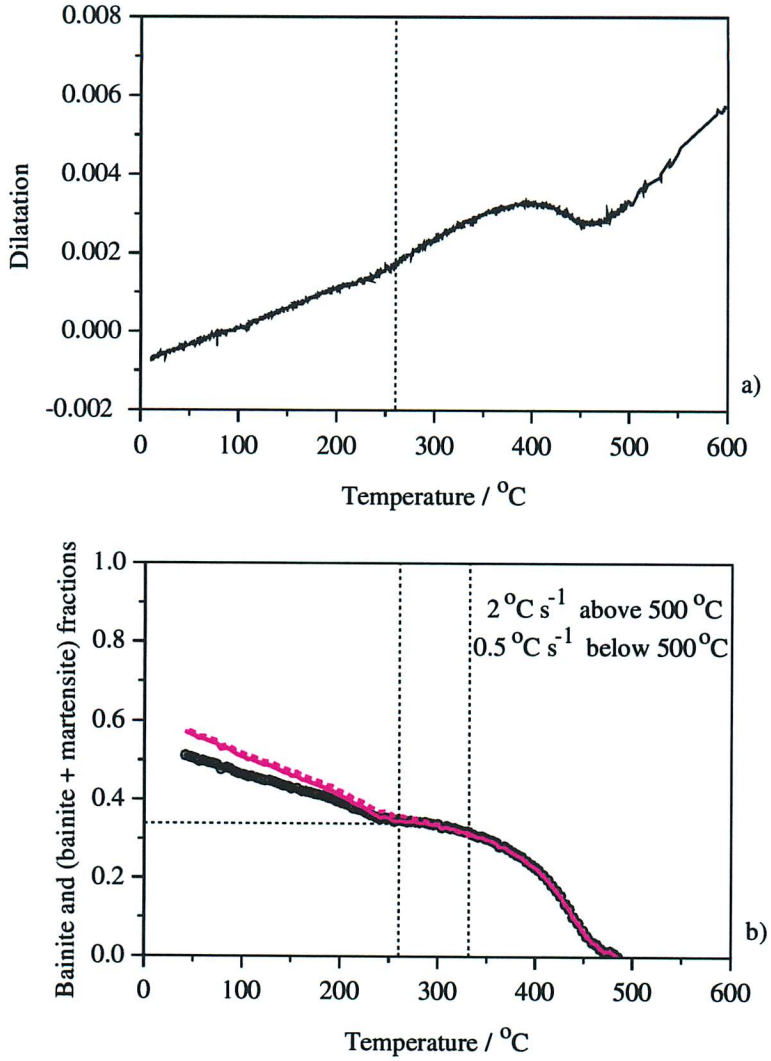

Fig. 8.2: a) Experimental dilatation curve (THERMEC) for alloy B with 296 μm γ austenite grain size. The alloy was cooled at 2°C s^{-1} above 500°C and at 0.5°C s^{-1} under 500°C. b) Comparison between the measured bainite fraction and the measured (bainite + martensite) fractions. The dotted magenta curve is for martensite allowed to form below 332°C (M_s) and the solid magenta curve is for martensite allowed to form below 260°C.

come from martensitic transformation, the fraction formed is found to be higher.

(ii) As a consequence, it is not really possible to determine exactly the fractions of martensite and bainite that are formed simultaneously below M_s. Due to variations in local austenite enrichment in carbon, it is likely that some regions that have been enriched more (between the laths or sheaves, for example) can still continue to transform into bainite to a limited extent, while less enriched blocky regions transform readily to martensite. The real bainite transformation curve is therefore located somewhere between the horizontal dotted line and the black transformation curve.

(iii) Figure 8.2.b is the only one that shows a distinct bump in the transformation curve due

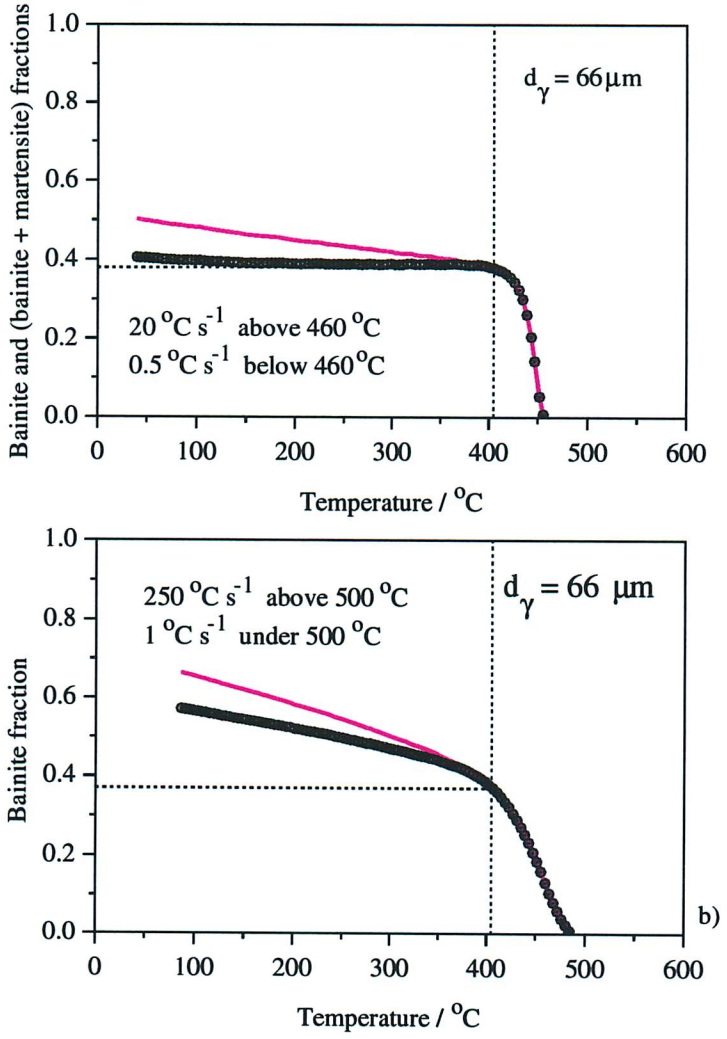

Fig. 8.3: Comparison between the measured bainite fraction and the measured (bainite + martensite) fraction for bi-slope transformation data on alloy C. The alloy (66 μm austenite grain size) was cooled at: a) 20°C s^{-1} above 460°C and at 0.5°C s^{-1} under 460°C; b) 250°C s^{-1} above 500°C and at 1°C s^{-1} under 500°C. Martensite is allowed to form below 405°C, the M_s temperature of the alloy.

to the formation of martensite. Two vertical dotted lines were drawn on this figure to show that choosing a value of $M_s > 260$ °C does not influence the magenta curve, which stays superposed on the black curve. This shows that martensite does not form above that temperature. Moreover, if M_s has a value of 260 °C (down from 332 °C originally), this corresponds to a bainite volume fraction of 0.35 formed above M_s, according to equations 5.1 and 6.1, which is consistent with Figure 8.2.b. The formation of 35 % of bainite led to a decrease of 72 °C in M_s by carbon enrichment of the residual austenite.

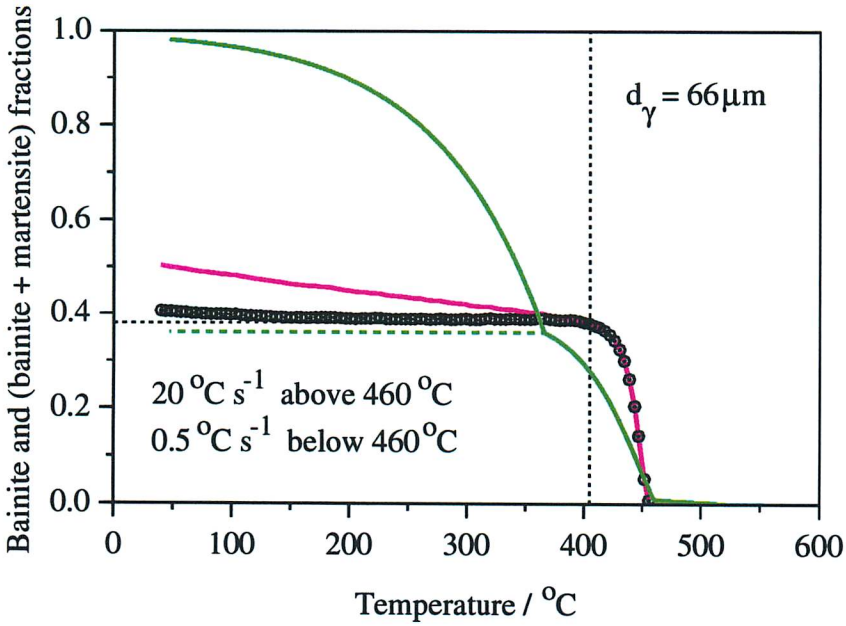

Fig. 8.4: Comparison between the measured bainite fraction and the predicted bainite (dotted green curve) and (bainite + martensite) fraction (green curves) for bi-slope transformation data on alloy C, using constants fitted on this alloy. The alloy (66 μm austenite grain size) was cooled at 20°C s^{-1} above 460°C and at 0.5°C s^{-1} under 460°C. Martensite is allowed to form below 405°C, the M_s temperature of the alloy.

The method is able to reproduce the trend known from martensite transformation theory and the Koistinen-Marburger relationship [1959] *i.e.* the martensite fraction increases with the undercooling below M_s, albeit at a slower rate.

Figure 8.1 shows that at ambient temperature little austenite is retained in microstructures of alloy A, less than 10%, as was determined by sigmametry. The measured fractions are also in agreement with the micrograph of Figure 5.23.

According to Figures 8.2 and 8.3, the retained austenite fractions in continuously cooled samples of alloys B and C are between 0.3 and 0.5, which is higher than for alloy A. This is expected in high-silicon steels. Figures 7.21 and 7.25 show significant amounts of retained austenite between sheaves, consistent with the measured values.

Finally, Figure 8.4 which reproduces the case of Figure 8.3.a but adding the predicted curves clearly shows that although the measured and predicted maximum bainite fractions are similar, the model overpredicts the amount of martensite that is formed by assuming that carbon is uniformly distributed in residual austenite. In the sample, however, most residual austenite is probably located in small areas between laths and sheaves which are sufficiently enriched in carbon so as not to transform to martensite at all.

8.3 Conclusions

Naturally, it has been found possible to determine the progress of martensitic transformation from dilatometric data in which bainite precedes martensite. The calculation requires the temperature at which martensitic transformation begins. For silicon-rich steels this can be estimated from the chemical composition of the residual austenite, assuming that the carbon partitioned from the bainite is uniformly redistributed. A further assumption is that the bainite reaction ceases once the austenite reaches its M_s temperature. Of course, the austenite may never reach its M_s temperature if it is sufficiently enriched in carbon, in which case it is retained to ambient temperature. The difference between the calculated and measured martensite fractions observed on Figure 8.4 has been attributed to local variations in residual austenite carbon content as the reaction progresses.

Chapter 9

Predictions with General Constants and Trends

'General' constants were determined with the whole isothermal dataset of this study (last line of Table 7.3). Such constants are not satisfying when trying to predict the transformation kinetics of a single experiment. Indeed, it was shown in Chapter 7 that several approximations exist in the model, so that even a set of constants determined on a set of experiments fail to reproduce the data measured in the same experiments. Alloy A was in this respect an exception (Chapter 6). However, it remains to be seen whether the model is able to reproduce known metallurgical trends when using general constants.

9.1 Predicted *CCT* Diagrams and Trends

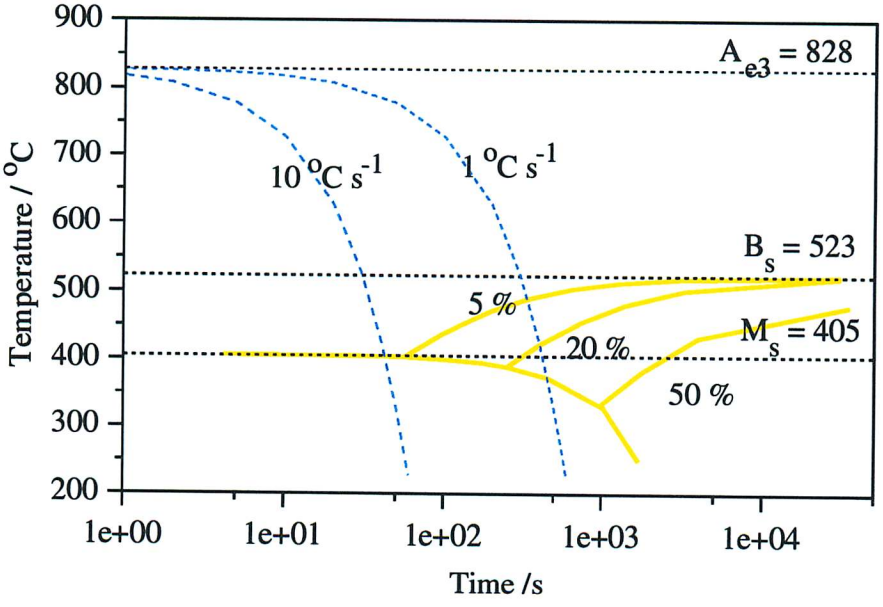

Fig. 9.1: *CCT* diagram of alloy C (66 μm γ grain size) predicted with the physical model using the 'general' constants.

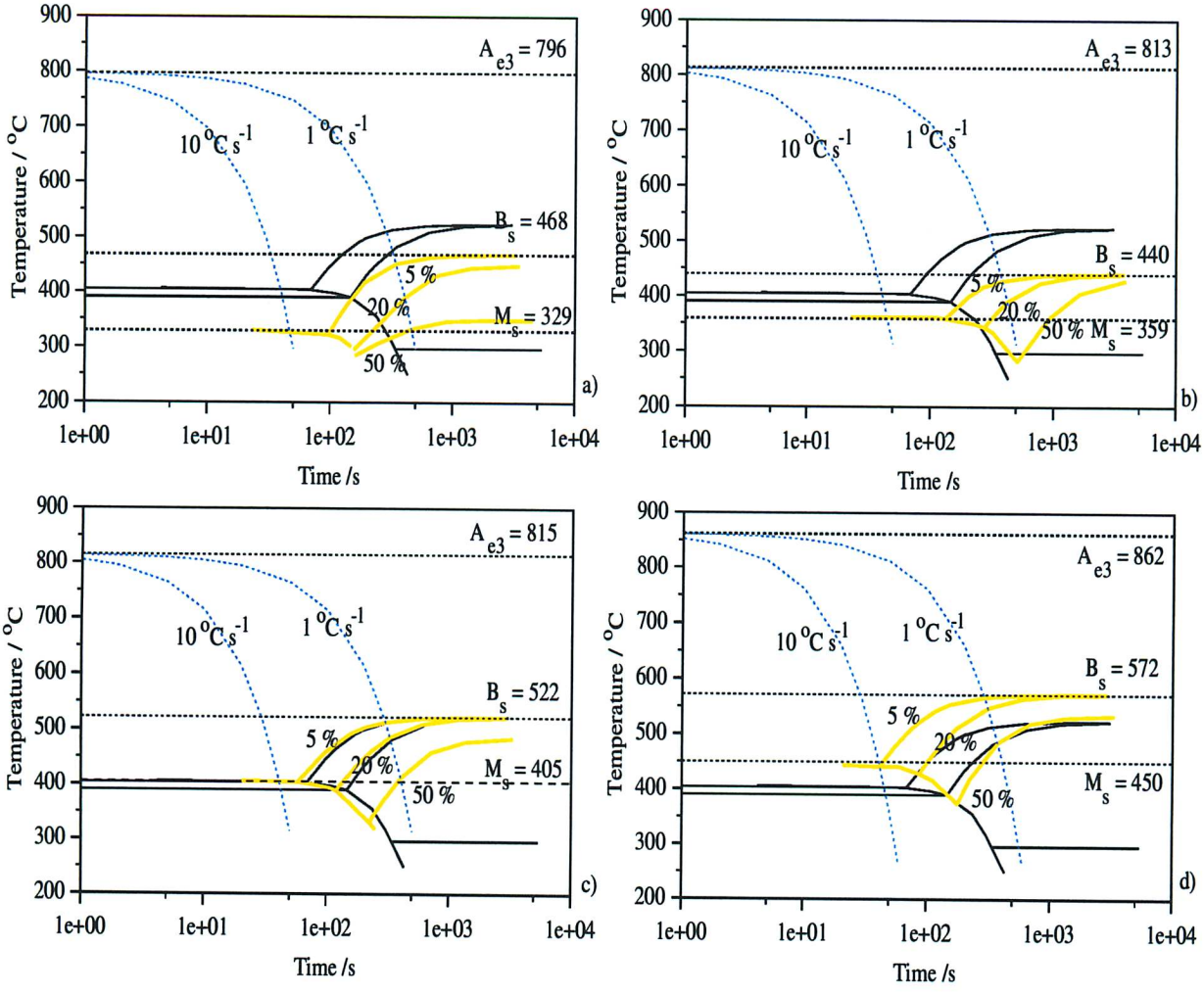

Fig. 9.2: *CCT* diagrams (in yellow) of alloy C with modified alloying contents, predicted with the physical model using the 'general' constants. a): with a carbon content of 0.3647 wt% (similar to alloy B); b) with a manganese content of 1 wt% (instead of 0.002 wt%); c) with a silicon content of 1 wt% (instead of 1.99 wt%); d) with a nickel content of 2 wt% (instead of 4.11 wt%). The diagrams are superposed on the diagram (in black) of Figure 9.1, which is for the original composition of alloy C.

The calculated *CCT* diagram of alloy C is represented on Figure 9.1 for an austenite grain size of 66 μm. It is reproduced on Figures 9.2 and 9.3 as black lines for the purpose of observing the predicted modifications induced by changes in the concentration of one of the chemical elements at a time. As a concentration is changed, the calculated B_s, M_s but also Ae_3 temperatures are altered. The Ae_3 temperature is by convention the temperature at which the origin of time is taken in a *CCT* diagram.

Figure 9.2.a shows that an increase of 0.18 wt% in carbon content depresses B_s by 55°C and M_s by 76°C. In addition, the bainite reaction is delayed to longer times. Carbon is known

to have the biggest effect on transformation kinetics as it is a very powerful austenite stabiliser (Chapter 2). The yellow *CCT* diagram of Figure 9.2.a is, in fact, almost the same as the *CCT* diagram of alloy B, as the composition of alloy C was modified for that purpose.

An increase of 1 wt% in manganese concentration, as depicted in Figure 9.2.b depresses B_s by 83°C and also retards the bainite transformation. M_s is only decreased by 46°C which results in a narrower bainite transformation range, covering only 81°C.

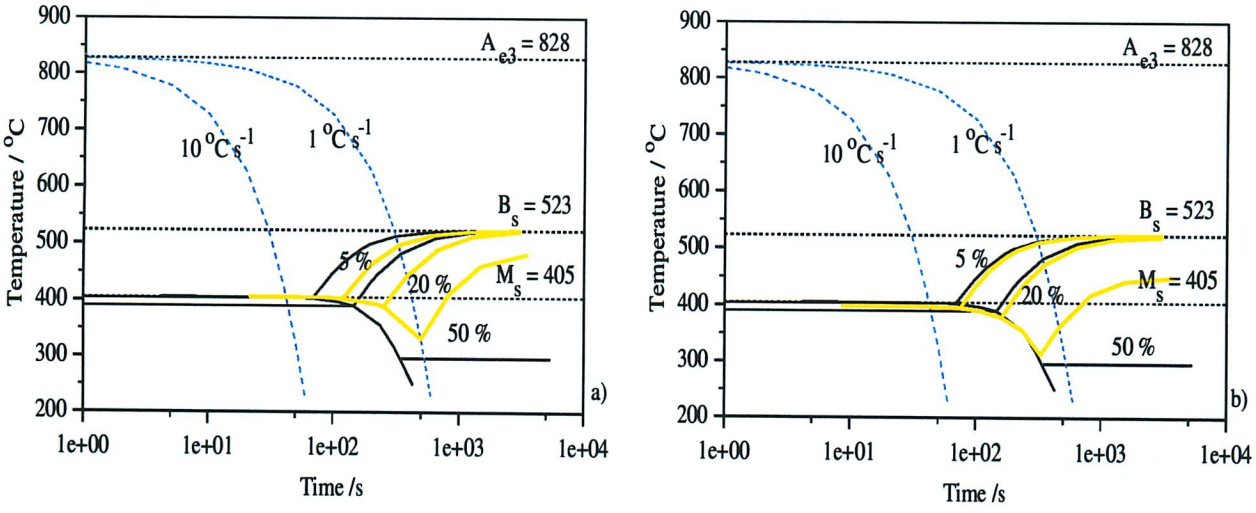

Fig. 9.3: *CCT* diagrams (in yellow) of alloy C with the physical model using the 'general' constants. a): with a modified γ grain size of 200 μm (instead of 66 μm); b) with a fraction of allotriomorphic ferrite formed prior to bainite of 0.2. The diagrams are superposed on the diagram (in black) of Figure 9.1, which is for the original composition of alloy C.

Figure 9.2.c confirms that silicon has very little influence on the kinetics and is mainly used in steels to suppress cementite precipitation. Decreasing the silicon concentration by 1 wt% does not affect the predicted B_s and M_s temperatures and the kinetics are barely faster than for the original composition. However, a 2 wt% decrease in the nickel concentration (Figure 9.2.d) results in an increase of 49 and 45°C in B_s and M_s respectively, and the bainite nose is shifted to smaller times. Nickel was introduced in large quantities in alloys B and C to improve hardenability. This role is demonstrated clearly on Figure 9.2.d.

Figure 9.3.a shows the effect on the bainite transformation kinetics of increasing the austenite grain size d_γ. The new *CCT* diagram is displaced to longer times, but B_s and M_s are unchanged. The new austenite grain size corresponds to the large experimental grain size of alloy C. It was shown in Chapter 7 that the measured kinetics are not much grain size-dependent, and certainly not as much as predicted by the physical model. It is believed

that the bainite kinetics are very sensitive to changes in d_γ for some alloys but not for others, and that in some alloys, the kinetics can be faster for large γ grain sizes than for small γ grain sizes.

Finally, Figure 9.3.b shows that the model, when it takes account of a prior fraction of allotriomorphic ferrite of 0.2, only reflects the change in austenite composition at the start of the bainite transformation. Austenite is then slightly enriched in carbon, which produces a small shift of the bainite nose to longer times and lower temperatures and M_s is also modified. However, the model cannot give any indication as to whether bainite nucleation is accelerated or slowed down by the presence of 'real' allotriomorphic ferrite at grain boundaries.

9.2 Conclusions

It has been demonstrated that the kinetic model is able to reproduce metallurgical trends; elements which increase hardenability retard the bainite reaction to an extent expected from thermodynamic considerations. There is nothing in the model, however, which can reproduce the observed (contradictory) effects of the austenite grain size. Although the model assumes that the number density of nucleation sites is related to the austenite grain size, grain boundary nucleation is not explicitly included since the conversion from extended volume to real volume assumes a random distribution of particles. What is needed to include effects such as site saturation is to treat the nucleation at grain surfaces in terms of an extended area as was done by Cahn [1956b].

Chapter 10

Conclusions and Suggestions for Further Work

The work presented in this thesis was undertaken in order to predict the rate at which bainite forms during the continuous cooling transformation of austenite. The methodology for doing this was based on an isothermal transformation model developed on the basis of the mechanism of the bainite reaction, recognising that many experimental observations now support a displacive mode of transformation in which the excess carbon is partitioned shortly after the growth event. There are, nevertheless, three or four adjustable constants which have to be obtained by fitting to experimental data. Many other models in the published literature have generally applied rather empirically, nucleation and ill–defined growth theory within the classical Johnson–Mehl–Avrami–Kolmogorov formalism. These latter models have limited applicability.

The physical model described above, due to Singh and Bhadeshia, based on the mechanism of transformation, was found to have a fundamental error in its autocatalysis function. This led to such great increases in the nucleation rate following the initial transformation event, that it became impossible for the theory to be flexible enough to represent many of the observed shapes of isothermal transformation curves, no matter what values were assigned to the fitting constants. This error was corrected by reverting to an earlier model due to Rees and Bhadeshia.

Several formalisms for converting this isothermal transformation model for continuous cooling conditions were considered. The most popular method involves additivity, which essentially assumes an identical temperature dependence for each of the processes involved in the development of microstructure. Although this was demonstrated to be approximately the case, the most satisfactory method simply involves the integration of the differential equation representing reaction rate over temperature. Indeed, this is the only method which can allow properly for changes in the bainite sub–unit size as a function of temperature.

Great emphasis was placed on the validation of the theories for converting isothermal data. Additivity requires several conditions to be verified and therefore is seldom rigorously

true. Bainite seems to fall into one of three categories of tranformations that can be assumed to be additive. Its sub-units are assumed to grow instantly until a limiting size is attained. But in practice, bi-isothermal experiments were carried out and it has been shown that only alloy A exhibited markedly different reaction rates at the two isothermal temperatures with very clear additivity.

Several problems associated with the reproducibility of experimental data were identified. Depending on the sensitivity of the dilatometric equipments as well as the sample size, significant delay times were sometimes observed before bainite transformation started. Moreover, when using two different samples or even the same sample twice with the same heat treatment, one transformation curve could be translated by as much as 40°C with respect to the other. Finally, an error bar of about 10% was associated with the maximum bainite fraction estimated from the dilatometric data and the austenite and ferrite lattice parameters.

The study of dilatation curves has shown that contrary to the general belief, the 'bump' for the martensite transformation disappears as soon as the fraction of bainite formed previously is superior to about 0.4. However, as expected, there is a continuous decrease in the slope of the dilatometric curves while transformation to martensite occurs. A similar method to the one for bainite was developed to measure, from dilatometric data, the amount of martensite formed in continuous cooling conditions, when it is preceded by bainite. The new method assumes that martensite inherits and keeps all the carbon present in the parent austenite when transformation to bainite ceases. In agreement with the Koistinen and Marburger relationship, the measured martensite volume fraction was shown to vary with the undercooling below M_s, although not to a similar extent.

The model adapted for continuous cooling has been used to predict the volume fractions of bainite and martensite (and retained austenite by difference) present in the microstructures of the three alloys. For alloy A, this was quite successful. For alloys B and C, predictions proved less accurate. Three main sources of errors that seem to undermine the model's potential have been identified and must be tackled in priority, if the model is to be improved further. These errors concern the stored energy of austenite, the nucleation rate (including autocatalysis) especially at austenite grain boundaries and the heterogeneous carbon distribution respectively:

(i) The values of θ_b observed during isothermal heat treatments in Chapter 7 were shown to be insensitive to the transformation temperature. The existence of an incomplete reaction is not questioned: the values of θ_b observed are far from the paraequilibrium values. By setting the value of the stored energy to a fixed value which leads to the T_0' criterion, the model loses a lot of flexibility. It ought to incorporate the strength and

elastic modulus of austenite, the driving force and the temperature, as such parameters are expected to have a marked influence on the stored energy and the phenomenon of plastic relaxation. Variations in these parameters could also explain why transformation rates can either decrease, remain more or less constant or even slightly increase with a decrease in temperature.

(ii) Various results regarding the effect of austenite grain size on bainite transformation kinetics were also observed. It seems that for certain alloys, contrary to the widely accepted theory of hardenability, a larger austenite grain size favours a faster transformation. It was observed in a previous study that one particular alloy with a large austenite grain size was able to develop each of its nuclei into a larger volume than it would have done had d_γ been smaller. Generally, it is clear from the work presented here that there is a lack of work done on the nucleation rates at austenite grain boundaries. For example, a suggestion was made to use the concept of an extended surface instead of an extended volume in order to take account of effects such as site saturation to treat the nucleation at austenite grain boundaries. Furthermore, as was demonstrated by the huge difference in the values of the autocatalysis factor observed in two previous theories, the understanding of autocatalysis is still limited to an empirical approach.

(iii) Last but not least is the inability of existing models to include the formation of carbides and the different enrichments in carbon observed in the two types of residual austenite, namely the blocky regions between sheaves and the small islands between individual sub-units. The model used in this study assumes that the enrichment is uniform, whereas it should be larger for the small regions between the laths. A consequence of this inadequacy is for example that the model can sometimes predict the absence of martensite altogether, when optical micrographs show that it is present in the blocky regions that have been enriched less and therefore have stabilised less.

Several interesting observations that are consistent with known metallurgical trends were made on high-quality optical micrographs. The presence of carbides in upper bainite for some tests on alloy A made the sheaves very distinguishable. Individual plates of martensite were observed in some small regions of retained austenite for alloys B and C and the role of carbon towards austenite stabilisation was clearly observed as small bands of austenite remained untransformed along the sheaves. Large amounts of retained austenite were observed between the laths in the two high-silicon steels where little carbide precipitation can occur. Sheaves of lower bainite etching dark were observed in alloy B.

The model proved its general suitability by correctly reproducing qualitatively known metallurgical trends regarding the effect of various chemical elements. In industrial conditions, the situation where no other phase forms before bainite is difficult to obtain as was the case even in laboratory tests where all the parameters were controlled. The presence of allotriomorphic ferrite can be simulated by changing the austenite composition at the beginning of transformation. Further work is needed to study the influence of this phase at austenite grain boundaries on the density and potency of bainite nucleation sites. This is a necessary step before a 'Grand-Model' taking into account all transformations can be developed.

To return to the main aim of the study, the present work has demonstrated that an economical set of parameters determined by fitting to isothermal data cannot usually be used to accurately predict anisothermal transformation kinetics. It is expected that once the three issues mentioned above have been successfully tackled, the formalism should however prove successful. The success observed for alloy A suggests that the formalism is in essence correct, which is in itself a major achievement.

Appendix 1

Heat Treatments

Alloy A

Experiment type	T_γ (°C)	Details	Hardness HV 20 kg load	γ_R %	Equipment
Isothermal	1200	525°C for 5 min	331, 316	4	THERMEC
		500°C for 5 min	299, 302	5.5	THERMEC
		475°C for 5 min	290, 299	5	THERMEC
		450°C for 5 min	289, 293	0	THERMEC
		425°C for 5 min	326	0	THERMEC
Isothermal	1050	525°C for 5 min	366		BÄHR
		510°C for 10 min			THERMEC
		500°C for 10 min			THERMEC
		485°C for 10 min			THERMEC
		475°C for 5 min			BÄHR
		475°C for 3 h	310	1	THERMEC
		470°C for 10 min			THERMEC
		450°C for 5 min			BÄHR
		430°C for 5 min			THERMEC
Isothermal + Interrupted Quenching	1050	450°C for 13 s	423		BÄHR
		450°C for 25 s	407		BÄHR
		450°C for 36 s	409		BÄHR
		450°C for 50 s	347		BÄHR
Bi-isothermal	1050	500°C for 100 s 450°C for 5 min		7	THERMEC

Table 1: Summary of isothermal heat treatments which gave bainite as the main constituent in alloy A, and associated values of hardness. γ_R % is the percentage of retained austenite in the microstructure determined by sigmametry (where available).

Experiment type	T_γ (°C)	**Details**	**Hardness HV 20 kg load**	γ_R %	**Equipment**
Water cooling	1200	Reference (Martensite)	426	0	
	1050		428	0	
Continuous cooling	1200	1°C s^{-1} until T_{amb}			THERMEC
	1200	2°C s^{-1} until T_{amb}			THERMEC
	1050	1°C s^{-1} until T_{amb}		6	THERMEC
Bi-slope	1050	2°C s^{-1} above 480°C 1°C s^{-1} under 480°C			THERMEC
		2°C s^{-1} above 470°C 0.5°C s^{-1} under 470°C		1	THERMEC
		1°C s^{-1} above 460°C 0.5°C s^{-1} under 460°C			THERMEC
		5°C s^{-1} above 650°C 0.5°C s^{-1} under 650°C		9.5	THERMEC
Bi-slope with Quench	1200	2°C s^{-1} above 546°C Quench under 546°C	398	1	THERMEC
		2°C s^{-1} above 540°C	416	1	THERMEC
		2°C s^{-1} above 520°C	346	3	THERMEC
		2°C s^{-1} above 500°C	302	9	THERMEC
	1050	2°C s^{-1} above 476°C Quench under 476°C	351	1	THERMEC
		2°C s^{-1} above 466°C	392	2	THERMEC
		2°C s^{-1} above 452°C	336	5	THERMEC
		2°C s^{-1} above 430°C	352	3	THERMEC

Table 2: Summary of cooling heat treatments which gave bainite as the main constituent in alloy A and associated values of hardness. γ_R % is the percentage of retained austenite in the microstructure determined by sigmametry (where available).

Alloy B

Experiment type	T_γ (°C)	Details	Hardness HV 20 kg load	Equipment
Isothermal	1200	460°C for 20 min		THERMEC
		408°C for 20 min		THERMEC
		389°C for 20 min	379	THERMEC
		360°C for 20 min		THERMEC
Isothermal	1050	460°C for 20 min	366, 310	THERMEC,BÄHR
		441°C for 20 min		THERMEC,BÄHR
		408°C for 20 min		THERMEC,BÄHR
		389°C for 20 min		THERMEC,BÄHR
		358°C for 20 min		THERMEC,BÄHR
		348°C for 20 min		THERMEC,BÄHR
Bi-isothermal	1200	5 min at 410°C 15 min at 360°C		THERMEC
Fast cooling	1200	Reference (Martensite)	604	THERMEC
Continuous cooling	1200	1°C s^{-1} until T_{amb}		THERMEC
	1200	0.75°C s^{-1} until T_{amb}	343	THERMEC
	1200	15 min at 800°C 1°C s^{-1} until T_{amb}		THERMEC
Bi-slope	1200	2°C s^{-1} above 500°C 0.5°C s^{-1} under 500°C	371	THERMEC
		2°C s^{-1} above 500°C 0.25°C s^{-1} under 500°C	318	THERMEC
		2°C s^{-1} above 500°C 0.1°C s^{-1} under 500°C	283	THERMEC

Table 3: Summary of heat treatments which gave bainite as the main constituent in Alloy B, and associated values of hardness (where available). T_{amb} is the symbol for ambient temperature.

Alloy C

Experiment type	T_γ (°C)	Details	Hardness HV 20 kg load	Equipment
Isothermal	1200	515°C for 10 min		THERMEC
Hollow specimen		495°C for 10 min		THERMEC
Hollow specimen		445°C for 5 min		THERMEC
Isothermal	1050	515°C for 5 min		THERMEC,BÄHR
Hollow if THERMEC		495°C for 5 min		THERMEC,BÄHR
Hollow if THERMEC		470°C for 5 min		THERMEC,BÄHR
Hollow if THERMEC		445°C for 5 min		THERMEC
Bi-isothermal Hollow specimen	1200	100 s at 470°C 500 s at 420°C	267	THERMEC
Fast cooling	1200	Reference (Martensite)	425	THERMEC
Fast cooling	1050	Reference (Martensite)	470	THERMEC
Bi-slope Hollow specimen	1200	20°C s^{-1} above 460°C 0.5°C s^{-1} under 460°C	348	THERMEC
	1200	20°C s^{-1} above 460°C 0.5°C s^{-1} under 460°C		BÄHR
	1200	250°C s^{-1} above 500°C 0.5°C s^{-1} under 500°C		BÄHR
	1200	250°C s^{-1} above 500°C 1°C s^{-1} under 500°C		BÄHR
Bi-slope	1050	20°C s^{-1} above 460°C 0.5°C s^{-1} under 460°C	310	BÄHR
	1050	250°C s^{-1} above 500°C 0.5°C s^{-1} under 500°C		BÄHR
	1050	250°C s^{-1} above 500°C 1°C s^{-1} under 500°C		BÄHR

Table 4: Summary of heat treatments which gave bainite as the main constituent in Alloy C, and associated values of hardness (where available). Solid specimens were used unless otherwise stated.

Appendix 2

The Computer Programs

1. The Physical Model

1.a General Method

Starting from the chemical composition of the alloy, its austenite grain size, the heat treatment schedule (divided in 1000 incremental steps) and the bainite-start temperature calculated as in Chapter 4, the model is able to estimate the bainite transformation kinetics, using the algorithm represented on Figure 1. The output consists of: v, ξ, θ_b, T, u, M_s, $v_{\alpha'}$ and v_γ, *i.e.* namely the bainite volume fraction, the normalised fraction, the maximum fraction at T, the temperature, the plate thickness, the martensite-start temperature of the enriched residual austenite, and the fractions of martensite and austenite. Other quantities such as the nucleation rate, the lattice parameters, the composition of the residual austenite and the transformation rate are also accessible.

In each incremental calculation step, all the quantities are recalculated to allow for changes in temperature and composition as the reaction progresses.

The ferrite and austenite lattice parameters are calculated using equations 4.5 to 4.7. The equilibrium mole fraction of carbon in ferrite is determined with the following relationship [Bhadeshia, 1982b], where the temperature is in °C:

$$\begin{aligned} x_\alpha = {} & 0.1528 \times 10^{-2} - 0.8816 \times 10^{-2} T + 0.2450 \times 10^{-1} T^2 \\ & - 0.2417 \times 10^{-1} T^3 + 0.6966 \times 10^{-2} T^4 \end{aligned} \tag{1}$$

The carbon content of the residual austenite x_γ is calculated using equation 6.1 and the plate thickness u using a neural network model [Singh and Bhadeshia, 1998b]. This requires a knowledge of the yield strength of austenite:

$$\begin{aligned} \sigma_\gamma = {} & \left[1 - 0.26 \times 10^{-2}(T-25) + 0.47 \times 10^{-5}(T-25)^2 - 0.326 \times 10^{-8}(T-25)^3\right] \\ & * \left[15.4\left(4.4 + 23\mathrm{C} + 1.3\mathrm{Si} + 0.24\mathrm{Cr} + 0.94\mathrm{Mo} + 1.2\mathrm{V}\right)\right] \end{aligned} \tag{2}$$

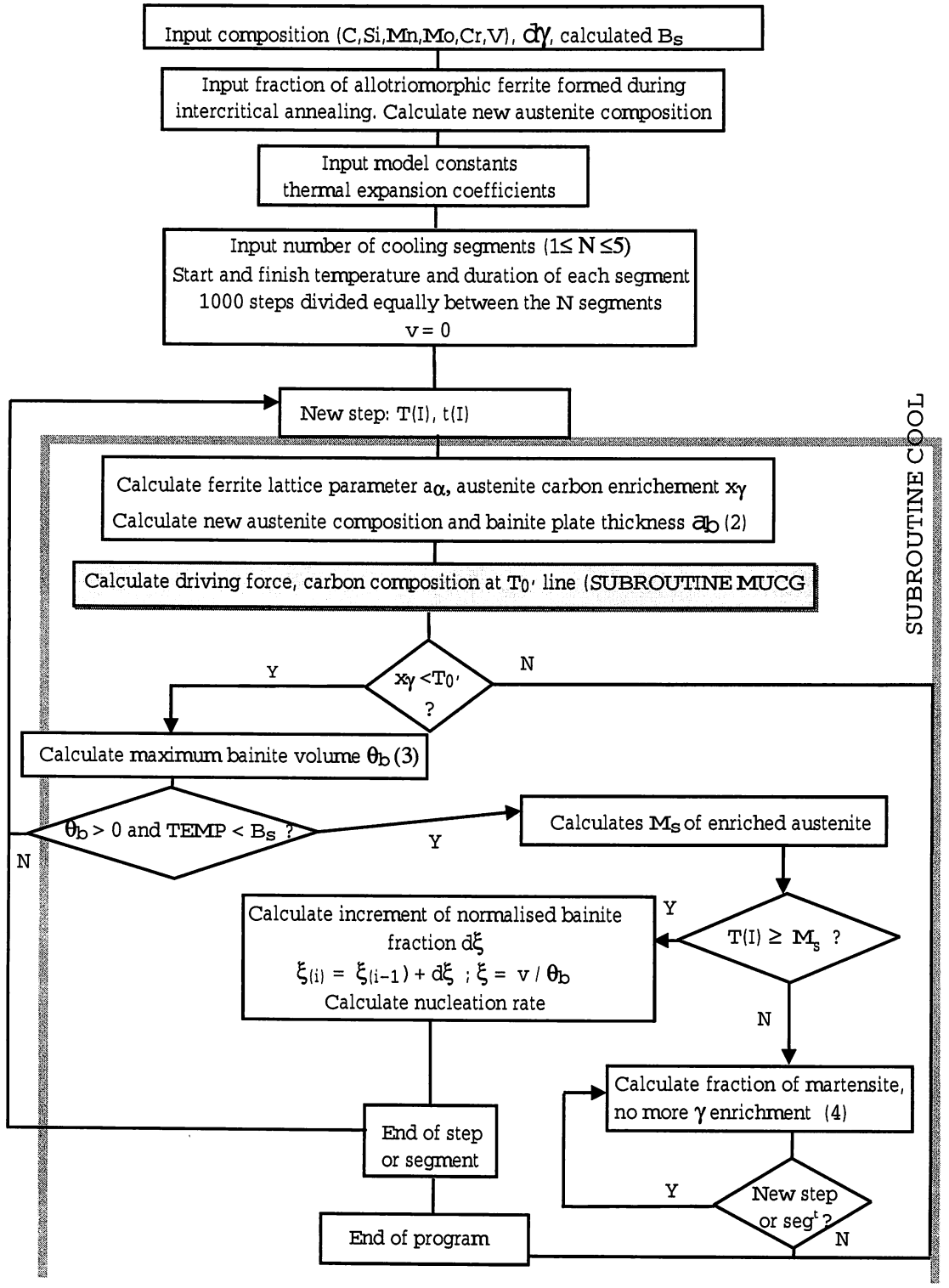

Fig. 1: Method used for estimating the bainite volume fraction. Numbers between parentheses refer to the corresponding equations.

where C, Si, Cr, Mo and V are the molar fractions of the corresponding elements and T is the temperature in°C.

The subroutine MAP STEEL MUCG calculates ΔG_m and the carbon concentrations at the T_0 and T_0' lines. It uses several auxiliary subroutines, the details of which are explained in the next section.

At each step, the maximum volume fraction of bainite θ_b is given by:

$$\theta_b = \frac{(x_{T_0'} - \bar{x})}{(x_{T_0'} - x_\alpha)} \tag{3}$$

$\theta_b > 0$ for $T < B_s$, the increment in fraction is then calculated using equation 3.2 and added to that existing given that $T > M_s$. In fact, the calculations deal with the normalised volume fraction ξ.

MAP STEEL MSTART calculates the martensite-start temperature as a function of the chemical composition [Bhadeshia, 1981]. When T falls below M_s of the enriched austenite, transformation to bainite is stopped (Figure 1). The fraction of martensite $v_{\alpha'}$ depends only on the undercooling below M_s and is calculated in MAP STEEL MART2, using the Koistinen and Marburger equation [1959].

$$v_{\alpha'} = 1 - \exp\Big(-0.011(M_s - T)\Big) \tag{4}$$

1.b The Subroutine MAP STEEL MUCG

The structure of the procedure is explained in Figure 2, where an arrow indicates that the output of one of the subroutines or functions is used by another.

Assuming that the free energy surface of austenite can be extrapolated into temperatures where it is not the stable phase, the T_0 temperature can be defined [Zener, 1946] such that stress free austenite and ferrite of the same composition have identical free energies. Thus, any transformation without a composition change can occur only below the T_0 temperature.

A model for the calculation of the T_0 temperature was presented by Aaronson *et al.* [1966a] and subsequently corrected by Shiflet *et al.* [1978]. This model is based on the Lacher [1937] and Fowler and Guggenhiem [1939] formalism and is considered to be particularly reliable at low temperatures. It can be adapted for alloy steels by the methods of Kinsman and Aaronson [Oblak and Hehemann, 1967] and Aaronson *et al.* [1966b].

Bhadeshia modified the equations of [Shiflet *et al.*, 1978] to allow the ferrite to inherit the full carbon content of the austenite and take account of the Zener ordering term, Δf^* [Fisher, 1949]. The value of x corresponding to the T_0 temperature, x_{T_0} is given by:

$$\Delta G^{\gamma \rightarrow \alpha} = 0 \tag{5}$$

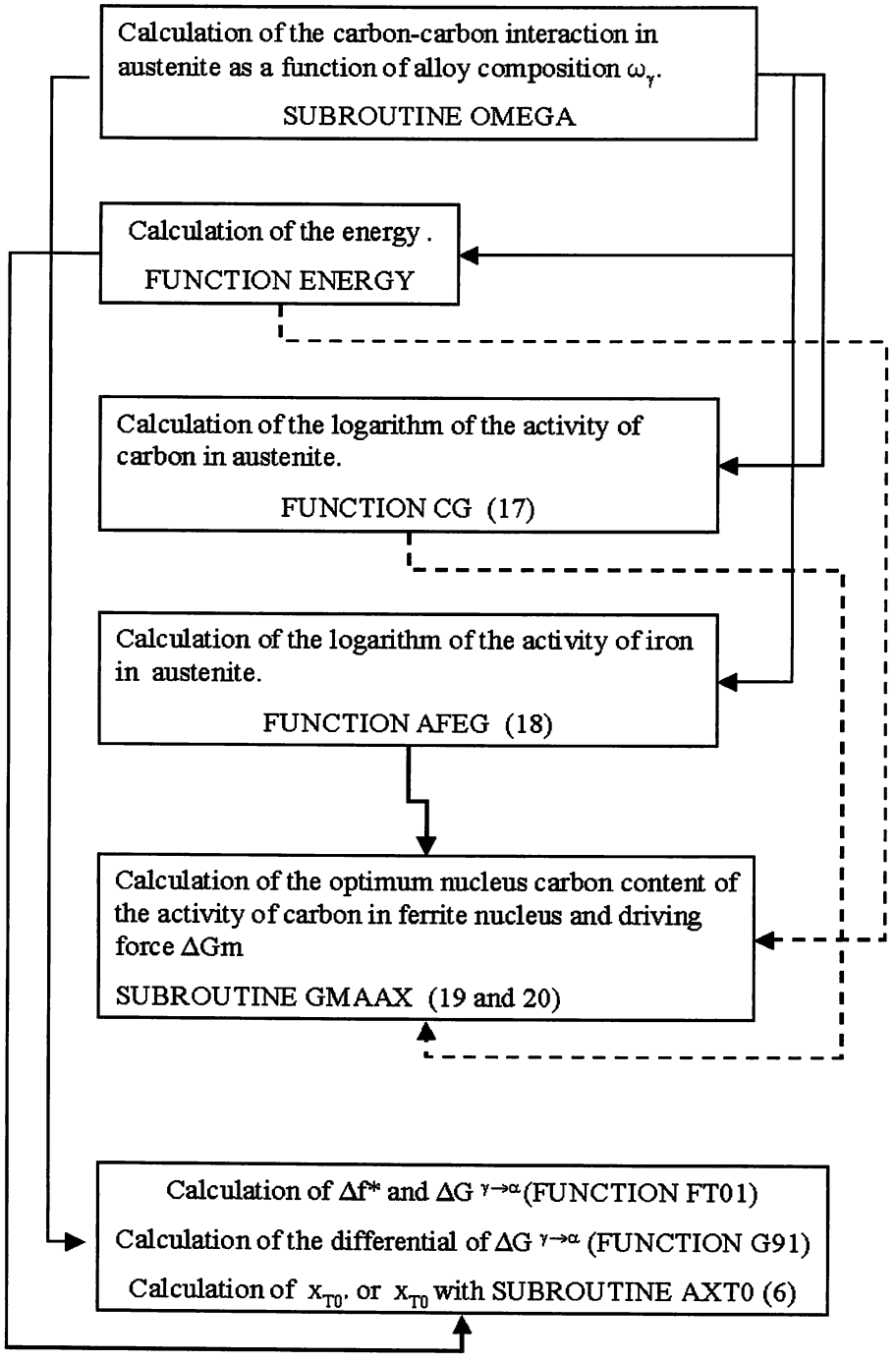

Fig. 2: Schematic diagram representing the successive calculations performed in the subroutine MAP STEEL MUCG. It calculates the available driving force ΔG_m and the carbon contents at the T_0 and T_0' lines for the temperature considered. Numbers between parentheses refer to the corresponding equations.

where

$$\begin{aligned}\Delta G^{\gamma\to\alpha} = {} & 2xRT\ln x + x(\Delta\bar{H}_\alpha - \Delta\bar{H}_\gamma - (\Delta S_\alpha - \Delta S_\gamma)T + 4\omega_\alpha - 6\omega_\gamma) \\ & - 4RT(1-x)\ln(1-x) + 5RT(1-2x)\ln(1-2x) \\ & - 6RTx\ln\left|\frac{\delta_\gamma - 1 + 3x}{\delta_\gamma + 1 - 3x}\right| - 6RT(1-x)\ln\left|\frac{1-\tau_\gamma + (4\tau_\gamma - 1)x - \delta_\gamma}{2\tau_\gamma(2x-1)}\right| \\ & + 3RTx\ln(3-4x) + 4RTx\ln\left|\frac{\delta_\alpha - 3 + 5x}{\delta_\alpha + 3 - 5x}\right| \\ & + (1-x)\left|141\sum_i Y_i(\Delta T_{magi} - \Delta T_{nmi}) + \Delta G_{Fe}^{\gamma\to\alpha}\left\{T - 100\sum_i \Delta T_{magi}\right\}\right| \\ & + \Delta f^*\end{aligned} \tag{6}$$

where

$$\delta_\alpha = \left|9 - 6x(2\tau_\alpha + 3) + (9 + 16\tau_\alpha)x^2\right|^{1/2} \tag{7}$$

$$\delta_\gamma = \left|1 - 2(1 + 2\tau_\gamma)x + (1 + 8\tau_\gamma)x^2\right|^{1/2} \tag{8}$$

$$\tau_\alpha = 1 - \exp(-\omega_\alpha/RT) \tag{9}$$

$$\tau_\gamma = 1 - \exp(-\omega_\gamma/RT) \tag{10}$$

In equation 6 [Bhadeshia and Edmonds, 1980], R is the gas constant, x is the mole fraction of carbon, and Y_i is the atom fraction of the ith substitutional alloying element when the presence of carbon is disregarded. Values for $\Delta G_{Fe}^{\gamma\to\alpha}$ were obtained from Kaufmann *et al.* [1963]. ΔT_{magi} and ΔT_{nmi} refer to the displacement in the temperature at which the free energy change $\Delta G_{Fe}^{\gamma\to\alpha}$ accompanying the $\gamma \to \alpha$ transformation in pure iron is evaluated in order to allow for the changes (per at. %) due to alloying elements effects on its magnetic and non-magnetic components, respectively. These components were obtained from Aaronson *et al.* [1966b]:

$$\Delta T_M = \sum_i \Delta T_{magi} = -3\text{Si} - 37.5\text{Mn} - 6\text{Ni} - 26\text{Mo} - 19\text{Cr} - 44\text{V} \tag{11}$$

where Si, Mn, Ni, Mo, Cr, V are atomic percentages of the corresponding elements. Similarly:

$$\Delta T_{NM} = \sum_i \Delta T_{nmi} = \Delta T_M - 3\text{Si} + 2\text{Mn} + 12\text{Ni} - 9\text{Mo} - 9\text{Cr} - 1\text{V} \tag{12}$$

The term $\left|141 \sum_i Y_i(\Delta T_{magi} - \Delta T_{nmi}) + \Delta G_{Fe}^{\gamma \rightarrow \alpha} \left\{ T - 100 \sum_i \Delta T_{magi} \right\}\right|$ is the output (in J mol $^{-1}$) of the function MAP STEEL ENERGY. The function $\Delta G_{Fe}^{\gamma \rightarrow \alpha}$ is expressed as:

$$\begin{aligned} \Delta G_{Fe}^{\gamma \rightarrow \alpha} = & -8.88909 + 0.26557(T - 1140) - 1.04923 \times 10^{-3}(T - 1140)^2 \\ & + 2.70013 \times 10^{-6}(T - 1140)^3 - 3.58434 \times 10^{-9}(T - 1140)^4 \end{aligned} \tag{13}$$

for temperatures superior to 940 K (667°C) and approximated to:

$$\Delta G_{Fe}^{\gamma \rightarrow \alpha} = 1.30089T - 1331 \tag{14}$$

for temperatures between 700 and 940 K (427 to 667°C) and

$$\Delta G_{Fe}^{\gamma \rightarrow \alpha} = 1.65786T - 1581 \tag{15}$$

for temperatures between 300 and 700 K (27 to 427°C) and

$$\Delta G_{Fe}^{\gamma \rightarrow \alpha} = 1.38T - 1499 \tag{16}$$

for temperatures less than 300 K (27°C).

The carbon-carbon interaction energy in austenite ω_γ (in J mol $^{-1}$), is calculated using the procedure of Shiflet *et al.* [1978] and Kinsman and Aaronson [reply to Oblak and Hehemann, 1967], which is coded in MAP STEEL OMEGA, and the optimised activity data of Uhrenius [1973]. The ω_γ value is expressed as a function of concentrations of various alloying elements. The carbon-carbon interaction energy in ferrite was evaluated by Bhadeshia [1980] to be 48570 J mol $^{-1}$, using the activity data of Lobo and Geiger [1976]. The other parameters, were determined to be:

$$\Delta \bar{H}_\alpha = 111918 \text{ J mol}^{-1} \text{ [Lobo and Geiger, 1976]}$$

$$\Delta S_\alpha = 51.44 \text{ J mol}^{-1}\text{K}^{-1} \text{ [Lobo and Geiger, 1976]}$$

$$\Delta \bar{H}_\gamma = 38575 \text{ J mol}^{-1} \text{ [Shiflet } et \text{ } al.\text{, 1978]}$$

$$\Delta S_\gamma = 13.48 \text{ J mol}^{-1}\text{K}^{-1} \text{[Shiflet } et \text{ } al.\text{, 1978]}$$

$\Delta\bar{H}_\alpha$ and ΔS_α are the excess partial molar enthalpy and entropy of solution of carbon in ferrite. Similarly, $\Delta\bar{H}_\gamma$ and ΔS_γ are the excess partial molar enthalpy and entropy of solution of carbon in austenite.

The functions MAP STEEL CG and MAP STEEL AFEG calculate the natural logarithms of the activity of carbon and iron in austenite respectively according to Aaronson *et al.* [1966a]:

$$\ln a_{c_\gamma} = 5\ln\left(\frac{1-2x_\gamma}{x_\gamma}\right) + \frac{6\omega_\gamma}{RT} + \frac{\Delta\bar{H}_\gamma - \Delta\bar{S}_\gamma^{xS}T}{RT} + 6\ln\left[\frac{-1+3x_\gamma+\delta_\gamma}{1-3x_\gamma+\delta_\gamma}\right] \tag{17}$$

$$\ln a_{Fe_\gamma} = 5\ln\left(\frac{1-x_\gamma}{1-2x_\gamma}\right) + 6\ln\left[\frac{1-2\tau_\gamma+(4\tau_\gamma-1)x_\gamma-\delta_\gamma}{2\tau_\gamma(2x_\gamma-1)}\right] \tag{18}$$

The subroutine MAP STEEL GMAAX uses Newton iteration and the calculated activities to obtain the optimum nucleus carbon content and the activity of carbon in the ferrite nucleus. The latter is equal to [Aaronson *et al.*, 1966a]:

$$\ln a_{c_\alpha} = 3\ln\left(\frac{3-4x_\alpha}{x_\alpha}\right) + \frac{4\omega_\alpha}{RT} + \frac{\Delta\bar{H}_\alpha - \Delta\bar{S}_\alpha^{xS}T}{RT} + 4\ln\left[\frac{-3+5x_\alpha+\delta_\alpha}{3-5x_\alpha+\delta_\alpha}\right] \tag{19}$$

The available driving force for nucleation, ΔG_m is given by:

$$\Delta G_m = RT(\ln a_{c_\alpha} - \ln a_{c_\gamma}) \tag{20}$$

The function MAP STEEL FT01 calculates the free energy change accompanying the transformation from austenite to ferrite of the same chemical composition (equation 6), including a Zener ordering term [Zener, 1946] and 400 J mol $^{-1}$ of stored energy for the calculation of the T_0' curve. The Zener term describes the ordering of carbon atoms that leads to the body-centred cubic lattice of ferrite becoming body-centred tetragonal. The degree of ordering increases as the carbon concentration increases, or as the transformation temperature decreases. MAP STEEL G91 calculates the differential (with respect to the carbon concentration at the T_0 boundary) of the function calculated in MAP STEEL FT01.

Finally, the subroutine MAP STEEL AXTO, which contains the two previous subroutines, calculates the carbon concentration (mole fraction) at the T_0 or T_0' boundary, at a specified temperature. As mentioned above, the right concentration has been found when the free energy change accompanying the transformation from austenite to ferrite of the same chemical composition becomes nil. The concentration is found by a Newton iteration procedure.

2. Determination of the Experimental Bainite Fraction

A certain number (specified by the user) of points are selected from dilatometric data to evaluate the bainite fraction. There are three columns of data, namely the temperature T, the dilatational strain $\frac{\Delta L}{L_0}$ and the time t. The dilatometric curve $\frac{\Delta L}{L_0}$ vs t must first be plotted in order to determine the time t_s at which expansion is first detected, an indication that transformation has started.

For continuous cooling transformations, the values of dilatations represent the difference between the measured length and that expected from thermal expansion. In the case of a bi-isothermal experiment, after the change in temperature has taken place, it is necessary to add the decrease in dilatation due to thermal contraction to the measured dilatational strain.

The algorithm used to calculate the fraction of bainite as a function of dilatation is summarised on Figure 3. The lattice parameters at ambient temperature and the thermal expansion coefficients of ferrite and austenite must be known. In MAP STEEL DILAT, the ferrite lattice parameter at ambient temperature $\bar{a}_\alpha$ is taken to be 2.870×10^{-10} m and is subsequently increased by 0.001×10^{-10} m up to 2.875×10^{-10} m, to have five sets of experimental data. The data corresponding to $\bar{a}_\alpha = 2.870 \times 10^{-10}$ m were systematically chosen in the present study.

The austenite lattice parameter at ambient temperature $\bar{a}_\gamma$ is given by [Dyson and Holmes, 1970]:

$$\bar{a}_\gamma = 3.573 + 0.00095\text{Mn} - 0.0002\text{Ni} + 0.0006\text{Cr} + 0.0031\text{Mo} + 0.0018\text{V} + 0.033\text{C} \qquad (21)$$

where the concentrations are the average alloy concentrations in wt%.

MAP STEEL PARAM obtains values for the carbon concentration and the lattice parameter of carbon-enriched austenite at a temperature T, due to partial transformation of austenite to ferrite [Bhadeshia *et al.*, 1991], where T is in K.

$$a_\gamma = a_{0\gamma} C_c (x_\gamma - \bar{x}) \Big(1 + e_\gamma (T - 298) \Big) \qquad (22)$$

$$x_\gamma = (\bar{x} - x_\alpha)[v\rho_\alpha / (1 - v)\rho_\gamma] + \bar{x} \qquad (23)$$

where $a_{0\gamma}$ and a_γ are the austenite lattice parameters at temperature T before and after carbon enrichment; $\bar{x}$ and x_γ are the weight fractions of carbon in the austenite before and after enrichment; e_γ is the thermal expansion coefficient of austenite; C_c is the change in

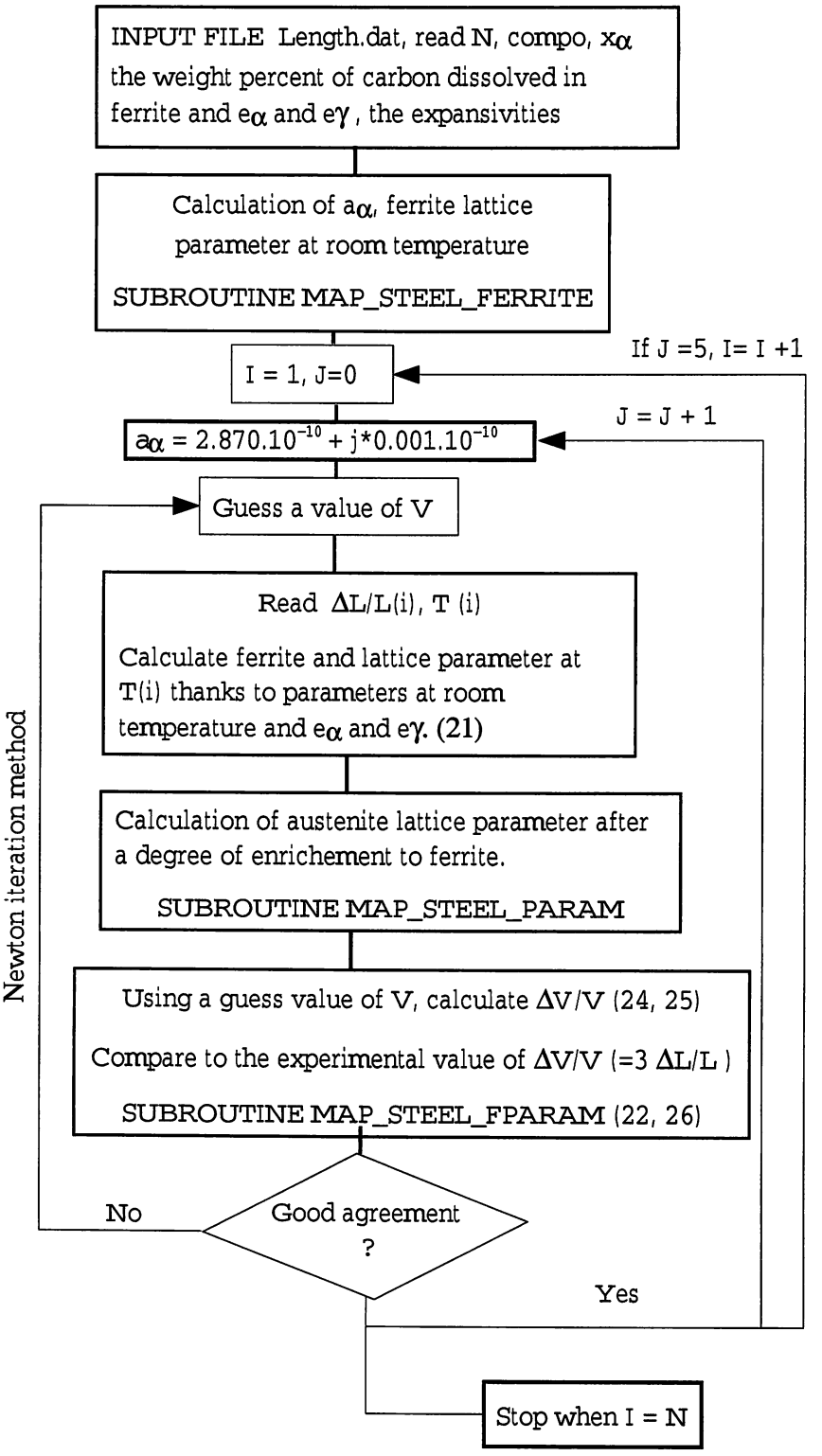

Fig. 3: Schematic diagram illustrating the method used for the determination of the experimental bainite volume fraction from the selected dilatation data. SUBROUTINE MAP STEEL DILAT. Numbers between parentheses refer to the corresponding equations.

the austenite lattice parameter caused by the addition of unit concentration of carbon (3.3×10^{-10}m, equation 21); x_α is the carbon concentration in the ferrite; v is the bainite volume fraction; ρ_a and ρ_g are the densities of ferrite (bainite) and austenite. Equation 23 is imposed by mass conservation. The densities are calculated from the lattice parameters, where it is assumed that all the atoms are Fe and no corrections are made for the compositional differences between the phases using the following:

$$\rho_\alpha = \frac{55.847 \times 2}{(6.0221367 \times 10^{23} a_\alpha^3)}$$

$$\rho_\gamma = \frac{55.847 \times 4}{(6.0221367 \times 10^{23} a_\gamma^3)}$$

Finally, subroutine MAP STEEL FPARAM uses calculated values for the lattice parameters for a given volume fraction of bainite to evaluate the expected fractional change in volume [Bhadeshia *et al.*, 1991]:

$$\frac{\Delta V}{V} = 1 - \frac{a_{0\gamma}^3}{\zeta + a_\gamma^3} \tag{24}$$

with

$$\zeta = \frac{2a_\alpha^3 - a_\gamma^3}{1 + [(2v_\gamma a_\alpha^3)/(v a_\gamma^3)]} \tag{25}$$

The output of the subroutine is the difference between this calculated value ($\frac{\Delta V}{V}$) and the experimentally measured fractional volume change taken as 3 $\frac{\Delta L}{L_0}$. The difference is decreased by iteration until the right value is found.

References

Aaronson, H. I., Domian, H. A., Pound, G.M., *Trans. Met. Soc. AIME* **236** 1966a 753

Aaronson, H. I., Domian, H. A., Pound, G.M., *Trans. Met. Soc. AIME* **236** 1966b 768

Agren, J., *Acta Metallurgica* **37** 1989 181

Ali, A., Bhadeshia, H. K. D. H., *Materials Science and Technology* **6** 1990 781

Ali, A., Bhadeshia, H. K. D. H., *Materials Science and Technology* **7** 1991 895

Andrews, K. W., *Journal of the Iron and Steel Institute* **203** 1965 721

Avrami, M., *Journal of Chemical Physics* **7** 1939 1103

Avrami, M., *Journal of Chemical Physics* **8** 1940 212

Babu, S. S., Bhadeshia, H. K. D. H., *Materials Science and Engineering* **A142** 1991 209

Babu, S. S., *Ph.D. Thesis- Acicular Ferrite and Bainite in Fe–Cr–C Weld Deposits,* University of Cambridge, UK, 1991 27

Babu, S. S., Hono, K., Sakuri, T., *Applied Surface Science* **67** 1993 321

The Bainite Committee of the Iron and Steel Institute of Japan, *Atlas for Bainitic Microstructures,* ISIJ, Japan, 1992

Barford, J., Owen, W. S., *J. Iron Steel Inst.* **197** 1961 146

Barnes, J. M., Muddle, B. C., Hodgson, P. D., *Proc. of Int. Conf. on Solid → Solid Phase Transformations,* ASM, Pittsburgh, Metals Park, OH., 1995 993

Bhadeshia, H. K. D. H., Edmonds, D. V., *Metallurgical Transactions A* **10A** 1979 895

Bhadeshia, H. K. D. H., *Metal Science* 1980 230

Bhadeshia, H. K. D. H., Edmonds, D. V., *Acta Metallurgica* **28** 1980 1265

Bhadeshia, H. K. D. H., *Metal Science* **15** 1981 175

Bhadeshia, H. K. D. H., *Acta Metallurgica* **29** 1981b 1117

Bhadeshia, H. K. D. H., *International Conference on Solid → Solid Phase Transformations,* eds H. I. Aaronson *et al.*, TMS-AIME, Warrendale, PA, USA, 1981c 1041

Bhadeshia, H. K. D. H., Waugh, A. R., *Proc. of Int. Conf. on Phase Transformations during the Thermal/Mechanical Processing of Steel,* Microstructure and Properties of Continuously Cooled Low-Carbon Bainitic Steels, 1981, 161

Bhadeshia, H. K. D. H., *Journal de Physique, Colloque C4* **43** 1982 443

Bhadeshia, H. K. D. H., Waugh, A. R., *Acta Metall.* **30** 1982 775

Bhadeshia, H. K. D. H., Waugh, A. R., *Int. Conf. on Phase Transformations in Ferrous Alloys,* eds Marder A. R. and Goldstein, J. I., ASM, Cleveland. OH, 1984 335

Bhadeshia, H. K. D. H., *Materials Science and Technology* **5** 1989 131

Bhadeshia, H. K. D. H., David, S. A., Vitek, J. M., Reed, R. W., *Materials Science and Technology* **7** 1991 686

Bhadeshia, H. K. D. H., *Bainite in Steels,* The Institute of Materials, London, 1992 451

Bhadeshia, H. K. D. H., *New bainitic Steels by Design, Displacive Phase Transformations and Their Applications in Materials Engineering,* edited by K.Inoue, K. Mukerjee, K. Otsuka, and H. Chen, The Minerals, Metals, Materials Society, 1998 69

Bhadeshia, H. K. D. H., Strang, A., Gooch, D. J., *International Materials Review* **43** 1998 45

Bhadeshia, H. K. D. H., *Materials Science and Technology* **15** 1999 22

Bhadeshia, H. K. D. H., *Materials Science and Engineering A* **A273-275** 1999b 58

Bhadeshia, H. K. D. H., *Bainite in Steels, second edition,* The Institute of Materials, London, 2001 406

Blondeau, J., *Heat Treatment,* Metals Society, London, 1976 286

Bramfitt, B. L, Speer, J. G., *Iron and Steelmaking* **17** 1990 65

Cahn, J. W., *Acta Metallurgica* **4** 1956a 572

Cahn, J. W., *Acta Metallurgica* **4** 1956b 449

Chance, J., Ridley, N., *Metallurgical Transactions A* **21A** 1981 1205

Chang, L. C., Bhadeshia, H. K. D. H., *Materials Science and Technology* **12** 1995 874

Chang, L. C., Bhadeshia, H. K. D. H., *Materials Science and Technology* **12** 1996 233

Chang, L. C., *Metallurgical and Materials Transactions A* **30A** 1999 909

Chester, N. A., Bhadeshia, H. K. D. H., *J.Phys.IV France 7* **C5** 1997 41

Chew, S., Griffiths, J. R., Stachurski Z. H., *Polymer* **30** 1989 874

Christian, J. W., *Physical Properties of Martensite and Bainite,* Spec. Rep. 93, Iron and Steel Inst., London, 1965

Christian, J. W., *The Theory of Transformations in Metals and Alloys,* Pergamon Press, Oxford, 1965b 489

Christian, J. W., *Theory of Transformations in Metals and Alloys,* Part 1, 2nd. edn. Pergamon Press, Oxford, 1975

Coates, D. E., *Metall.Trans.* **4** 1973a 1077

Coates, D. E., *Metall.Trans.* **4** 1973b 2313

Davenport, E. S., Bain, E. C., *Trans. AIME* **90** 1930 117

Davenport, A. S., *Trans. Met. Soc. AIME* **145** 1941 301

Dearden, J., O'Neill, H., *Guide to the Selection and Welding of Low Alloy Structural Steels,* Institute of Welding Transactions, 1940, 203

Donnay, B., Herman, J. C., Leroy, V., *Microstructure evolution of C-Mn Steels in the Hot Deformation Process: the STRIPCAM Model,* Dunkerque, 1995, 23

Dyson, D. J., Holmes, B., *J. Iron Steel Inst.* **208** 1970 469

Enomoto, M., *Tetsu-to-Hagane* **80** 1994 73

Fang, L., Wood, W. E., Atteridge, D. G., *Metallurgical and Materials Transactions A* **28A** 1997 5

Fisher, J. C., *Met Trans* **185** 1949 688

Fowler, R. H., Guggenhiem, E. A., *Statistical Thermodynamics,* Cambridge University Press, New York, 1939 442

Giraud E., Jacques, P., Ratchev, P., Van Humbeeck, J., Verlinden, B., Aernoudt, E., *Materials Science and Engineering* **A273-A275** 1999 471

Graham, L. W., Axon, H. J., *J. Iron Steel Inst.* **191** 1959 361

Grube, W. L., Rouze, S. R., *High Temperature-High Resolution Metallography,* Gordon and Breach, New York, 1967 313

Hansen, *Constitution of Binary Alloys,* 2nd edition, McGraw-Hill, 1958

Hawbolt, E. B., Kamat, R., Chau, B., Brimacombe, J. K., *Application of Isothermal Phase Transformation Kinetics to Predict Continuous Cooling Behaviour,* Proceedings of an International Conference on Solid-Solid Phase Transformations, 1981, 522

Hehemann, R. F., *Phase Transformations,* AM, Metals Park, Ohio, USA, 1970 397

Hehemann, R. F., Kinsman, K. R., Aaronson, H. I., *Metall. Trans.* **3** 1970b 1077

Hillert, M., *Paraequilibrium,* Internal Report, Swedish Inst. Met. Res., Stockholm, Sweden, 1953

Hillert, M., *Decomposition of Austenite by Diffusional Processes,* eds. V. F. Zackay and H. I. Aaronson, Interscience, New York, 1962 197

Hillert, M., *Metall. Trans. A* **6A** 1975 5

Huang, C. Y., Yang, J. R., Wang, S. C., *Mat. Trans. JIM* **34** 1993 658

Hultgren, A., *Jernkontorets Ann.* **135** 1951 403

Irvine, Pickering, J., *J. Iron Steel Inst.* **187** 1957 292

Jacques, P., Giraud E., Catlin, T., Geerlofs, N., Kop, T., Van der Zwaag, S., Delannay, F., *Materials Science and Engineering* **A273-A275** 1999 475

Jones, S. J., Bhadeshia, H. K. D. H., *Acta Mater.* **45** 1997 2911

Josefsson, B., Andren, H. O., *Proc. of the 35th Int. Field Emission Symp.,* Oak Ridge, TN, 1988, 18

Josefsson, B., Andren, H. O., *Recent Trends in Welding Science and Technology,* eds S. A. David and J. Vitek, ASM International, OH, 1989 243

Jung, Y. C., Ohmori, Y., Nakai, K., Ohtsubo, H., *ISIJ International* **37** 1997 789

Kaufman, L., Radcliffe, S. V., *Decomposition of Austenite by Diffusional Processes,* eds. V. F. Zackay and H. I. Aaronson, Interscience, New York, 1962 313

Kaufman, L., Clougherty, E. V., Weiss, R. J., *Acta Metall.* **11** 1963 323

Kinsman, K. R., Eichen, E., Aaronson, H. I., *Metall. Trans. A* **6** 1975 303

Kirkaldy, J. S., *Can. J. Phys.* **36** 1958 899

Krielaart, G. P., Van der Zwaag, S., *Materials Science and Technology* **14** 1998 10

Ko, T., Cottrell, S. A., *J. Iron Steel Institute* **172** 1952 307

Koistinen, D. P., Marburger, R. E., *Acta Metallurgica* **7** 1959 59

Kriesement, O., Wever, F., *Mechanism of Phase Trans. in Met.,* Institute of Metals, Monograph and Rep. Ser. No 18, London, 1956 253

Krüger, P., *J. Phys. Chem. Solids* **54** 1993 1549

Kuban, M. B., Jayaraman, R., Hawbolt, E. B., Brimacombe, J.K., *Metall. Transactions A* **17A** 1986 1493

Kurdjumov, G. V., Sachs, G., *Z. Phys.* **64** 1930 325

Lacher, J. R., *Proc. Cambridge Phil. Soc.* **33** 1937 518

Larn, R. H., Yang, J. R., *Materials Science and Engineering* **A278** 1999a 278

Larn, R. H., Yang, J. R., *Materials Science and Engineering* **A264** 1999b 139

Lee, J. L., Pan, Y. T., Hsieh, K. C., *Materials Transactions, JIM* **39** 1998 196

Lee, J. K., *Prediction of $\gamma \rightarrow \alpha$ Transformation During Continuous Cooling of Steel,* 41st MWSP Conf. Proc., ISS, 37, 1999 975

Lobo, J. A., Geiger, H., *Metallurgical Transactions A* **7A** 1976 1347

Lusk, M., Jou, H. J., *Metallurgical and Materials Transactions B* **28A** 1997 287

Manohar, P. A., Chandra, T., Killmore C. R., *ISIJ International* **36** 1996 1486

Matsuzaki, A., Bhadeshia, H. K. D. H., Harada, H., *Acta Metallurgica et Materiala* **42** 1994 1081

Matsuzaki, A., Bhadeshia, H. K. D. H., *Materials Science and Technology* **15** 1999 518

Medina, S. F., Mancilla, J. E., *ISIJ International* **36** 1996 1070

Minote, T., Torizuka, S., Ogawa, A., Niikura, M., *ISIJ International* **36** 1996 201

Mujahid, S. A., Bhadeshia, H. K. D. H., *Acta Metallurgica et Materialia* **41** 1993 967

Nakamura, T., Nagakura, S., *Int. Conf. on Martensitic Transformations (ICOMAT 86),* The Japan Institute of Metals, 1986, 1057

Nishiyama, Z., *Sci. Rep. Tohoku Univ.* **23** 1934 325

Oblak, J. M., Hehemann, R. F., *Transformations and Hardenability in Steels,* Climax Moly., Ann Arbor, MI, 1967 15

Oka, M., Okamoto, H., *Displacive Phase Transformations and Their Applications in Materials Engineering,* Edited by K. Inoue, K. Mukherjee, K. Otsuka and H. Chen; The Minerals, Metals and Materials Society, 1998, 79

Olson, G. B., Bhadeshia, H. K. D. H., Cohen, M., *Metallurgical Transactions A* **21A** 1990 805

Park, S. H., Yue, S., Jonas, J. J., *Metallurgical Transactions A* **23A** 1992 1641

Pham, T. T., Hawbolt, E. B., Brimacombe, J. K., *Metallurgical and Materials Transactions A* **26A** 1995 1987

Purdy, G. R., Weichert, D. H., Kirkaldy, J. S., *TMS-AIME* **230** 1964 1025

Quidort, D., *Ph.D Thesis- Mécanismes et Modélisation des Cinétiques de la Transformation Bainitique dans les aciers,* ENSEEG, Grenoble, France, 1999

Rees, G. I., Bhadeshia, H. K. D. H., *Materials Science and Technology* **8** 1992 985

Rees, G. I., Perdrix, J., Maurickx, T., Bhadeshia, H. K. D. H., *Materials Science and Engineering* **A194** 1995 179

Robertson, J. M., *J. Iron Steel Institute* **119** 1929 391

Robson, J. D., Bhadeshia, H. K. D. H., *Materials Science and Technology* **13** 1997 631

Rudberg, E., *Jernkontorets Ann.* **136** 1952 91

Sandvik, B. P. J., *Metallurgical Transactions A* **13A** 1982 789

Scheil, E., *Anlaufzeit der Austenitumwandlung. Archiv fur das Eisenhuttenwesen* **8** 1935 565

Shiflet, G. J., Bradley, J. R., Aaronson, H. I., *Metall. Trans. A* **9** 1978 999

Shipway, P. H., Bhadeshia, H. K. D. H., *Materials Science and Technology* **11** 1995 1116

Shipway, P. H., Bhadeshia, H. K. D. H., *Materials Science and Engineering* **A223** 1997 179

Singh, S. B., *Ph.D. Thesis,* University of Cambridge, UK, 1998a

Singh, S. B., Bhadeshia, H. K. D. H., *Materials Science and Engineering* **A245** 1998b 72

Smith, Y. E., Siebert, C. A., *Metall. Trans* **2** 1971 1711

Srinivasan, G. R., Wayman, C. M., *Acta Metallurgica* **16** 1968 609

Stark, I., Smith, G. D. W., Bhadeshia, H. K. D. H., *Solid → Solid Phase Transformations,* Institute of Metals, London, 1988 211

Stark, I., Smith, G. D. W., Bhadeshia, H. K. D. H., *Metall. Trans. A* **21A** 1990 847

Steven, W., Haynes, A. J., *J. Iron Steel Inst.* **183** 1956 349

Sugden, A. A. B., Bhadeshia, H. K. D. H., *Metallurgical Transactions A* **20A** 1989 1811

Swallow E., Bhadeshia, H. K. D. H., *Materials Science and Technology* **12** 1996 121

Takahashi, M., Bhadeshia, H. K. D. H., *J. Mater. Sci. Lett.* **8** 1989 477

Takahashi, M., Bhadeshia, H. K. D. H., *Materials Science and Technology* **6** 1990 592

Thelning, *Steel and its Heat Treatment,* Bofors Handbook, Butterworth, 1975

Thomson, R. C., *Carbides in Steels,* Unpublished work, Cambridge, 1998

Todinov, M. T., *Metallurgical and Materials Transactions B* **29B** 1998 269

Trivedi, R., *Metall. Trans.* **1** 1970 921

Tsivinsky, S. V., Kogan, L. I., Entin, R. I., *Problems of Metallography and the Physics of Metals,* B. Ya Lybubov editor, State Scientific Press, Moscow (Translation published by the Consultants Bureau Inc., New York, 1959, 1955 185

Tsuji, N., Matsubara, Y., Sakai, T., Saito, Y., *ISIJ International* **37** 1997 797

Tsuzaki, K., Ueda, T., Fujiwara, K., Maki, T., *Proc. 1st Japan International SAMPE Symposium and Exhibition,* eds N. Igata *et al.*, Society for Advancement of Materials and Process Engineering, Japan, 1989 799

Tsuzaki, K., Kodai, A., Maki, T., *Metallurgical and Materials Transactions A* **25A** 1994 2009

Umemoto, M., Komatsubara, N., Tamura, I., *The Equivalent Cooling Curve- A New Method to Describe Continuous Cooling Transformation Kinetics on TTT Diagrams,* Proceedings of an International Conference on Solid-Solid Phase Transformations, 1981, 1111

Umemoto, M., Horiuchi, K., K., Tamura, I., *Transactions ISIJ* **22** 1982a 854

Umemoto, M., Nishioka, N., K., Tamura, I., *Transactions ISIJ* **22** 1982b 629

Umemoto, M., Horiuchi, K., Tamura, I., *Transactions ISIJ* **23** 1983 690

Uhrenius, B., *Scand. J. Metall.* **2** 1973 177

Verdi, C., Visintin, A., *Acta Metall.* **11** 1987 2711

Wang, S. C., Yang, J. R., *Materials Science and Engineering* **A154** 1992 43

Wang, S. C., Kao, P. W., *Journal of Materials Science* **28** 1993 5169

Wierszyllowski, I. A., *Metallurgical Transactions A* **22A** 1991 993

Yamamoto, S., Yokoyama, H., Yamada, K., Niikura, M., *ISIJ International* **35** 1995 1020

Young, C. H., Bhadeshia, H. K. D. H., *Materials Science and Technology* **10** 1994 209

Zarei Hanzaki, A., Hodgson, P. D., Yue, S., *ISIJ International* **35** 1995 79

Zarei Hanzaki, A., Hodgson, P. D., Yue, S., *Metallurgical and Materials Transactions A* **28A** 1997 2405

Zener, C., *Trans. AIME* **167** 1946 550